

Mass spectrometric gas phase diagnostics in particle forming flames

Von der Fakultät für Ingenieurwissenschaften,
Abteilung Maschinenbau und Verfahrenstechnik
der
Universität Duisburg-Essen

zur Erlangung des akademischen Grades
eines
Doktors der Ingenieurwissenschaften
Dr.- Ing.
genehmigte Dissertation

von
Yasin Hüseyin Karakaya
aus
Duisburg

Referentin: Prof. Dr. rer. nat. Tina Kasper
Korreferent: Prof. Dr. rer. nat. Christof Schulz
Tag der mündlichen Prüfung: 11.05.2021

Abstract

Functional materials in the form of nanoparticles and coatings offer a high potential for applications in energy conversion and in biomedicine due to their size-dependent properties. Alongside the chemical composition, the control of the morphology can open up new dimensions for the use of nanoparticles. The research unit FOR2284 of the German Research Foundation is focused on the gas phase synthesis of special materials consisting of iron oxide and silicon dioxide. The objective of the research unit is to develop design rules for technical synthesis processes based on a fundamental understanding of the gas phase processes. The initial step of the gas phase synthesis is the decomposition of the precursor by the reactions with flame species. Tetramethylsilane (TMS) is a frequently used precursor for the silicon dioxide synthesis. The reactivity of the precursor in the flame is investigated. It comprises the decomposition kinetics and flame interaction of different precursors. For the experimental analysis time-of-flight molecular beam mass spectrometry is used. A large number of intermediate species (silicon-containing monomers, hydrocarbon species and silicon containing clusters) are analyzed in tetramethylsilane (TMS)-doped $\text{H}_2/\text{O}_2/\text{Ar}$ flames. Based on these findings, a chemical reaction mechanism for different flame equivalence ratios ($\varphi = 0.6 - 1.2$) and different precursor concentrations (TMS = 400 - 800 ppm) is developed and evaluated. The decomposition kinetics of TMS are analyzed experimentally and simulatively by a systematic study. The results indicate that in the gas phase synthesis of silica particles, two distinct particle formation pathways are active, the path $\text{SiO} \rightarrow (\text{SiO})_n \rightarrow \text{Particle}$ and the path $\text{Si}(\text{OH})_4 \rightarrow \text{Si}_4\text{O}_{10}\text{H}_4 \rightarrow \text{Particle}$.

Iron pentacarbonyl is used as the precursor for the iron oxide synthesis. Some species in synthesis flames are not detectable with the time-of-flight molecular beam mass spectrometer system. For this reason, a novel and very sensitive sampling technique for the measurement of naturally occurring ions is used for the investigation of flames. Initially, this technique is evaluated in a methane flame. In an extensive study on methane ion chemistry, a quantification approach using equilibrium calculations is tested. After the evaluation of the technique, the flame structure of iron pentacarbonyl ($\text{Fe}(\text{CO})_5$)-doped $\text{H}_2/\text{O}_2/\text{Ar}$ flames for the production of iron oxide is analyzed. The results indicate that iron oxides (Fe_2O_3 , Fe_4O_5 and Fe_5O_5) and iron hydroxides ($\text{Fe}(\text{OH})_2$ and $\text{Fe}(\text{OH})_3$) are formed in synthesis flames. Two oxidation states of iron (Fe(II) and Fe(III)) occur spatially separated in the flame. A database comprising reaction kinetics data of species with Fe/C/O/H- and Si/C/O/H-elements is provided and used for the evaluation and creation of chemical reaction kinetics models. This work represents the first results for the optimization of the gas phase synthesis of special nanomaterials.

Zusammenfassung

Funktionale Materialien in Form von Nanopartikeln und Beschichtungen bieten aufgrund ihrer größenabhängigen Eigenschaften ein hohes Potenzial für Anwendungen in der Energieumwandlung und in der Biomedizin. Die Steuerung der Morphologie kann, neben der chemischen Zusammensetzung, neue Dimensionen für den Einsatz von Nanopartikeln eröffnen. Die Forschungsgruppe FOR2284 der Deutschen Forschungsgemeinschaft befasst sich daher mit der Gasphasensynthese spezieller Materialien bestehend aus Eisenoxid und Siliziumdioxid. Ihr Fokus besteht in der Entwicklung von Designregeln für technische Syntheseverfahren, die auf dem grundlegenden Verständnis der vorliegenden Partikelbildungsprozesse basieren. Der erste Schritt der Synthese ist die Zersetzung des Prekursors durch die Reaktion mit Flammenspezies. Tetramethylsilan (TMS) ist ein häufig verwendeter Prekursor für die Synthese von Siliziumdioxid. Das Ziel dieser Arbeit ist die Untersuchung der Reaktivität des Prekursors, dies umfasst die Zersetzungskinetik und die Flammenwechselwirkung. Mit Hilfe der Flugzeit-Molekularstrahl-Massenspektrometrie werden eine große Anzahl an Zwischenspezies (siliziumhaltige Monomere, Kohlenwasserstoffspezies und siliziumhaltige Cluster) in Tetramethylsilan (TMS)-dotierten $\text{H}_2/\text{O}_2/\text{Ar}$ Flammen bestimmt. Auf der Basis dieser Ergebnisse wird ein chemischer Reaktionsmechanismus für verschiedene Flammenäquivalenzverhältnisse ($\varphi = 0,6 - 1,2$) und verschiedene Prekursorkonzentrationen (TMS = 400 - 800 ppm) entwickelt und ausgewertet. Zusätzlich wird die Zersetzungskinetik von TMS in Flammen durch eine systematische Studie experimentell und simulativ analysiert. Die Resultate weisen darauf hin, dass bei der Gasphasensynthese von Siliziumdioxidpartikeln insbesondere zwei Partikelbildungswege aktiv sind, zum einen der Pfad $\text{SiO} \rightarrow (\text{SiO})_n \rightarrow \text{Partikel}$ und zum anderen der Weg $\text{Si}(\text{OH})_4 \rightarrow \text{Si}_4\text{O}_{10}\text{H}_4 \rightarrow \text{Partikel}$.

Eisenpentacarbonyl wird als Prekursor für die Eisenoxid-Synthese verwendet. Einige Spezies sind mit dem Flugzeit-Molekularstrahl-Massenspektrometer System nicht nachweisbar. Daher wird für die Untersuchung der Eisenoxid-Syntheseflammen eine neuartige und sehr empfindliche Probenentnahmetechnik zur Messung natürlich vorkommender Ionen eingesetzt. Zunächst wird dieses Verfahren mit Hilfe einer Methanflamme, aufgrund ihrer gut dokumentierten Chemie, evaluiert. In einer umfangreichen Studie über die Methan-Ionenchemie wurde ein Quantifizierungsansatz mittels Gleichgewichtsberechnungen getestet. Nach der Evaluierung der Messmethode wird die Flammenstruktur von Eisenpentacarbonyl ($\text{Fe}(\text{CO})_5$)-dotierten $\text{H}_2/\text{O}_2/\text{Ar}$ -Flammen für die Erzeugung von Eisenoxid analysiert. Die Ergebnisse zeigen, dass Eisenoxide (Fe_2O_3 , Fe_4O_5 und Fe_5O_5) und Eisenhydroxide ($\text{Fe}(\text{OH})_2$ und $\text{Fe}(\text{OH})_3$) in Syntheseflammen gebildet werden. Zwei Oxidationszustände von Eisen (Fe(II) und Fe(III)) treten in der Flamme räumlich getrennt auf. Es wird eine Datenbank mit reaktionskinetischen Daten von Spezies mit Fe/C/O/H- und Si/C/O/H-Elementen bereitgestellt und für die Auswertung und Erstellung von Modellen der chemischen Reaktionskinetik verwendet. Diese Arbeit stellt erste Ergebnisse für die Optimierung der Gasphasensynthese spezieller Nanomaterialien dar.

Preface

This thesis is the result of my studies as a PhD student from May 2015 to March 2021 at the University of Duisburg-Essen at the faculty of engineering in the work group mass spectrometry in reacting flows.

Prof. Dr. Tina Kasper was my major supervisor throughout the studies. During the time, we spent working together and I appreciated her professionalism and her overall personality. In addition, she enabled me to collaborate with many other inspiring scientists in various international projects and within the DFG research unit FOR2284. I was given the opportunity to present my research work at numerous scientific conferences. These significantly contributed to the development of my skills and allowed me to gain valuable experiences.

I am grateful for the constructive discussions with my co-supervisor Prof. Dr. Christof Schulz within the framework of the DFG research unit FOR2284.

I would like to thank Prof. Dr. Atakan for his confidence in me, who made the first contact and recommended me for the chair of thermodynamics. I appreciate his valuable contributions in particular to the preparation of my presentations.

It was a great honor to have been allowed to profit in so many ways in collaboration with of these experienced scientists.

I would like to thank the technical staff Stephan Steinbrink and Dipl.-Ing. Andreas Görnt for their help translating theoretical knowledge into practical research. I would like to thank our secretary Lisa Meiers for her organization support.

I am thankful for the fruitful cooperation's within the DFG research unit FOR2284, especially with Johannes Sellmann, Dr. Paul Sela, Dr. Sebastian Peukert, Dr. Irenäus Wlokas, Dr. Sebastian Kluge, Hossein Janbazi and Alexander Levish.

My colleague and friend Sascha Lau didn't just join me for his academic degree; we also had the opportunity to teach exercise lessons for the subject thermodynamics in the international course together.

The best memories at the international conferences were made with my colleague and friend Dr. Dennis Kaczmarek. I will remember and cherish those forever.

I would like to thank my office colleague PhD Munko Gonchikzhapov for sharing many of his family moments with me.

An almost unimaginable number of cups of coffee and at least as many discussions on all scientific and everyday topics were enjoyed in the microscopy laboratory. I would like to

thank all my colleagues from the department of thermodynamics for their valuable input – and the occasional cookie.

Furthermore, the student research assistants Anton Ditmann, Joe Attiah, Adrian Krummnow, Julian Malte-Wenning, Xiaoyu Zhao, Ünal Erdogan and Pengshan Dai accompanied me. I would like to thank you for the support in the laboratory and on the computer. I thank my colleague Martin Höner for his support in construction works.

I was able to share my joy about my first paper as a co-author within the collaboration with my colleague Dr. Awad Alquaity from the King Abdullah University of Science and Technology.

The collaboration with Dr. Denis Knyazkov from the Novosibirsk State University was always an inspiration whether it was in the office or the laboratory.

The measurement campaigns were enjoyed together with my colleague Dr. Thomas Bierkandt, Dr. Patrick Oßwald, Dominik Krüger and Dr. Markus Köhler from the German Aerospace Center and Dr. Erdal Akyildiz from the University of Duisburg-Essen and Dr. Patrick Hemberger from the Swiss Light Source.

I am thankful for the fruitful advices from Dr. Lennart Caspers, Charlotte Rudolph, Michael Aps, Julian Quenel and Dr. Peter Oketch during the preparation of this thesis.

In addition to my work at the university, I would like to thank my colleagues from the Oberhausen basketball department of TC Sterkrade 1869 for their cooperation during my voluntary work and my teammates who helped me to develop my personality.

I would like to thank my family who put in a lot of effort for me.

Table of content

Abstract	IV
Zusammenfassung	VII
Preface	IX
Table of content	XI
1 Introduction	1
1.1 Research focus.....	2
1.2 Organization of the thesis.....	2
2 Theoretical background	5
2.1 Pathways of gas phase synthesis of nanoparticles	5
2.2 Premixed flames	8
2.3 Ions in flames	9
2.4 Molecular beam.....	10
2.5 Time-of-flight mass spectrometry	13
2.5.1 Electron ionization	13
2.5.2 Principle of time-of-flight mass analysis	14
2.5.3 Two-stage ion extraction and reflectron	16
3 Modeling of premixed flames	19
3.1 Conservation equations	19
3.2 Reaction kinetics	21
3.2.1 Chemical reaction rate constants	21
3.2.2 Pressure dependence of rate constants.....	23
3.3 Thermodynamics.....	25
3.4 Heat and mass transport	26
3.4.1 Multicomponent formulation	26
3.4.2 Mixture-averaged formulation.....	28
3.5 Analysis of reaction mechanisms.....	31
3.5.1 Reaction flow analysis	31
3.5.2 Sensitivity analysis.....	32
4 Experiments and methodology	33
4.1 Experimental setup.....	33

4.2 Mass spectrometry.....	34
4.2.1 Molecular beam sampling.....	34
4.2.2 Mass spectrometer system.....	35
4.2.3 Quantitative data reduction.....	36
4.2.4 Direct calibrations.....	37
4.2.5 Indirect calibration.....	38
4.2.6 Ion sampling.....	40
4.3 Temperature.....	40
4.4 Error analysis.....	42
5 Conceptual research guidelines and motivation.....	45
6 Mass spectrometric study on the combustion of tetramethylsilane and the formation of silicon oxide clusters in premixed laminar low- pressure synthesis flames.....	49
6.1 Abstract.....	49
6.2 Introduction.....	50
6.3 Experimental.....	51
6.4 Data Analysis.....	52
6.5 Quantum chemical calculations of ionization energies of silicon-containing species.....	56
6.6 Results and discussion.....	58
6.6.1 Influence of TMS on species and temperature profiles.....	58
6.6.2 Silicon containing intermediates.....	61
6.6.3 Formation and growth of silicon oxide clusters.....	67
6.7 Conclusion.....	68
7 Development and evaluation of a chemical kinetics reaction mechanism for tetramethylsilane-doped flames.....	71
7.1 Abstract.....	71
7.2 Introduction.....	71
7.3 Experiment.....	73
7.4 Modeling approach.....	74
7.4.1 Calculation of thermodynamic data.....	75
7.4.2 Reaction mechanism optimization.....	75
7.5 Results and discussion.....	76
7.5.1 Thermodynamic data.....	76
7.5.2 Kinetics model.....	78

7.5.3	Comparison with different loads of TMS	96
7.6	Conclusions	100
8	Experimental and numerical study on the influence of equivalence ratio on key intermediates and silica nanoparticles in flame synthesis.....	101
8.1	Abstract	101
8.2	Introduction	101
8.3	Experiment and flame conditions.....	103
8.4	Numerical modeling and setup.....	104
8.5	Results and discussion.....	104
8.5.1	Temperatures and main flame species	104
8.5.2	TMS and carbon-containing composition products	107
8.5.3	Initial intermediates of TMS	109
8.5.4	Cluster and particle formation pathways	110
8.5.5	Particle characterization.....	113
8.6	Conclusion.....	114
9	New insights into methane-oxygen ion chemistry	115
9.1	Abstract	115
9.2	Introduction	116
9.3	Experimental details and ion chemistry model	117
9.3.1	Experimental setup and method.....	117
9.3.2	Numerical methods and model	118
9.4	Results and discussion.....	119
9.4.1	Neutral species	119
9.4.2	Cation Measurements.....	119
9.4.3	Modeling Results	123
9.5	Conclusions	124
10	Investigation of the combustion of iron pentacarbonyl and the formation of key intermediates in iron oxide synthesis flames	127
10.1	Abstract	127
10.2	Introduction.....	127
10.3	Experiment and flame conditions	129
10.3.1	Flame conditions.....	129
10.3.2	Photoionization molecular beam mass spectrometry (PI-MBMS)	129
10.3.3	Electron ionization molecular beam mass spectrometry (EI-MBMS).....	130

10.3.4	Ion sampling.....	131
10.3.5	Flame temperature.....	133
10.4	Numerical setup	133
10.5	Results and discussion	133
10.5.1	Influence of Fe(CO) ₅ on temperature, and product and radical species	133
10.5.2	Thermal decomposition of Fe(CO) ₅	135
10.5.3	Cationic flame structure	137
10.6	Conclusions.....	149
11	Influence of the sampling probe on flame temperature, species, residence times and on the interpretation of ion signals of methane/oxygen flames in molecular beam mass spectrometry measurements.....	151
11.1	Abstract.....	151
11.2	Introduction.....	152
11.3	Experiment and flame conditions.....	154
11.3.1	Flame conditions	154
11.3.2	Ion sampling (Flame C)	155
11.3.3	Electron ionization TOF analysis with expansion sampling (Flame B) and with molecular beam sampling (Flame A).....	156
11.3.4	Temperature measurements	157
11.4	Simulations.....	157
11.4.1	One-dimensional simulation	157
11.4.2	Two-dimensional simulation.....	157
11.5	Results and discussion	159
11.5.1	Influence of the sampling probe on flame temperature, species and residence times.....	159
11.6	Interpretation of ion signals	175
11.6.1	Temperatures in the molecular beam	177
11.6.2	Temperatures of probe and flame	179
11.6.3	Calculation of mole fraction profile of methanol based on protonated methanol ion signals.....	180
11.7	Conclusions.....	183
12	Summary	185
13	Outlook	191
	Bibliography.....	193

Appendix A of chapter 6	209
Appendix B of chapter 7	211
Appendix C of chapter 8	227
Appendix D of chapter 9	229
Appendix E of chapter 10	235
Appendix F of chapter 11	239
List of symbols	245
List of figure captions	249
List of table captions	257
List of publications	259

1 Introduction

In the last decades many fundamentals are obtained about the complex interaction of high-temperature reactions in fluid flows [1]. The gained information is used to optimize practical processes for energy conversion with the focus on high efficiency and little pollutant generation. Over time many experimental and methodical tools were developed to analyze the multi-scale and multi-phase problems like fuel evaporation, gas-phase reactions and particle growth, mostly in the context of soot formation. The experimental and computational tools used for combustion research can be utilized to gain new insights into the synthesis of nanomaterials and provide predictive process controllability of their production. Typically, combustion system studies are limited to compounds made up of the elements C, H, O and N, with metallic and organometallic substances usually used for materials synthesis. Quantification and numerical modeling of the nanoparticle synthesis processes need further research.

In the field of materials science, there is a high interest in developing functional materials in the form of powders or coatings which consist of both the metallic and organometallic elements and their oxides. Nanoparticles with up to a 100 nm diameter have unique size-dependent properties such as reduced melting temperature [2], increased electrical conductivity [3], mechanical strength [4] and reactivity [5]. In biomedicine, nanoparticles are used as, e.g. biological label [6], contrast medium [7], drug delivery [8], cancer therapy [9] and ultra violet protection [10]. For energy conversion-related applications nanoparticles or coatings are applied as anode materials in batteries [11], for enhancing solar cell efficiencies [12] and as catalysts for fuel cell reactions [13].

A detailed review of synthesis methods and applications can be found in [14] while the underlying kinetics and diagnostic challenges of gas phase synthesis are given in [1]. The established method of gas phase synthesis can further be divided into two types: Gas phase and spray. Spray flame pyrolysis (FSP) synthesis is a promising and versatile method for the fast and scalable synthesis of nanostructured materials with tailored functionalities [15]. The advantage of the spray method is that its main limitation is set by the solubility of the precursor in the solvent used for the spraying. As a result, a variety of compounds can be used and combined. The gas phase synthesis - a continuous flow process - can be scaled up with respect to the output volume and metastable materials in terms of composition and crystal structure can be obtained by quenching methods after the particles are formed in the reaction zone [1]. Most wet-phase methods are operated in batch mode and end up with thermodynamically stabilized materials. Consequently, spray flames produce materials beyond the materials spectrum of wet-phase methods. A comprehensive understanding of the synthesis process is difficult to obtain because many processes are involved. The kinetics of precursors and the interaction with flame species play an important role in both flame types but can only be studied well in gas phase.

Only a few previous studies focus on the analysis of the concentration profiles of atoms and molecules of precursor species using optical methods such as laser induced fluorescence (LIF) [16-20] or molecular beam mass spectrometry (MBMS) [21-23] in reacting flows. The latter is an established method in the field of combustion research [24-31]. Here, a sample is

injected into a mass spectrometer system to analyze its composition. Once different species including atoms, molecules, and clusters at different stages of the process have been identified, the chemical reaction pathways leading to the particles can be inferred. The resulting chemical reaction mechanisms are important input data for the simulation of the synthesis, which will ultimately help to design and control the entire synthesis process.

1.1 Research focus

Progress in moving away from empirical methods-based design towards knowledge-based design of the production of nanomaterials for a specific application is impeded by a lack of knowledge on the fundamental processes governing the synthesis at each step of the process. The high potential for the application of nanomaterials is not fully tapped and can only be exploited when beside the variation of the chemical composition of the particles their structures can be controlled, too.

To achieve these goals, the research unit FOR2284 of the German Research Foundation focuses on the investigation of the elementary steps of gas phase synthesis including precursor chemistry, particle inception, particle-particle interactions and in situ functionalization. A complete understanding of the initial elementary steps of precursor decomposition and its flame interaction is a prerequisite for process design and control.

The *research focus of this work* lies on the investigation of the gas phase synthesis of nanoparticles in premixed flames and the formation of silicon dioxide and iron oxide materials. The *scientific questions* that will be addressed include how different precursors decompose, which of the formed intermediates react towards particles, how the precursor chemistry interacts with the flame chemistry, and how the flame conditions influence the synthesis process. To address these issues, mole fraction profiles of reactants, intermediates and product species must be obtained. Molecular beam mass spectrometry (MBMS) is employed as an analytical inline technique. It must be adapted to the special requirements of the investigation of particle synthesis processes. This includes adequate solutions to the clogging tendency of the sampling probe. These challenges can only partly be overcome with the established MBMS methods. The advancement of experimental techniques for in-line process analysis and process control in synthesis flames is a prerequisite for the primary goals. For the measurement of highly elusive intermediates a new sampling system is developed and tested. This sampling system helps to collect data complementary to the established molecular beam technique. The experimental data are needed as a base for the development and evaluation of chemical reaction mechanisms.

The particle phase is *not the subject of this investigation*, as this requires other experiments and modeling techniques.

1.2 Organization of the thesis

This thesis is structured in 13 chapters. The current chapter is the introduction into the global context and shows the scientific questions of this work that deals with the precursor chemistry and the interaction with the flame chemistry in flame reactors. In chapter 2, the theoretical background of the gas phase synthesis, laminar low-pressure flames, ions in

flames, molecular beam and time-of-flight mass spectrometry is introduced. This is followed by the description of the fundamental principles of the modeling of one-dimensional flames and the methods used for the analyses of the reaction mechanisms (chapter 3). Chapter 4 addresses the details of the experiments and the methodologies used for the evaluation of the experimental data. Chapter 5 describes the concept and motivation of the investigation. The scientific results are presented in the main body of this thesis (chapters 6-11), which have been published in peer-reviewed journals and presented at scientific conferences. Each chapter contains a short introduction and is then divided into several sections such as, modeling, experiments and discussion of the results. Finally, they are concluded with a summary.

Chapter 6 describes the mass spectrometric investigation of the combustion of the frequently used precursor tetramethylsilane and offers insights into the chemical reaction pathways in silicon dioxide synthesis flames. Chapter 7 describes the development of the chemical reaction mechanism of tetramethylsilane in a flame and evaluates how various precursor concentrations influence the pathways. Chapter 8 presents an assessment of the developed chemical reaction mechanism of a silicon-containing precursor for varied flame equivalence ratios.

Chapters 9 -11 comprise the development of a mass spectrometric analysis of particle-laden flows with aid of a novel ion sampling technique. Several topics are addressed. First, the new technique is applied to a neat hydrocarbon flame and its ability to detect flame species is evaluated. Second, it is tested for the analysis of the formation routes of iron oxide nanoparticles in a synthesis flame and third the initial work on developing a quantification method is described. The last chapters are the summary, outlook, appendices, bibliography, and the list of publications.

2 Theoretical background

In chapter 2, the fundamental theoretical background for this thesis is explained. It consists of subsections for the principle of the gas phase synthesis, laminar low-pressure flames, ions in flames, molecular beam, ionization and mass spectrometer systems.

2.1 Pathways of gas phase synthesis of nanoparticles

The simplified principle of the SiO_2 particle formation in the gas phase is exemplarily shown in Figure 2-1 [32]. Frequently used precursors for the gas phase synthesis of silicon dioxide nanoparticles are silane (SiH_4), tetrachlorsilan ($\text{Si}(\text{Cl})_4$), tetraethyl orthosilicate (TEOS), hexamethyldisiloxane (HMDSO) and tetramethylsilane (TMS), which contain the elements of interest, which is silicon. Within this work, tetramethylsilane (TMS) is introduced in the gas phase into the premixed $\text{H}_2/\text{O}_2/\text{Ar}$ flame. The precursor reacts with flame species like O_2 , H_2 , O , OH , H and H_2O and decomposes to smaller molecules. Subsequently, condensable monomers are formed that then form the first particle and grow to bigger agglomerates [32]. The above-mentioned precursors have in common that the reaction kinetics of the precursor decomposition, its interaction with the flame and the routes of particle formation are not completely understood. A detailed description of the initial particle formation needs knowledge of the molecular intermediates.

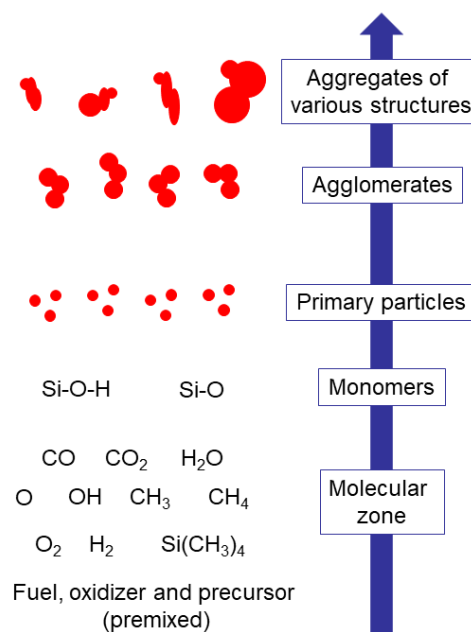


Figure 2-1. Principle of silicon dioxide particle formation in a flame. The schematic is based on [32].

TMS is studied in many studies under pyrolytic conditions [33-35]. The only studies about its oxidation are performed in a vessel and were done by Baldwin et al. [36] and Reed et al. [37] (Table 2-1). For TMS, they suggest an H-abstraction from the molecule by reaction

with H/O/OH and O₂ and a subsequent production of a peroxide by reaction with O₂. Baldwin et al. [36] propose two likely reaction schemes to produce the first silanol (Table 2-1). Many studies focus on the investigation of the particle formation routes in the gas phase synthesis. In silane flames, the particle formation is postulated to proceed via self-clustering of SiO and SiO₂ (Table 2-2). As a consequence, SiO, which is an important intermediate since it is often said to link gas and particle phase, came into focus of many studies like those of Feroughi et al. [19] in hexamethyldisiloxane (HMDSO) doped flames and Glumac [38] in hexamethyldisilazane (HMDS) doped flames. On the basis of equilibrium calculations for TEOS, Si(OH)₄ as important intermediate for particle formation has been in the limelight for many studies [39-41]. The particle phase is investigated in various studies. The particle size profiles in HMDSO-doped flames were measured by Feroughi et al. [19] or in SiH₄-doped H₂/O₂/Ar flames by Lindackers et al. [42]. An overview of the effect of the precursor on the flame-made particle characteristics is given by Briesen et al. [43]. The particle growth mechanisms are explained by Ulrich et al. [44-47].

Table 2-1. Initial reactions of tetramethylsilane, TMS

Initial decomposition	<ul style="list-style-type: none"> • $\text{Si}(\text{CH}_3)_4 + \text{H} \rightarrow (\text{CH}_3)_3\text{SiCH}_2 + \text{H}_2$ [36] • $\text{Si}(\text{CH}_3)_4 + \text{OH} \rightarrow (\text{CH}_3)_3\text{SiCH}_2 + \text{H}_2\text{O}$ • $\text{Si}(\text{CH}_3)_4 + \text{O} \rightarrow (\text{CH}_3)_3\text{SiCH}_2 + \text{OH}$ • $\text{Si}(\text{CH}_3)_4 + \text{O}_2 \rightarrow (\text{CH}_3)_3\text{SiCH}_2 + \text{HO}_2$
Peroxide formation	<ul style="list-style-type: none"> • $(\text{CH}_3)_3\text{SiCH}_2 + \text{O}_2 \rightarrow (\text{CH}_3)_3\text{SiCH}_2\text{O}_2$ [36]
Silanol formation	<ul style="list-style-type: none"> • $(\text{CH}_3)_3\text{SiCH}_2\text{O}_2 + \text{H}_2 \rightarrow (\text{CH}_3)_3\text{SiCH}_2\text{O}_2\text{H} + \text{H}$ [36] <ul style="list-style-type: none"> ○ $(\text{CH}_3)_3\text{SiCH}_2\text{O}_2\text{H} \rightarrow (\text{CH}_3)_3\text{SiOH} + \text{CH}_2\text{O}$ • $(\text{CH}_3)_3\text{SiCH}_2\text{O}_2 \rightarrow (\text{CH}_3)_3\text{SiO} + \text{CH}_2\text{O}$ <ul style="list-style-type: none"> ○ $(\text{CH}_3)_3\text{SiO} + \text{H}_2 \rightarrow (\text{CH}_3)_3\text{SiOH} + \text{H}$

Table 2-2. Routes from monomer to cluster and particles

Cluster / Particle formation	<ul style="list-style-type: none"> • $(\text{SiO})_n + \text{SiO} \leftrightarrow (\text{SiO})_{n+1} \rightarrow \text{Particle}$ [48] • $(\text{SiO}_2)_n + \text{SiO}_2 \leftrightarrow (\text{SiO}_2)_{n+1} \rightarrow \text{Particle}$ for $1 \leq n \leq 9$
Particle formation	<ul style="list-style-type: none"> • $\text{Si}(\text{OH})_4 \rightarrow \text{Particle}$ [39]

Iron pentacarbonyl (Fe(CO)₅) is frequently used for the gas phase synthesis of iron oxides. There are many studies dealing with the reaction kinetics of Fe(CO)₅ [21, 22, 49-54], but there is still a lack of knowledge about its decomposition in the flame. Its first reaction mechanism was proposed by Linteris et al. [50] who investigate its inhibition effect on

flames (see Table 2-3). Its decomposition product $\text{Fe}(\text{CO})_2$ can undergo bimolecular reactions as listed in Table 2-3 according to Wen et al. [55].

Staude et al. [56] updated the reaction mechanism regarding the measurements of Hecht et al. [54] who measured atomic iron for various $\text{Fe}(\text{CO})_5$ concentrations in premixed $\text{H}_2/\text{O}_2/\text{Ar}$ by means of laser-induced fluorescence (LIF). The original reaction kinetics model was further evaluated by Gerasimov et al. [21, 22] who measured for the first time a set of species profiles comprising the species (Fe , FeOH , FeO_2 and $\text{Fe}(\text{OH})_2$) with aid of molecular beam mass spectrometry in premixed $\text{H}_2/\text{O}_2/\text{N}_2$ flames at atmospheric pressure. Based on the comparisons of the total concentrations of measured and simulated iron-containing species, they further propose that the simulation of species such that Fe_2O_3 , and $\text{Fe}(\text{OH})_3$ could be missing parts of the reaction mechanism, which could not be detected in the gas phase so far. The original $\text{Fe}(\text{CO})_5$ mechanism [50] was updated by Wlokas et al. [52] through a new decomposition rate of iron pentacarbonyl as well as new thermochemical data for Fe , FeO and $\text{Fe}(\text{OH})_2$. In addition, new reactions for the formation of a hypothetical Fe_2O_3 in the gas phase were introduced. Feroughi et al. [53] found evidence of non-oxidized Fe . They discuss a mechanism via intermediate formation of iron clusters and elemental iron particles and a subsequent oxidation. They modified and merged the mechanism of Rumminger et al. [50], Wlokas et al. [52] and Wen et al. [55] to describe the pyrolysis of $\text{Fe}(\text{CO})_5$ and the formation of Fe -clusters. This merged reaction mechanism of $\text{Fe}(\text{CO})_5$ was further evaluated by Kluge et al. [57] who measured Fe by Fe -LIF and FeO species by gas sensors based on intracavity laser absorption spectroscopy (ICLAS) measurements. They determined the deposition of the particle phase with aid of a quartz crystal microbalance (QCM), which reveals a prompt peak related to particles close to the burner (first particle zone) and an increase at larger distances (second particle zone). Since their measurements reveal that Fe and FeO have vanished before the second particle forming zone starts, they conclude that other species contribute to the formation of the late-stage particles, such as $\text{Fe}(\text{OH})_2$. The influence of precursor concentration on composition, structure, morphology and size in premixed $\text{H}_2/\text{O}_2/\text{Ar}$ flames was studied by Janzen et al. [58].

Apart from the current theoretical knowledge of both material systems, there is still a lack of experimental data regarding the detailed description of the reaction kinetics of the precursor decomposition and the particle formation in the flame.

Table 2-3. Reactions and routes of iron in the gas phase

Thermal decomposition	• $\text{Fe}(\text{CO})_5 \rightarrow \text{Fe} + 5 \text{CO}$	[50]
O-atom cycle	• $\text{Fe} \rightarrow \text{FeO}_2 \rightarrow \text{FeO} \rightarrow \text{Fe}$	[50]
H-atom cycle	• $\text{FeO} \rightarrow \text{Fe}(\text{OH})_2 \rightarrow \text{FeOH} \rightarrow \text{FeO}$	[50]
Particle formation	• $\text{Fe} \rightarrow \text{Fe}_n \rightarrow \text{Particle}$	[55]
Pathway through $\text{Fe}(\text{CO})_2$	<ul style="list-style-type: none"> • $\text{Fe}(\text{CO})_2 + \text{Fe} \leftrightarrow \text{Fe}_2\text{CO} + \text{CO}$ • $\text{Fe}(\text{CO})_2 + \text{Fe}_n \leftrightarrow \text{Fe}_2\text{CO} + \text{CO}, n = 2 - 6$ • $\text{Fe}(\text{CO})_2 + \text{Fe}_n\text{CO} \leftrightarrow \text{Fe}_{n+1}(\text{CO})_2 + \text{CO}, n = 1, 2$ • $\text{Fe}(\text{CO})_2 + \text{Fe}(\text{CO})_2 \leftrightarrow \text{Fe}_2(\text{CO})_3 + \text{CO}$ 	[55]
Particle formation	• $\text{Fe}(\text{OH})_2 \rightarrow \text{Fe}_2\text{O}_3 \rightarrow \text{Particle}$	[52]

2.2 Premixed flames

Laminar flames are frequently used to investigate the reaction kinetics of fuels [25, 29, 31]. These types of flames are stabilized on the porous matrix of a burner through which the premixed reactants are introduced. The initial cold gas composition of the flame is well-defined due to the prior premixing of the fuel and the oxygen. A parameter to describe the initial flame composition is the equivalence ratio, which denotes the ratio of the mole fraction of the oxygen and the fuel to the stoichiometric ratio of the oxygen and the fuel:

$$\varphi = \frac{\frac{x_{\text{O}_x}}{x_{\text{Fuel}}}}{\left(\frac{x_{\text{O}_x}}{x_{\text{Fuel}}}\right)_{\text{Stoichiometric}}} . \quad (2-1)$$

Three characteristic equivalence ratios can be distinguished. In the stoichiometric case ($\varphi = 1$), the fuel and oxygen are completely consumed. In the fuel-lean case ($\varphi < 1$) there is an excess of the oxygen. Under fuel-rich conditions ($\varphi > 1$), the amount of the oxygen is limited and consequently there is an excess of fuel.

The fluid flow exiting the burner is laminar because of the very small gas velocity. It has almost no divergence in radial direction and only changes as a function of the distance coordinate, which also means that there is no time-dependent fluctuation of species and temperature at a defined position in the flame.

Three characteristic flame zones are present in the flame as shown in Figure 2-2: Preheat zone, reaction zone and recombination zone. The narrow preheat zone is directly downstream of the burner surface. In the preheat zone, fuel and oxygen have their maximum mole fraction and are heated due to heat and mass transport by heat conduction and back diffusion from the reaction zone. The reaction zone is further downstream. In the reaction

zone, the fuel and oxygen react and decompose to smaller molecules, while intermediates are formed and reach their maximum mole fractions in the flame. The temperature rises rapidly up to the end of the reaction zone due to the exothermic oxidation of the fuel. Simultaneously, the mole fractions of the product species rise until they reach their equilibrium composition in the recombination zone. The gradients in the equilibrium composition and flame temperature become zero. Heat losses to the surroundings can lead to a slight decrease in flame temperature and a small change in equilibrium composition. Laminar flames are typically operated at low pressures (20-160 mbar), which leads to the expansion of their characteristic flame zones. Consequently, high spatial resolution of the one-dimensional temperature and species profiles measurements is achieved.

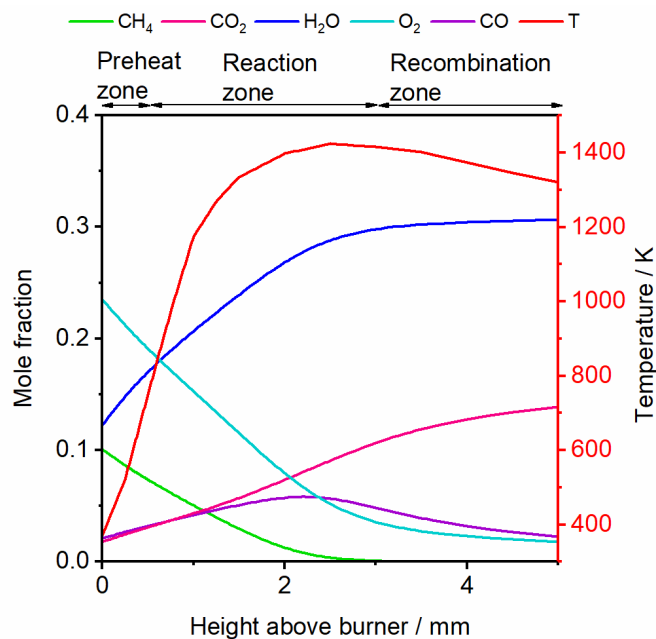


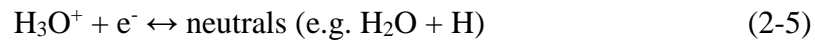
Figure 2-2. Schematics of the species and temperature profiles in one-dimensional flames. The red curve indicates the temperature profile, the blue curve indicates the precursor and/or oxygen, the green curve and the black curve indicate the formation of intermediate species along the centerline of the flame. The figure is adapted from [59].

2.3 Ions in flames

In hydrocarbon flames, ions are present alongside the neutral flame species. The neutral flame species account for the major part of the flame chemistry and are present in mole fractions which are many orders of magnitude larger than the mole fractions of ions. The mole fractions of the ionic species are less than 10^{-8} [60]. Despite their small mole fractions, ions can be used to get insights into how neutral species grow and decay. The flame ions are formed from neutral flame species. If both the ion and the neutral counterpart can be

measured, similarities in the profiles of ions and the counterpart are observed. Further details can be found in [61] and in chapter 9-11 [30, 62].

The most common scheme for the formation of naturally occurring ions in hydrocarbon flames is initiated by chemi-ionization, where the flame radicals CH and O react with each other and form the first cation CHO^+ and an electron by reaction (2-2) [61]. The chemi-ion CHO^+ transfers its proton to water, which has a higher proton affinity, so that H_3O^+ is formed by a proton-transfer reaction (2-3). In subsequent proton-transfer reactions primary ions (AH^+) are formed according to the reaction (2-4), where (A) indicates any neutral species in the flame, e.g. intermediates and product species. In the recombination zone of the flame, the hydronium ion H_3O^+ recombines with an electron and forms neutrals (2-5). Also, other ions can undergo recombination reactions with electrons and form neutral species (2-6). A more detailed description of the ion formation reactions is given in [61].



2.4 Molecular beam

For the mass spectrometric analysis, a gas sample must be transferred to the mass spectrometer. In reactive flows, the reactions must be quenched so the composition does not change while the sample is analysed. One possibility is molecular beam sampling, which was used in this work and is explained in more detail in the following.

Figure 2-3 shows a schematic of the formation of a molecular beam. The gas expands supersonically from p_0 to p_1 through an orifice D_0 of an aperture. The supersonic expansion is characterized by a mean free path length of the molecules that is significantly smaller than the orifice of the aperture. Consequently, during the supersonic expansion the molecules collide with each other very frequently. The energy balance for a perfect gas with constant heat capacity flowing through an adiabatic sampling probe yields

$$\frac{w_1^2}{2} - \frac{w_0^2}{2} = h_0 - h_1 = c_p \cdot (T_0 - T_1), \quad (2-7)$$

where w denotes the flow velocity and h the specific enthalpy. The index 0 indicates the entry of the aperture and the index 1 indicates the end of the expansion. The fast expansion of the gas after passing the inlet orifice is treated as isentropic. Both friction and heat losses are neglected. Because of the expansion, a redistribution occurs: The kinetic energy of the

gas flow increases, while the enthalpy of the gas and consequently the temperature of the gas flow decreases.

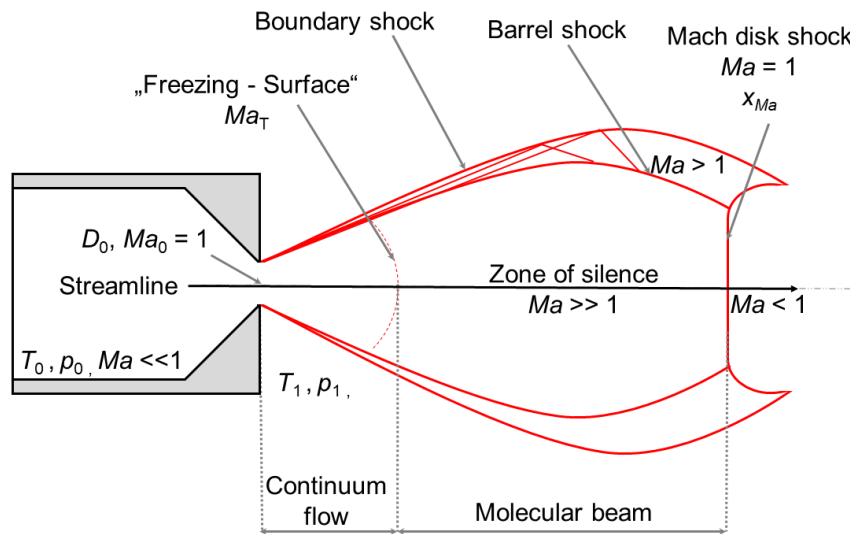


Figure 2-3. Schematic of a supersonic expansion and its characteristic shocks. The streamline indicates the direction of the flow. The schematic is adapted from [63].

Figure 2-3 shows the characteristic shocks during the supersonic expansion of a gas flow. The different regions will be described in the following. For the description of the supersonic expansion the Mach number Ma is a characteristic quantity and is defined as the ratio between the speed of the gas flow w and the speed of sound c according to

$$Ma = \frac{w}{c}. \quad (2-8)$$

The speed of sound is calculated by

$$c = \sqrt{\kappa \frac{RT}{M}}, \quad (2-9)$$

where R denotes the molar universal gas constant, T the temperature of the flow, M the molar mass of the flow. The isentropic coefficient $\kappa = c_p/c_V$, is expressed as the ratio of the isobaric and the isochoric heat capacities c_p and c_V , respectively.

For $Ma < 1$ the gas flow velocity w is smaller than the speed of sound velocity c , while $Ma > 1$ represents supersonic flow. At the orifice of the aperture the flow reaches a Mach number of $Ma = 1$, when the ratio of p_0 and p_1 exceeds a critical value of G

$$G = \left(\frac{\kappa + 1}{2} \right)^{\frac{\kappa}{\kappa - 1}}. \quad (2-10)$$

For all gases the critical value G depends on the isentropic coefficient and is less than 2.1 [63]. In this case the pressure inside the molecular beam is independent of the background pressure p_1 and is approximately p_0/G [63]. To describe the change of the Mach number as a function of the distance to the orifice, the conservation equations for mass, momentum and energy for the gas flow have to be solved. By means of the method-of-characteristics for axial symmetric flows, e.g. through a round aperture, the Mach number can be described as a function of the distance x according to [64, 65]

$$Ma(x) = A \left(\frac{x - x_0}{D} \right)^{\kappa-1} - \frac{1}{2A} \frac{[(\kappa + 1)/(\kappa - 1)]}{[(x - x_0)/D]^{\kappa-1}}, \quad (2-11)$$

where D is the diameter of the aperture. The values for the constants A and G are tabulated for various isentropic coefficients κ and can be found in [64, 65]. The equation (2-11) is referred to as continuum isentropic flow. The end of the continuum isentropic flow is described by the terminal Mach number and is defined as [65]

$$Ma_T = G \left(\frac{\lambda_0}{D\epsilon} \right)^{-(\kappa-1)/\kappa}, \quad (2-12)$$

where λ_0 is the length of the mean free path at the aperture, and ϵ is the collision efficiency. Behind the continuum flow, the gas expands further and the molecular beam is formed. The molecular beam is characterized by a small number of collisions between the molecules, high Mach numbers ($Ma \gg 1$), narrow velocity distributions, low constant temperatures, constant density distribution. The core of the molecular beam is also described as the zone of silence, where the chemical reactions are frozen and the highly reactive species are conserved. The zone of silence is limited at the sides by the boundary shock and at the front by the Mach disk ($Ma = 1$) (Figure 2-3). The location of the Mach disc x_{Ma} only depends on the ratio between the pressures p_0 , p_1 and the diameter D of the aperture and can be calculated by [65]

$$x_{Ma} = 0.67D \sqrt{\frac{p_0}{p_1}}. \quad (2-13)$$

The mass flow through an aperture and an isentropic adiabatic expansion is described by

$$\dot{m} = \frac{1}{4} \cdot \pi D_0^2 p_0 \sqrt{\frac{\kappa M}{RT_0}} \cdot \left(\frac{2}{\kappa + 1} \right)^{\frac{\kappa+1}{2(\kappa-1)}}. \quad (2-14)$$

The molecular beam is a prominent method to quench chemical reactions for a subsequent mass spectrometric analysis. In many applications, the molecular beam is formed by a conical sampling probe. The conical shape reduces perturbation of the flow field of the

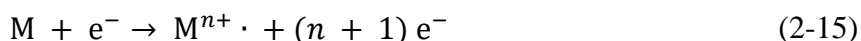
flame. Behind the sampling probe, a skimmer penetrates into the zone of silence and extracts the core of the molecular beam.

2.5 Time-of-flight mass spectrometry

Time-of-flight mass spectrometers are used for the elemental analysis of molecules or atoms by separating their ions according to their time-of-flight. The time-of-flight is correlated with the mass-to-charge ratio (m/z) of an ion. Figure 2-4 schematically shows an orthogonal Time-of-flight mass spectrometer, which is described below. A more detailed description of this setup and different types of setups can be found in [66, 67].

2.5.1 Electron ionization

Electron ionization involves ionizing the molecules with the aid of a high-energy electron beam. If an electron hits a molecule with high kinetic energy and transfers the energy which is needed to remove an electron from the molecule, ionization can occur according to



and ions with $n = 1-3$ number of electrons are formed [67]. The ionization energy of most flame molecules is between 6 – 16 eV. The threshold energy needed for ionization is called ionization energy. If the ionization energy of the molecule is exceeded, the electron deposits more energy in the molecule than needed for simple ionization and the molecule can fragment into smaller products. To avoid fragmentation of the molecule electron ionization is performed close to the ionization threshold. More details of ionization methods can be found in references [66, 67].

In the ionization chamber, a heated filament (cathode) is an often-used approach to generate an electron beam. The ions are accelerated in various electric fields to control their kinetic energy and their path in the ionization chamber. The generated electron beam intersects with the molecular beam of molecules from the sample and then discharges at a collector anode.

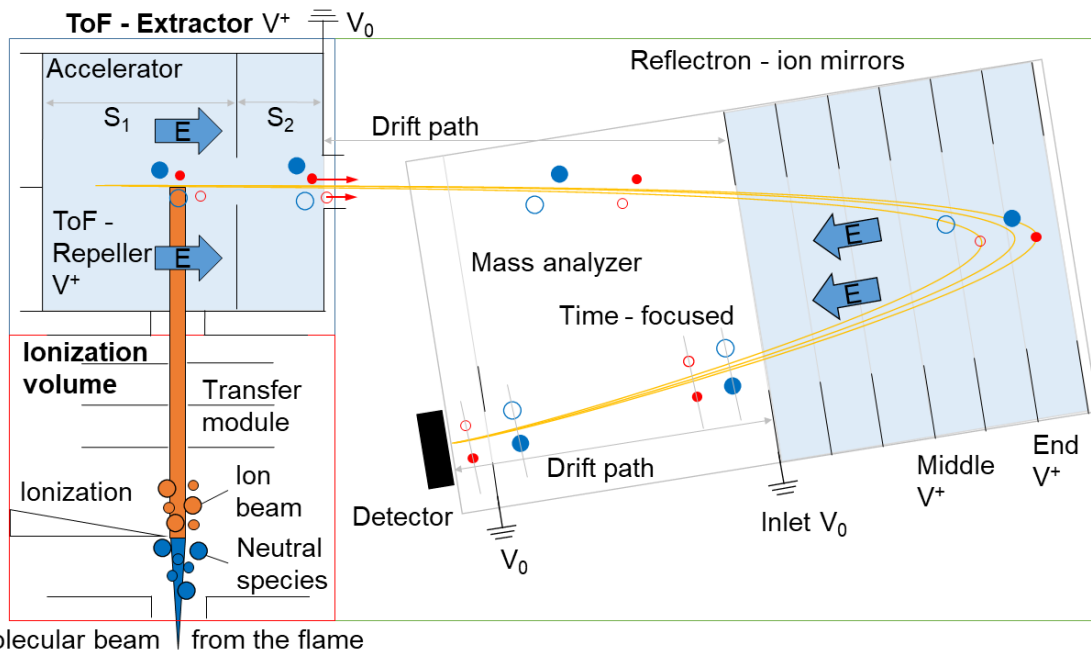


Figure 2-4. Schematic representation of an orthogonal time-of-flight mass spectrometer system with a reflectron divided in modular sections: Sample inlet, ionization source and transfer lenses (red section), and accelerator (blue section), mass analyzer (green section). Light ions (red filled and empty spheres) and heavy ions (blue filled and empty spheres) in the orthogonal accelerator and in the drift range with lower (empty spheres) and higher (filled spheres) kinetic energy. The different lengths of the red arrows indicate different kinetic energies of the ionized molecules. Ions with different kinetic energies are time-focused after reflection. The schematic is based on [67].

2.5.2 Principle of time-of-flight mass analysis

The ions are accelerated in an electric field, then enter a field-free drift path and subsequently are separated in the mass analyzer based on their time-of-flights. The principles of the time-of-flight analysis are described below.

The electric potential energy E_{el} to move an ion with the electrical charge q in the homogeneous electric field of a plate capacitor between two points is related to the potential difference U and is given by

$$E_{el} = q \cdot U = e \cdot z \cdot U, \quad (2-16)$$

where z is the integer charge number and the elementary charge is $e = 1.602176634 \cdot 10^{-19}$ C [68]. The electrical energy is equal to the potential energy of the ion and is completely converted into kinetic energy in the acceleration region

$$E_{el} = e \cdot z \cdot U = E_{pot} = E_{kin} = \frac{1}{2} \cdot m_i \cdot v^2. \quad (2-17)$$

With m_i mass of ion i and $m_i = M_i \cdot m_u$, where M_i is the molar mass in atomic mass units and the atomic mass unit, $m_u = 1.66053906660 \cdot 10^{-27}$ kg [68], which corresponds to the mass of 1/12 of the ^{12}C -isotope. Rearranging to the velocity v of the ion yields

$$v = \sqrt{\frac{2 \cdot e \cdot z \cdot U}{m_i}}. \quad (2-18)$$

For a uniform motion, the velocity v is defined as

$$v = \frac{s}{t}. \quad (2-19)$$

Since the drift path s is known, the time-of-flight of an ion is

$$t = \sqrt{\frac{m_i}{z}} \cdot \frac{s}{\sqrt{2 e U}}. \quad (2-20)$$

The following proportionality applies to the time dependence of the ions of different mass and charge during the drift in field-free space

$$t \propto \sqrt{\frac{m_i}{z}}.$$

This relationship shows that for the same ion charge z lighter ions have a shorter time-of-flight. Additionally, it can be concluded that for the same m/z , the time-of-flight of the ions will not differ significantly. A high mass resolution is necessary to separate the ions of the same nominal mass, e.g. CO with $m/z = 27.9949$ and C_2H_4 with $m/z = 28.0313$. The mass resolution R is defined as $R = m/\Delta m$, where $\Delta m/z$ corresponds to the smallest difference for which a signal can still be separated at m/z . The resolution can also be expressed in terms of the time-of-flight. A method commonly used in practice is the FWHM – method (full width at half maximum height), where for Δm the peak width at half height of m/z is used to calculate R (2-21)

$$R = \frac{\frac{m}{z}}{\Delta\left(\frac{m}{z}\right)} = \frac{m}{\Delta m} = \frac{t}{2 \cdot \Delta t}. \quad (2-21)$$

2.5.3 Two-stage ion extraction and reflectron

The ions from the sample are produced in the ionization chamber. An ion transfer module consisting of electrostatic lenses transfers the ions by applying a potential gradient into the extraction module, which is the region between the repeller and extractor. Initially, no voltage is applied to the repeller, so this region is field free and the ions can continue in their direction. Then a voltage is applied to the repeller. By the resulting electric field, the ions are pushed in orthogonal direction to their original trajectory. When all ions are in the flight tube the voltage is switched off and the orthogonal accelerator is filled again. After the filling process, the ions are extracted and their time-of-flight is measured. The two-stage extraction module is combined with a reflectron, which increases the spatial resolution and directs the ions optimally to the detector. The ions are registered by means of an MCP. The principle of the two-stage extraction and the reflectron is explained below.

Ideally, all ions are accelerated by the same amount and have the same starting energy. When ions of the same m/z are ionized at different starting positions, then they are accelerated for different periods of time and for a different distance in the acceleration field. As a result, ions of the same m/z enter the mass analyzer with different kinetic energies and consequently with different velocities.

Wiley and McLaren developed a two-stage ion extraction to compensate the influence of the different starting points of ions with the same m/z [69]. It is built from three electrodes, so that two different acceleration potentials can be applied. The benefit of the extraction method is, that all ions with the same m/z are spatially focused by adjusting the acceleration voltage in the two sections.

Time-of-flight mass spectrometers can be operated in two modes: Linear mode and reflectron mode. In linear mode, the ions move on a linear trajectory prior to hitting the detector. The mass resolution in linear mode is around $R = 500$ [67]. The small resolution R in the linear mode is a consequence of the short drift path. In order to separate neighboring masses, e.g., $m/z = 28$ for CO, N₂ and C₂H₄, a higher mass resolution is required. A higher resolution can be achieved by extending the drift path s of the ions. An extension of the drift path in the linear mode by lengthening the flight tube would result in an excessive increase in the exit angle of the ion beam and a reduction of the focus on the detector.

For this reason, a reflectron can be used to extend the drift path of the ions. It consists of ion mirrors and creates a retarding electric field, which reflects the ions and forces them to pass through the drift path a second time (see Figure 2-4). The combination of the two stage extraction and the reflectron was developed by Mamyrin [70] to compensate the energy distribution and to increase the resolution of the mass analyzer.

Ions of the same m/z with a higher kinetic energy penetrate deeper into the reflectron than ions with lower kinetic energy resulting in longer residence times in the reflector. As a result the ion reflection focuses the spatial distribution of the ions and leads to a narrower time-of-flight distribution of ions with the same m/z before hitting the detector.

A common technique to realize a proper ion detection is by using a micro-channel plate (MCP) [67]. It is a plate with parallel cylindrical channels. These are microscale electron multiplier channels. A plate enables an amplification of 10^2 - 10^4 and this value can be increased by using several plates up to 10^8 [66]. MCP have very fast response times, which

are well suited for the mass analyzer. The large sensitive area of the MCP enables the detection of large ion beams from the analyzer without additional focusing. At the output of the plate, a metal anode collects the secondary electrons of all channels and the current is measured. The analog output signal of the MCP can be converted into a computer-based format via a fast analog-to-digital converter. Other types of ion detectors are described in [66, 67]. The whole range of ions is displayed in a single time-of-flight spectrum for each sample. In the work described in this thesis an ion counting technique is employed to improve the signal-to-noise ratio of the signals. Only signals that exceed a preselected threshold voltage are counted as events. The threshold is chosen so that each event corresponds to a single ion. Spectra are obtained by averaging over many events.

3 Modeling of premixed flames

The fundamentals of modeling laminar flames are explained in chapter 3. It contains the description of the assumptions, conservation equations, reaction kinetics, thermodynamics, heat and mass transport and the tools used for the analysis of reaction mechanisms.

Some assumptions are made for the numerical calculation of the one-dimensional flame structure, as listed in the following according to Warnatz et al. [71, 72]. The gases will be assumed to be ideal gases. For upwards burning flames, external forces, e.g. gravitation, buoyancy are not considered. Viscous effects can be neglected as well. The kinetic energy of the gas flow is negligible. Local thermal equilibrium is achieved in the flame.

For the quantitative description of the local composition in the flame the quantities mole fraction or mass fraction are used. The mole fraction x_k denotes the ratio of the number of moles n_k of each species and to overall number of moles of the mixture n and the mass fraction y_k is the ratio of the mass of each species m_k to the overall mass of the mixture m according to

$$x_k = \frac{n_k}{n} \quad \cap \quad y_k = \frac{m_k}{m}. \quad (3-1)$$

Both, the mass fraction and the mole fraction are related by

$$y_k = x_k \frac{M_k}{\bar{M}}. \quad (3-2)$$

The mean molar mass of the overall mixture \bar{M} in terms of the mole fraction is described by

$$\bar{M} = \sum_k^K x_k M_k. \quad (3-3)$$

3.1 Conservation equations

The flame structure can be described by partial differential equations comprising species conservation, axial momentum conservation, and energy conservation as a function of a distance coordinate z (3-4) - (3-8). A more detailed description can be found in [73].

The equations are solved numerically with specified boundary conditions and predefined input parameters, e.g., mass flow, area of the burner surface, pressure, temperature profile and initial gas composition.

For ideal gases, the relation between the mass density and p the pressure, R the universal gas constant and \bar{M} the mean molar mass of the mixture can be calculated by the equation of state (3-4).

In steady-state, the mass continuity, as a function of the axial component z is shown in equation (3-5), where ρ is the mass density, and u is the axial velocity of the gas. Equation (3-5) indicates that the mass flow $\dot{m} = \rho u A$ is constant, where A represents the area of the burner surface, on which the flame is stabilized.

The axial momentum of the mixture is given in equation (3-6), where p is the pressure and μ is the viscosity. This equation can be used to determine a local pressure change. In many applications, the pressure is kept constant. Consequently, the axial momentum equation is not needed for isobaric, frictionless flat flames and is not described in detail. For further details see Ref. [73].

The species conservation equation considers the diffusion flow due to concentration gradients $j_{k,z}$ of a species k and a source term $\dot{\omega}_k$ that describes the formation or consumption of each species by chemical reactions, and is given in equation (3-7), where y_k is the mass fraction and M_k the molar mass of the species k .

The energy conservation equation describes the change of the flame temperature along the distance z and is given in equation (3-8), where λ denotes the thermal conductivity of the mixture, h_k is the enthalpy of the species k . Since the solution of the energy equation leads to significantly higher temperatures than typically observed in experiments (no heat losses are considered in equation (3-8)), alternatively a measured temperature profile is predefined as input parameter for the solution of the numerical system.

Equation-of-state:

$$\rho = \frac{p \bar{M}}{R T}. \quad (3-4)$$

Overall mass continuity:

$$\frac{\partial(\rho u)}{\partial z} = 0, \quad (3-5)$$

Axial momentum:

$$\rho u \frac{\partial u}{\partial z} = -\frac{\partial p}{\partial z} + \frac{\partial}{\partial z} \left(\mu \frac{\partial u}{\partial z} \right), \quad (3-6)$$

Species continuity:

$$\rho u \frac{\partial y_k}{\partial z} = -\frac{\partial j_{k,z}}{\partial z} + \dot{\omega}_k M_k, \quad (3-7)$$

Thermal energy:

$$\rho u c_p \frac{\partial T}{\partial z} = \frac{\partial}{\partial z} \left(\lambda \frac{\partial T}{\partial z} \right) - \left(\sum_{k=1}^K c_{p,k} j_{k,z} \right) \frac{\partial T}{\partial z} - \sum_{k=1}^K h_k \dot{\omega}_k M_k, \quad (3-8)$$

3.2 Reaction kinetics

In this subsection the fundamentals for the reaction kinetics and the dependence of reaction rates on temperature and pressure are described.

3.2.1 Chemical reaction rate constants

In general, elementary reactions in a reaction mechanism can be represented by



with the k^{th} species and K total number of species, with the i^{th} reaction and I total number of reactions, the forward and reverse stoichiometric coefficient are represented as v'_{ki} and v''_{ki} , respectively. The symbol ψ_k represents the species k .

The difference between the rate constants for the forward direction $k_{f,i}$ and the reverse direction $k_{r,i}$ of the reaction is represented as q_i , which is called the rate of progress q_i of a reaction i

$$q_i = k_{f,i} \prod_{k=1}^K [\psi_k]^{v'_{ki}} - k_{r,i} \prod_{k=1}^K [\psi_k]^{v''_{ki}}, \quad (3-10)$$

$$[\psi_k] = \psi_k \frac{p}{RT}, \quad (3-11)$$

where $[\psi_k]$ (3-11) is the concentration of the species k . The net formation and consumption $\dot{\omega}_k$ of species k in all reactions is

$$\dot{\omega}_k = \sum_{i=1}^I v_{ki} q_i, \quad (3-12)$$

where v_{ki} is the net stoichiometric coefficient for species k in reaction i , obtained by the difference of the stoichiometric coefficients for the forward and reverse directions of the reaction i

$$v_{ki} = v''_{ki} - v'_{ki}. \quad (3-13)$$

The reaction rate for a reaction i has a strong temperature dependence. The reaction rate coefficients of the forward reaction can be calculated by the modified Arrhenius formulation

$$k_i(T) = A_i T^{\beta_i} e^{\left(\frac{-E_i}{RT}\right)}, \quad (3-14)$$

where A_i denotes the pre-exponential factor, β_i the constant temperature exponent and the activation energy E_i which is needed to overcome the energy barrier to start the reaction. The pre-exponential factor A_i depends on the order of the rate constant. A detailed explanation for the description of the pre-exponential factor for the different types of rate-constants can be found in [72].

Some species have an increased collisional efficiency compared to other species when acting as collisional partner. For example, in the third-body reactions $2O + M \leftrightarrow O_2 + M$, water as a collisional partner M has a higher collisional efficiency compared to other species. This enhanced collisional efficiency and the concentration of the species k must be considered in the rate of progress variable as

$$q_i = \left(\sum_{k=1}^K \alpha_{ki} [\psi_k] \right) \left(k_{f,i} \prod_{k=1}^K [\psi_k]^{v'_{ki}} - k_{r,i} \prod_{k=1}^K [\psi_k]^{v''_{ki}} \right), \quad (3-15)$$

where α_{ki} is the collisional efficiency of species k in reaction i .

In equilibrium, the rate of progress for the forward direction is equal to the reverse direction and equation (3-10) can be written as

$$k_{f,i} \prod_{k=1}^K [\psi_k]^{v'_{ki}} = k_{r,i} \prod_{k=1}^K [\psi_k]^{v''_{ki}}. \quad (3-16)$$

The ratio of the rate constants of the forward and the reverse direction of the reaction is equal to the equilibrium constant $K_{c,i}$ and the relation is

$$\frac{k_{f,i}}{k_{r,i}} = K_{c,i} = \prod_{k=1}^K [\psi_k]^{v_{ki}}, \quad (3-17)$$

The reverse rate coefficients $k_{r,i}$ are related to the equilibrium constant $K_{c,i}$ according to

$$k_{r,i} = \frac{k_{f,i}}{K_{c,i}}, \quad (3-18)$$

where $K_{c,i}$ can be calculated with aid of the concentrations or by the relation to the equilibrium constant in terms of the partial pressures according to

$$K_{c,i} = K_{p,i} \left(\frac{p^\circ}{RT} \right)^{\sum_{k=1}^K v_{ki}}, \quad (3-19)$$

where v_{ki} is calculated by equation (3-13). When the sum of the stoichiometric coefficients on the reactant side is equal to the sum on the product side, $K_{c,i}$ is equal to $K_{p,i}$. The equilibrium constant $K_{p,i}$ can be calculated with aid of thermodynamic values,

$$K_{p,i} = \exp\left(\frac{\Delta S_i^\circ}{R} - \frac{\Delta H_i^\circ}{RT}\right), \quad (3-20)$$

where $\Delta S_i^\circ(T)$ denotes the reaction entropy at standard pressure, $\Delta H_i^\circ(T)$ is the reaction enthalpy at standard pressure. The change of enthalpy $\Delta H_i^\circ(T)$ for the reaction i between reactants and products can be calculated by

$$\frac{\Delta H_i^\circ}{RT} = \sum_{k=1}^K v_{ki} \frac{H_k^\circ}{RT}, \quad (3-21)$$

and the change of the entropy $\Delta S_i^\circ(T)$ by

$$\frac{\Delta S_i^\circ}{R} = \sum_{k=1}^K v_{ki} \frac{S_k^\circ}{R}. \quad (3-22)$$

3.2.2 Pressure dependence of rate constants

Some reactions are dependent on the pressure, e.g. unimolecular reactions. The Lindemann theory [73] is a commonly used functional form to parameterize the pressure-dependence of their reaction rates.

A unimolecular dissociation reaction where the reactant C dissociates to the products A and B is in general given as one reaction according to



The rate of consumption of the reactant C is defined by

$$\frac{d[C]}{dt} = -k_{\text{uni}}[C], \quad (3-24)$$

where k_{uni} is the net observed rate constant of the unimolecular dissociation reaction. The observed rate constant k_{uni} is a function of temperature and pressure. With respect to the description of the pressure dependence of rate constants, in the Lindemann theory [73] a sequence of elementary reactions participating in the decomposition of the reactant C is

proposed. The initial pressure-dependent reaction is the activation of the reactant C by bimolecular collisions with M to the activated molecule C* (3-25), followed by deactivation of C* by collisions with reactant molecule M (3-26), unimolecular decomposition of the activated molecules C* to the decomposition products A and B (3-27), and the recombination of the decomposition products A and B to the activated molecule C* (3-28)



In steady state of the reactions (3-25)-(3-28), the rate of formation of product A or B is

$$\frac{d[A]}{dt} = \frac{d[B]}{dt} = \frac{k_{+1}k_{+2}[M]}{k_{-1}[M] + k_{+2}} [C] = k_{\text{uni}}[C]. \quad (3-29)$$

The pseudo-first order rate constant of the unimolecular dissociation reaction can be described by the Lindemann-mechanism, which is

$$k_{\text{uni}} = \frac{k_{+1}k_{+2}[M]}{k_{-1}[M] + k_{+2}}. \quad (3-30)$$

It shows its dependence on the concentration of the collision partner [M], which is depending on the pressure. Three cases must be considered for an adequate description of the pressure dependence: The limits for high and low pressures and the fall-off range.

At the high-pressure limit, where $[M] \rightarrow \infty$ and $k_{-1}[M] \gg k_{+2}$, $k_{\text{uni},\infty}$ is defined by

$$\lim_{[M] \rightarrow \infty} \frac{k_{+1}k_{+2}[M]}{k_{-1}[M]} = k_{\text{uni},\infty} = A_{\infty} T^{\beta_{\infty}} e^{\left(\frac{-E_{\infty}}{RT}\right)}. \quad (3-31)$$

At the low-pressure limit, where $[M] \rightarrow 0$, $k_{\text{uni},0}$ is defined by

$$k_{\text{uni},0} = k_{+1}[M] = A_0 T^{\beta_0} e^{\left(\frac{-E_0}{RT}\right)}. \quad (3-32)$$

The rate constants in the intermediate fall-off range can be described by

$$k_{\text{uni}} = k_{\text{uni},\infty} \cdot \left(\frac{p_r}{1 + p_r} \right) \cdot F, \quad (3-33)$$

where the $F = 1$ [74] and indicates the broadening factor. The pressure p_r can be obtained by the ratio of the reaction rates at the low-pressure limit– $k_{\text{uni},0}$ and the high pressure-limit $k_{\text{uni},\infty}$

$$p_r = \frac{k_{\text{uni},0} [M]}{k_{\text{uni},\infty}}. \quad (3-34)$$

A more refined description of the transition region can be obtained according to Gilbert et al. [74], where the broadening factor F is defined by

$$\log F = \log F_{\text{cent}} \left\{ 1 + \left[\frac{\log p_r + c}{n - 0.14 \cdot (\log p_r + c)} \right]^2 \right\}^{-1}, \quad (3-35)$$

with

$$c = -0.4 - 0.67 \log F_{\text{cent}},$$

$$n = 0.75 - 1.27 \log F_{\text{cent}}.$$

The quantity F_{cent} is the intersection of the low-pressure and the high-pressure limits of the rate constants and is described by

$$F_{\text{cent}} = (1 - \alpha)e^{-T/T^{***}} + \alpha e^{-T/T^*} + e^{-T^{**}/T}, \quad (3-36)$$

where α , T^* , T^{**} , T^{***} are specific parameters and needed as input for each pressure dependent reaction. In summary, a total of 10 specific parameters are needed to describe the transition in the fall-off region, which are A_∞ , β_∞ , E_∞ , A_0 , β_0 , E_0 , α , T^* , T^{**} and T^{***} .

3.3 Thermodynamics

Thermodynamic quantities are needed to solve the conservation equations. The isobaric heat capacity and the enthalpies of formation of each species are used in the energy conservation equation (3-8). The thermodynamic quantities of gases are highly temperature dependent. The standard molar enthalpy at standard pressure is given in equation (3-39) and the standard molar entropy is described in equation (3-40) at standard pressure by

$$H_k^\circ(T) = \int_{298}^T C_{p,k}^\circ dT + H_k^\circ(298), \quad (3-37)$$

$$S_k^\circ(T) = \int_{298}^T \frac{C_{p,k}^\circ}{T} dT + S_k^\circ(298), \quad (3-38)$$

where $C_{p,k}^\circ$ is the molar heat capacity at constant pressure, $H_k^\circ(298)$ denotes the standard enthalpy of formation and $S_k^\circ(298)$ is the standard entropy of formation at temperature $T = 298$ K [73]. For a great number of species, the thermodynamic data are tabulated in a compact way and are made usable for modeling software. The handling of the data is done by an interpolation scheme. For this purpose, the thermodynamic data are described as a function of the temperature T for species k . The NASA-polynomials are widely used functions and can be found in [75]. The polynomials for the tabulated thermodynamic data are given for the molar heat capacity $C_{p,k}^\circ(T)$ (3-39), enthalpies of formation $H_k^\circ(T)$ (3-40) and entropies of formation $S_k^\circ(T)$ (3-41) for the individual species. The coefficients a_1 - a_7 for the individual species are tabulated for the two temperature ranges in [75]. The polynomials cover the high temperature range from 1000 - 6000 K using the first seven coefficient and the low temperature range from 200 - 1000 K using the second set of seven coefficients.

$$\frac{C_{p,k}^\circ(T)}{R} = a_{1,k} + a_{2,k}T + a_{3,k}T^2 + a_{4,k}T^3 + a_{5,k}T^4, \quad (3-39)$$

$$\frac{H_k^\circ(T)}{RT} = a_{1,k} + \frac{a_{2,k}T}{2} + \frac{a_{3,k}T^2}{3} + \frac{a_{4,k}T^3}{4} + \frac{a_{5,k}T^4}{5} + \frac{a_{6,k}}{T}, \quad (3-40)$$

$$\frac{S_k^\circ(T)}{R} = a_{1,k} \ln T + a_{2,k}T + \frac{a_{3,k}T^2}{2} + \frac{a_{4,k}T^3}{3} + \frac{a_{5,k}T^4}{4} + a_{7,k}. \quad (3-41)$$

The molar specific heat capacity of gas mixtures at a constant pressure is calculated by

$$\bar{C}_p = \sum_k^K C_{p,k} \cdot x_k \quad (3-42)$$

3.4 Heat and mass transport

3.4.1 Multicomponent formulation

In the one-dimensional flame, heat and mass transport is well defined. Heat transport proceeds by thermal conduction and the transport of chemical species takes place by molecular diffusion. The relevant transport parameters such as diffusion coefficients D_{kl} , D_k^T and thermal conductivity λ can be solved in the simulation within the multicomponent model [73], which is explained in the following. The diffusive flux of enthalpy is given by

$$j_q^{\text{diff}} = \left(\sum_{k=1}^K c_{pk} j_{k,z} \right) \frac{\partial T}{\partial z}, \quad (3-43)$$

where the multicomponent species flux $j_{k,z}$ is according to the Fick law defined by

$$j_{k,z} = \rho y_k V_k, \quad (3-44)$$

$$V_k = \frac{1}{x_k \bar{M}} \cdot \sum_k^K M_k D_{kl} d_k - \frac{D_k^T}{\rho y_k T} \frac{\partial T}{\partial z} \quad (3-45)$$

$$d_k = -\frac{\partial x_k}{\partial z} + (x_k - y_k) \frac{1}{p} \frac{\partial p}{\partial z}, \quad (3-46)$$

where y_k is the mass fraction, V_k is the diffusion velocity of the species k and is calculated in terms of the mole fraction x_k and the diffusion coefficient D_{kl} , thermal diffusion coefficient D_k^T and the driving force d_k .

Thermal conduction j_q^{cond} is caused by a temperature gradient following the Fourier law and is defined in equation (3-47). The thermal conductivity λ of the mixture can be calculated by equation (3-48)

$$j_q^{\text{cond}} = \frac{\partial}{\partial z} \left(\lambda \frac{\partial T}{\partial z} \right) \quad (3-47)$$

$$\lambda = \frac{1}{2} \left[\sum_{k=1}^K x_k \lambda_k + \frac{1}{\sum_{k=1}^K x_k / \lambda_k} \right] \quad (3-48)$$

where x_k denotes the mole fractions and λ_k is the individual species' conductivity [76].

The collision integrals $\Omega_{kl}^{(1,1)*}$ and $\Omega_{kl}^{(2,2)*}$ are needed for the solution of a system of equations, which is the so called L-matrix [77], from which the species thermal conductivities λ_k and diffusion coefficient D_k^M are obtained. More details about the L-matrix can be found in [73]. In the following the methods for obtaining the collision integrals are explained, which correct the ideal model of rigid spheres [73] by accounting for molecular interactions. When species k and l are either polar or non-polar, the collision integrals $\Omega_{kl}^{(1,1)*}$ and $\Omega_{kl}^{(2,2)*}$ depend on the reduced temperature T_{kl}^* . They can be determined from the tables based on Lennard-Jones potentials given in Monchick and Mason [78]. The reduced temperature T_{kl}^* is defined by

$$T_{kl}^* = \frac{k_b T}{\epsilon_{kl}}. \quad (3-49)$$

For each species, the specific transport coefficients such as the collision diameter σ_k and the well depth ϵ_k are given as input data for the calculation of the transport parameter in the simulation. From the transport coefficients of the individual species, the well depth ϵ_{kl} and the collision diameter σ_{kl} of the interaction are estimated by

$$\epsilon_{kl} = \sqrt{\epsilon_k \epsilon_l}, \quad (3-50)$$

$$\sigma_{kl} = \frac{\sigma_k + \sigma_l}{2}. \quad (3-51)$$

The Stockmayer potential is used to describe the transport coefficients for the interaction between polar and non-polar species. The collision integrals $\Omega_{kl}^{(1,1)*}$ and $\Omega_{kl}^{(2,2)*}$ depend on the reduced temperature T_{kl}^* and the reduced dipole moment δ_{kl}^* and can be determined from the reported data of Monchick and Mason [78]. The interaction is described by the well-depth ϵ_{kl} and collision diameter σ_{kl} , which are given by

$$\epsilon_{kl} = \sqrt{\epsilon_k \epsilon_l} \cdot \left(1 + \frac{1}{4} \frac{\alpha_l}{\sigma_l^3} \frac{\bar{\mu}_k}{\sqrt{\epsilon_k \sigma_k^3} \sqrt{\epsilon_l}} \sqrt{\frac{\epsilon_k}{\epsilon_l}} \right), \quad (3-52)$$

$$\sigma_{kl} = \frac{1}{2} (\sigma_k + \sigma_l) \cdot \left(1 + \frac{1}{4} \frac{\alpha_l}{\sigma_l^3} \frac{\bar{\mu}_k}{\sqrt{\epsilon_k \sigma_k^3} \sqrt{\epsilon_l}} \sqrt{\frac{\epsilon_k}{\epsilon_l}} \right)^{-1/6}, \quad (3-53)$$

The reduced dipole moment δ_{ik}^* is defined by

$$\delta_{kl}^* = \frac{1}{2} \frac{\bar{\mu}_k \bar{\mu}_l}{\epsilon_{kl} \sigma_{kl}^3}, \quad (3-54)$$

where $\bar{\mu}_k$ and $\bar{\mu}_l$ denote the dipole moments of species k and l .

3.4.2 Mixture-averaged formulation

The mixture-averaged formulation is often a sufficient representation for the heat and mass transport [73]. It is used for the one-dimensional simulations, which are shown in chapter 6-11. In this case the diffusive flux $j_{k,z}$ which is shown in equation (3-55) with the diffusion-velocity V_k for the k^{th} species (3-56) is represented as

$$j_{k,z} = \rho y_k V_k, \quad (3-55)$$

$$V_k = -\frac{1}{x_k} D'_{kl} \frac{\partial x_k}{\partial z}. \quad (3-56)$$

The mixture-averaged diffusion coefficients D'_{kl} for species k in the mixture is

$$D'_{kl} = \frac{1 - y_k}{\sum_{k \neq l} x_k / D_{kl}} \quad (3-57)$$

with the binary diffusion coefficients D_{kl} given as

$$D_{kl} = \frac{3}{16} \frac{\sqrt{2 \pi k_b^3 T^3 / m_{kl}}}{p \pi \sigma_{kl}^2 \Omega_{kl}^{(1,1)*}}. \quad (3-58)$$

The reduced mass m_{kl} of the molecules m and l defined as $m_{kl} = \frac{m_k m_l}{m_k + m_l}$. In the mixture-averaged formulation, the thermal conduction j_q^{cond} is calculated by Eq. (3-47)-(3-48) and the pure species conductivity as input as calculated by equation (3-59)-(3-73)

$$\lambda_k = \frac{\mu_k}{M_k} (f_{\text{trans}} C_{V,\text{trans}} + f_{\text{rot}} C_{V,\text{rot}} + f_{\text{vib}} C_{V,\text{vib}}), \quad (3-59)$$

with the pure species viscosities μ_k described as

$$\mu_k = \frac{5}{16} \frac{\sqrt{\pi m_k k_b T}}{\pi \sigma_k^2 \Omega_{kk}^{(2,2)*}}. \quad (3-60)$$

where m_k denotes the mass of a single k molecule.

The translational, rotational and vibrational contributions on the individual species conductivities (see Eq. (3-61)-(3-65)) are given by Warnatz et al. [72]

$$f_{\text{trans}} = \frac{5}{2} \left(1 - \frac{2}{\pi} \frac{C_{V,\text{rot}}}{C_{V,\text{trans}}} \frac{A}{B} \right), \quad (3-61)$$

$$f_{\text{rot}} = \frac{\rho D_{kk}}{\mu_k} \left(1 + \frac{2}{\pi} \frac{A}{B} \right), \quad (3-62)$$

$$f_{\text{vib}} = \frac{\rho D_{kk}}{\mu_k}, \quad (3-63)$$

$$A = \frac{5}{2} - \frac{\rho D_{kk}}{\mu_k}, \quad (3-64)$$

$$B = Z_{\text{rot}} + \frac{2}{\pi} \left(\frac{5}{3} \frac{C_{V,\text{rot}}}{R} + \frac{\rho D_{kk}}{\mu_k} \right), \quad (3-65)$$

The vibrational contribution is calculated with the aid of the relation

$$C_{V,\text{vib}} = C_V - C_{V,\text{trans}} - C_{V,\text{rot}}, \quad (3-66)$$

The total molar heat capacity can be determined by the temperature dependent polynomials which are described in chapter 3.3. The translational contribution $C_{v,\text{trans}}$ is described by

$$C_{V,\text{trans}} = \frac{3}{2} N k_b \quad (3-67)$$

The rotational contribution $C_{V,\text{rot}}$ for linear molecules is given by Eq. (3-68) and for non-linear molecules given by Eq. (3-69)

$$C_{V,\text{rot}} = N k_b \quad (3-68)$$

$$C_{V,\text{rot}} = \frac{3}{2} N k_b \quad (3-69)$$

where k_b denotes the Boltzmann's constant and N represents the number of molecules. For the case of a single atom the pure species conductivity is

$$\lambda_k = \frac{5}{2} \mu_k \frac{C_{V,\text{trans}}}{M_k}, \quad (3-70)$$

The self-diffusion coefficient D_{kk} is needed as input for Eq. (3-63)-(3-65) and is can be calculated with the aid of the relation

$$D_{kk} = \frac{3}{8} \frac{\sqrt{\pi k_b^3 T^3 / m_k}}{p \pi \sigma_k^2 \Omega_{kk}^{(1,1)*}}. \quad (3-71)$$

The temperature-dependent rotational relaxation collision number Z_{rot} is calculated according to Parker [79] and Brau and Jonkman [80], which is

$$Z_{\text{rot}}(T) = Z_{\text{rot}}(298) \frac{F(298)}{F(T)}, \quad (3-72)$$

where

$$F(T) = 1 + \frac{\pi^{3/2}}{2} \left(\frac{\epsilon/k_b}{T} \right)^{1/2} + \left(\frac{\pi^2}{4} + 2 \right) \left(\frac{\epsilon/k_b}{T} \right) + \pi^{3/2} \left(\frac{\epsilon/k_b}{T} \right)^{3/2}. \quad (3-73)$$

3.5 Analysis of reaction mechanisms

The precursor and flame chemistry are combined in a reaction mechanism that is used as input for the simulation. This section describes the methods to analyze quality of the reaction mechanism and to obtain the contribution of individual reactions to the production and consumption of a species, determining the important reaction pathways, and the sensitivity of parameters on the solution of the simulation.

3.5.1 Reaction flow analysis

Two types of reaction flow analysis can be performed to identify dominant reactions from the reactants to the products: The integral and the local reaction flow analysis. An integrated reaction flow analysis considers a specific region in the flame, e.g. the whole reaction zone, while a local reaction flow considers the production and consumption of a species at a specific location. The normalized production contribution [81] of a reaction to a species is defined by

$$C_{k,i}^p = \frac{\max(v_{k,i}, 0)q_i}{\sum_{i=1}^I \max(v_{k,i}, 0)q_i} \quad (3-74)$$

The normalized consumption contribution is given by

$$C_{k,i}^c = \frac{\min(v_{k,i}, 0)q_i}{\sum_{i=1}^I \min(v_{k,i}, 0)q_i} \quad (3-75)$$

where k denotes a species in reaction i , the net stoichiometric coefficient $v_{k,i}$ and the rate of progress q_i . The functions $\max(x, y)$ and $\min(x, y)$ imply that the maximum and minimum values are used between the two values x and y in the calculation, respectively.

For a specific time t or a location in the flame the production and consumption contribution can be shown according to

$$|C_{t,i,k}| < \varepsilon \left| \sum_{i=1}^I C_{t,i,k} \right| \quad (3-76)$$

with a limiting value of e.g. $\varepsilon = 1\%$ [72], the species k to K , the reactions i to I . The reaction path flow can be displayed with respect to each element, e.g. C, O, H and other elements that are considered in the reaction mechanism. When a reaction does not exceed a certain

contribution to the production and consumption of the species, this reaction can be considered unimportant.

3.5.2 Sensitivity analysis

The influence of uncertainties of parameters such as the rate constant k_r on the initial mole fraction x_k of a species can be determined with aid of a sensitivity analysis. For a local sensitivity analysis a system of first order ordinary differential equations consisting of I number of reactions and K number of species in terms of the elementary sensitivity coefficient [72] is given by

$$\frac{\partial}{\partial t} \left(\frac{\partial x_k}{\partial k_r} \right) = \frac{\partial}{\partial k_r} F_k(x_1, \dots, x_K; k_1, \dots, k_I), \quad (3-77)$$

where x_k can be the mole fraction of the species k at time t with the input parameter such as the reaction rate constant k_r . The first-order elementary sensitivity coefficient is defined by

$$S_{k,r} = \frac{\partial x_k}{\partial k_r}. \quad (3-78)$$

The sensitivity analysis enables to identify rate-determining or rate-limiting steps. The combination of reaction pathway analysis and sensitivity analysis is used to identify how relevant a species or reaction is.

4 Experiments and methodology

This section covers the details of the experimental setup comprising the description for the burner types, liquid precursor supply, the mass spectrometer system, temperature measurements and the applied methods used in this work. Finally, in the last subchapter the uncertainties of the experimental setup are reported.

4.1 Experimental setup

Two types of burners are used in this work (see Figure 4-1): The particle synthesis burner [23, 57] and the McKenna-type burner [24, 82-84]. Each burner unit is housed in an individual reactor chamber and is supported with a continuous gas flow. Both burner units are arranged in such way that the flames burn from the bottom to the top. All flames are operated at low pressure to expand the characteristic flame zones. The differences in the geometry of both burners are explained in the following.

The particle synthesis burner consists of a cooling flange, a mixing chamber and a burner matrix. The latter is made of sintered bronze with a diameter of 36 mm. The flange of the mixing chamber is water-cooled. The burner unit can be moved up and down via a translation system and a stepping motor. The axial distance between the sampling probe or thermocouple and the burner is named height-above-burner (HAB) in this work. In the particle synthesis reactor, this distance can be varied in vertical direction within $HAB = 0 - 250$ mm with an accuracy of ± 0.1 mm.

The matrix of the McKenna type burner has a diameter of 60 mm. It consists of sintered bronze and is cooled by an incorporated copper coil. The whole burner is mounted on a translation system in a reactor chamber and the height can be adjusted in vertical direction between $0 - 30$ mm with an accuracy of ± 0.1 mm.

For both setups, close to the burner surface (in the preheat- and reaction zone) the step size was chosen to be 0.25 mm. At larger HAB, where the gradients are less pronounced the step size was chosen between 1 to 5 mm.

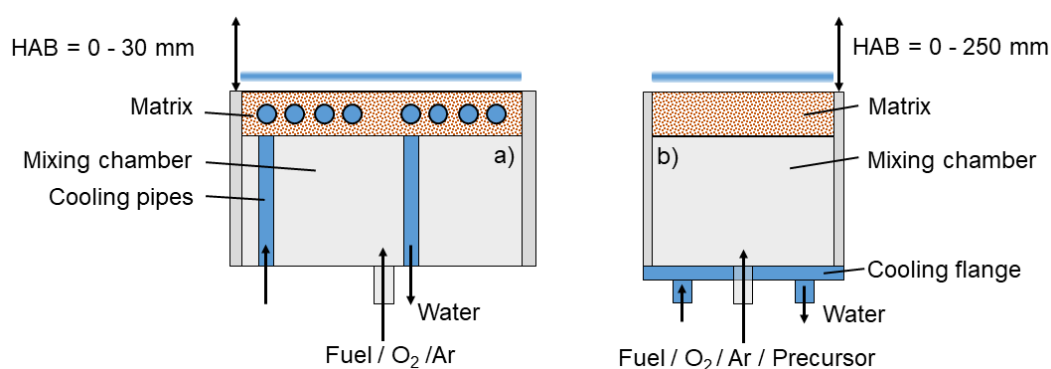


Figure 4-1. Schematics of the burner types: a) McKenna-type burner, b) Particle synthesis burner. The arrows indicate the direction of the flows.

The gaseous fuel, oxygen, argon and the precursor are introduced into the burner as mixture. Liquid precursors need to be evaporated before they are mixed with the gases.

A liquid precursor is delivered by a syringe pump (Figure 4-2). The precursor is cooled to avoid premature evaporation of the precursor. The precursor is fed through a capillary tube from the syringe into the mixing chamber of an evaporator. Inside the own-constructed evaporator, the gaseous precursor is mixed with argon. To avoid condensation of the evaporated precursor, all supply lines are heated with heating wires. The pressure of the evaporator is held constant at 1 bar with aid of a needle valve, which is located between the burner and the mixing chamber. The pressure is monitored by a pressure gauge.

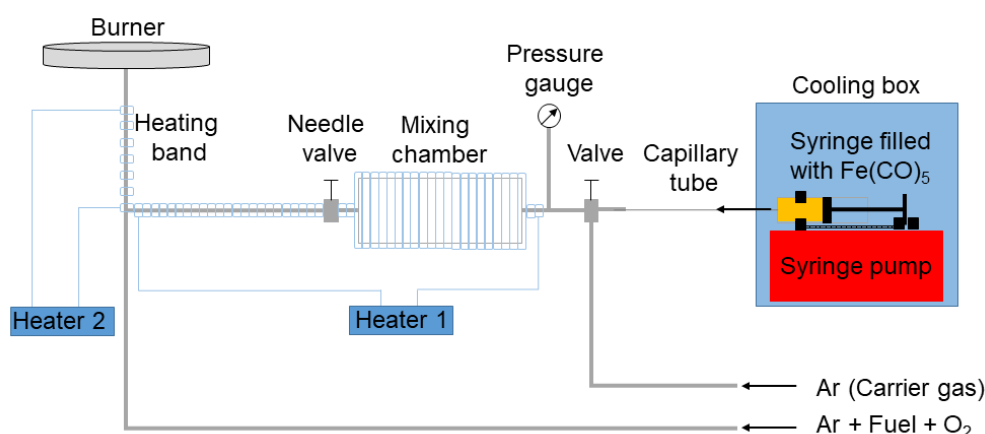


Figure 4-2. Schematics of the precursor supply system. The schematics is adapted from [62].

4.2 Mass spectrometry

This section focuses on the description of the molecular beam sampling, mass spectrometric setup and the quantification of the mass spectrometric data. The ion sampling technique is explained in chapter 4.2.6. The temperature measurements are explained in detail in chapter 4.3.

4.2.1 Molecular beam sampling

A molecular beam is formed inside the sampling probe, where reactions between the molecules are quenched. Quartz sampling probes are used because of their heat resistance and to avoid catalytic effects at the surface.

A scheme of the arrangement of the conical sampling probes and the pressures in the different chambers of the molecular beam inlet is shown in Figure 4-3. The height of the conical quartz sampling probe is 45 mm, the thickness 1.5 mm, the outer bottom diameter is 56 mm and the inner bottom diameter is 40 mm, the cone has an angle of 25° , and the orifice diameter of the aperture is $90 \mu\text{m}$. The sampling probe and its flange are water-cooled to withstand the heat transfer from the flame. A skimmer with an aperture diameter of 1.2 mm is located behind the quartz sampling probe, which extracts the core of the molecular beam and then transfers this gas sample to the mass spectrometer system for analysis (Figure 4-3).

The skimmer is positioned in front of the Mach disk so that changes in species profiles due to collisions with background gases are not expected. The Mach disk is explained in Figure 2-3.

The molecular beam sampling system is connected to the mass spectrometer via an expansion chamber. At a reactor pressure of 30 mbar the first stage is at a pressure of about 10^{-4} mbar and the second stage at a pressure of 10^{-6} mbar.

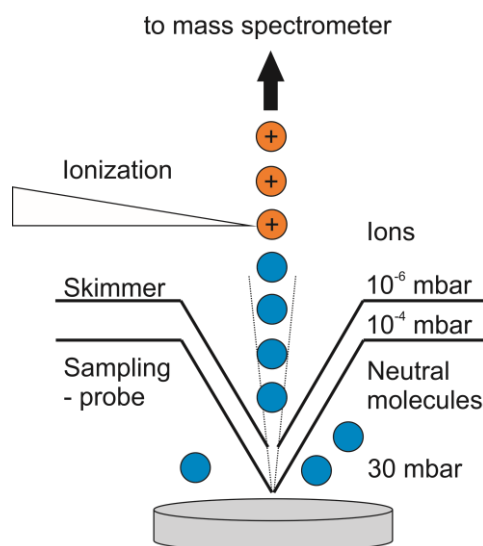


Figure 4-3. Schematics of the molecular beam sampling in a low-pressure flame. The blue symbols indicate the molecules, atoms and clusters from the flame. The triangular figure represents the electron beam. The orange symbols indicate their ions after electron ionization. The schematics is adapted from [62].

4.2.2 Mass spectrometer system

In the mass spectrometer the composition of the flame sample is analyzed. The general principles of the mass spectrometer which was used in this work can also be found in the work of Gonchikzhapov et al. [85] and Karakaya et al. [86].

The characteristic components of the present mass spectrometer system are: Electron ion source, ion transfer module, orthogonal ion extraction system according to Wiley-McLaren [69], two stage-ion reflector for efficient energy focusing [87], and multi-channel plate detector. The species in the gas sample are ionized by electron ionization. In the ionization source a tungsten filament releases the electrons, which are guided by two permanent magnets into the ionization zone and intersect the molecular beam. The ion transfer module consists of electrostatic lenses and aligns the orthogonal ion beam. It also transfers the ions into the ion extraction module. By help of a two-stage ion extraction, the different starting points of the ions can be compensated. A multi-channel plate detector is used to register the time-of-flights of the ions. A digitizer (Fast P7888 multi scaler) is used for the acquisition of the time-of-flight spectra. The maximum repetition rate of the spectrometer system is 40 kHz. The time-of-flight mass spectrometer has a resolution of $R = 3000$ at $m/z = 28$. Individual peaks with the same nominal mass can be deconvoluted when Si-containing

species, C-H species and C-H-O species are simultaneously present in the gas mixture. The individual time-of-flight is converted into the mass-to-charge ratio via a quadratic equation

$$m = at^2 + bt + c, \quad (4-1)$$

with the coefficients a , b and c that needs to be determined from known pairs of time-of-flight and mass-to-charge ratios. The coefficients can be obtained in calibration measurements following the introduction of known gases.

4.2.3 Quantitative data reduction

The mass spectrometric signal for the individual ion i is given by equation (4-2) and depends on various parameters by

$$S_i(E) = x_i \cdot c \cdot SW \cdot \phi \cdot MD_i \cdot FKT(h) \cdot \int \sigma_i(E) f(E) dE, \quad (4-2)$$

where x_i is the mole fraction, c is an instrument-dependent proportionality constant, SW is the number of single measurements (sweeps), ϕ is the number of electrons which are involved in the electron ionization process, MD_i is a mass discrimination factor, FKT is the temperature and height specific instrument function, $\sigma_i(E)$ the ionization cross-section at energy E and $f(E)$ the energy distribution function [82]. The mass discrimination factor for each species is assumed to be the same, except for hydrogen.

For various positions in the flame, a mass spectrum is recorded. It contains the signals of all species present in the flame. The mass spectrometric signal of the ion can be represented by a Gaussian curve. A program for peak-integration was used to integrate the individual signal intensity of the ions [88]. The area of each signal found by integration and is plotted as a function of the HAB. For the quantification of the individual stable species, the ion signals are related to argon and a calibration factor is calculated. With that calibration step the number of unknown parameters is reduced. The mole fraction x_i of the species i only depends on the signal intensities S_i and of the reference species argon S_{Ar} , the mole fraction of argon x_{Ar} and a calibration factor $k_{i,Ar}$ and is defined by

$$\frac{S_i}{S_{Ar}} = \frac{x_i}{x_{Ar}} \cdot k_{i,Ar}. \quad (4-3)$$

C, O and H elemental balances are used to determine the calibrations factors for the reactants and major product species such as fuel, precursor, O_2 , Ar, CO, CO_2 and H_2O . When the calibration factors are obtained, the argon mole fraction is calculated for each HAB assuming that the sum of the mole fractions for these species is equal to one (equation (4-4)). The

contributions of intermediates with small mole fractions are neglected to be able to solve the element balance with a small number of direct calibration measurements. With aid of the known signal intensities and the calibration factors, the argon mole fraction can be expressed by equation (4-5)

$$x_{\text{Ar}} + \sum_i^I x_i = 1. \quad (4-4)$$

$$x_{\text{Ar}} = \left(1 + \sum_{i \neq \text{Ar}} \frac{S_i}{S_{\text{Ar}}} \cdot \frac{1}{k_{i,\text{Ar}}} \right)^{-1}. \quad (4-5)$$

There are four procedures to obtain the intensity calibration factors for flame and precursor species:

1. The calibration factors are obtained by direct calibration for stable species (CO, CO₂, TMS), where the signal intensities from a measurement of each species is compared in a mixture of known composition with argon (chapter 4.2.4, chapter 6.4).
2. Major species such as fuel, precursor, H₂O, O₂, CO₂ and CO are calibrated from the C, H and O elemental balance by internal calibrations based on the routine from ref. [31, 82]. A limited number of directly measured calibration factors is used in this approach.
3. For species that are not stable enough to create well-determined mixtures, an indirect calibration method is used, which is similar to the procedure described by Biordi et al. [89] (chapter 4.2.5, chapter 6.4).
4. For silicon-containing species, where the ionization energy is unknown, a calibration factor is calculated using the Si-balance after subtraction of contribution of directly calibrated silicon-containing species. It is assumed that the solid particle formation is not significant and all species have the same ionization cross-section (chapter 4.2.5, chapter 6.4).

4.2.4 Direct calibrations

The mole fractions of the intermediate species can be determined by equation (4-3). The reference species and the species S_i have to be present at each position in the flame. The dilution gas argon is used as reference species since it is not consumed or formed. For stable species, cold gas mixtures are produced with known composition of x_i , x_{Ar} , S_i and S_{Ar} to obtain the species- and energy-dependent calibration factor $k_{i,\text{Ar}}$. The calibration factors are obtained with the same instrument settings as used for the flame measurements. These mixtures are either commercial mixtures such as for, e.g., Ar, CO₂ and CO, or are produced by direct mixing the different gases like H₂, CH₄, O₂, and C₂H₄. Mixtures with a liquid precursor can be generated by using an evaporator and subsequent mixing with the reference gas argon (chapter 4.1). This procedure was employed for TMS, Fe(CO)₅ and CH₃OH. Gas mixtures containing the precursor can also be produced with the partial pressure method, which were used in some measurements for Fe(CO)₅ (chapter 4.1). In this process, the

precursor is introduced into an initially evacuated container up to a certain pressure. Afterwards the carrier gas is filled up to the final pressure. The mixture is delivered by mass flow controllers into the burner unit, where it can be mixed with other gases.

4.2.5 Indirect calibration

The method of indirect calibration is used when direct calibrations were not possible. Direct calibrations were not possible for intermediate species that could not be bought or that were not stable and could not be introduced in a mixture, e.g., methyl radicals. In this method, the calibration factors are calculated with aid of the electron-ionization cross sections of the species and it relies on the following relationship

$$\frac{S_i}{S_{Ar}} = \frac{x_i}{x_{Ar}} \cdot \frac{\int \sigma_i(E)f(E)dE}{\int \sigma_{Ar}(E)f(E)dE} \quad (4-6)$$

The electron ionization cross-section represents the efficiency with which a molecule can be ionized. It is smallest close to the ionization threshold of the molecule (minimum energy needed for the ionization of the species). Close to the threshold it increases linearly and then curves towards a maximum which is typically near 70 eV for most molecules. The ionization cross-sections of almost all the species have similar profile shapes when plotted against the electron energy, but start increasing at the individual ionization energy of each species. The values for the ionization cross section of the molecule are given in the unit mega barn (1 mb = 10⁻¹⁸ cm²). The energy distribution can be represented by a Gaussian distribution given by

$$f(E) = \frac{1}{\sqrt{2\pi}\theta} \cdot \exp\left[-\frac{(E - \mu)^2}{2\theta^2}\right], \quad (4-7)$$

with $\mu = E_{Max}$ and $\theta = FWHM / 2(2\ln 2)^{0.5}$.

For some species the electron-ionization cross sections are not available. In this case, they can be estimated by the RICS-method (relative ionization cross-section method), which was developed by Biordi et al. [89] and is based on (4-8)

$$\frac{\sigma_i(E_1 = IE_i + b)}{\sigma_R(E_2 = IE_R + b)} = \frac{\sigma_i(70 \text{ eV})}{\sigma_R(70 \text{ eV})} \quad (4-8)$$

Here, the assumption is that the electron ionization cross-section ratio of chemically similar compounds at the same energy difference b from their ionization energy threshold is equivalent to the ratio of their electron ionization cross sections at 70 eV. The ionization efficiency curves of chemically similar species have the same shape and are shifted by the difference of the ionization energies and are scaled by the ratio of the ionization cross sections at 70 eV. The cross sections for many species can be found in the NIST Chemistry

WebBook [90]. The ionization energies of organic species containing C, H and O for 70 eV can be calculated by an empirical correlation developed by Sauter and Fitch [91]. Ionization energies are needed for accurately shifting the ionization cross-section curves. The cross sections were calculated by quantum chemical calculations for silicon-containing species like TMS, $\text{Si}(\text{CH}_3)_3\text{CH}_2\text{OO}$, HSiO , SiOH , SiO_2 , $\text{Si}(\text{OH})_4$, $\text{Si}(\text{OH})_3$, $\text{Si}(\text{CH}_3)_3\text{OH}$, $\text{Si}(\text{CH}_3)_3\text{O}$, $\text{Si}(\text{CH}_3)_2\text{OH}$ and $\text{Si}(\text{CH}_3)(\text{OH})_2$ [86]. Since the signal of TMS was directly calibrated, the cross-section at the same energy difference b from the ionization energy IE was set to the same value by

$$\sigma_i(\text{IE}_i + b) = \sigma_{\text{TMS}}(\text{IE}_{\text{TMS}} + b) \quad (4-9)$$

$$b = E - \text{IE}_i \quad (4-10)$$

The calibration factor k_i of the silicon-containing species i is then calculated by

$$\frac{\sigma_i(E_1 = \text{IE}_i + b)}{\sigma_{\text{TMS}}(E_2 = \text{IE}_{\text{TMS}} + b)} = \frac{k_i}{k_{\text{TMS}}} \quad (4-11)$$

For silicon-containing species with unknown ionization energy like the silicon-containing clusters $\text{Si}_4\text{O}_{10}\text{H}_4$, $\text{Si}_5\text{O}_{12}\text{H}_4$ and $\text{Si}_6\text{O}_{14}\text{H}_4$, a calibration factor is determined by the Si-elemental balance after subtraction of the calibrated silicon-containing species and assuming that the solid phase is not formed and that these species have the same ionization cross sections. With this assumptions the residual of the Si-containing mole fractions is calculated for each HAB by

$$x_{\text{Si}}(\text{HAB} = 0) = x_{\text{TMS}}(\text{HAB}) + x_{\text{Si-intermediates}}(\text{HAB}) + x_{\text{Si-residual}}(\text{HAB}) \quad (4-12)$$

where x_{TMS} denotes the mole fraction of TMS and $x_{\text{Si-intermediates}}$ denotes the mole fraction of the calibrated Si-containing species. The mole fraction ratio of each silicon-containing species and the mole fraction of the residual mole fraction $x_{\text{Si-residual}}$ is equal to the ratio of the corresponding signal intensities assuming equal cross sections

$$x_i = \frac{S_i}{S_{\text{total}}} \cdot x_{\text{Si-residual}} \quad (4-13)$$

To determine the mole fraction at all HAB a calibration factor is calculated by

$$k_i = \frac{S_i}{S_{\text{Ar}}} \cdot \frac{x_{\text{Ar}}}{x_i} \quad (4-14)$$

With aid of the calibration factor the remaining mole fraction profiles can be determined by rearranging equation (4-14).

4.2.6 Ion sampling

Naturally occurring ions in the flame are sampled with the aid of a novel ion sampling technique (Figure 4-4). An additional ionization is not needed to produce the ions from the sample. Neutral species are pumped out of the ion transfer optics and consequently are not transmitted to the mass spectrometer. The setup is used in various studies and details can be found in [30, 62].

The flame gases are sampled via a metallic sampling probe, which has a height of 28 mm, a base diameter of 39 mm and an orifice diameter of 550 μm . A potential of +300 V is applied to the sampling probe and to the burner to achieve a homogeneous electric field. Typical pressures in the reactor chamber are between 120-160 mbar. These comparatively high pressures are needed to ensure that the molecular beam penetrates into the ion funnel. The interface has three differentially pumped vacuum stages. Each stage contains the ion guides and is separated through beam forming lenses with small apertures. The first pressure stage operates at 3 mbar, the second stage at 10^{-3} mbar and the third at 10^{-6} mbar. The flight tube of the mass spectrometer is maintained at 10^{-7} mbar.

In the first stage a low-capacitance printed circuit board (pcb) ion funnel is used for the transmission and focusing of the ions. Ions are guided by an octapole- (second stage) and a quadrupole-ion guide (third stage) and subsequently through the Einzel lenses to the extraction volume and are introduced into the mass analyzer of the spectrometer.

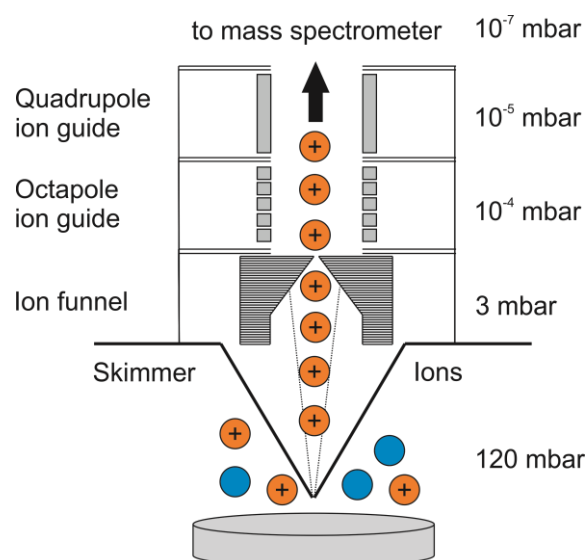


Figure 4-4. Schematic of the ion sampling TOF. The schematic is adapted from [62].

4.3 Temperature

The flame temperature is measured by a thermocouple of the type R or S with a junction diameter of up to 200 μm . The thermocouples are coated with either SiO_2 or Al_2O_3 to avoid catalytic reactions. To measure an unperturbed temperature profile, the thermocouple is

positioned with a distance of 15 mm to the sampling probe to avoid its influence. Perturbed temperature profiles were measured where the thermocouple was positioned close to the sampling probe. The perturbation on the temperature profile is caused by the sampling probe and is discussed in more detail in [82] and in chapter 11. When the thermocouple is positioned in the flame, various heat transfer mechanisms occur. These include convection between the gases and the thermocouple surface, radiation to the surroundings and conduction inside the thermocouple wires and catalytic reactions. Catalytic effects are minimized by the non-catalytic coating on the thermocouple. The influence of the conduction is reduced by avoiding temperature gradients through aligning the thermocouple wires along an isothermal line of the flame. According to Shaddix [92] the heat conduction and the radiation of heat to the surroundings are the major heat transfer mechanisms which need to be considered in the energy balance for the thermocouple. Under steady-state conditions, the temperature of the flame can be calculated by

$$T_{\text{Flame}} = T_{\text{Thermocouple}} + \left(\frac{\varepsilon_{\text{TC}} \sigma}{hA} \right) \cdot (T_{\text{Thermocouple}}^4 - T_{\text{Surroundings}}^4), \quad (4-15)$$

where A is the surface of the thermocouple, $T_{\text{Thermocouple}}$ (T_{TC}) is the temperature of the thermocouple, T_{Flame} is the temperature of the flame, h is the heat transfer coefficient, ε_{TC} is the emissivity of the thermocouple, σ is the Stefan-Boltzmann constant [92, 93]. The thermocouple measurement is calibrated with the flame temperatures, which can be found in [16] by the procedure described in the study of Bahlawane et al. [93].

The sampling probe can have a significant effect on the flame temperature profile. Its influence on the flame temperature is taken into account according to the procedure described in the study of Struckmeier et al. [82]. For a continuum flow, the molecular flow rate through the aperture of the sampling probe can be described by

$$\dot{N} = AN_a p_0 \sqrt{\frac{\kappa}{M \cdot R \cdot T}} \cdot \left(\frac{2}{\kappa + 1} \right)^{\frac{\kappa+1}{2(\kappa-1)}}, \quad (4-16)$$

where A is the area of the sampling probe aperture, N_a is the Avogadro number, p_0 is the pressure, κ is ratio of the heat capacities, molar gas constant R , molar mass M , temperature T . The ratio of the heat capacities κ does not change significantly for different positions in the flame. The values from equation (4-16) that are either constant or can be estimated by a constant factor are combined in the constant C_1 . The molecular flow rate is proportional to the height specific instrument function FKT of the mass spectrometric signal and is given by

$$\dot{N} = C_1 \sqrt{\frac{1}{M \cdot T}} \propto \text{FKT}(\text{HAB}). \quad (4-17)$$

The proportionality is indicated by the symbol \propto . The FKT can be determined for each HAB by the ratio of the signal intensity and the corresponding mole fraction of the species argon, which is not consumed or produced in the flame, from equation (4-2). The constant C_1 is calculated at a position far downstream in the flame for a known temperature, e.g., by a thermocouple measurement. Finally, the temperature of the flame can be calculated with aid of the height specific instrument function FKT and the constant C_1 by

$$T = \frac{1}{\overline{M}} \left(\frac{C_1}{\text{FKT}(\text{HAB})} \right)^2. \quad (4-18)$$

The resulting temperature profile is used as input for the simulation.

For the measurement of the flame temperature, the thermocouple is coated with a non-catalytic material such as aluminum oxide (Al_2O_3). The coating is applied by dip coating on the thermocouple. The sol consists of aluminium triisopropylate (ATI, $\text{C}_9\text{H}_{21}\text{O}_3\text{Al}$) as the source, diethylene glycol monoethylether ($\text{C}_6\text{H}_{14}\text{O}_3$) as solvent, and acetic acid (CH_3COOH) as the catalyst. The procedure for the preparation of the sol is based on the method of Bahlawane [94] for the improvement of graphite oxidation resistance. The thermocouple is dipped in the sol and heating in a bunsen burner flame leads to the formation of the aluminium oxide layer. The procedure is repeated 20-30 times. The aluminium oxide layer is finally visible on the thermocouple. Another common non-catalytic material for the coating is SiO_2 [95, 96]. To coat the thermocouple with silicon dioxide (SiO_2), is dipped, e.g., in silicone oil and passing through a Bunsen burner flame. The procedure is repeated 20-30 times until a coating on the thermocouple is visible.

4.4 Error analysis

For the estimation of the quality of the quantification method, the statistic error induced by the used measuring instruments is determined by using the Gaussian error propagation law as described in [97].

In general, the error sources are mass flow controllers, the electro pneumatic pressure regulator, the vertical translation system, the mass spectrometer system and the syringe pump. Some uncertainties such as the fluctuations in the pressure are determined during the measurements. Other uncertainties are obtained by reproducibility measurements. The burner chamber is directly connected to the mass spectrometer system. The sample is drawn from the flame via a sampling probe. The flame sampling must be considered as a source of error. A detailed characterization of the flame sampling is presented in chapter 11. For the simulation of 1D-simulations the perturbed temperature profile is used as input. The perturbed temperature profile is calculated by the height specific instrumental function of the mass spectrometric system as described in chapter 4.3. The thermocouple measurements are calibrated to the flame temperature profiles that are taken from [16]. The uncertainty of

the radiation correction of the thermocouple measurements is estimated to be 5-10%. The final uncertainties in the temperatures presented throughout this work is in the range of 70 - 140 K. Mass flow controllers deliver the initial composition of the gases including fuel, oxygen and argon. The tolerances of the mass flow controllers from MKS are provided from the manufacturer. The measurement uncertainties are quantified by the manufacturer and are at $\pm 1\%$ at full-scale and $\pm 5\%$ in the worst case (referred to the volume flow). For the mass spectrometer system (described in chapter 4.2.2) the reproducibility measurements show a relative error of $\leq 5\%$. This error includes the uncertainties of the mass spectrometer system and the manual integration of the signals.

For the determination of overall uncertainty of the measurement, the uncertainties of the mass spectrometer system and the mass flow controller are considered in the calculation. The Gaussian error propagation law is used to calculate the statistical error in the mole fraction of a species. Quantification of the total statistic error σ_f of the overall uncertainty of the value f can be calculated according to the Gaussian error propagation law (see Eq. (4-19)). The function ∂f depends on the variables x_1 to x_n with the number of variables n . The uncertainties of the individual uncertainties are described as σ_1 to σ_n .

$$\sigma_f = \sqrt{\left(\frac{\partial f(x_1, x_2, \dots, x_n)}{\partial x_1}\right)^2 \cdot \sigma_1^2 + \dots + \left(\frac{\partial f(x_1, x_2, \dots, x_n)}{\partial x_n}\right)^2 \cdot \sigma_n^2} \quad (4-19)$$

For the determination of the mole fraction of a species such as methane the direct calibration method can be used which is described in chapter 4.2.4. The calculation of the mole fraction is considered as a function which contains the variables the signal intensities S of the species I and of the reference gas argon, the mole fraction of argon and the calibration factor $k_{i,Ar}$

$$x_i = \frac{S_i}{S_{Ar}} \cdot \frac{x_{Ar}}{k_{i,Ar}} \quad (4-20)$$

For the Gaussian error propagation law a multitude of 1. Order partial derivatives of function $x_i(S_i, S_{Ar}, x_{Ar}, k_{i,Ar})$ of the variables $x_{Ar}, S_i, S_{Ar}, k_{i,Ar}$ are needed and are shown in (4-21)-(4-24)

$$\frac{\delta}{\delta x_{Ar}} x_i(S_i, S_{Ar}, x_{Ar}, k_{i,Ar}) = \frac{S_i}{S_{Ar}} \cdot \frac{1}{k_{i,Ar}} \quad (4-21)$$

$$\frac{\delta}{\delta S_i} x_i(S_i, S_{Ar}, x_{Ar}, k_{i,Ar}) = \frac{1}{S_{Ar}} \cdot \frac{x_{Ar}}{k_{i,Ar}} \quad (4-22)$$

$$\frac{\delta}{\delta S_{Ar}} x_i(S_i, S_{Ar}, x_{Ar}, k_{i,Ar}) = \frac{x_{Ar}}{k_{i,Ar}} \cdot S_i \cdot \left(-\frac{1}{S_{Ar}^2} \right) \quad (4-23)$$

$$\frac{\delta}{\delta k_{i,Ar}} x_i(S_i, S_{Ar}, x_{Ar}, k_{i,Ar}) = \frac{S_i}{S_{Ar}} \cdot x_{Ar} \cdot \left(-\frac{1}{k_{i,Ar}^2} \right) \quad (4-24)$$

With the aid of the Gaussian error propagation (Equation (4-19)-(4-24)), the absolute uncertainty σ_f in the mole fraction of the mole fraction x_i of species i can be calculated by

$$\sigma_f = \sqrt{\left(\frac{\delta}{\delta x_{Ar}} x_i(S_i, S_{Ar}, x_{Ar}, k_{i,Ar}) \right)^2 \cdot \sigma_{x_{Ar}}^2 + \left(\frac{\delta}{\delta S_i} x_i(S_i, S_{Ar}, x_{Ar}, k_{i,Ar}) \right)^2 \cdot \sigma_{S_i}^2 + \left(\frac{\delta}{\delta S_{Ar}} x_i(S_i, S_{Ar}, x_{Ar}, k_{i,Ar}) \right)^2 \cdot \sigma_{S_{Ar}}^2 + \left(\frac{\delta}{\delta k_{i,Ar}} x_i(S_i, S_{Ar}, x_{Ar}, k_{i,Ar}) \right)^2 \cdot \sigma_{k_{i,Ar}}^2} \quad (4-25)$$

The relative total error of the species mole fractions is then calculated and results in $\leq 14\%$. For the calibration of species using electron ionization cross sections, the uncertainties of the mole fractions depend on the uncertainties of the electron ionization cross sections, which range between $\pm 30\%$ and a factor of 2-3 for known electron ionization cross sections and estimated electron ionization cross sections, respectively. These uncertainties are in line with other studies [24, 28].

5 Conceptual research guidelines and motivation

This chapter comprises the *description of the concept* for this thesis and is divided into two parts. Each part is separated as follows: Initially a short introduction is given to narrow the research field, followed by a more general summary of the scientific questions of this thesis and finally each scientific question is described in more detail. The chapters 6-11 have been published as individual peer-reviewed journal articles and in international conferences.

For the fundamental understanding of the gas phase synthesis of complex nanomaterials, two target systems are defined in the framework of the research group FOR2284, that are silicon dioxide and iron oxide. *Silicon dioxide* is of particular interest for many application fields. It is widely used and offers a high potential for future applications such as battery storage, photoluminescence and printable electronics. Several studies show the use of silicon-containing precursors. A short literature review can be found in chapter 2.1. Tetramethylsilane (TMS) is used as the precursor for the silicon dioxide synthesis in $H_2/O_2/Ar$ flames. Only few studies available in the literature focused on the combustion of TMS. It becomes clear that the detailed reaction kinetics of TMS is not well studied. Also, the interaction between the precursor and the flame chemistry is not well understood. These fundamentals of the material synthesis are still missing and are investigated in this work. Moreover, for the design and control of the synthesis process simulations are needed. The reaction mechanism is an important input for the simulation. The validity of the reaction mechanism is evaluated for appropriate synthesis conditions.

In chapter 6 the *combustion of TMS* and the formation of silicon oxide clusters in premixed $H_2/O_2/Ar$ low-pressure flames are investigated by means of EI-TOF-MBMS. The task is to determine the decomposition pathway of the precursor in the flame. Also, the interaction between the flame and the precursor chemistry is studied. Dominant combustion intermediates are identified. The knowledge of the intermediate species gives insight into precursor decomposition and the particle growth. The results are condensed to a list of potential reaction pathways. Overall, this work comprises the first step towards the building up of a database consisting of reaction kinetics data that are needed for the development and evaluation of a reaction mechanism model. The reaction mechanism is needed for the computational simulation of the synthesis flames.

In chapter 7, a *chemical reaction mechanism for TMS* is developed in cooperation with colleagues from the DFG research unit FOR2284. The performance of the reaction mechanism is evaluated for various synthesis conditions. Numerous experimental data are obtained from TMS oxidation in hydrogen flames with the aid of EI-TOF-MBMS. The flame conditions comprise the variation of the initial TMS amount in a lean hydrogen/oxygen flame. The next step is the evaluation if the reaction mechanism can reproduce the interaction between precursor and flame chemistry for different equivalence ratios of the flame.

The *influence of the equivalence ratio on key intermediates* in synthesis flames is studied in chapter 8. The developed reaction mechanism model is evaluated for hydrogen/oxygen flames with different equivalence ratios. The focus is on the determination of the initial decomposition step of TMS. Further, the impact of the equivalence ratio on silicon-containing intermediates are analyzed. These experimental data can provide information about differences in the reaction pathways for different flame conditions and varied positions in the flame.

In summary, the *first part of this thesis* (chapter 6 – chapter 8) is dedicated to the investigation of silicon dioxide synthesis flames. The studies evaluate the reactivity of TMS in flames, address questions about the interaction between the precursor and the flame chemistry, and investigate which intermediates contribute to particle growth.

Iron oxide is the second target material that is analyzed in the framework of the DFG research unit FOR2284. Iron pentacarbonyl $\text{Fe}(\text{CO})_5$ is a frequently used precursor for the gas phase synthesis of iron oxides. A literature review is given in chapter 2.1. The interaction between the precursor and the flame chemistry has previously been investigated in several studies [52, 53, 56, 57]. The reaction mechanism for the oxidation of $\text{Fe}(\text{CO})_5$ already exists in the literature. The precursor decomposition and the interaction between the flame and the precursor chemistry are still not evaluated in detail. Experimental data for the evaluation of the reaction mechanism are rare. So far a few iron-containing species like iron atoms are measured using Fe-LIF and FeO with the aid of ICLAS [57]. In the literature, the only study that focuses on MBMS measurements is from Gerasimov et al. [21]. Their work and experience show that the intrusive sampling from iron oxide synthesis flames is challenging due to several reasons. Amongst the most important are clogging of the sampling probe and fragmentation during electron ionization. Consequently, a new sampling method is applied, which is very sensitive. This sampling method focuses on the extraction of naturally occurring ions from flames. There is an ongoing discussion about the relevance of the ions on the flame chemistry in the available literature. In general, ions occur in much smaller concentrations than the neutral molecules in the flame. Consequently, the kinetics of ions seem not to be relevant for the flame chemistry. In the overall context of this work, it will be analyzed if the ions can potentially be used as indicators for the molecules in the flame. The task is to identify dominant ions and link their signals to the molecules from which the ions originate. Before this connection can be done, the ion formation pathways need to be investigated in flames.

In chapter 9, the already intensively documented *methane ion chemistry* in flames is used to test the ion sampling technique in a collaborative work with the colleagues from the university Kaust. This test case is used to identify dominant ions in methane flames. Subsequently, the reactions leading to the formation of the ions can be revealed.

The *combustion of $\text{Fe}(\text{CO})_5$* is studied in chapter 10. Many studies have already focused on the reactivity of $\text{Fe}(\text{CO})_5$, e.g. Linteris et al. [50] postulated many pathways for the iron-system. However, only a limited number of experimental data exist that can be used to evaluate the existing chemical reaction kinetics models of the combustion of $\text{Fe}(\text{CO})_5$ from

the literature. The decomposition of $\text{Fe}(\text{CO})_5$ to smaller molecules is so far not evaluated. Also, the identity of the important growth species that lead to particle formation is not known in detail. In the literature, it is postulated that particles are formed at two positions. The first position of particle formation is located close to the burner surface due to the clustering of iron atoms [57, 98-100]. Fe is an important intermediate, but it is not clear how it is oxidized in the flame. The role of hydroxides is not well understood, e.g., the reaction mechanism of $\text{Fe}(\text{CO})_5$ from Wlokas et al. [52] contains $\text{Fe}(\text{OH})_2$ but not $\text{Fe}(\text{OH})_3$. Another question is what is formed in the exhaust FeO as postulated by Hai Wang for ferrocene [101] or Fe_2O_3 as postulated in [22, 51, 52] for $\text{Fe}(\text{CO})_5$.

In chapter 11, the major tasks are to study the *influence of the sampling probe on the flame structure and the interpretation of the ion signal*. The flame sampling of the mass spectrometer systems is characterized with the aid of two-dimensional CFD. Using the ion sampling technique, these ions can be analyzed with a mass spectrometer. The conversion from ions to neutrals is important to take the next step towards the quantitative application of the new sampling technique. The focus is on a comparable simple case to demonstrate the potential for the technique. The approach used for the quantification is based on the observation that neutral flame species are converted to ions in proton transfer reactions. The challenge of exploiting this connection for quantification is that the chemical relationship between the ion and the neutral molecule as well as the relationship between the concentration of the ion and the concentration of the neutral molecule must be fully understood. A proof-of-concept is presented for the quantification of methanol based on the relative ion concentration of CH_5O^+ . An important assumption of this quantification method is that the proton transfer reactions are in equilibrium. The equilibrium positions of the reactions are very temperature sensitive. For this reason, it is necessary to determine the temperature that has to be used when calculating the equilibrium values. The sampling probe has a significant influence on the flame temperature. The characterization of the flame sampling is of particular importance for the accurate determination of the temperatures experienced by the molecules throughout the flame.

In summary, the *second part of this thesis* (chapter 9 - chapter 11) is dedicated to evaluate a novel ion sampling method for the investigation of particle forming flames. Initial attempts are made to interpret ion signals from flames. This technique is applied to the investigation of the intermediates formed from $\text{Fe}(\text{CO})_5$ in order to answer the question which iron intermediates occur during the oxidation of Fe in a flame.

6 Mass spectrometric study on the combustion of tetramethylsilane and the formation of silicon oxide clusters in premixed laminar low-pressure synthesis flames

The content of this chapter was published in *Journal of Physical Chemistry A* 122, 7131-7141 (2018), *Y. Karakaya, S. Peukert, T. Kasper, Mass spectrometric study on the combustion of tetramethylsilane and the formation of silicon oxide clusters in premixed laminar low-pressure synthesis flames* and is reprinted with permission from American Chemical Society. Copyright © 2018, American Chemical Society.

CRedit¹ author statement: Y. Karakaya designed and built the experimental setup, performed the experiments, chose the experimental flame and precursor conditions, evaluated the mass spectrometric data, visualized the data and wrote the original draft of the manuscript. S. Peukert provided quantum chemical calculations and contributed to the interpretations of the results. T. Kasper provided discussions of the results and contributed to the manuscript.

6.1 Abstract

This work investigates the decomposition of tetramethylsilane and the formation of silicon oxide clusters in a laminar premixed low-pressure hydrogen flame using molecular-beam mass spectrometry (MBMS). A comprehensive list of the species that exist in the gas phase was compiled and spatially resolved mole fraction profiles of species in the flame were obtained. Quantitative data in dependence of height above the burner were obtained for all major species and intermediates. The MBMS detection technique allowed to monitor Si-C-O-H, and Si-O-H-containing compounds as well as C₁-C₂ species. The measured data show that the reaction of tetramethylsilane is initiated by H-abstraction from a methyl group and subsequent formation of oxygenated species. The measurements suggest that combustion of tetramethylsilane in a hydrogen flame proceeds mainly by a stepwise substitution of the methyl ligands by hydroxyl groups. Molecular and radical intermediates like Si(CH₃)₂OH, Si(OH)₃, and Si(OH)₄ are formed in the reaction zone. Significant amounts of Si(OH)₄ are present at large distances above the burner. A repetitive growth pattern suggests that the monomer Si(OH)₄ is a likely species initiating the formation and growth of larger silicon oxide clusters, e.g. Si₄O₁₀H₄, Si₅O₁₂H₄, and Si₆O₁₄H₄, that can form nanoparticles in subsequent reactions.

¹ CRedit (Contributor Roles Taxonomy)

6.2 Introduction

Each year, several million tons of nanoparticles of iron oxide [57], tungsten oxide [23], silicon dioxide [19], in a size range of 10-100 nm are produced in flame reactors on the industrial scale for a variety of applications [32, 102] such as medical technology and pharmaceutical industry. The synthesis in a flame reactor is particularly attractive since it produces high-purity nanoparticles at scalable production rates in a continuous gas phase synthesis process. To obtain the desired particles, different aspects of the process are investigated as function of several process parameters. For example, particle morphology was studied by Pratsinis et al. [43, 102, 103] as function of the oxidator and fuel flow rates, and precursor concentration, whereas the process of particle formation itself was investigated by Zachariah et al. [104]. Another parameter that influences the process and particles are the precursors [43]. Consequently, the thermodynamics and kinetics of the reaction pathways leading to the formation of silicon dioxide nanoparticles from silicon containing precursors such as SiH_4 [42], SiCl_4 [105], and hexamethyldisiloxane (HMDSO) [19] are of considerable interest.

Premixed, laminar low-pressure flames stabilized on model burners are valuable tools for the investigation of combustion kinetics [21, 29, 31, 82, 89, 106-109] and it is the aim of this work to extend the established technique of molecular-beam mass spectrometry (MBMS) to the investigation of the decomposition of tetramethylsilane (TMS) and cluster growth in flat, premixed, laminar $\text{H}_2/\text{O}_2/\text{Ar}$ low-pressure flames.

So far, the thermal decomposition of TMS has been primarily studied because of its application as a precursor compound for silicon carbide (SiC) under pyrolytic conditions. Most of these studies were conducted in flow reactor systems [33, 35, 110, 111]. Lemieux et al. [33] investigated the flash pyrolysis of TMS in a temperature range of 660 K-1470 K. Baldwin et al. [35] investigated the thermolysis of TMS in a pulsed-stirred-flow system in a temperature range of 840-1055 K at a pressure of 1 bar and proposed a reaction mechanism containing initiation and propagation reaction sequences, radical-radical chain termination reactions, and secondary dissociation reactions for Si-C-H and hydrocarbon species. Most recently, Sela et al. [34] investigated the thermal decomposition of TMS and proposed a reaction mechanisms under pyrolytic conditions. Behind reflected shock waves, Sela et al. measured the consumption of TMS and the formation of stable end-products time-resolved and temperature-dependent by applying time-of-flight mass-spectrometry and GC/MS. The primary decomposition step is the scission of one Si-C bond to form a trimethylsilyl and a methyl radical. The trimethylsilyl radical can either subsequently lose the remaining methyl groups or sila-isobutene can be formed by dissociation of a C-H-bond. The intermediate sila-isobutene then can take part in a series of polymerization and elimination reactions, which can lead to the formation of SiC-films and particles.

Under oxidative conditions, TMS and other Si-containing species can be used as precursor compounds for Si-O-containing nanoparticles. Almost no chemical kinetic analysis of TMS oxidation was reported yet. Reed [37] investigated the oxidation of TMS in a furnace reactor at temperatures between 650-1010 K and a pressure of 5 bar. Reed proposed a reaction

sequence to explain the formation of detected short-lived silicon species like $(\text{CH}_3)_3\text{SiO}$, $(\text{CH}_3)_2\text{Si}(\text{OH})_2$, and $(\text{CH}_3)_3\text{SiOH}$, which is initiated by an H-abstraction from TMS as the first step. In the reaction model of Reed [37], the mechanism of Baldwin et al. [35] was extended by the reaction between TMS and O_2 and several reactions between flame radicals and silicon species.

In the context of silica nanoparticle formation, the molecule $\text{Si}(\text{OH})_4$ is regarded as an important intermediate. Phadungsukanan et al. [40] calculated thermochemical data, i.e., heat capacities, enthalpies of formation and entropies, for 180 species that appear during the combustion of tetraethoxysilane (TEOS), which is another well-known precursor compound used in flame synthesis. Based on their thermochemical data, Phadungsukanan et al. [40] calculated the equilibrium composition of the TEOS gas phase system as a function of temperature. Their analysis shows that the equilibrium concentrations of the silicates at atmospheric pressure and high temperatures are not significant. Instead, $\text{Si}(\text{OH})_4$ is identified as the most stable monomer during the combustion of TEOS in the temperature range of 1100 - 1500 K. Its equilibrium mole fraction is several orders of magnitude larger than the mole fractions of other monomers or silicates [40].

In most combustion studies of silicon containing precursors in low-pressure flames, e.g. silane (SiH_4) [48], silicon tetrachloride (SiCl_4) [105], TMS [16], HMDSO [19], it is assumed that gaseous SiO and SiO_2 form and contribute to the growth of clusters [16, 19, 48, 112]. However, Shekar et al. [41] state that gaseous SiO_2 is very unstable compared to $\text{Si}(\text{OH})_4$, so that lower equilibrium concentrations are expected and the dimerization and dehydration of $\text{Si}(\text{OH})_4$ is more likely to lead to the formation of large clusters than the dimerization of gaseous SiO_2 molecules.

In this study we investigate the decomposition of TMS and the formation of clusters in laminar $\text{H}_2/\text{O}_2/\text{Ar}$ low-pressure flames by means of MBMS. The aim of this work is to identify the destruction pathway of TMS and crucial intermediates which are responsible for cluster growth. In addition, qualitative and quantitative species profiles provide insights into reaction sequences.

6.3 Experimental

All flames were stabilized on a 36 mm diameter sintered bronze burner. The burner is installed upright in a low-pressure flame reactor. Gas samples are taken from the flame along the center line of the burner through a quartz nozzle with an orifice (diameter 130 μm) at the tip. The distance between burner and nozzle was varied in vertical direction between $\text{HAB} = 0 - 230$ mm (HAB, height above the burner) with a stepper motor to obtain spatially resolved profiles for each species. A molecular beam expansion is achieved by a pressure reduction from 30 mbar in the reactor to 10^{-4} mbar in the first expansion stage. The expansion quenches the reactions and allows the detection of reactive species. The core of the beam is extracted by a skimmer into the ionization chamber of the time-of-flight mass spectrometer system (mass resolution $m/\Delta m = 2400$, Company Kaesdorf, Munich) with a pressure of 10^{-7} mbar. The expansion quenches the reactions and allows the detection of

reactive species. A schematic drawing is provided in the supplemental material (appendix A). The gas sample is ionized by electrons with a low kinetic energy of 17 eV to avoid excessive fragmentation produced by a filament and electron optics for shaping and pulsing the electron-beam. Additionally, kinetic electron energies of 70 eV are used for ionization to increase sensitivity. The electron beam has an energy distribution with a full width at half maximum of 0.5 eV (FWHM). All flame species, including argon, can be detected simultaneously at 17 eV. The ions are mass-separated by an orthogonal time of flight-mass spectrometer (TOF-MS) and detected on a multichannel plate. The signals are digitized by a multiscaler operated in ion counting mode so that one ion is registered per mass spectrum. 10^7 mass spectra are summed to obtain sufficient sensitivity for the detection of mole fractions in the $x = 10^{-6}$ range. Under these conditions, each integrated mass peak in the accumulated spectrum is proportional to the mole fraction of the respective species in the gas sample weighted by the ionization efficiency of the substance. Convolved ion signals can be separated, because the TOF-MS has a high mass resolution of $m/\Delta m = 2400$. All investigated flames have a total volume flow of 2 slm. The initial molar composition of the flame gases is $\text{H}_2/\text{O}_2/\text{Ar} = 0.2725/0.2275/0.5000$. One flame was doped with 600 ppm TMS (referenced to the total volume flow of 2 slm). TMS (Sigma-Aldrich, purity of 99 %) was metered with a syringe pump with an accuracy of $\pm 2\%$ of the delivered volume and evaporated in a home-built evaporator at 60 °C. Calibrated mass flow controllers regulate the gas flow with an accuracy of $\pm 5\%$. The pressure in the burner chamber was regulated with a throttle valve and maintained at 30 mbar with an accuracy of $\pm 0.1\%$. Temperature profiles along HAB were measured using aluminum oxide coated thermocouples (type S). These temperature profiles are corrected for radiation losses by the procedure of Bahlawane et al. [93] and we expect an error in the thermocouple measurement of ± 100 K. The instrument is calibrated using compounds of known mass and the calibration is refined for flame spectra with combustion species.

6.4 Data Analysis

The quantitative evaluation of the mass spectrometric raw data is based on the procedures described in Kasper et al. [31] and Struckmeier et al. [82]. Burner scans are carried out at electron energies of 17 eV for the evaluation of the major and intermediate species and for the evaluation of the clusters, the electron energies are adjusted to 70 eV in order to improve the signal-to-noise ratios of the profiles. The mole fraction of species i is connected to the mass spectrometric signal by Eq. (6-1):

$$S_i = x_i \cdot A \cdot SW \cdot \phi \cdot FKT \cdot MD_i \cdot \int \sigma_i(E) \cdot f(E) dE \quad (6-1)$$

Here, S_i is the integrated mass spectrometric signal intensity, x_i the mole fraction of species i , A the instrument factor, SW the number of time-of-flight mass spectra summed at each

data point, \emptyset number of electrons involved in the ionization process, FKT is a temperature-dependent sampling function, and $\sigma_i(E)$ is the ionization cross-section of species i at the ionization energy E with $f(E)dE$ representing a Gaussian distribution function. Argon was used as the reference species in all experiments. The intermediate profiles x_i can be determined depending on the signal intensities and calibration factors by Eq. (6-2) relative to argon:

$$\frac{S_i}{S_{Ar}} = \frac{x_i}{x_{Ar}} \cdot \frac{\int \sigma_i(E) \cdot f(E)dE}{\int \sigma_{Ar}(E) \cdot f(E)dE} = \frac{x_i}{x_{Ar}} \cdot k_i \quad (6-2)$$

To determine the mole fractions from Eq. (6-2), the calibration factors and the argon mole fraction profile must first be obtained. The determination of the mole fraction profile of the reference species argon is carried out by the routine from [29, 31]. All major species of the flame ($\text{Si}(\text{CH}_3)_4$, O_2 , H_2 , H_2O , CO , CO_2) are added up to one as shown in Eq. (6-3):

$$x_{\text{tot}} = x_{Ar} + \sum_i x_i = 1 \quad (6-3)$$

Using the signal ratios and calibration factors from Eq. 2 and Eq. 3, the argon mole fraction profile x_{Ar} can be calculated by (6-4).

$$x_{Ar} = \frac{1}{1 + \sum \frac{S_i}{S_{Ar}} \cdot \frac{1}{k_i}} \quad (6-4)$$

For the calculation of the argon mole fraction profile x_{Ar} , the calibration factors of the major species ($\text{Si}(\text{CH}_3)_4$, O_2 , H_2 , H_2O , CO and CO_2) from the C, H, O and Si -balance are used. Signals and calibration factors of minor flame species e.g. O, OH, H, and silicon containing species are not considered. It is estimated from previous measurements that the error of the major species mole fractions is not greater than 20 %.

In this work, three routines were used to determine the calibration factors of the flame and precursor species:

1. The calibration factors of mole fractions of the major species (H_2 , O_2 , Ar, H_2 , CO_2 , CO) are obtained from the C, H, O balance based on the routine from ref. [29, 31, 82].
2. The calibration factors of CO , CO_2 and $\text{Si}(\text{CH}_3)_4$ were calculated by comparing the signal intensities from a measurement of each species in a mixture of known composition with argon. The calibration measurements were carried out with exactly the same instrument settings as the flame measurements.

3. Species, which were not available or are not applicable for direct calibration, are quantified by indirect calibration using a similar procedure to the relative ionization cross section (RICS) method developed by Biordi [89]. Electron ionization cross sections usually behave linearly near the ionization potential. Biordi assumes that the cross sections of an intermediate species can be estimated from the cross section of a species with known ionization cross section curves by shifting the curve by the difference in ionization energy of the stable and intermediate species. If available, the curves are also scaled to the ratio of the ionization cross sections at 70 eV. The cross sections at 70 eV of the species of interest here are not available, so that the scaling step had to be omitted in this work. Based on the only cross sections that have been reported in the literature for silicon containing species, e.g. SiH_4 , Si_2H_6 , $\text{Si}(\text{CH}_3)_4$, SiO and SiO_2 [113, 114], we assume that this omission will not greatly increase the inaccuracy of the method because they vary by less than 30% at 17 eV. Ionization energies are needed to shift the ionization cross section curves appropriately. They were calculated in this work by quantum chemical calculations for the most important intermediates of interest: SiO_2 [114], $\text{Si}(\text{OH})_4$, $\text{Si}(\text{CH}_3)_2\text{OH}$, $\text{Si}(\text{CH}_3)(\text{OH})_2$, and $\text{Si}(\text{OH})_3$. As directly calibrated reference species, $\text{Si}(\text{CH}_3)_4$ was used, so that the cross section at the same energy difference b from the ionization energy IE is set to the same value:

$$\sigma_i(\text{IE}_i + b) = \sigma_{\text{TMS}}(\text{IE}_{\text{TMS}} + b) \quad (6-5)$$

If the flame measurement is performed at the energy E , b is obtained by:

$$b = E - \text{IE}_i \quad (6-6)$$

The calibration factor of species i is then obtained by:

$$k_i = k_{\text{TMS}} \cdot \frac{\sigma_i(E)}{\sigma_{\text{TMS}}(\text{IE}_{\text{TMS}} - \text{IE}_i + b)} \quad (6-7)$$

The RICS method is also used to estimate calibration factors for CH_4 [115], C_2H_4 [115], C_2H_6 [115]. The calibration factors estimated with this procedure may introduce errors on the order of a factor of 2 into the mole fraction calculations.

4. For all other silicon-containing species with unknown ionization potentials, a calibration factor is calculated from the silicon-balance after subtraction of the calibrated species under the assumptions that the loss of Si from the element balance by formation of solid silicon-containing particles is insignificant and that these species have the same ionization cross

sections. With these assumptions, the mole fractions of intermediate silicon species were obtained by the following steps. After determination of the intermediate mole fractions of TMS, SiO₂, Si(OH)₄, Si(OH)₃, Si(CH₃)₂OH, Si(CH₃)(OH)₂ with Eq. (6-1) the mole fraction of the remaining silicon species is obtained with Eq. (6-8):

$$\begin{aligned} x_{\text{Si}}(\text{HAB} = 0) \\ = x_{\text{TMS}}(\text{HAB}) + x_{\text{Si-intermediates}}(\text{HAB}) + x_{\text{Si-residual}}(\text{HAB}) \end{aligned} \quad (6-8)$$

With the assumption of equal cross sections, the mole fraction ratio reduces to a signal ratio and the mole fraction of each remaining silicon species can be determined at maximum ion signal according to:

$$x_i = \frac{S_i}{S_{\text{total}}} \cdot x_{\text{Si-residual}} \quad (6-9)$$

With S_i : signal of species i , S_{total} : sum of the signals of the residual silicon species. To calculate the mole fractions at all HAB a calibration factor k_i is determined:

$$k_i = \frac{S_i}{S_{\text{Ar}}} \cdot \frac{x_{\text{Ar}}}{x_i} \quad (6-10)$$

Finally, the mole fraction for each silicon species is calculated by rearranging Eq. (6-10). A tabulated list of all mole fractions is given in the supplemental material (see appendix A).

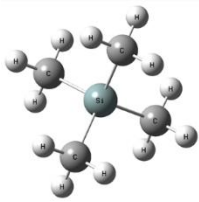
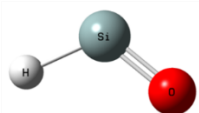
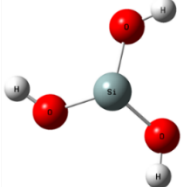
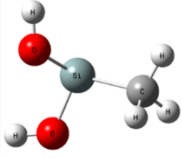
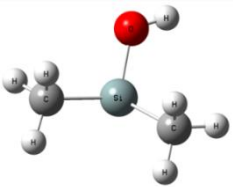
An error propagation of the uncertainties of the mass flow controllers to the element balances leads to an absolute error of 20 % in the argon mole fraction. Since signal ratios are used in the data reduction, errors due to fluctuations in, e.g. gas flow, pressure, and ionization energy, are compensated and only the uncertainties of the cross sections have a significant influence on the absolute uncertainties of the mole fractions. The error in the cross sections is usually under ± 50 % [113, 114]. The error for experimentally determined calibration factors is expected to be 15 %. For intermediate species calibrated by the modified RICS method the absolute uncertainty of the mole fractions is between 30 - 60 %. By assuming equal cross sections for all remaining silicon species, an additional error of up to a factor of two is expected. Another source of uncertainty is fragmentation of the molecules during ionization. It cannot be completely avoided due to the width of the electron energy distribution even at the low electron energy of 17 eV. Here, the fragmentation pattern of TMS was determined by calibration and flame signals were corrected by comparing with cold gas measurements. Fragmentation contributions of other silicon containing

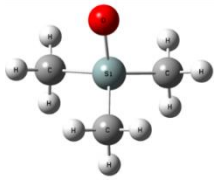
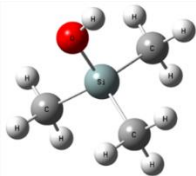
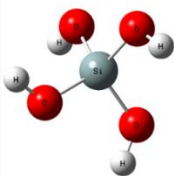
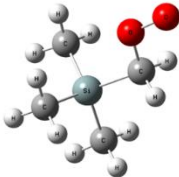
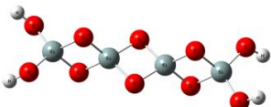
intermediates will be very small due to the small intermediate concentrations but cannot be excluded.

6.5 Quantum chemical calculations of ionization energies of silicon-containing species

Ionization energies (IE) were calculated for "vertical" ionization processes, which are relevant for the determination of calibration factors for silicon-containing species as described above. The molecular ions M^+ have the same structure as the starting molecules or radicals M . First, the structures of the neutral species M were optimized at the B3LYP/6-311++G (d, p) theory level and analyzed by a subsequent frequency analysis at the same level of theory in order to verify that energy calculations are not conducted on transition state structures. All calculations in this work have been carried out using the Gaussian09 software package [116]. Subsequently, the energies E of the species M and the corresponding ions M^+ , $E(M)$ and $E(M^+)$ were calculated at the CCSD(T)/aug-cc-pvtz and UCCSD(T)/aug-ccpvtz theory levels, respectively. For neutral species with multiplicity $S = 1$, the CCSD(T) method was used and for neutral species with multiplicity $S = 2$ and for all molecule ions, the UCCSD(T) method was applied. The ionization energy IE of M , $IE(M)$, is then $IE(M) = E(M^+) - E(M)$. Since the coupled cluster iterations failed to converge, it was not possible to calculate electronic energies for two ion species by using the UCCSD(T)-method: $Si(CH_3)_3O^+$ and $Si(CH_3)_3(CH_2)OO^+$. According to De Proft and Geerlings [117], IEs as well as electron affinities and chemical hardness can be also calculated with reasonable accuracy using DFT with a large basis set such as cc-pVTZ or aug-cc-pVTZ. Since CCSD(T)- and UCCSD(T)-methods did not work for $Si(CH_3)_3O^+$ and $Si(CH_3)_3(CH_2)OO^+$, the IEs of these two radicals have been calculated at the B3LYP/aug-cc-pVTZ level of theory. Table 6-1 shows the structures and ionization energies of the most abundant silicon-containing species along with the corresponding calibration factors (k). It can be noted that the calculated IE for SiO_2 is in very good agreement with the experimentally determined value by Kostko et al. [118]. Concerning TMS, three experimentally based vertical IEs are reported on the NIST-database: 10.29 [119], 10.4 [120], and 10.57 [121] eV, whereas the calculation gives 10.62 eV. Theory over predicts the experimental data, which were obtained from photoelectron spectroscopy, but overall the calculated IE is still in good agreement. To verify if the CCSD(T) method is able to reasonably predict IEs, we also carried out calculations for few other compounds for which vertical IEs are known: $SiCl_4$, SiO , CH_4 , SiH_4 , and SiH_3 . On the NIST-database [122], following experimental vertical IEs (in eV) can be found for these species: 12.1, 11.5, 13.6, 12.3, and 8.7 eV. The CCSD(T)/UCCSD(T) calculated IEs are: 12.0, 11.5, 14.4, 12.8, and 8.8 eV. Except for CH_4 , the overall agreement is very good. Therefore, we expect that with average uncertainties below ± 0.5 eV, the CCSD(T)/UCCSD(T)-calculations are able to predict IEs quite well. In their paper on the ionization potential of SiO_2 , Kostko et al. [118] also applied the CCSD(T)-method to calculate the stretch potentials for SiO_2 and SiO_2^+ , which supports the assumption that this high-level-method is probably accurate for determining IEs.

Table 6-1. Calculated ionization energy thresholds (at CCSD(T) and UCCSD(T)/aug-cc-pVTZ level of theory) and molecular geometries of the most abundant silicon containing species. Calibration factor (k) at 17 eV obtained with RICS method. The ionization potentials of most of the abundant silicon containing species are not available in literature.

m/z	Assigned to Species	Molecular geometry	„Vertical“ IE eV	Literature values / eV	k (17 eV)
88	Si(CH ₃) ₄		10.62	10.29 [119] 10.4 [120] 10.57 [121]	42.31
45	HSiO		9.62	-	49.48 (RICS)
	Si(OH)		7.01	-	73.48 (RICS)
60	SiO ₂		12.65	12.60 eV [118]	8.65 (RICS)
79	Si(OH) ₃		8.25	-	62.08 (RICS)
77	Si(CH ₃)(OH) ₂		7.73	-	66.86 (RICS)
75	Si(CH ₃) ₂ (OH)		7.42	-	69.72 (RICS)

89	$\text{Si}(\text{CH}_3)_3\text{O}$		11.05 ^a	-	36.33 (RICS)
90	$\text{Si}(\text{CH}_3)_3\text{OH}$		10.40	-	42.31 (RICS)
96	$\text{Si}(\text{OH})_4$		11.81	-	20.54 (RICS)
119	$\text{Si}(\text{CH}_3)_3(\text{CH}_2)\text{OO}$		10.37 ^a	-	42.58 (RICS)
276	$\text{Si}_4\text{O}_{10}\text{H}_4$		-	-	37.75

^a Calculated at the B3LYP/aug-cc-pVTZ level of theory

6.6 Results and discussion

6.6.1 Influence of TMS on species and temperature profiles

Major species and temperature profiles of a neat hydrogen flame (flame A) and a doped flame (flame B: 600 ppm $\text{Si}(\text{CH}_3)_4$) were investigated. Tabulated mole fractions of flame A and B can be found in the supplemental material (see appendix A). Figure 6-1 compares mole fractions of the major species in the two flames, which are ionized at $\text{EI} = 17$ eV. The structure of the neat flame is simulated with the flame code of Chemical Workbench

(Kintech Lab Ltd.) [123] and the reaction mechanism of Li et al. [124] using a perturbed temperature profile determined with the procedure described by Struckmeier et al. [82] as input. The resulting perturbed temperature profile is given in the supplemental material. Exhaust gas mole fractions and profile shapes are well reproduced by the simulation but deviations occur near the burner. They are particularly evident for the hydrogen profile and in part caused by its high rate of diffusion in the flame. In addition, the deviations can be attributed to a combination of a radial cooling and a suction effect [82] of the nozzle on the flame that could not be captured in the one-dimensional simulation. The simulation shows that the mole fractions of the small flame radicals H, O, and OH sum to about 5% in the exhaust gas. Simulation results are not explicitly shown here, but are given in the supplemental material. Since the small radicals were neglected in the element balance and calculation of the argon mole fraction, the experimental argon profile is systematically too high. The offset in the argon profile influences the mole fractions for all other species. The uncertainty of the argon profile related to omission of radicals will translate to intermediate species. Because of the ion counting approach used in this work, the noise level is close to 1 count and only signals with more than 10 counts are evaluated so that signal intensity does not contribute significantly to the errors. The major species profiles of the doped flame B have the same profile forms but are shifted towards the burner. They reach similar exhaust gas mole fractions as in flame A. This effect indicates that TMS addition leads to an acceleration of the reactions in the preheat and reaction zones and is also reflected in the unperturbed temperature profiles also presented in Figure 6-1.

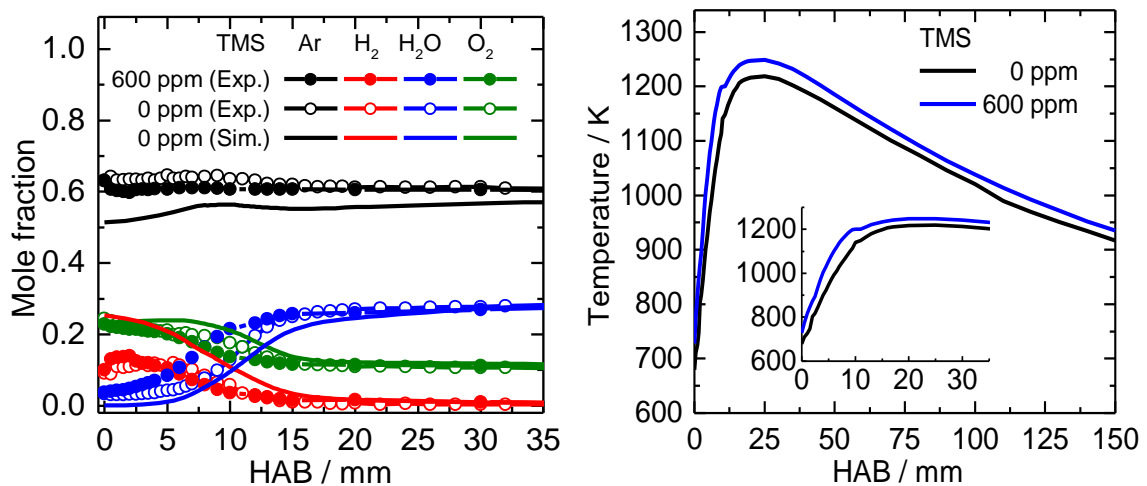


Figure 6-1. Left: Open symbols show the experimental mole fraction profiles of the major species in a neat hydrogen flame, closed symbols a H₂ flame doped with 600 ppm TMS and lines indicate the profiles simulated with the mechanism of Li et al. [124] for the neat flame (TMS = 0 ppm), (Profiles evaluated with electron ionization energy EI = 17 eV, flame A and B); Right: Temperature profiles in a laminar low-pressure H₂/O₂/Ar-flame with addition of TMS (0/600 ppm) measured with a thermocouple.

The temperature profile in Figure 6-1 shows that in the TMS-doped flame the temperature rises more steeply close to burner, while its exhaust gas reaches a similar and slightly larger

temperature than flame A. For transition metals, catalytic cycles have been observed in flames which lead to an acceleration or deceleration of the fuel conversion [51]. Whether such processes are active in this TMS doped flame or whether the acceleration is caused by the exothermal TMS conversion, needs to be evaluated by future modeling studies.

Close to the burner the TMS conversion leads to the formation of small hydrocarbons, e.g. CH_4 and C_2H_4 . Figure 6-2 shows that CH_4 is formed earlier in the flame than C_2H_4 . There are several pathways for the formation of CH_4 . Lemieux et al. suggest that during pyrolysis CH_4 production is initiated by the dissociation of TMS to trimethylsilyl and methyl radicals. By Si-C bond fission, another methyl group can be released, i.e., trimethylsilyl radicals can react to dimethyl-silylene ($\text{Si}(\text{CH}_3)_2$). Lemieux et al. propose that CH_4 can be formed either by elimination of CH_4 from $\text{Si}(\text{CH}_3)_2$, or by bimolecular reactions, when methyl radicals abstract hydrogen atoms from TMS and small hydrocarbons, which are formed during TMS combustion. Another possibility for CH_4 formation during a unimolecular reaction can be related to a roaming channel. For neo-pentane, which is the analog hydrocarbon to TMS, the possibility of methyl radical roaming was explored by Sivaramakrishnan et al [125]. For neo-pentane, roaming directly yields methane and isobutene. Quantum chemical and transition state theory calculations indicate that in particular at temperatures below 1000 K, the roaming reaction becomes the dominant dissociation process with branching fractions of more than 80%. By analogy, a roaming of methyl radicals in TMS dissociation would result in the formation of methane and sila-isobutene. Neither experimental nor theoretical investigations have been dedicated to the possibility of roaming during TMS decomposition, but it seems to be another plausible pathway for CH_4 formation at temperatures below 1000 K.

C_2H_4 is formed by the recombination of methyl radicals to C_2H_6 and subsequent H-abstraction. Other detected hydrocarbon flame species are e.g. HCHO and CHO_2 . Figure 6-2 also shows the mole fraction profiles of CO_2 and CO. In those figures, which present species mole fraction profiles, we have used solid curves to guide the eye. These solid curves were obtained by fitting experimental data points with a spline function. The carbon balance of all gaseous carbon species can help to answer the question if any carbon is bound to the SiO_2 nanoparticles that are formed in the flame. The maximum theoretical carbon mole fraction is 2400 ppm, if 600 ppm of $\text{Si}(\text{CH}_3)_4$ are added to the flame. At all positions in the flame, the carbon balance is equal or larger than the theoretical value so that it can be concluded that no significant amount of carbon is bound to SiO_2 particles. According to Figure 6-2, deviations between expected and experimental values are well within the error limits. The error bars shown in Figure 6-2 are calculated based on the uncertainties of species mole fractions, weighted by their quantitative contribution to the carbon balance.

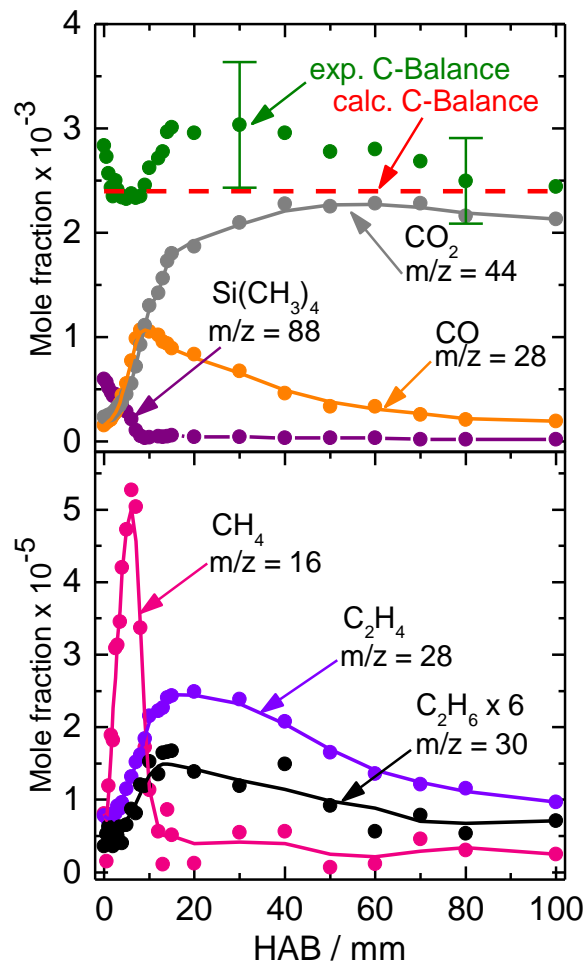


Figure 6-2. Mole fraction profiles of hydrocarbon species in the $\text{H}_2/\text{O}_2/\text{Ar}$ -flame with addition of TMS. The carbon balance reveals that all carbon is accounted for in the gas phase species. Solid curves were obtained by fitting experimental data points by a spline function; profiles are evaluated with electron ionization energy $\text{EI} = 17 \text{ eV}$.

6.6.2 Silicon containing intermediates

The identification of the intermediates, which are formed during the oxidation of TMS, is the first step towards answering the question which gaseous species are responsible for the formation and growth of silicon oxide clusters in a flame. Figure 6-3 shows the most abundant Si-C-O-H and Si-O-H species and their maximum mole fractions in flame B. Interestingly, many species have hydroxyl groups attached to the silicon, e.g. $\text{Si}(\text{OH})_4$, $\text{Si}(\text{CH}_3)_2(\text{OH})_2$, and $\text{Si}(\text{CH}_3)_2(\text{OH})$. The molecular geometry of the most abundant silicon-containing species is shown in Table 6-1.

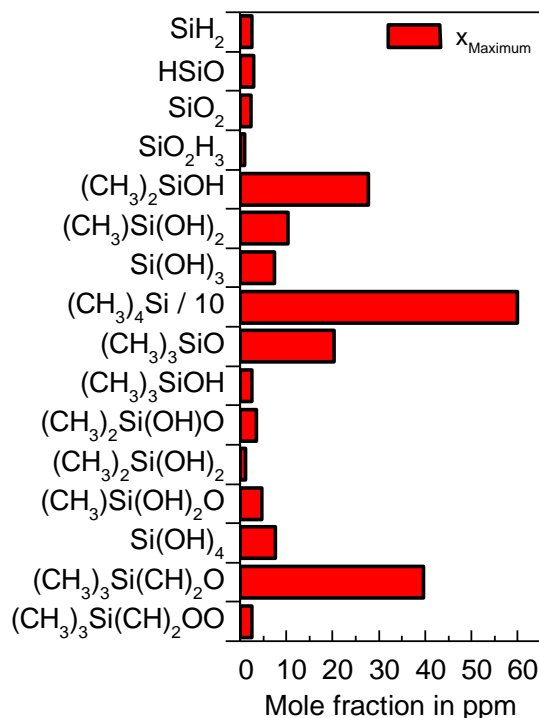


Figure 6-3. Maximum mole fractions (in ppm) of silicon containing combustion products of TMS in a H₂/O₂/Ar-flame. Maximum mole fractions are evaluated with electron ionization energy EI = 17 eV.

TMS is consumed completely at HAB = 8 mm. Nearly all silicon species formed in this region of the reaction zone have only one silicon atom. According to Baldwin et al. [36], TMS decomposition is initiated by H-abstraction through reactions with flame radicals, e.g. O, OH, and H to form (CH₃)₃SiCH₂. The (CH₃)₃SiCH₂ radical continues to react with oxygen and a peroxide is formed ((CH₃)₃SiCH₂ + O₂ = (CH₃)₃SiCH₂OO). The mass spectra reveal an intermediate with the correct sum formula of the peroxide. Electron ionization MBMS measurements cannot distinguish between isomers, so the observed species may be an isomer of the expected peroxide. However, the temperature in these flames is comparatively low and beside (CH₃)₃SiCH₂OO also the methyl peroxide (CH₃OO) could be detected close to the burner surface, corroborating the interpretation of the observed signal as at $m/z = 119$ as trimethylsilylperoxide. Figure 6-4a shows that the mole fraction of the peroxide (CH₃)₃SiCH₂OO with $m/z = 119$ peaks in the coldest part of flame closer to the burner (at HAB = 3mm) than all other detected species listed in Figure 6-3.

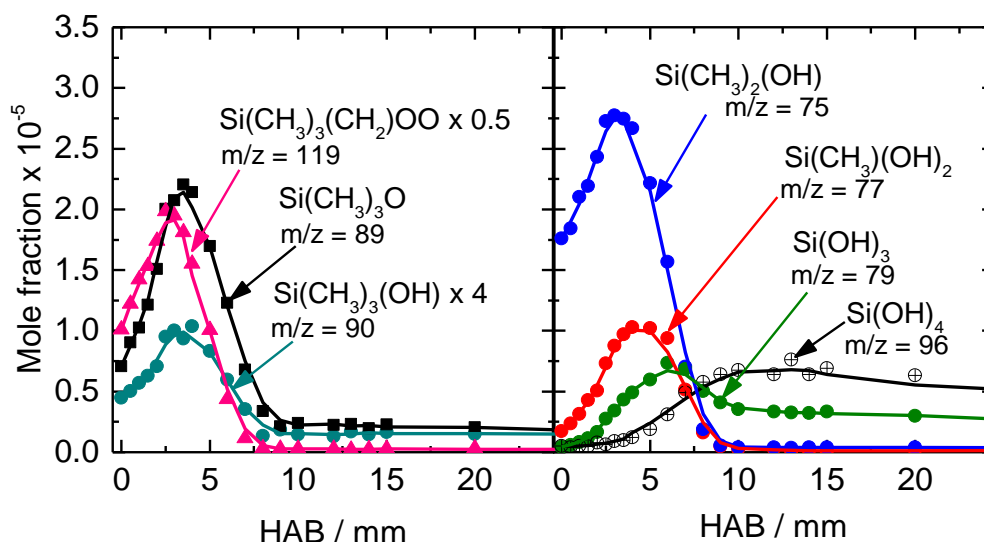


Figure 6-4. a) First decomposition steps of TMS in a hydrogen flame to form peroxides, b) Formation of Si(OH)_4 by a stepwise loss of methyl groups and recombination with a hydroxyl group. Profiles are evaluated with electron ionization energy $EI = 17$ eV.

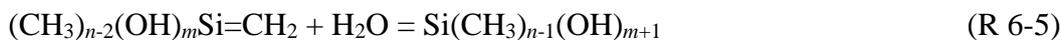
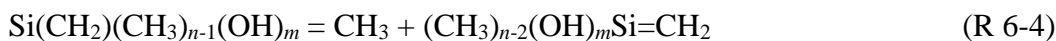
Baldwin et al. [36] describe that the peroxide $(\text{CH}_3)_3\text{SiCH}_2\text{OO}$ can react with H_2 to form the hydroperoxide $(\text{CH}_3)_3\text{SiCH}_2\text{OOH}$. $(\text{CH}_3)_3\text{SiCH}_2\text{OOH}$ as well as $(\text{CH}_3)_3\text{SiCH}_2$ mole fractions were below the detection limit in the flames investigated here. Instead, a large signal on $m/z = 103$ corresponding to $(\text{CH}_3)_3\text{SiCH}_2\text{O}$ was registered. $(\text{CH}_3)_3\text{SiCH}_2\text{O}$ could be formed from $(\text{CH}_3)_3\text{SiCH}_2\text{OO}$, e.g. according to $(\text{CH}_3)_3\text{SiCH}_2\text{OO} = ((\text{CH}_3)_3\text{SiCH}_2\text{O} + \text{O})$ or in reactions like $(\text{CH}_3)_3\text{SiCH}_2\text{OO} + \text{H} = (\text{CH}_3)_3\text{SiCH}_2\text{O} + \text{OH}$ with other flame radicals, but very similar profile shapes of the peroxide and $(\text{CH}_3)_3\text{SiCH}_2\text{O}$ suggest that $(\text{CH}_3)_3\text{SiCH}_2\text{O}$ might also be a fragment of the peroxide formed in the ionization process. In that case, the mole fraction of $(\text{CH}_3)_3\text{SiCH}_2\text{OO}$ in Figure 6-4a represents a lower limit because its signal intensity is reduced by the fragmentation process. The reaction mechanisms proposed by Baldwin et al. [36] and Tuazon et al. [126] do not consider such reactions. Instead, the peroxide $(\text{CH}_3)_3\text{SiCH}_2\text{OO}$ decomposes to $(\text{CH}_3)_3\text{SiO}$ ($m/z=89$) shown in Figure 4a and HCHO ($m/z = 30$) ($(\text{CH}_3)_3\text{SiCH}_2\text{OO} = (\text{CH}_3)_3\text{SiO} + \text{HCHO}$). Both products are measured here. The molecular reaction of $(\text{CH}_3)_3\text{SiO}$ with H_2 forms trimethylsilanol ($(\text{CH}_3)_3\text{SiO} + \text{H}_2 = (\text{CH}_3)_3\text{SiOH} + \text{H}$) (see Figure 6-4a). Both, $(\text{CH}_3)_3\text{SiCH}_2\text{OO}$ and $(\text{CH}_3)_3\text{SiO}$ are formed earlier than all other silicon species shown in Figure 6-3 and thus represent the first steps in the decomposition of TMS, which is initiated by H-abstraction. This reaction sequence can be repeated until Si(OH)_4 is formed.

The dissociation of TMS to $\text{Si(CH}_3)_3$ and CH_3 is a predominant reaction step under pyrolytic conditions [33, 127], but a methyl loss can also occur under flame conditions. An evaluation of the profile with mass $m/z = 73$ ($\text{Si(CH}_3)_3$) was not possible, because it was convoluted with the signal of the most abundant fragment of TMS and could not be recovered by the fragmentation correction. A similar issue affects the profile of the methyl radical. Figure 6-3 illustrates that $m/z = 75$ $(\text{CH}_3)_2\text{SiOH}$, $m/z = 77$ $(\text{CH}_3)\text{Si(OH)}_2$, $m/z = 79$ Si(OH)_3 , $m/z = 96$ Si(OH)_4 are the most abundant silicon containing intermediates with interpretable profiles. For this reason, in addition to the reactions discussed above, we propose another

possible sequence to form Si(OH)_4 : Starting from $(\text{CH}_3)_3\text{SiOH}$, Si(OH)_4 can be formed by a stepwise loss of methyl radicals and recombination of the silyl with hydroxyl radicals. This reaction sequence with $n, m = 1-4$ and $m + n = 4$ can be summarized as follows:



Figure 6-4b clearly shows the presence of $\text{Si(CH}_3)_x(\text{OH})_y$ intermediates, which supports the proposed sequence summarized by (R 6-1) and (R 6-2). However, in these silanoles, the energies for dissociating Si-C bonds at 298 K, calculated applying the G4 [128] composite method implemented in the Gaussian09 software [116], are around 90 kcal/mol, which makes a stepwise loss of methyl groups due to Si-C bond fissions not favourable at temperatures below 1000 K. The question remains if $\text{Si(CH}_3)_x(\text{OH})_y$ intermediates can be produced by other reactions. Another possibility to form these silanoles up to $(\text{CH}_3)\text{Si(OH)}_3$ can be envisioned by following sequence:



Beginning with TMS, a H-abstraction (R 6-3) leads to a $\text{Si(CH}_3)_3\text{CH}_2$ radical. This radical can decompose by losing a methyl group (R 6-4), which gives the molecule sila-isobutene ($(\text{CH}_3)_2\text{Si}=\text{CH}_2$). Due to the Si-C double bond, addition reactions are possible. The hydration (R 6-5) then results in the formation of $(\text{CH}_3)_3\text{Si(OH)}$. This sequence can be repeated, giving $\text{Si(CH}_3)_2(\text{OH})_2$ and $\text{Si(CH}_3)(\text{OH})_3$. Due to lower energetic barrier heights compared to Si-C bond fissions, the proposed pathway (R 6-3) – (R 6-5) seems to be more likely to occur at temperatures below 1000 K. However, (R 6-3) – (R 6-5) do not give Si(OH)_4 . In order to produce Si(OH)_4 from $\text{Si(CH}_3)(\text{OH})_3$, the loss of the remaining methyl group and the addition of an OH radical would be required (see (R 6-1) and (R 6-2)).

Figure 6-5 shows possible decomposition pathways of TMS in a hydrogen flame and the formation of stable monomers and the first smaller silicon oxide clusters. The labelled species were detected experimentally. The chemical geometry of the experimental detected labelled species from Figure 6-5 is shown in Table 6-1.

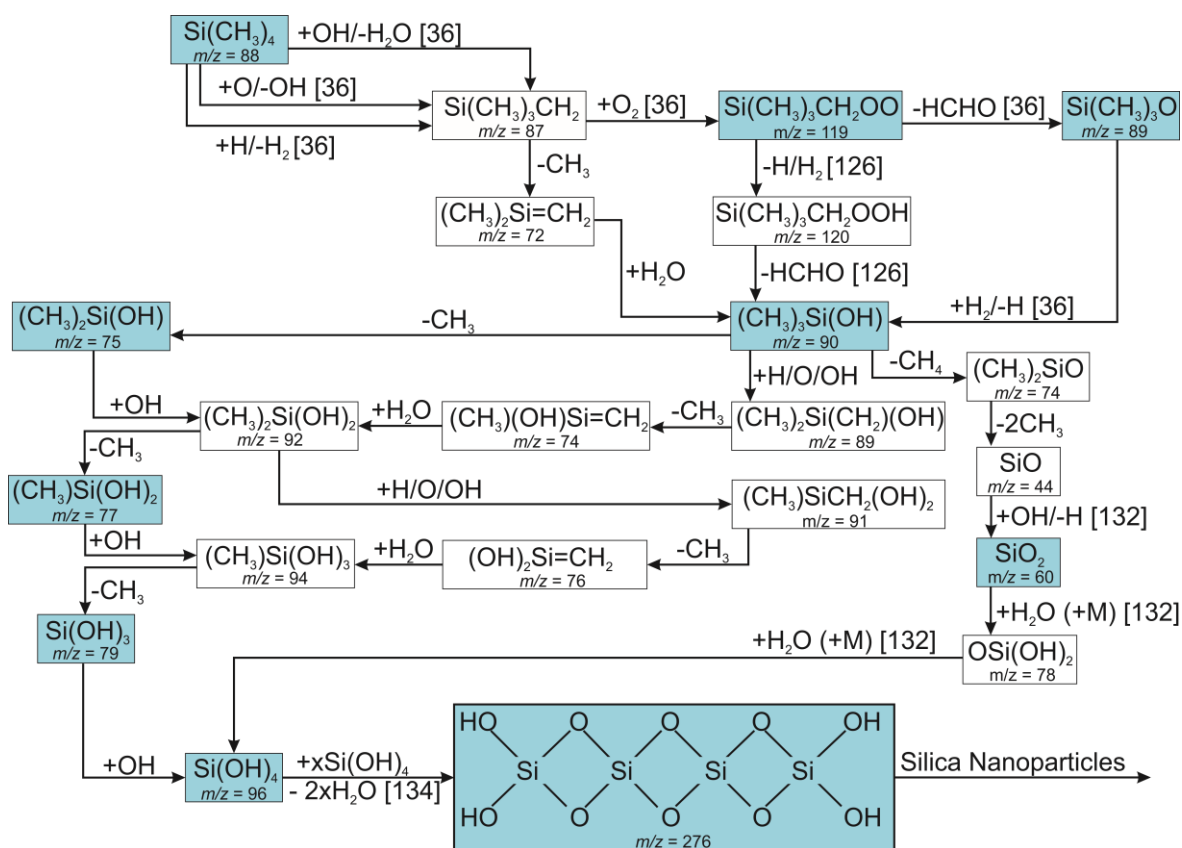


Figure 6-5. Postulation of reaction pathway from precursor to the first silicon oxide clusters (explained in Section 6.6.3 Formation and growth of silicon oxide clusters) based on experimental data (labelled in blue). The schematic of the reaction pathway proposes which species may contribute to particle formation. Numbers in parentheses correspond to reactions from literature.

Figure 6-4b shows that the number of hydroxyl group increases with increasing distance from the burner and this observation is also qualitatively reflected in the reaction pathways presented in Figure 6-5. Another species that was detected by mass-spectrometry, is SiO_2 . One possibility to explain SiO_2 formation is that TMS completely dissociates to Si ($\text{Si}(\text{CH}_3)_4 = \text{Si} + 4\text{CH}_3$) which then can be oxidized by e.g. O_2 and OH to SiO ($\text{Si} + \text{O}_2 = \text{SiO} + \text{O}$) and SiO_2 ($\text{SiO} + \text{OH} = \text{SiO}_2 + \text{H}$). However, since TMS consumption in the flame takes primarily place by H-abstractions and if roaming would be the primary unimolecular dissociation channel at temperatures below 1000 K, formation of Si-atoms is not to be expected. Instead, there is a possibility to explain the formation of SiO by $(\text{CH}_3)_3\text{SiOH}$ decomposition. Besides bond-fissions, this silanol derivative could also decompose by elimination reactions: $(\text{CH}_3)_3\text{SiOH} = \text{H}_2\text{O} + (\text{CH}_3)_2\text{Si}=\text{CH}_2$ and $(\text{CH}_3)_3\text{SiOH} = (\text{CH}_3)_2\text{Si}=\text{O} + \text{CH}_4$. Both processes represent four-center eliminations. Their transition state structures obtained from calculations at the B3LYP/6-31+G(d,p) level of theory are presented in Figure 6-6:

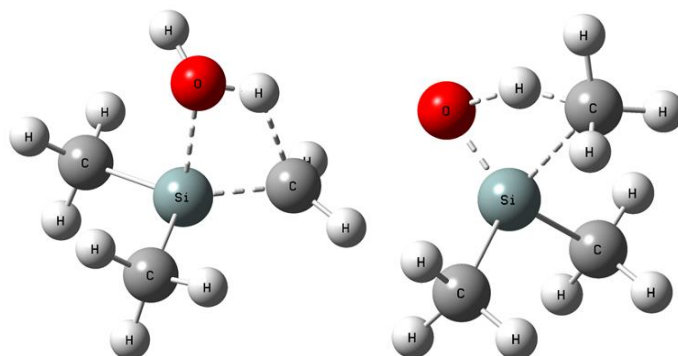


Figure 6-6. Transition state structures for two possible unimolecular reactions of $(\text{CH}_3)_3\text{SiOH}$ (Calculations at B3LYP/6-31+G(d,p) level of theory): Elimination of H_2O (left) and elimination of CH_4 (right).

The direct elimination of CH_4 would yield dimethyl-siloxane, $(\text{CH}_3)_2\text{Si}=\text{O}$. The loss of two methyl groups would then result in the formation of SiO : $(\text{CH}_3)_2\text{Si}=\text{O} = 2\text{CH}_3 + \text{SiO}$. The Si-C standard bond dissociation energy in $(\text{CH}_3)_2\text{Si}=\text{O}$ is calculated to be nearly 86 kcal/mol. Calculated bond dissociation energies and barrier heights mentioned in this work were obtained by using the G4-method [128] and refer to standard conditions. Beside bond fission, the siloxane could also undergo a keto-enol tautomerism: $(\text{CH}_3)_2\text{Si}=\text{O} = (\text{CH}_3)(\text{OH})\text{Si}=\text{CH}_2$. The barrier height for this process is calculated to be approximately 57 kcal/mol and for the reverse reaction, $(\text{CH}_3)(\text{OH})\text{Si}=\text{CH}_2 = (\text{CH}_3)_2\text{Si}=\text{O}$, it was calculated to be 44 kcal/mol. Beside the tautomerism, the enol-form itself can only decompose by Si-C and C-H bond fissions, which have similar bond dissociation energies like those in $(\text{CH}_3)_2\text{Si}=\text{O}$. Neglecting bimolecular reactions, for the tautomerism the chemical equilibrium is expected to be on the side of the keto-form, i.e., the siloxane.

It is interesting to note that starting from the silanol $\text{Si}(\text{CH}_3)_3(\text{OH})$, reactions (R 6-3) and (R 6-4), discussed above, would also result in the formation of the enol $(\text{CH}_3)(\text{OH})\text{Si}=\text{CH}_2$. As described, the enol can isomerize to the siloxane, which then can lose both methyl groups leading to SiO formation. Therefore, reactions (R 6-3) and (R 6-4) can also contribute to SiO and hence to SiO_2 and $\text{Si}(\text{OH})_4$.

Unfortunately, neither the siloxane, nor the enol were observed during the MBMS-measurements. The compound $(\text{CH}_3)_2\text{Si}=\text{O}$ is also supposed to be an important intermediate during the pyrolysis of cyclosiloxanes [129, 130]. However, it was only possible to monitor this siloxane by IR spectroscopy after stabilizing it from gas phase in argon matrices at ~ 12 K [131]. It is not clear why $(\text{CH}_3)_2\text{Si}=\text{O}$ seems to be so unstable, but its elusive character may be the reason why it is not possible to detect it in gas phase at high temperatures and the same problem might also apply for the enol form.

The mass-spectrometric observation of SiO_2 offers another plausible possibility to produce $\text{Si}(\text{OH})_4$. Plane et al [132] describe a two-step hydration of SiO_2 to $\text{Si}(\text{OH})_4$, where water is added sequentially as described in the reactions $\text{SiO}_2 + \text{H}_2\text{O} (+\text{M}) = \text{OSi}(\text{OH})_2$ and $\text{OSi}(\text{OH})_2 + \text{H}_2\text{O} (+\text{M}) = \text{Si}(\text{OH})_4$. They predict that $\text{Si}(\text{OH})_4$ can contribute to particle formation after subsequent polymerization [132]. Figure 6-7 shows that $\text{Si}(\text{OH})_4$ and SiO_2

are still present in significant quantities at high HAB. The main difference in the profile shapes is that Si(OH)_4 is consumed faster than SiO_2 . It is likely that Si(OH)_4 contributes to cluster growth in this part of the flame. It reaches its minimum at $\text{HAB} \approx 50\text{-}60$ mm and then stays constant. This profile shape suggests that equilibrium is reached; most likely by a reaction involving water. HSiO and SiO_2 (see Figure 6-7) often appear in numerical models, and are assumed to contribute directly to cluster growth in the flame.

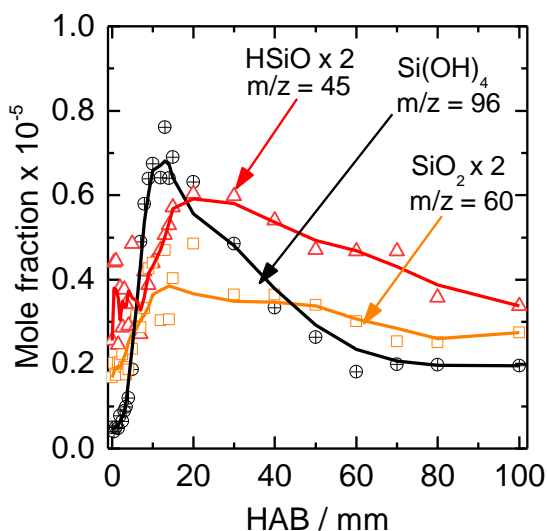


Figure 6-7. Silicon-intermediates in a $\text{H}_2/\text{O}_2/\text{Ar}$ -flame with addition of 600 ppm TMS (flame B). Profiles are evaluated with electron ionization energy $\text{EI} = 17$ eV.

6.6.3 Formation and growth of silicon oxide clusters

This study is concerned with the gas phase species and small clusters and the instrument was optimized for the detection of these species. While TMS decomposes to gaseous molecules, silicon oxide clusters are formed in the flame. A small ionization energy of $\text{EI} = 17$ eV has been used to minimize the fragmentation of the mononuclear silicon-containing intermediates. The concentration of the silicon containing intermediates is very small and the measurement therefore very time consuming. A second ionization energy of 70 eV has been used to measure the profiles in order to evaluate the silicon oxide clusters. Fragmentation may occur at 70 eV, but the profiles of the silicon oxide clusters show different profile shapes indicating that they are only minimally affected by fragmentation.

Here, a sequential increase in species mass by 60 u is observed leading to clusters with $m/z = 276$ ($\text{Si}_4\text{O}_{10}\text{H}_4$), $m/z = 336$ ($\text{Si}_5\text{O}_{12}\text{H}_4$), $m/z = 396$ ($\text{Si}_6\text{O}_{14}\text{H}_4$). Figure 6-8 shows the profiles of the silicon clusters, which initially rise and then decay again. Clusters with two and three silicon atoms were not detected. The identity of the clusters suggests that they are covalently bound, i.e., they might be formed by a stepwise addition of Si(OH)_4 and

elimination of 2 H₂O molecules. As the cluster mass increases, the maximum mole fraction shifts to higher HAB. Another hint to consider Si(OH)₄ as the predominant growth-species is that the maxima of the clusters occur in a flame region where the mole fraction of Si(OH)₄ decreases. The existence of larger stable silicon oxide clusters, with the structure (SiO₂)_nO₂H₄ with $n = 4$ and $n = 8$ e.g. Si₄O₁₀H₄ is confirmed by experiments of Xu et al. [133], who have generated silicon oxide clusters from porous silicon material using laser ablation and identified them by mass spectrometry.

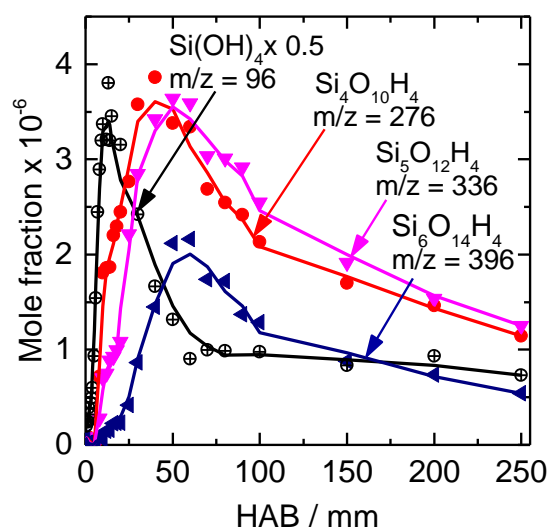


Figure 6-8. Formation of silicon oxide clusters with the structure (SiO₂)_nO₂H₄ with $n = 4$ and $n = 8$ in a H₂/O₂/Ar-flame with addition of 600 ppm of TMS, Cluster profiles evaluated with electron ionization energy EI = 70 eV.

Theoretical calculations by Xu et al. [133] and Timoshkin et al. [134] show that the silicon oxide clusters can have different structures, e.g. a tetrahedral cage structure or a linear chain structure. The clusters with $m/z = 336$ (Si₅O₁₂H₄) and $m/z = 396$ (Si₆O₁₄H₄) cannot form a cage structure in which each silicon atom is coordinated tetrahedrally by oxygen. For these species a chain structure seems more likely.

6.7 Conclusion

The focus of this work is the mass spectrometric identification of the intermediates from the first decomposition steps in the oxidation of TMS and the identification of species which are responsible for the formation and growth of silicon oxide clusters in H₂/O₂/Ar-flames. During the MBMS-measurements, C₁-C₂, Si-O-H, Si-C-O-H, and Si₄-Si₆ species were detected. In addition, the work provides insights into possible chemical reaction steps. Almost all of the carbon from TMS is converted to CO₂, CO, and small amounts of hydrocarbons, e.g., CH₄, C₂H₄ and C₂H₆. The carbon balance shows that all carbon is converted quantitatively to CO₂ and CO in the exhaust gas so that it can be inferred that the silicon dioxide nanoparticles are free of carbon residues. An increase in temperature is

observed in the reaction zone when neat $\text{H}_2/\text{O}_2/\text{Ar}$ - flames are doped with TMS, indicating that TMS initiates the oxidation reaction at lower temperatures. The rise in temperature shifts the species profiles closer to the burner surface. $\text{Si}(\text{OH})_4$ persists in significant amounts in the exhaust gas of the flame after the complete conversion of TMS and seems to be a major contributor to cluster formation and growth. Different reaction pathways for the formation of $\text{Si}(\text{OH})_4$ were discussed which can be summarized as followed: The whole process is initiated by H-abstraction from a methyl group. By recombination of the product radical $\text{Si}(\text{CH}_3)_3\text{CH}_2$ with O_2 , a peroxide can be formed, which can decompose and further react to yield the silanol $(\text{CH}_3)_3\text{SiOH}$. An alternative path to this silanol is the radical decomposition $\text{Si}(\text{CH}_3)_3\text{CH}_2 = \text{CH}_3 + (\text{CH}_3)_2\text{Si}=\text{CH}_2$, followed by H_2O addition to the sila-isobutene. Starting from $(\text{CH}_3)_3\text{SiOH}$, the intermediates $\text{Si}(\text{CH}_3)_x(\text{OH})_y$ can be formed by a stepwise replacement of methyl with hydroxyl groups. This replacement can take place either by subsequent Si-C bond fissions and addition of hydroxyl radicals (reaction sequence (R 6-1) and (R 6-2)) or by a series of H-abstractions, loss of methyl groups and H_2O addition (reaction sequence (R 6-3)-(R 6-5)). $(\text{CH}_3)_3\text{SiOH}$ can, among other possible unimolecular channels, undergo a four-center-elimination of CH_4 to yield the siloxane $(\text{CH}_3)_2\text{Si}=\text{O}$, which can decompose to SiO . Besides unimolecular decomposition of $(\text{CH}_3)_3\text{SiOH}$, also the reaction sequence (R 6-3)-(R 6-5) has the potential to contribute to SiO -formation: One possible intermediate appearing in the reaction sequence (R 6-3)-(R 6-5) is the enol $(\text{CH}_3)(\text{OH})\text{Si}=\text{CH}_2$, which can tautomerize to $(\text{CH}_3)_2\text{Si}=\text{O}$. $\text{Si}(\text{OH})_4$ is then produced by oxidation of SiO to SiO_2 followed by a two-step hydration. Concerning cluster growth, a comparison between the species profiles of $\text{Si}(\text{OH})_4$ and the clusters shows that the clusters reach their maxima when the $\text{Si}(\text{OH})_4$ decreases steeply in the exhaust gas of the flame, indicating that $\text{Si}(\text{OH})_4$ is consumed by the cluster formation. Clusters with four to six silicon atoms and with mass gaps of 60 u, presumably due to addition of $\text{Si}(\text{OH})_4$ and elimination of 2 H_2O , were observed with $m/z = 276$ ($\text{Si}_4\text{O}_{10}\text{H}_4$), $m/z = 336$ ($\text{Si}_5\text{O}_{12}\text{H}_4$), and $m/z = 396$ ($\text{Si}_6\text{O}_{14}\text{H}_4$). The data set provided in this work offers the basis for the development of a chemical kinetics reaction mechanism that can describe the chemistry from gas phase precursor consumption to silicon oxide cluster formation. With the availability of such a mechanism, simulations could model the initial steps towards particle-growth, the formation of possible side-products, as well as local heat release. These capabilities are needed to optimize flame reactor systems with respect to particle yield and particle size distributions.

7 Development and evaluation of a chemical kinetics reaction mechanism for tetramethylsilane-doped flames

The content of this chapter was published in *Chemical Engineering Science* 209, 115209, (2019), H. Janbazi, Y. Karakaya, T. Kasper, C. Schulz, I. Wlokas and S. Peukert, *Development and evaluation of a chemical kinetics reaction mechanism for tetramethylsilane-doped flames* and is reprinted with permission from Elsevier.

CRedit² author statement: Y. Karakaya performed the experiments, chose the precursor- and flame conditions, evaluated the experimental data and contributed to the interpretations of the results. H. Janbazi's contributions included writing the original draft, setting up the reaction mechanism and doing the simulations. T. Kasper, C. Schulz and I. Wlokas provided input to the discussions of the results. S. Peukert provided quantum chemical calculations of the reaction rate parameters and discussions of the results. All authors edited the manuscript.

7.1 Abstract

Tetramethylsilane (TMS) is a precursor for flame synthesis of silica (SiO₂) nanoparticles. A chemical reaction mechanism was developed for the oxidation of TMS in a lean low-pressure ($p \approx 30$ mbar) H₂/O₂/Ar flame using species mole fractions, obtained from molecular-beam mass spectrometry (MBMS) measurements in a matrix-supported flat flame doped with 600 ppm TMS. The thermodynamic data of Si-containing species were determined from quantum-chemical calculations at the G4 level of theory. The formation and subsequent consumption of Si(OH)₄, one of the main products of TMS oxidation, and the formation of Si₄O₁₀H₄ clusters are hypothesized to be the primary pathway in the synthesis of silica nanoparticles. The reaction rate coefficients are either estimated via an algorithmic optimization procedure or are assumed based on analogies to similar reactions in the literature. The mechanism was further validated based on MBMS measurements with the same base flame doped with 400 and 800 ppm TMS.

7.2 Introduction

The importance of gas-phase nanoparticle synthesis by thermal decomposition of vapor-phase precursor compounds has motivated many experimental studies and numerical simulations with the goal to understand the underlying molecular and particle-forming processes [1, 103, 135, 136]. Many studies on the Si/H/O system were conducted on SiH₄ combustion: Lindackers et al. [42] investigated low-pressure H₂/O₂/Ar flat flames doped with SiH₄. Britten et al. [137] developed a mechanism of 70 elementary reactions and 25 species for SiH₄ combustion. Besides SiH₄, other silicon-containing species were investigated in the context of materials synthesis. Shekar et al. [39] developed a kinetics mechanism that can be applied for numerical simulations of flames doped with

² CRedit (Contributor Roles Taxonomy)

tetraethylorthosilicate (TEOS). A detailed kinetics model of the thermal pyrolysis of TEOS was proposed by Nurkowski et al. [138]. In their model, possible pathways for TEOS decomposition were suggested based on analogies to ethanol combustion and, also in analogy to the ethanol high-temperature chemistry, a set of rate rules describing the decomposition of $-\text{OC}_2\text{H}_5$ moieties in TEOS has been derived. In addition, Nurkowski et al. [139] provided a skeletal mechanism for TEOS oxidation in H_2/O_2 flames. Recently, Chen et al. [140] described a detailed reaction mechanism for the oxidation of octamethylcyclotetrasiloxane (OMCTS).

Besides the radical-assisted oxidation in synthesis flames, precursor decomposition kinetics have also been investigated under pyrolytic conditions: Sela et al. [34] investigated the decomposition of tetramethylsilane ($\text{Si}(\text{CH}_3)_4$; TMS) and tetramethoxysilane (TMOS) behind reflected shock waves and derived elementary kinetics mechanisms [141]. In particular, TMS pyrolysis has been previously studied, e.g., by Baldwin et al. [35], Clifford et al. [110], and Taylor and Milazzo [142]. In all these studies, a combination of a flow reactor with gas chromatography was used to detect major stable reaction products. Under pyrolytic conditions, for example in chemical vapor deposition (CVD) reactors, TMS is also used as a precursor for the production of SiC films and particles and it has the advantage to be a safe, non-explosive and non-corrosive precursor [143].

TMS can be employed as precursor for the production of silica nanoparticles in flames. In a counter-flow diffusion flame, Zachariah and Semerjian [144] investigated the influence of SiH_4 , hexamethyldisiloxane (HMDSO), and TMS on the growth of silica particles and found that particle formation from TMS and HMDSO starts to occur later and at higher temperatures than from SiH_4 . In another recent study on HMDSO- and TMS-doped flames, Chrystie et al. [16] studied the influence of the precursor on the gas-phase reactions before the formation of silica nanoparticles with focus on SiO-based chemistry. They measured temperature fields in the flame and quantitative SiO mole-fraction profiles [16, 145] along the height above the burner (HAB) via laser-induced fluorescence (LIF) imaging using NO and SiO as target species. They observed a double-peak behavior of SiO profiles, which was also reported by Zachariah and Burgess Jr [104], Glumac [38] and Feroughi et al. [19].

Despite the large interest in silica-nanoparticle synthesis from the oxidation of silanes, few studies have proposed detailed reaction mechanisms for the combustion of silanes. In many previous investigations, global reaction models or possible reaction pathways, without providing reaction rates and thermochemical species data, have been reported.

The first attempt to analyze the high-temperature combustion chemistry of TMS was undertaken by Reed [37], who used the TMS pyrolysis reaction scheme reported by Baldwin et al. [35] as a basis for developing a reaction model for TMS oxidation.

Recently, Karakaya et al. [86] proposed a possible decomposition pathway of TMS in a $\text{H}_2/\text{O}_2/\text{Ar}$ flame and discussed the formation of stable monomers and the first smaller silicon oxide clusters based on their experimental observations. They conducted molecular-beam mass-spectrometry (MBMS) measurements on a premixed laminar low-pressure flame to detect Si-C-O-H- and Si-O-H-containing molecules as well as small hydrocarbons. Changes of mole fraction were observed along the HAB. Their quantitative measurements of temperature and species mole-fraction profiles are a stepping stone to the development of a kinetics mechanism. However, due to the unknown thermodynamic properties of many

intermediate species and unknown reaction rates, it was not possible to test the performance of the postulated reaction pathways of TMS proposed by Karakaya et al. [86]. This is one example that emphasizes the need to obtain thermodynamic data for silanes and siloxanes as well as theoretical calculations of reaction rates to facilitate reaction mechanism development.

In this work, we propose a more detailed kinetics model for the oxidation of TMS, which is developed based on species mole-fraction profiles obtained during MBMS measurements in low-pressure flames. The possible reaction pathways between crucial intermediates are discussed. Rate coefficients of important reactions are estimated by means of optimizing our kinetics model against quantitative mole-fraction profiles, analogies to similar reactions in hydrocarbon chemistry, and theoretical calculations. In addition, the thermochemical data of many intermediate species during oxidation of TMS are also calculated for the first time. To better understand the structure of the mechanisms discussed in this work, reaction-path analyses were carried out. Lastly, the developed mechanism is further validated through comparing predicted species profiles with experimental data from MBMS measurements in low-pressure $\text{H}_2/\text{O}_2/\text{Ar}$ flames doped with 400 and 800 ppm TMS.

7.3 Experiment

The formation and depletion of selected reaction products of TMS combustion (e.g., SiO_2 , CO_2 , CO , CH_4) was investigated in laminar $\text{H}_2/\text{O}_2/\text{Ar}$ low-pressure flat flames by MBMS. Details on the experiment, the data analysis, and uncertainties of the mole fractions can be found in Karakaya et al. [86] and only a brief description is given here: All flames were stabilized on a 36 mm diameter sintered bronze burner installed in a low-pressure reactor at 30 ± 0.03 mbar. At various HAB, gas samples were taken from the flame along the center line of the burner through a quartz nozzle. The distance between burner matrix and nozzle was varied in a range of zero to 100 mm HAB. The chemical composition of the samples changes only in the axial direction.

The flame conditions of the present work are shown in Table 7-1. The change in the base flame's equivalence ratio due to doped amount of precursor is neglected. The errors for the reported mole fractions depend on the calibration procedure and range between 15% for major species, 30–60% for most hydrocarbon intermediates and TMS, and a factor of two for silicon-containing intermediates.

Table 7-1. Summary of flame conditions in the present work. Flow rates are in standard liter per minute (273.15 K, 1013.25 mbar).

Flame	H_2 / slm	O_2 / slm	Ar / slm	φ	Pressure / mbar	TMS (ppm)	Ref.
A	0.545	0.455	1	0.6	30	0	[86]
B	0.545	0.455	1	0.6	30	600	[86]
C	0.545	0.455	1	0.6	30	400	This work
D	0.545	0.455	1	0.6	30	800	This work

Flame temperature measurements close to the sampling probe were conducted with an aluminum oxide coated thermocouple (type S) with a thickness of $r = 200 \mu\text{m}$. A radiation correction for heat losses of the thermocouple is performed by the method described by Bahlawane et al. [93]. The uncertainty of the temperature measurement is evaluated to ± 100 K. Additionally, the temperature dependence of the argon signal (referred to as FKT function) is evaluated to get the relative perturbed temperature profile as described by Cool et al. [146] and Struckmeier et al. [82]. This temperature profile includes the influence of the nozzle on the flame temperature and will be used for the simulations of flame A–D.

7.4 Modeling approach

One-dimensional flames and their structures are popular targets for modeling studies to validate chemical kinetics reaction mechanisms. Considering detailed kinetics in 2D or 3D simulations of reactive flows significantly increases the computational cost and the complexity of the simulations. The experimental data, which were modeled in this study, were determined in a flat burner-stabilized flame, which provides a nearly one-dimensional flame structure for the region close to the burner surface.

In this work, temperature profiles of the low-pressure flames (flames C and D) are determined. Before their use in modeling, the temperature data were smoothed. During the optimization procedure, the laminar premixed flame was simulated with the prescribed temperature profile.

For developing a kinetics model for the oxidation of TMS, we first attempted to identify the major pathways that connect the precursor with the final products. Then we calculated thermochemical data, i.e., heat capacities, enthalpies of formation, and entropies, of Si–C–O–H-containing species. These thermochemical data were expressed in the format of NASA polynomials. Finally, we determined rate coefficients, either by analogy to hydrocarbon chemistry, by RRKM (Rice-Ramsperger-Kassel-Marcus) calculations or by optimization of the kinetics model against experimental data. The RRKM calculations were carried out with the KiSThelP code [147]. Lennard-Jones potential parameters were estimated for the Si-containing species using the rules in Eqs. (7-1) and (7-2). The well-depth ϵ is the maximum energy of attraction between a pair of molecules and the collision diameter σ is the distance at which the intermolecular potential between the two molecules is zero. The volume-increments V_i for Si, H, CH₃, OH, CH₂, and O are 29.7, 2.8, 19.6, 9.7, 16.5, and 6.0 Å³, respectively [148, 149].

$$\epsilon/K = 1.21 T_b \quad (7-1)$$

$$\sigma/\text{\AA} = 1.45 \left(\sum_{i=1}^n V_i \right)^{1/3} \quad (7-2)$$

In Eq. 7-1, T_b is the boiling point of the corresponding species.

7.4.1 Calculation of thermodynamic data

The required thermodynamic data of the species and intermediates involved in the reaction mechanism were determined from quantum-chemical calculations at the G4 level of theory using the GAUSSIAN 09 package [116, 128]. Standard enthalpies of formation were calculated using the atomization-energy method. In this method, the standard enthalpy of formation at 0 K is obtained as the difference between the *ab initio* calculated (ai) atomization enthalpy of a compound and the experimentally determined enthalpy of formation of the gaseous atom:

$$\begin{aligned} & \Delta H_f^0(0\text{K}, \text{Si}_a\text{O}_b\text{C}_c\text{H}_d) \\ &= a\Delta H_{f,\text{gas,exp}}^0(0\text{K}, \text{Si}) + b\Delta H_{f,\text{gas,exp}}^0(0\text{K}, \text{O}) \\ &+ c\Delta H_{f,\text{gas,exp}}^0(0\text{K}, \text{C}) + d\Delta H_{f,\text{gas,exp}}^0(0\text{K}, \text{H}) - [aH_{\text{ai}}^0(0\text{K}, \text{Si}) \quad (7-3) \\ &+ bH_{\text{ai}}^0(0\text{K}, \text{O}) + cH_{\text{ai}}^0(0\text{K}, \text{C}) + dH_{\text{ai}}^0(0\text{K}, \text{H}) \\ &- H_{\text{ai}}^0(0\text{K}, \text{Si}_a\text{O}_b\text{C}_c\text{H}_d)] \end{aligned}$$

In Eq. (7-3), $\Delta H_f^0(0\text{K}, \text{Si}) = 446.2\text{ kJ/mol}$, $\Delta H_f^0(0\text{K}, \text{O}) = 246.8\text{ kJ/mol}$, $\Delta H_f^0(0\text{K}, \text{C}) = 711.5\text{ kJ/mol}$, and $\Delta H_f^0(0\text{K}, \text{H}) = 216.1\text{ kJ/mol}$ [150]. By applying enthalpy corrections to $\Delta H_f^0(0\text{K})$, standard enthalpies of formation at 298 K, ΔH_f^0 , are calculated [151].

Simmie and Sheahan [152] reported that among the most common composite methods, CBS-QB3, CBS-APNO, G3 and G4, the G4 approach is the most accurate one for calculating enthalpies of formation via the atomization procedure. The results of our previous works, in which a numerical method for deriving group additivity values for Si–C–H-containing species was presented [153], suggests that this conclusion also applies for silicon-organic compounds. Consequently, the G4 method was used in this work for obtaining thermodynamic data for silicon organic molecules.

7.4.2 Reaction mechanism optimization

For all one-dimensional flame simulations in this paper, the devised TMS oxidation kinetics model is merged with the C1 mechanism from Li et al. [154]. The resulting mechanism was optimized against the experimental data with a genetic algorithm-based method; details of the optimization process can be found in the work by Sikalo et al. [155, 156]. The optimization technique aims at finding improved reaction rate coefficients that minimize the error between the reaction mechanism and the reference data. In other words, the optimization alters the three Arrhenius parameters until the reaction mechanism predicts the reference data. In principle, predefined uncertainty ranges for each reaction in the mechanism can be considered for the optimization, but the elementary reactions of the C1

hydrocarbon mechanism and the initial TMS oxidation steps, i.e. H-atom abstractions from TMS, were protected against the optimization algorithm. For most of the reactions in the mechanism in Table 7-3, however, no uncertainty ranges are available, since none of these secondary reactions have been studied in detail by laboratory experiments or kinetics theories. The rate coefficients are estimated in such a way that the experimental data can be reproduced by the kinetics model. During the optimization procedure, the burner-stabilized flame model within the library of one-dimensional reacting flow models implemented in Cantera [157] is used for the evaluation of the deviation between experiment and simulation. Convergence can be achieved more easily if reasonable initial values of key rate coefficients are provided because the optimization technique allows only small changes during each iteration step. Therefore, initial estimates are used that are based on RRKM calculations, reaction analogies, experiments, or theory reported in literature. The activation energies (E_a/R) in the current mechanism were rounded to a precision of 1 K.

While reaction mechanisms for hydrocarbons are developed and iteratively improved based on a large body of experimental and theoretical data as well as experience with the reaction patterns of these molecules, such data and experience are simply not available to the same extent for TMS-based nanoparticle synthesis. The goal of this work is to develop an initial mechanism that represents the available data, even if the errors in the estimated rate coefficients could be high because the optimization procedure is not well constrained by a wide variation of validation experiments, experimental and theoretical rate coefficients, etc. The mechanisms and the simulations performed with this mechanism will help to identify promising targets for future experimental and theoretical investigations, which in turn will provide the necessary constraints and allow the gradual improvement of the reaction mechanism with respect to physical and chemical correctness.

7.5 Results and discussion

7.5.1 Thermodynamic data

Based on the molecular properties (molecular structures, frequencies and moments of inertia) obtained from the quantum chemical calculations, thermodynamic data $C_p(T)$, $H_f(T)$ and $S(T)$ were derived by using the GPOP program [158]. The vibrational frequencies calculated at the B3LYP/6-31G(2df,p) level of theory during the G4 procedure were scaled by 0.99 for the zero point energy calculation and by 0.97 for the vibrational partition function calculations [128]. Internal rotations around the bonds of CH₃ and OH groups attached to carbon and/or silicon atoms were treated as hindered rotations using the Pitzer-Gwinn approximation as implemented in GPOP [159]. Rotational barrier heights for CH₃ and OH rotors were obtained from relaxed potential energy surface (PES) scans at the B3LYP/6-31G(2df,p) level of theory with dihedral angles used as coordinates for the scans. Figure 7-1 shows an example for PES-scans of a CH₃ and OH moiety to obtain the barrier heights V_0 .

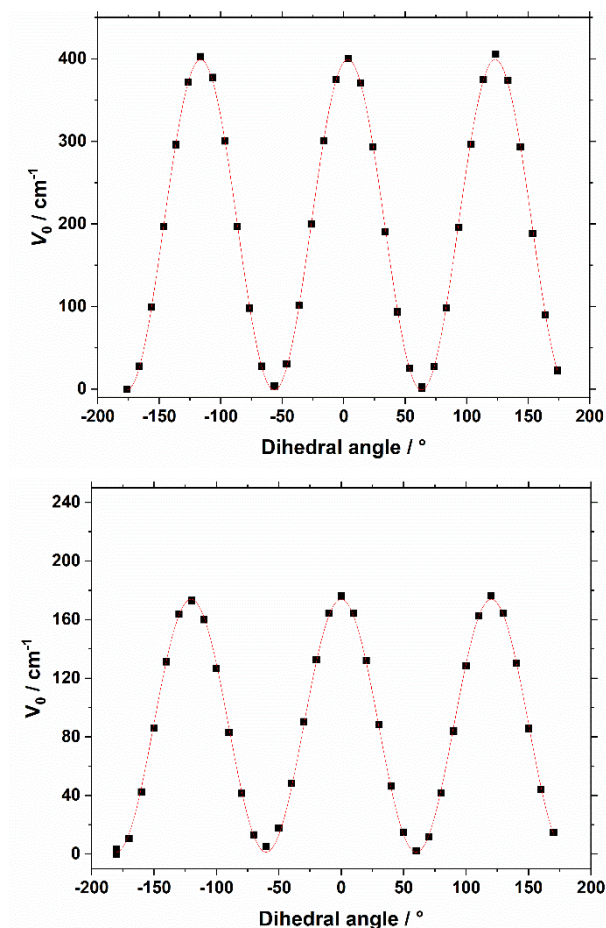


Figure 7-1. Potentials of CH₃ (left) and OH rotors in trimethyl-silanol (Si(CH₃)₃OH) with maxima at 400 and 175 cm⁻¹.

It is difficult to assess the quality of the thermodynamic data due to the lack of experimental reference data. To develop group-additivity values for silicon-organic molecules containing Si, C, and H atoms, we have also calculated thermodynamic data for selected silanes. For these compounds, good agreement with available experimental thermodynamic data was obtained: The calculated values of ΔH_f^0 for SiH₄, Si₂H₆, Si₃H₈, and Si(CH₃)₄ are 28.0, 70.6, 106.1, and -237.9 kJ/mol, respectively. The corresponding experimental values are 34.1, 71.5 [160], 108.4 [161], and -233.2 kJ/mol, respectively [162]. The deviations between calculated and experimental values are on average below 8.0 kJ/mol but it is more realistic to assume larger uncertainties regarding the thermochemical data of silicon-organic compounds than of hydrocarbon compounds. For sila-isobutene ((CH₃)₂SiCH₂), the G4-calculation gives $\Delta H_f^0 = 60.7$ kJ/mol. Available experimental values are 20.9 [162], 36.0 [163], and 64.8 kJ/mol [164]. Allendorf et al. [165] calculated thermodynamic data for a series of different silicon-organic compounds and they obtained a value of 51.5 kJ/mol. For trimethylsilanol (Si(CH₃)₃OH), ΔH_f^0 calculated is -493.1 kJ/mol. The recommended reference value of ΔH_f^0 for this compound is reported to be -499.5 kJ/mol [166]. For the other silanols and corresponding radicals, it is not possible to clearly assess the error in calculated enthalpies of formation due to the lack of available experimental data. Table 7-2 lists the species, for which thermodynamic properties were calculated in the present work.

Table 7-2. Standard enthalpies of formation predicted by the G4-method.

Species	$\Delta H_f^0 / (\text{kJ/mol})$	Species	$\Delta H_f^0 / (\text{kJ/mol})$
$(\text{CH}_3)_2\text{SiCH}_2$	60.7	$\text{Si}(\text{CH}_3)_2\text{OH}$	-248.9
$(\text{CH}_3)_3\text{SiCH}_2$	-21.2	$\text{Si}(\text{CH}_3)\text{CH}_2\text{OH}$	-203.7
$\text{Si}(\text{CH}_3)_3$	24.1	TMS	-219.3
$\text{Si}(\text{CH}_3)_2$	136.9	$\text{Si}(\text{CH}_3)_2\text{O}$	-255.2
$\text{Si}(\text{CH}_3)$	301.1	$\text{Si}(\text{CH}_3)_2(\text{OH})_2$	-773.6
$\text{Si}(\text{CH}_3)_3\text{OH}$	-493.1	$\text{OSi}(\text{CH}_3)_3$	-219.2
$\text{Si}(\text{OH})_4$	-1345.6	$\text{OSi}(\text{OH})_2$	-811.2
$\text{Si}(\text{OH})_3$	-799.2	$\text{HSiO}(\text{OH})$	-471.1
$\text{Si}(\text{OH})_2$	-503.4	$(\text{CH}_3)_3\text{SiCH}_2\text{O}_2$	-143.5
$\text{Si}(\text{CH}_3)(\text{OH})_3$	-1062.5	$\text{Si}_4\text{O}_{10}\text{H}_4(\text{linear})$	-3599.5
$\text{Si}(\text{CH}_3)(\text{OH})_2$	-520.8	$(\text{CH}_3)_2\text{Si}(\text{CH}_2)(\text{OH})$	-293.9
$(\text{CH}_3)(\text{OH})\text{SiCH}_2$	-220.5	$(\text{CH}_3)\text{Si}(\text{CH}_2)(\text{OH})_2$	-574.4
$(\text{OH})_2\text{SiCH}_2$	-461.1	$(\text{CH}_3)\text{SiO}$	-100.4

Even though the uncertainties of calculated species cannot be reported because accurate experimental reference data are not available, the sensitivity of the simulations to the enthalpies of formation can be tested. A set of simulations is performed, in which the standard enthalpies of formation of TMS, $(\text{CH}_3)_3\text{SiCH}_2\text{O}_2$, $\text{OSi}(\text{CH}_3)_3$, and $(\text{CH}_3)_3\text{SiCH}_2$ were changed by ± 4.2 kJ/mol. The results are shown in Figure B-3 - Figure B-6 in the supplementary material (see appendix B). It can be seen that the modelling is not very sensitive to the ± 4.2 kJ/mol change of standard enthalpies of formation as one of the important thermodynamic properties.

7.5.2 Kinetics model

Figure 7-2 shows simulated and measured mole-fraction profiles of major species in an undoped $\text{H}_2/\text{O}_2/\text{Ar}$ flame (flame A). For sake of comparison, the predictions of three different reaction mechanisms are shown in comparison to the experimental profiles: The low-pressure lean $\text{H}_2/\text{O}_2/\text{Ar}$ flame was simulated with the hydrogen-combustion mechanism by Ó Conaire et al. [167], the C1 combustion mechanism by [154], and the hydrogen and syngas combustion mechanism by Varga et al. [168]. The measured temperature profile of the undoped base flame is used as an input for the simulation. The slight deviations close to the burner surface can originate from the nozzle effect on the flame [82]. The simulated profiles using all three reaction mechanisms agree well with each other and thus the reaction mechanism of Li et al. [154] was chosen as base mechanism. The colored areas in Figure 7-2 and the other figures containing measured mole-fraction data, represent experimental uncertainty ranges.

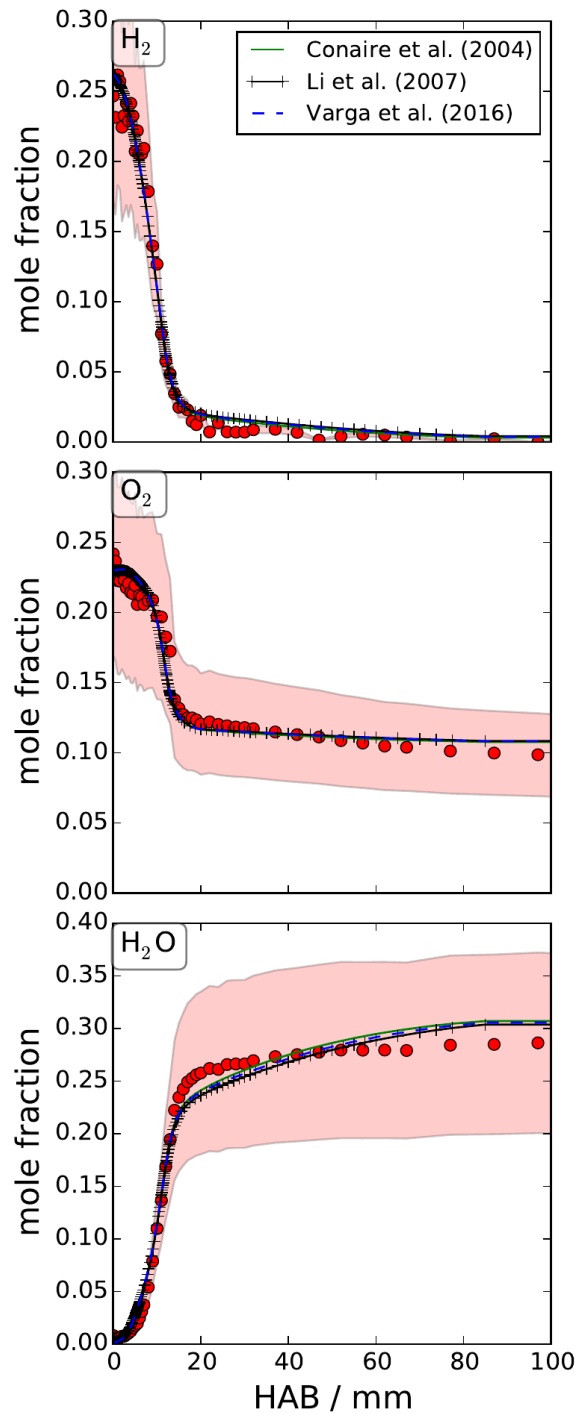


Figure 7-2. Mole fraction profiles of the major species along the as a function of height above burner (HAB) in flame A. The points are experimental data and the curved lines are the simulation results. The colored area shows the uncertainty range of the measured data.

Figure 7-3 shows the measured and calculated mole fraction profiles of the major species O_2 , H_2 , H_2O , CO , and CO_2 in the flame doped with 600 ppm TMS (flame B) as well as the measured temperature profile of the doped flame, which is prescribed in the simulations.

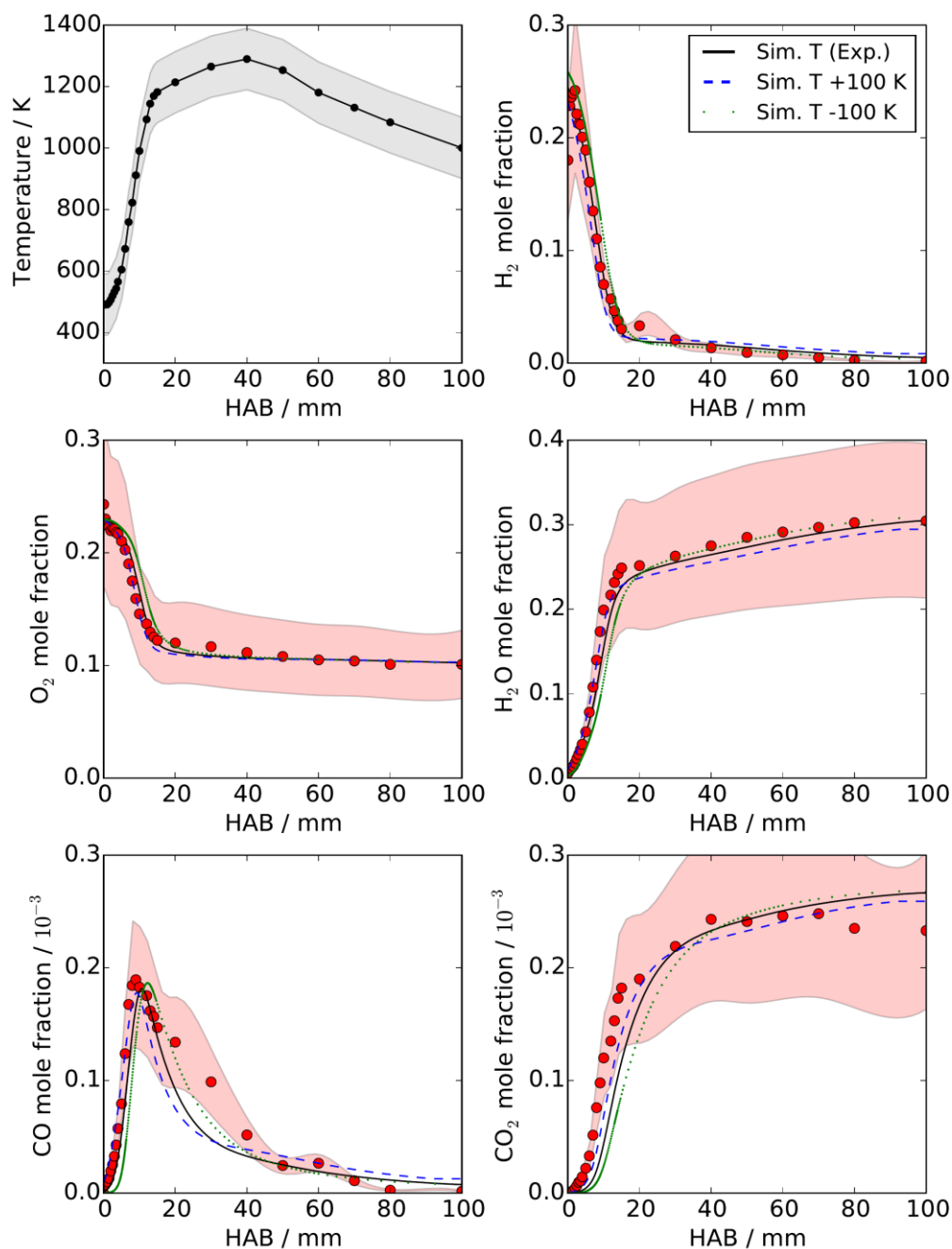


Figure 7-3. Sensitivity of major species' mole fractions on the measured temperature; simulations are performed with experimental temperature, shifted +100 K up, and shifted -100 K down. The colored areas represent the uncertainties of mole-fraction and temperature measurements. Symbols: experiment; lines: simulations.

For the simulations shown in Figure 7-3 and the figures appearing thereafter (except Figure 7-4), the reaction mechanism in Table 7-3 for TMS oxidation chemistry is merged with the C1 mechanism from Li et al. [154]. Table 7-3 includes the reactions related to TMS combustion and formation of silica clusters.

Table 7-3. List of reactions for describing TMS oxidation. Units of $k = A T^b \exp(-E_a/RT)$ are cm, s, mol, and K. As described in the text: Simulations were carried out using global reactions 14, 18, and 19. Reactions 14a–e, 18a–f, and 19a–e are suggested to explain the underlying chemistry behind these global processes and are discussed in the text. Also reactions 21 and 25–28 are global reactions. $\text{Si}_2(\text{OH})_8$ is envisioned as a hydrogen-bonded adduct of two $\text{Si}(\text{OH})_4$ molecules.

No.	Reaction	A	b	E_a/R	Ref.
1	$\text{TMS} + \text{OH} = \text{H}_2\text{O} + (\text{CH}_3)_3\text{SiCH}_2$	1.48E + 05	2.56	162	This work
2	$\text{TMS} + \text{H} = \text{H}_2 + (\text{CH}_3)_3\text{SiCH}_2$	4.97E + 06	2.40	3101	Peukert et al. [169]
3	$\text{TMS} + \text{O} = \text{OH} + (\text{CH}_3)_3\text{SiCH}_2$	2.50E + 06	2.50	2720	This work
4	$\text{TMS} + \text{O}_2 = \text{HO}_2 + (\text{CH}_3)_3\text{SiCH}_2$	3.98E + 11	0.00	25136	Reed [37]
5	$\text{TMS} + \text{HO}_2 = \text{H}_2\text{O}_2 + (\text{CH}_3)_3\text{SiCH}_2$	1.00E + 13	0.00	9742	Reed [37]
6	$(\text{CH}_3)_3\text{SiCH}_2 + \text{O}_2 = (\text{CH}_3)_3\text{SiCH}_2\text{O}_2$	5.00E + 12	0.00	4026	This work
7	$(\text{CH}_3)_3\text{SiCH}_2 = (\text{CH}_3)_2\text{SiCH}_2 + \text{CH}_3$	1.00E + 15	0.00	26580	This work
8	$(\text{CH}_3)_2\text{SiCH}_2 + \text{H} = \text{Si}(\text{CH}_3)_3$	1.06E + 12	0.51	620	This work
9	$\text{Si}(\text{CH}_3)_3 + \text{OH} = \text{Si}(\text{CH}_3)_3\text{OH}$	6.00E + 13	0.00	0	This work
10	$\text{Si}(\text{CH}_3)_3\text{OH} = (\text{CH}_3)_2\text{SiCH}_2 + \text{H}_2\text{O}$	1.84E + 12	0.37	36142	This work
11	$\text{Si}(\text{CH}_3)_3\text{OH} = \text{CH}_4 + \text{Si}(\text{CH}_3)_2\text{O}$	1.59E + 21	-2.3	32934	This work
12	$(\text{CH}_3)_3\text{SiCH}_2\text{O}_2 = \text{OSi}(\text{CH}_3)_3 + \text{CH}_2\text{O}$	1.40E + 12	0.00	10064	This work
13	$\text{OSi}(\text{CH}_3)_3 + \text{H}_2 = \text{Si}(\text{CH}_3)_3\text{OH} + \text{H}$	4.70E + 12	0.00	2617	This work
14	$\text{OSi}(\text{CH}_3)_3 + \text{M} \rightarrow 3 \text{CH}_3 + \text{SiO} + \text{M}$	1.20E + 13	0.00	4026	This work
14a	$\text{OSi}(\text{CH}_3)_3 = \text{Si}(\text{CH}_3)_2\text{O} + \text{CH}_3$	1.00E + 15	0.00	26580	This work
14b	$(\text{CH}_3)_2\text{SiCH}_2 + \text{O}_2 = \text{Si}(\text{CH}_3)_2\text{O} + \text{CH}_2\text{O}$	5.29E + 11	0.00	1804	Davidson et al. [170]
14c	$\text{Si}(\text{CH}_3)_2\text{O} = (\text{CH}_3)\text{SiO} + \text{CH}_3$	1.93E + 76	-18.26	53265	This work
14d	$(\text{CH}_3)\text{SiO} = \text{CH}_3 + \text{SiO}$	3.00E + 12	0.00	33796	Chen et al. [140]
14e	$\text{Si}(\text{CH}_3)_2\text{O} = (\text{CH}_3)(\text{OH})\text{SiCH}_2$	5.33E + 27	-4.56	30450	This work
15	$\text{SiO} + \text{O}_2 = \text{SiO}_2 + \text{O}$	1.00E + 10	0.80	3249	Chen et al. [140]
16	$\text{SiO} + \text{OH} = \text{H} + \text{SiO}_2$	1.00E + 09	0.80	755	Chen et al. [140]
17	$\text{SiO} + \text{O} + \text{M} = \text{SiO}_2 + \text{M}$	2.5E + 12	0.00	2166	Chen et al. [140]
18	$\text{Si}(\text{CH}_3)_3\text{OH} + \text{OH} \rightarrow \text{Si}(\text{CH}_3)_2(\text{OH})_2 + \text{CH}_3$	1.60E + 08	2.65	2094	This work
18a	$\text{Si}(\text{CH}_3)_3\text{OH} + \text{H} = (\text{CH}_3)_2\text{Si}(\text{CH}_2)(\text{OH}) + \text{H}_2$	4.97E + 07	2.65	3101	This work
18b	$\text{Si}(\text{CH}_3)_3\text{OH} + \text{OH} = (\text{CH}_3)_2\text{Si}(\text{CH}_2)(\text{OH}) + \text{H}_2\text{O}$	1.48E + 05	2.56	162	This work
18c	$\text{Si}(\text{CH}_3)_3\text{OH} + \text{O} = (\text{CH}_3)_2\text{Si}(\text{CH}_2)(\text{OH}) + \text{OH}$	2.50E + 07	2.50	2720	This work
18d	$(\text{CH}_3)_2\text{Si}(\text{CH}_2)(\text{OH}) = (\text{CH}_3)(\text{OH})\text{SiCH}_2 + \text{CH}_3$	1.00E + 15	0.00	26580	This work
18e	$(\text{CH}_3)(\text{OH})\text{SiCH}_2 + \text{H}_2\text{O} = \text{Si}(\text{CH}_3)_2(\text{OH})_2$	3.60E + 09	0.43	3869	This work
18f	$\text{OSi}(\text{CH}_3)_3 = (\text{CH}_3)_2\text{Si}(\text{CH}_2)(\text{OH})$	1.00E + 13	0.00	10824	Reed [37]
19	$\text{Si}(\text{CH}_3)_2(\text{OH})_2 + \text{OH} \rightarrow \text{Si}(\text{CH}_3)(\text{OH})_3 + \text{CH}_3$	1.70E + 08	2.65	4107	This work
19a	$\text{Si}(\text{CH}_3)_2(\text{OH})_2 + \text{H} = (\text{CH}_3)\text{Si}(\text{CH}_2)(\text{OH})_2 + \text{H}_2$	5.74E + 06	2.38	3583	This work
19b	$\text{Si}(\text{CH}_3)_2(\text{OH})_2 + \text{OH} = (\text{CH}_3)\text{Si}(\text{CH}_2)(\text{OH})_2 + \text{H}_2\text{O}$	1.48E + 05	2.56	162	This work
19c	$\text{Si}(\text{CH}_3)_2(\text{OH})_2 + \text{O} = (\text{CH}_3)\text{Si}(\text{CH}_2)(\text{OH})_2 + \text{OH}$	2.50E + 06	2.50	2720	This work
19d	$(\text{CH}_3)\text{Si}(\text{CH}_2)(\text{OH})_2 = (\text{OH})_2\text{SiCH}_2 + \text{CH}_3$	1.00E + 15	0.00	26580	This work
19e	$(\text{OH})_2\text{SiCH}_2 + \text{H}_2\text{O} = \text{Si}(\text{CH}_3)(\text{OH})_3$	3.60E + 09	0.43	3869	This work

20	$\text{Si}(\text{CH}_3)(\text{OH})_3 \rightarrow \text{CH}_3 + \text{Si}(\text{OH})_3$	1.00E + 15	0.00	13496	This work
21	$\text{Si}(\text{OH})_3 + \text{OH} = 0.5 \text{Si}_2(\text{OH})_8$	3.50E + 16	0.00	4277	This work
22	$\text{Si}(\text{OH})_3 + \text{OH} \rightarrow \text{Si}(\text{OH})_4$	2.60E + 14	0.00	3372	This work
23	$\text{SiO}_2 + \text{H}_2\text{O} \rightarrow \text{OSi}(\text{OH})_2$	1.31E + 10	0.00	4026	This work
24	$\text{OSi}(\text{OH})_2 + \text{H}_2\text{O} \rightarrow \text{Si}(\text{OH})_4$	1.17E + 13	0.00	0	This work
25	$\text{Si}_2(\text{OH})_8 \rightarrow 0.5 \text{Si}_4\text{O}_{10}\text{H}_4 + 3.0 \text{H}_2\text{O}$	4.89E + 05	0.00	12329	This work
26	$\text{Si}(\text{OH})_4 \rightarrow 0.25 \text{Si}_4\text{O}_{10}\text{H}_4 + 1.5 \text{H}_2\text{O}$	4.70E + 05	0.00	10165	This work
27	$\text{SiO} + (\text{SiO})_n \rightarrow (\text{SiO})_{n+1} \rightarrow \text{particles}$	8.70E + 14	1.93	4006	This work
28	$n \text{Si}_4\text{O}_{10}\text{H}_4 \rightarrow (\text{SiO}_2)_{4n}\text{O}_2\text{H}_4 + (2n-2) \text{H}_2\text{O} \rightarrow \text{particles}$	2.70E + 14	0.00	1258	This work

The simulations reproduce the experimental profiles quite well, but the deviation near the burner surface must be due to high diffusion rates in the flame that are not captured in the simulation. The error of the temperature measurement is ± 100 K. To consider the possible uncertainty of the temperature measurements, the experimental temperature profile is shifted 100 K up and down and the simulations are repeated. Figure 7-3 shows the effect of the assumed temperature on the predicted mole fractions of major species. It can be seen that temperature uncertainties within ± 100 K result in a shift of the calculated mole-fraction profiles along HAB, but altogether, the shape of the calculated profiles is not changed. Calculated mole fractions of Si-containing species are also sensitive to the prescribed temperature. For the development of a TMS mechanism, the measured temperature is used, but the sensitivity of Si-containing species to the measured temperature for flame B (600 ppm TMS) is studied and shown in Figure B-8 in the supplemental material (see appendix B). Considering the mole fraction data, the overall uncertainties are estimated to be ± 10 –30%. The uncertainty in measured temperatures also translates into an uncertainty in optimized rate coefficients. For most rate coefficients, a temperature error of ± 100 K leads to an increase/decrease by approximately a factor of two. For three rate coefficients, those of reactions R12, R20, and R26, the resulting uncertainties are substantially larger: In case of k_{12} and k_{26} , this temperature error results in an increase/decrease of around +300% and –80%, respectively. The largest temperature sensitivity is observed for k_{20} , where we get an increase/decrease of around +550% and –90%, respectively. The reason for these pronounced temperature sensitivities are the higher activation energies of these three reactions in comparison to the other optimized reaction rate constants.

Figure 7-4 shows the measured and calculated mole-fraction profiles of CH_4 . One essential factor that influences the prediction of CH_4 is related to the mechanism, which is used for modeling the reactions of small hydrocarbons. When merging the TMS kinetics model with the C1–C3 mechanism by Ranzi et al. [171], the simulated mole fractions of CH_4 are within the experimental uncertainty range.

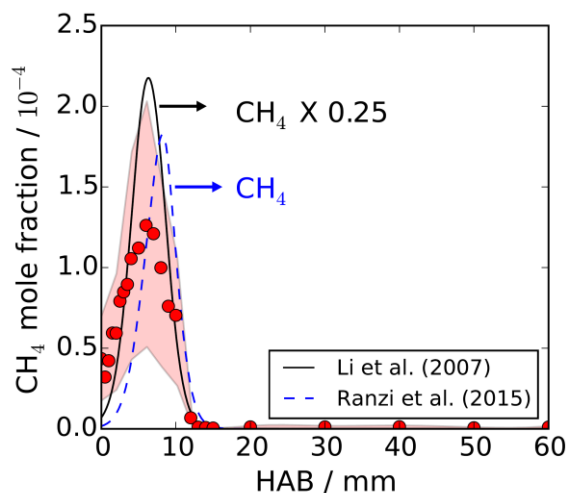


Figure 7-4. Measured and calculated CH_4 mole-fraction profiles as a function of height above burner (HAB). The colored area represents the uncertainty range of the measurement. Simulations were performed with the C1–C3 mechanism of Ranzi et al. [171] (blue dashed line) and the C1 mechanism from Li et al. [154] (black line)

Another explanation for the over prediction of CH_4 is related to uncertainties in the underlying global reactions R14, R18, and R19, in which methyl radicals are assumed to be rapidly released by bond fissions. According to the present TMS mechanism, this fast release of CH_3 radicals leads to an over prediction of CH_4 . For clarification, all simulations were performed with global reactions R14, R18, and R19, instead of the elementary reactions R14a–e, R18a–f, and R19a–e (see Table 7-3) that are assumed to be behind the global reactions. For simulating mole fractions of Si–C–O–H-containing species, the present TMS oxidation model has been merged with the Li et al. [154] mechanism. Though the mechanism of Ranzi et al. [171] leads to a better prediction of the CH_4 mole fractions, we did not apply that mechanism for all simulations for the following reasons: First, the simulated mole fractions of Si-containing species are not affected by the hydrocarbon combustion model; second, the Ranzi et al. [171] mechanism is much larger than the Li et al. [154] mechanism. The Ranzi et al. [171] mechanism contains 107 species and more than 2600 reactions, whereas the Li et al. [154] mechanism includes only 19 species and less than 100 reactions which makes the simulations almost 12 times faster than those using the Ranzi et al. [171] mechanism. For the purpose of computational efficiency and since the simulations of Si-containing products and intermediates are not affected by the hydrocarbon combustion chemistry, the smaller mechanism was chosen. The simulated mole fractions of major species and Si-containing species with the Li et al. [154] and Ranzi et al. [171] mechanisms are presented in Figure B-2 in the supplemental material (see appendix B). The mechanism of Ranzi et al. [171] predicts only the CH_4 mole-fraction profile better than Li et al. [154] mechanism and overall both mechanisms perform within the uncertainty ranges of the measurements. It can be concluded that the Si sub-mechanism developed in this work is almost independent of the hydrocarbon combustion chemistry. In case of simulating a TMS doped $\text{H}_2/\text{O}_2/\text{Ar}$ low-pressure flame with methane added, the authors recommend to merge the TMS mechanism with a detailed hydrocarbon mechanism such as the one of Ranzi et al. [171].

Figure 7-5 outlines the reaction pathway from the precursor to silica nanoparticles and helps to better understand the discussions below.

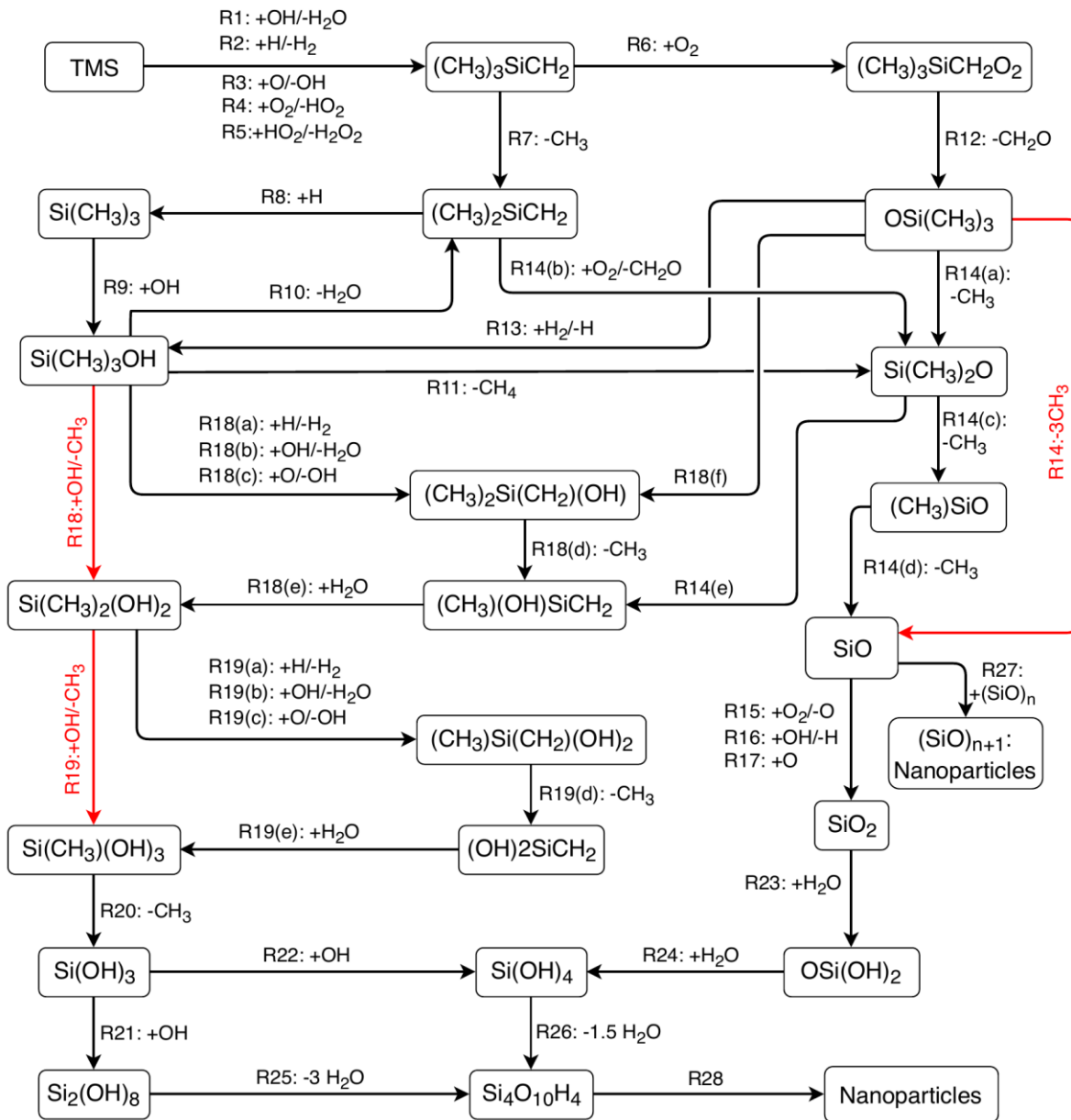


Figure 7-5. Schematics of the reaction pathway for the oxidation of TMS based on the list of reactions in Table 7-3. The red-colored reactions are introduced as global reactions.

Figure 7-6 shows measured and calculated mole-fraction profiles of TMS. The red-colored surface shows the uncertainty range of $\pm 30\%$ for the measured TMS mole fraction. TMS is consumed completely at 8 mm HAB, at which the temperature rises up to 800 K, but according to the simulated mole fraction profile, TMS is predicted to be completely consumed at 6 mm HAB. The simulated TMS profile shows a concave-up behavior in contrast to the concave-down behavior of the experiment. It is possible that the deviations are due to the probing effect which can affect the flame flow and temperature field. Hartlieb et al. [172] studied the effects of a sampling nozzle on the structure of a low-pressure flame.

In addition, Deng et al. [173] investigated numerically perturbed laminar flames to enhance the interpretability of measurements obtained from mass spectrometry with molecular-beam sampling. It can be seen later in this work that the simulations predict the peak positions of Si-intermediates quite well which indicates that these profiles are less affected by sampling issues. At the early stage, the depletion of TMS is initiated by H-atom abstractions through reactions with flame radicals OH, H, O, O₂, and HO₂, which are considered in our kinetics model in terms of reactions R1 to R5. The rate coefficients for R1 to R5 are taken either from literature or estimated based on analogies. The rate coefficients of the initial H-atom abstractions from TMS are not optimized in this work. At these temperatures, the primary step of the unimolecular TMS decomposition (a Si–C bond fission), is slow, i.e., $k < 10^{-3} \text{ s}^{-1}$, and does not significantly contribute to its depletion. The consumption of TMS is caused in particular by the H-atom abstractions R1–R3. The rate coefficient for R1 is estimated by analogy to the reaction of OH + neopentane. The rate coefficients of this reaction were directly measured by Sivaramakrishnan et al. [174] by UV-absorption spectrometry behind reflected shock waves. For R2, the rate coefficient was taken from literature: Peukert et al. [169] conducted a shock-tube and modeling study on the reactions H + SiH₄ and H + TMS. They have shown that due to very similar C–H bond dissociation energies, TMS and the analog hydrocarbon, neo-pentane, have very similar reactivities towards H-atom abstractions. The rate coefficient of R3 is estimated in analogy to the reaction of O + neopentane calculated by Cohen and Westberg [175].

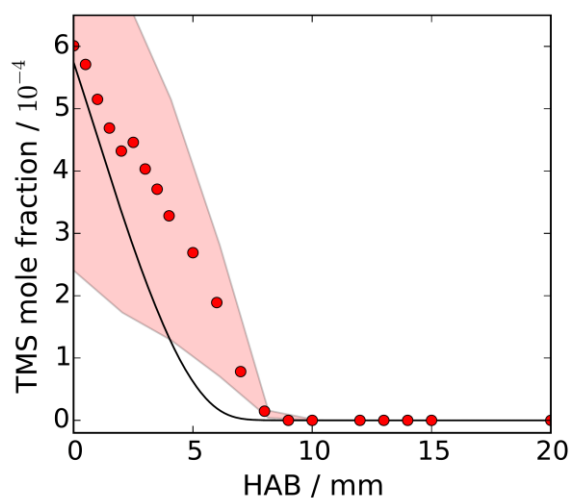


Figure 7-6. Measured and calculated mole-fraction profiles for TMS in the flame B. The colored area shows the uncertainty range of the measurement. Symbols: experiment; line: simulation.

As a result of H-atom abstractions, (CH₃)₃SiCH₂ radicals are a primary Si-containing intermediate. They can either react with oxygen to form (CH₃)₃SiCH₂O₂ (R6) or they can dissociate to (CH₃)₂SiCH₂ by releasing CH₃ radicals (R7). The rate coefficient for R7 is estimated by analogy to Si(CH₃)₃ = Si(CH₃)₂ + CH₃ proposed by Sela et al. [34]. The (CH₃)₂SiCH₂ itself can further react with hydrogen to form Si(CH₃)₃ (R8). The rate coefficient for R8 is estimated by analogy to the reaction of H + iso-C₄H₈ calculated by Curran [176]. The peroxide species (CH₃)₃SiCH₂O₂ (or its isomers) has also been detected by Karakaya et al. [86] (Figure 7-7). (CH₃)₃SiCH₂O₂ radicals in turn can decompose to

$\text{OSi}(\text{CH}_3)_3$ and CH_2O (R12). The rate coefficients for R6 and R12 were initially taken from Davidson and Thompson [177] and optimized in such a way that the simulated profile of $(\text{CH}_3)_3\text{SiCH}_2\text{O}_2$ reproduces the measurement (Figure 7-7).

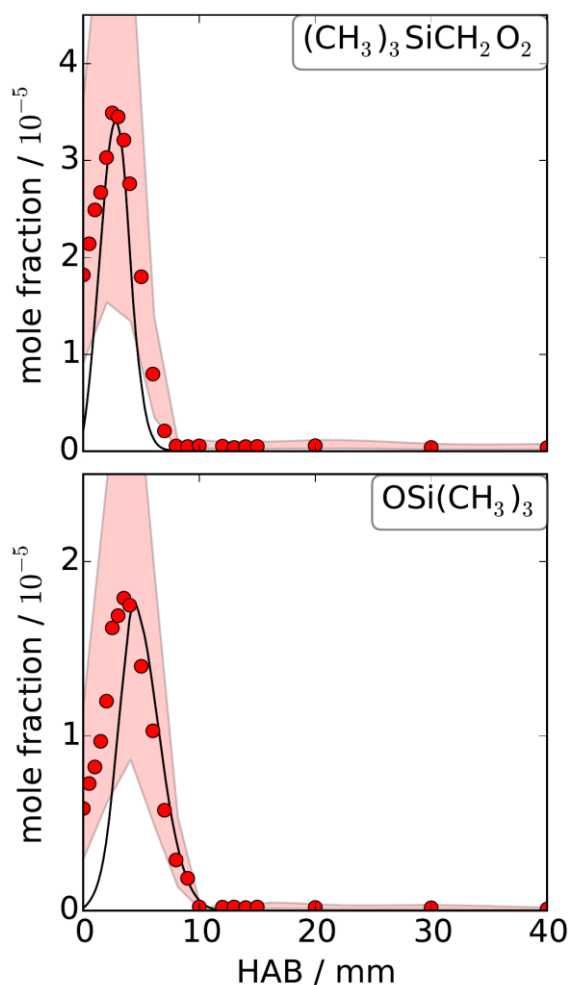


Figure 7-7. Measured and simulated mole-fraction profiles of $(\text{CH}_3)_3\text{SiCH}_2\text{O}_2$ and $\text{OSi}(\text{CH}_3)_3$ as a function of HAB for Flame B. The colored area shows the uncertainty range of a factor of two for the measured data.

Figure 7-7 also shows measured and simulated $\text{OSi}(\text{CH}_3)_3$ profiles. The bimolecular reaction of $\text{OSi}(\text{CH}_3)_3$ and H_2 forms $\text{Si}(\text{CH}_3)_3\text{OH}$ (R13). Another possibility for $\text{OSi}(\text{CH}_3)_3$ consumption can be a stepwise release of CH_3 to form SiO . The rate coefficient for R14a is estimated by analogy to $\text{Si}(\text{CH}_3)_3 = \text{Si}(\text{CH}_3)_2 + \text{CH}_3$ proposed by Sela et al. [34]. The first Si–C bond fission from $\text{OSi}(\text{CH}_3)_3$ yields $\text{Si}(\text{CH}_3)_2\text{O}$, which is the Si-containing analog to acetone. In principle, this molecule is expected to be a stable species. $\text{Si}(\text{CH}_3)_2\text{O}$ itself can further decompose via Si–C bond fission or it can undergo tautomerization towards an enol. With an energy barrier of 238.1 kJ/mol, the tautomerization $\text{Si}(\text{CH}_3)_2\text{O} = (\text{CH}_3)(\text{OH})\text{SiCH}_2$, with $(\text{CH}_3)(\text{OH})\text{SiCH}_2$ being the enol-form of the siloxane, is the energetically preferred process at low temperatures. The reverse reaction from the enol to the siloxane tautomer has a barrier height of 186.2 kJ/mol. These barrier heights were calculated using the G4 method and refer to $T = 0$ K and exclude zero-point energies. The equilibrium will be clearly on the side of the siloxane form $\text{Si}(\text{CH}_3)_2\text{O}$. Figure 7-8 shows calculated rate coefficients of

reactions R14c and R14e at $p = 30$ mbar over the 600–1200 K temperature range. Since argon is used as bath gas in the MBMS measurements, argon was also used as bath gas in these calculations. This procedure applies to all RRKM calculations reported in this work.

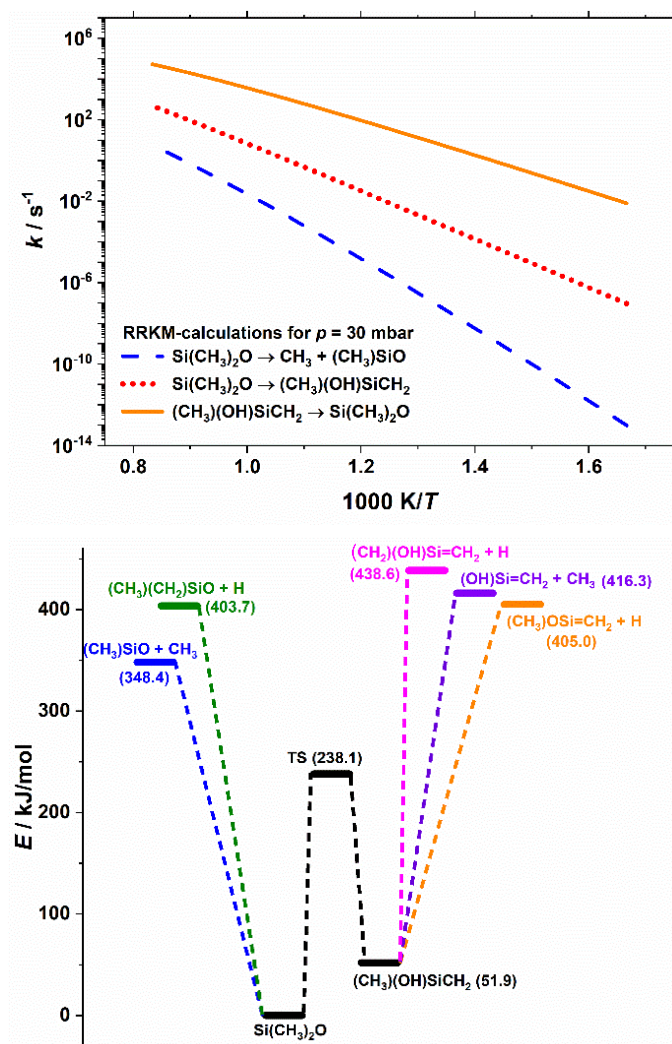


Figure 7-8. Top: RRKM calculations for reaction $\text{Si}(\text{CH}_3)_2\text{O} \rightarrow (\text{CH}_3)\text{SiO} + \text{CH}_3$, for tautomerization $\text{Si}(\text{CH}_3)_2\text{O} \rightarrow (\text{CH}_3)(\text{OH})\text{SiCH}_2$, and for the reverse process $(\text{CH}_3)(\text{OH})\text{SiCH}_2 \rightarrow \text{Si}(\text{CH}_3)_2\text{O}$. All calculations were carried out for 30 mbar and cover 600–1200 K; Bottom: Relative stationary point energies (values in parentheses are relative to the energy of $\text{Si}(\text{CH}_3)_2\text{O}$) for the unimolecular reactions of $\text{Si}(\text{CH}_3)_2\text{O}$ calculated at the G4 level of theory (present work).

The RRKM models including molecular properties and barrier heights for these reactions as well as calculated rate constant data for different pressures are included in the supplemental material (see appendix B). For calculating rate coefficients of the Si–C bond fission R14c, a RRKM Gorin model was applied [178, 179]. These reactions were also discussed by Karakaya et al. [86] and the theoretical rate coefficient data suggest that $\text{Si}(\text{CH}_3)_2\text{O}$ is primarily removed by Si–C bond fissions, since the equilibrium of the tautomerization process is on the side of $\text{Si}(\text{CH}_3)_2\text{O}$. Besides tautomerization, the enol form can also only decompose by bond fissions, which have bond dissociation energies above 335 kJ/mol (Figure 7-8).

In the low-pressure flame at temperatures below 1000 K, this unimolecular reaction should be negligible. The experimental evidence indicates that $\text{Si}(\text{CH}_3)_2\text{O}$, or an isomer with the same composition, is a reactive compound, even though it has not been observed in gas-phase studies before. To the best of our knowledge, it has only been detected by cryogenic infrared spectroscopy in an argon matrix at temperatures around 12 K [131]. The reason for the high reactivity of $\text{Si}(\text{CH}_3)_2\text{O}$ remains unknown, but destruction by flame radicals may be a tentative explanation. The reactivity of this intermediate molecule may be regarded as an additional possible justification for assuming quite large rate coefficient values for the global reaction (R14). When we tried to use the sequence of reactions R14a–e, the genetic algorithm could not find optimized rate coefficients in such a way that it will be possible to simulate the experimental mole-fraction profiles of $\text{OSi}(\text{CH}_3)_3$ and of the subsequent products $\text{Si}(\text{OH})_x$ and SiO_2 . To circumvent the sequence of reactions R14a–e, the decomposition of the radical $\text{OSi}(\text{CH}_3)_3$ was written as a global reaction and led to successful optimization and simulation. These issues indicate that important pathways may be missing from the proposed mechanism but that the overall reaction sequence represented by reaction R14 is reasonable and in agreement with literature.

The global reaction $\text{OSi}(\text{CH}_3)_3 \rightarrow \text{SiO} + 3\text{CH}_3$ was considered in flame studies reported by Chagger et al. [112], Yeh et al. [180], and Ma et al. [181] on particle formation during HMDSO oxidation. The rate coefficient of the global reaction R14 is optimized to be able to reproduce the experimental $\text{OSi}(\text{CH}_3)_3$ mole-fraction profile. Similar to the intermediate $(\text{CH}_3)_3\text{SiCH}_2\text{O}_2$, the calculated peak and shape of $\text{OSi}(\text{CH}_3)_3$ are in a very good agreement with the measurement.

Experimental observations illustrate that $(\text{CH}_3)_2\text{SiOH}$, $(\text{CH}_3)\text{Si}(\text{OH})_2$, $\text{Si}(\text{OH})_3$, and $\text{Si}(\text{OH})_4$ are the most abundant species among the detected compounds. Karakaya et al. [86] proposed a series of reactions, which form $\text{Si}(\text{OH})_4$ starting from $\text{Si}(\text{CH}_3)_3\text{OH}$. One possibility consists in stepwise losses of methyl radicals and recombination of silyl with hydroxyl radicals. We also considered this as a possible pathway for $\text{Si}(\text{OH})_4$ formation, but with rate constants that are typical for C–C bond fissions of stable molecules as start values for an optimization procedure, the algorithm did not predict any significant formation of $\text{Si}(\text{OH})_4$.

Karakaya et al. [86] provided another pathway to form $\text{Si}(\text{OH})_4$ by reaction of $\text{Si}(\text{CH}_3)_3\text{OH}$ with flame radicals H, O, and OH. They reported that due to high Si–C bond-dissociation energies of around 376 kJ/mol, these series of reactions R18a–f and R19a–e are more likely to happen. The rate coefficients for reaction of $\text{Si}(\text{CH}_3)_3\text{OH}$ with flame radicals H and OH and reaction of $\text{Si}(\text{CH}_3)_2(\text{OH})_2$ with H and OH are estimated again by analogy to reaction of TMS and neopentane with H and OH, respectively. Regarding $\text{Si}(\text{CH}_3)_3\text{OH}$, the calculated O–H bond-dissociation energy is 486.7 kJ/mol, and the calculated C–H bond-dissociation energy is 412.3 kJ/mol. Since bond-dissociation energies and reactivities towards H-atom abstraction correlate with each other, H-atom abstractions from the OH moieties of $\text{Si}(\text{CH}_3)_3\text{OH}$ and $\text{Si}(\text{CH}_3)_2(\text{OH})_2$ have not been considered. The rate coefficients of reactions of $\text{Si}(\text{CH}_3)_3\text{OH}$ and $\text{Si}(\text{CH}_3)_2(\text{OH})_2$ with O atoms are assumed to be analogue to the rate coefficients of the O + neopentane abstraction, which were calculated by Cohen and Westberg [175] by transition-state theory. The rate coefficients of the unimolecular decomposition steps of $(\text{CH}_3)_2\text{Si}(\text{CH}_2)(\text{OH})$ and $(\text{CH}_3)\text{Si}(\text{CH}_2)(\text{OH})_2$ radicals to lose methyl groups are assumed based on analogy to $\text{Si}(\text{CH}_3)_3 = \text{Si}(\text{CH}_3)_2 + \text{CH}_3$ (Sela et al. [34]). The

rate coefficients of the hydration steps (18e and 19e) to form $\text{Si}(\text{CH}_3)_2(\text{OH})_2$ and $\text{Si}(\text{CH}_3)(\text{OH})_3$ are assumed based on analogy to $\text{H}_2\text{SiO} + \text{H}_2\text{O} = \text{HSiO}(\text{OH}) + \text{H}_2$ calculated by Zachariah and Tsang [182].

With the above mentioned rate-coefficient estimates for these reaction sets, the experimental $\text{Si}(\text{CH}_3)_3(\text{OH})$, $\text{Si}(\text{OH})_3$, and $\text{Si}(\text{OH})_4$ mole fractions could not be matched and optimization required the introduction of two global reactions R18 and R19. The rate coefficients for reactions R18 and R19 are optimized so that our simulation is able to reproduce the measured $\text{Si}(\text{CH}_3)(\text{OH})_3$ mole-fraction profile. Figure 7-9 shows that after optimizing R18 and R19, the shape and the maximum peak of the simulated $\text{Si}(\text{CH}_3)(\text{OH})_3$ mole-fraction profile are in a very good agreement with the measurements. Figure 7-9 also shows the simulated and measured profile of $\text{Si}(\text{OH})_3$. Now, the simulation can reproduce both, the profile shape and maximum. Unfortunately, the optimization procedure results in A and T^n factors that exceed the collision limit; for example, at $T = 900$ K, $1.7 \times 10^8 T^{2.65} \approx 1.1 \times 10^{16} \text{ cm}^3 \text{ mol}^{-1} \text{ s}^{-1}$. The corresponding rate constant k_{R18} at 900 K is $1.05 \times 10^{15} \text{ cm}^3 \text{ mol}^{-1} \text{ s}^{-1}$. For the purpose of matching experimental mole fractions of $\text{Si}(\text{OH})_x$ and $\text{Si}(\text{CH}_3)_3(\text{OH})$ species, it was not possible to avoid exceeding the collision limit. This observation indicates that other potentially important reaction pathways contributing to the formation and consumption of these species are missing. Furthermore, we suggest to treat the profile of $\text{Si}(\text{OH})_3$ as tentative, since we cannot exclude that the profile is overlapped by fragments of bigger silicon-containing species. The rate coefficients of reactions R19 and R20 were also optimized to fit the measured $\text{Si}(\text{OH})_3$ mole fractions.

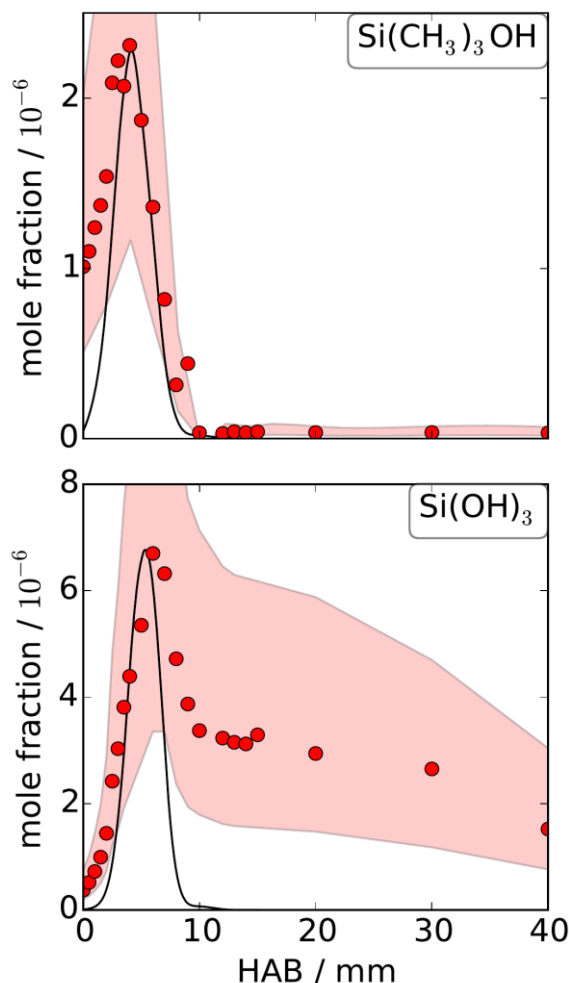


Figure 7-9. Measured and simulated profiles of $\text{Si}(\text{CH}_3)_3\text{OH}$ and $\text{Si}(\text{OH})_3$. The colored area shows the uncertainty range of a factor of two for the measured data.

There is a discussion in the literature about the contribution of SiO_2 and $\text{Si}(\text{OH})_4$ in the formation of silica nanoparticles. Many studies hypothesize that gas-phase SiO_2 is a major species that initiates the clustering and formation of silica nanoparticles. Other studies reported that $\text{Si}(\text{OH})_4$ is the major species that contributes the most to particle formation [39, 40]. In addition, some kinetics models available for silanes and siloxanes chose either SiO_2 or $\text{Si}(\text{OH})_4$ as the target species for their particle formation model. $\text{Si}(\text{OH})_4$ was found to be a major intermediate during the combustion of TEOS [39]. Shekar et al. [39] showed that the dimerization and dehydration of $\text{Si}(\text{OH})_4$ plays a key role in the formation of silica nanoparticles.

In this work, the dimerization of $\text{Si}(\text{OH})_4$ is introduced in terms of the global reaction R21 ($\text{Si}(\text{OH})_3 + \text{OH} \rightarrow 0.5\text{Si}_2(\text{OH})_8$). According to Shekar et al., the species “ $\text{Si}_2(\text{OH})_8$ ” can be envisioned as a hydrogen-bonded complex of two $\text{Si}(\text{OH})_4$ molecules. This complex is regarded as an intermediate towards the formation of large molecular clusters like $\text{Si}_4\text{O}_{10}\text{H}_4$ (Reaction R25) Without R21, $\text{Si}(\text{OH})_3$ would be quantitatively converted to $\text{Si}(\text{OH})_4$, which would be in contradiction with the measured MBMS data for $\text{Si}(\text{OH})_4$ mole fractions. In contrast, Feroughi et al. [19] suggested that nanoparticle formation takes place from the secondary chemistry of gaseous SiO_2 . According to the mass spectrometric data of Karakaya et al. [86], only low mole fractions of SiO_2 were detected in comparison to $\text{Si}(\text{OH})_4$.

Figure 7-10 depicts simulated mole-fraction profiles of SiO_2 and Si(OH)_4 in comparison to the measured profiles. In this study, we considered a two-step hydration of SiO_2 (R23 and R24) described by Plane et al. [132] to form Si(OH)_4 . [132] estimated the rate coefficients for reactions of R23 and R24 using RRKM theory for mesospheric conditions, which could not be applied in our flame conditions. Consequently, we optimized the rate coefficients of R23 and R24, which led to very good agreement between experiment and simulation for SiO_2 and Si(OH)_4 regarding the shape and peak. The shape of the profile suggests that Si(OH)_4 is consumed faster than SiO_2 and reaches the equilibrium.

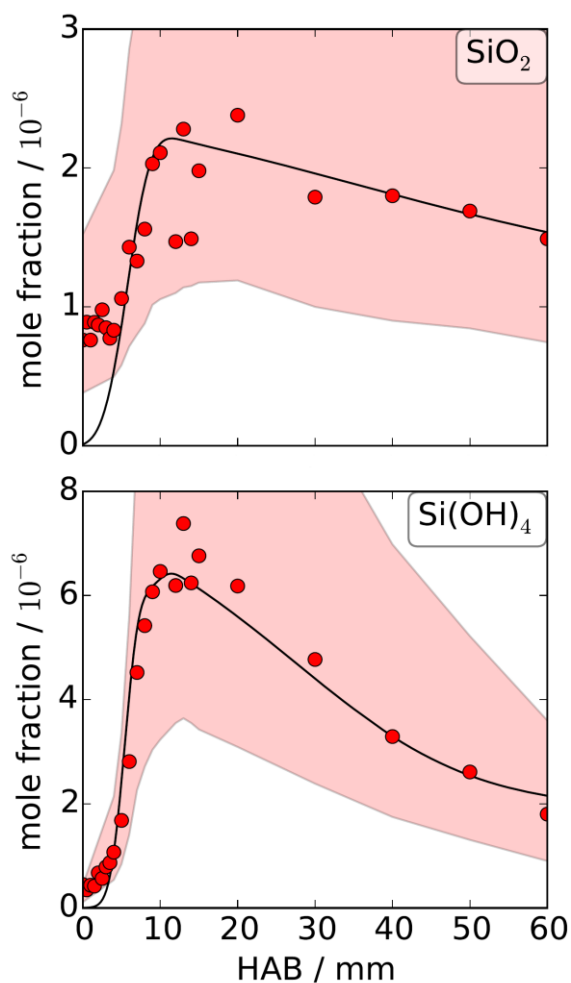


Figure 7-10. Measured and simulate profiles of SiO_2 and Si(OH)_4 . The colored area shows the uncertainty range of a factor of two for the measured data.

This observation is also reflected in our mechanism. Figure 7-11 shows a reaction-path analysis for Si-containing gas-phase species involved in TMS oxidation at 800 K. The diagram in Figure 7-11 indicates that Si(OH)_4 is consumed faster than SiO_2 . The thickness and color intensity of each arrow in this diagram is relative to the maximum reaction rate at this temperature. The reaction-path diagrams at 600, 700, and 1000 K are provided in the supplemental material (see appendix B, Figure B-1). The path analysis also illustrates that in the present model, the formation of large molecular silicon clusters like $\text{Si}_4\text{O}_{10}\text{H}_4$, which were detected by Karakaya et al. [86], primarily takes place via the path, which involves $\text{Si(CH}_3)_3\text{OH}$ and Si(OH)_3 .

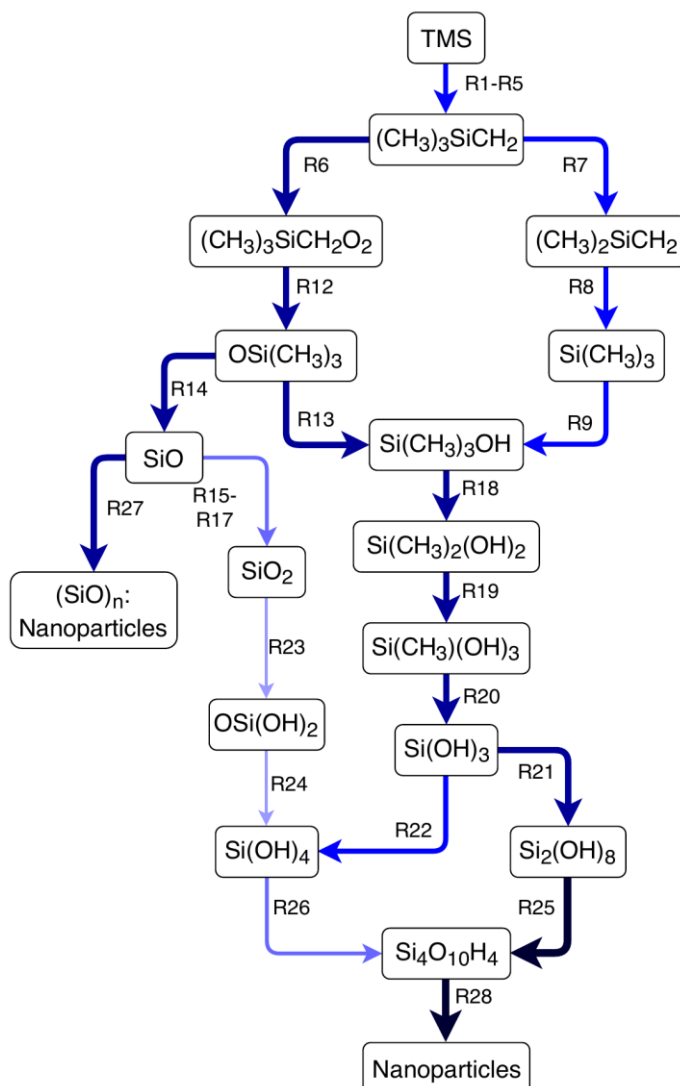
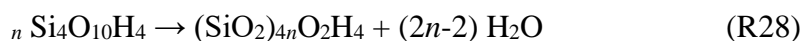


Figure 7-11. Reaction pathways of element of Si for gas-phase species at 800 K and 30 mbar.

$\text{Si}(\text{OH})_4$ is an important intermediate in our mechanism, since silicon clusters such as $\text{Si}_4\text{O}_{10}\text{H}_4$, $\text{Si}_5\text{O}_{12}\text{H}_4$, and $\text{Si}_6\text{O}_{14}\text{H}_4$ are suggested to be formed by stepwise addition of $\text{Si}(\text{OH})_4$ and elimination of H_2O . This assumption is in conflict with the mechanism published by Chen et al. [140] who assumed in their model that $\text{Si}(\text{OH})_4$, which is produced from hydrolysis of OMCTS, dehydrates to form SiO_2 as particle-forming species. Cluster structures like $\text{Si}_4\text{O}_{10}\text{H}_4$ are also reported in the experimental work of Xu et al. [133]. Timoshkin [134] shows that silicon oxide clusters can have different structures such as tetrahedral cages or linear chains. Figure 7-12 shows the simulated and measured profiles of the $\text{Si}_4\text{O}_{10}\text{H}_4$ cluster. The rate coefficient of R28 is optimized to match the experimental $\text{Si}_4\text{O}_{10}\text{H}_4$ mole-fraction profile. The colored area shown in Figure 7-12 shows the uncertainty range of the measured mole fractions. In the mechanism developed in this work, $\text{Si}_4\text{O}_{10}\text{H}_4$ is formed by self-clustering of $\text{Si}(\text{OH})_4$ (R26). The consumption of $\text{Si}_4\text{O}_{10}\text{H}_4$ and, correspondingly, the growth of larger Si-O-containing clusters are considered by introducing the global reaction (R28), which represents a self-clustering of $\text{Si}_4\text{O}_{10}\text{H}_4$:



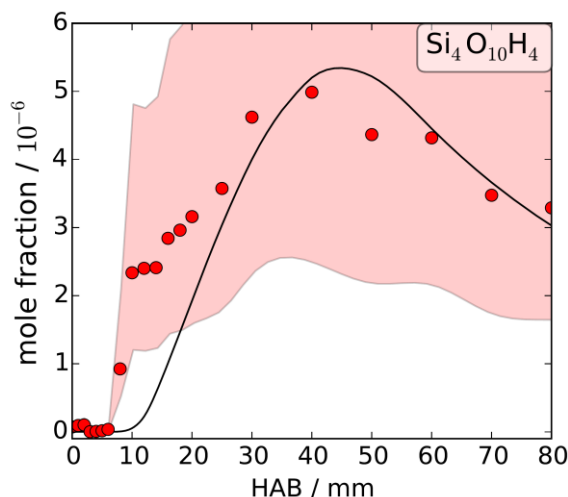
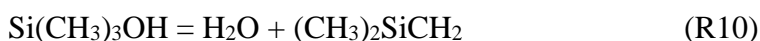
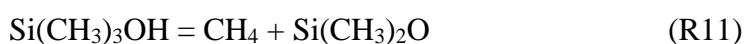


Figure 7-12. Measured and simulated profiles of $\text{Si}_4\text{O}_{10}\text{H}_4$. The colored area shows the uncertainty range of a factor of two for the measured data.

With respect to silica particle formation, SiO and SiO_2 are generally regarded as the primary particle forming intermediate species. Karakaya et al. [86] did not detect SiO because of interference with the signal of carbon dioxide in mass spectrometry, but SiO was monitored selectively by laser-induced fluorescence in flames [16]. Zachariah and Burgess [104] reported a double-peak structure in SiO mole-fraction profiles in SiH_4 doped counter-flow diffusion flames. Glumac [38] could also detect such behavior for SiO by performing LIF and emission spectroscopy in low-pressure H_2/O_2 /hexamethyldisilazane flames as well as Feroughi et al. [19], who observed it in low-pressure H_2/O_2 /HMDSO flames. A possible detailed cluster formation pathway has been described by Suh et al. [48], who suggested a clustering and self-clustering mechanism of SiO , SiO_2 , SiH_2O , and HSiOOH involving the formation of metastable $(\text{SiO})_n$ clusters. In the present work, we have introduced one global reaction, R27, to also account for the possibility of nanoparticle formation by SiO . The measured SiO_2 mole fractions shown in Figure 7-10 depend on the rate coefficients of reactions R15–R17, R23, and R27. For R15–R17, we have adopted rate coefficient data from the mechanism from Chen et al. [140] and the rate coefficient of R27 was optimized to match the experimental SiO_2 mole-fraction profile. Without R27, all intermediate SiO molecules would be transformed to SiO_2 according to R15–R17. Reaction R27 and R28 were both implemented in the mechanism to remove Si-containing species from the gas phase into the condensed phase.

Originally, we suspected that the thermal decomposition of the intermediate compound $\text{Si}(\text{CH}_3)_3\text{OH}$ can have an impact on SiO and hence on SiO_2 production. Karakaya et al. [86] reported that there are two possible and energetically preferred unimolecular reaction channels: The elimination of CH_4 , and the elimination of H_2O .



Based on the present G4 calculations, the barrier heights for reaction R11 is calculated to be 270.3 kJ/mol and for reaction R10 to be 309.4 kJ/mol. Based on these values, R11 could have been a process contributing to the consumption of $\text{Si}(\text{CH}_3)_3\text{OH}$ at temperatures below 1000 K. Figure 7-13 shows RRKM calculations of rate coefficients of reaction R11 and R10 at $p = 30$ mbar.

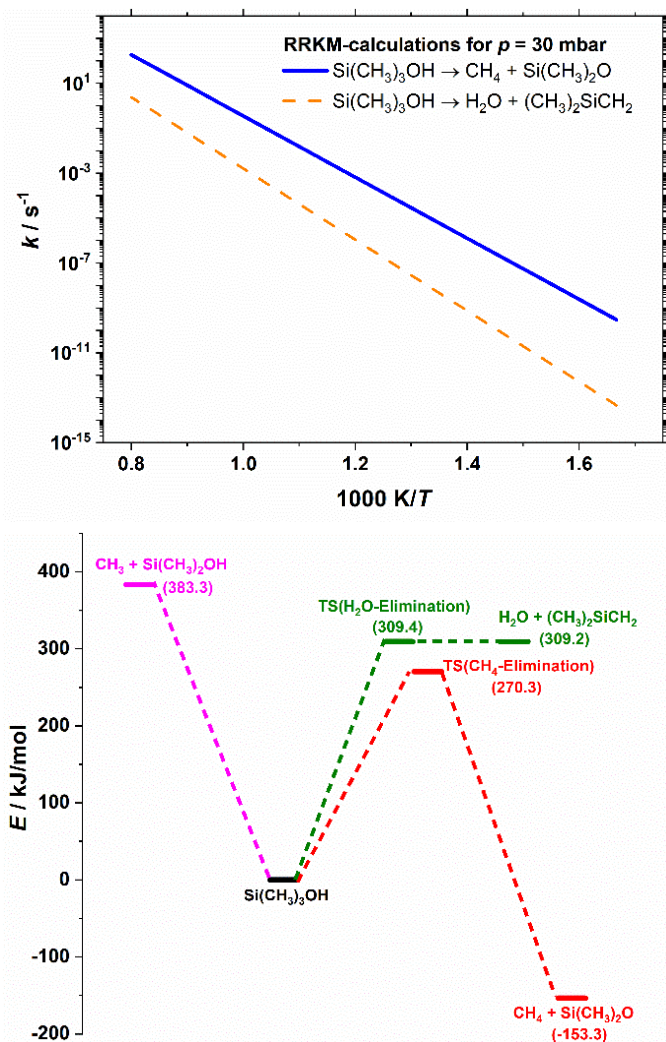


Figure 7-13. *Top:* RRKM calculations for CH_4 and H_2O elimination reactions of $\text{Si}(\text{CH}_3)_3\text{OH}$; both calculations were carried out for 30 mbar and 600–1200 K. *Bottom:* Relative stationary point energies (values in parentheses are relative to the energy of $\text{Si}(\text{CH}_3)_3\text{OH}$) for the unimolecular reactions of $\text{Si}(\text{CH}_3)_3\text{OH}$ calculated at the G4 level of theory (present work).

Since reaction R11 yields $\text{Si}(\text{CH}_3)_2\text{O}$, which can decompose via Si–C bond fission to CH_3 radicals and SiO , we assumed that R11 might also influence the SiO_2 mole fractions and cluster formation. Using the calculated rate coefficients shown in Figure 7-13 for 30 mbar, reaction R11 is too slow to have significant impact. Figure 7-13 also includes a potential energy surface of the main $(\text{CH}_3)_3\text{SiOH}$ decomposition channels and it can be seen that at $T < 1000$ K, besides the elimination reactions, bond fissions will not contribute to the decomposition of this silanol. According to the present G4 calculation, the reverse reaction of H_2O elimination seems to be without a barrier, i.e., the energy of the products H_2O and

silane-isobutene $(\text{CH}_3)_2\text{SiCH}_2$ is approximately 0.2 kJ/mol below the energy of the transition state structure. As mentioned in section 6.1 there is a substantial uncertainty regarding the calculated and experimentally determined thermochemistry of $(\text{CH}_3)_2\text{SiCH}_2$. It is very likely that also the reverse reaction between H_2O and $(\text{CH}_3)_2\text{SiCH}_2$ is a reaction with at least a small energy barrier.

When we tried to apply detailed reaction sequences (R14a–e, R18a–f, R19a–e) using the rate coefficients k_{11} obtained from the RRKM calculation, the algorithm did not determine an optimized rate coefficient that reasonably predicts SiO_2 and $\text{Si}(\text{OH})_x$ mole fractions. This is another reason why we had to employ the global reactions R14 and R18.

Altogether it was possible to devise a reaction mechanism that is able to reproduce measured mole fractions in a TMS-doped low-pressure $\text{H}_2/\text{O}_2/\text{Ar}$ flame. However, it turned out to be necessary to employ global reactions. When we tried to use more detailed reaction sequences with rate coefficients estimated by means of RRKM theory or analogies to similar reactions, the algorithm was not able to converge to a set of optimized rate coefficients that makes it possible to reproduce experimental data. This indicates that still important parts of TMS oxidation chemistry are missing and that – with respect to unimolecular reactions – one needs to be cautious to apply analogies between Si-containing species and analog hydrocarbons. Table 7-4 summarizes, which rate coefficient parameters were determined through analogy, calculation or optimization. In this study, we proposed rate coefficient parameters for a total number of 44 reactions (elementary and global reactions) and among them, 16 are based on analogies, nine are taken from literature, four were calculated by RRKM theory, and 16 were derived from optimization.

Table 7-4. Source of reaction rates used in the TMS mechanism.

Analogy	R1: Analogy to OH + neopentane [174] R3, R18(c), and R19(c): Analogy to O + neopentane [175] R7, R14(a), R(18)e, and R19(d): Analogy to $\text{Si}(\text{CH}_3)_3 = \text{Si}(\text{CH}_3)_2 + \text{CH}_3$ [34] R8: Analogy to H + iso-C ₄ H ₈ [176] R18a and R19a: Analogy to TMS + H (R2) R18b and R19b: Analogy to TMS + OH (R1) R18e: Analogy to $\text{H}_2\text{SiO} + \text{H}_2\text{O}$ reported by [182]
Literature	R2: [169] R4, R5, and R18(f): [37] R14b: [170] R14d, R15, R16, and R17: [140]
Theoretical calculation	R10, R11, R14c, and R14e: RRKM theory
Optimization	R6 and R12: Optimized against experimental profile of $(\text{CH}_3)_3\text{SiCH}_2\text{O}_2$ R9, R18, and R19: Optimized against the experimental profile of $\text{Si}(\text{CH}_3)_3\text{OH}$ R13: Optimized against the experimental profile of $\text{Si}(\text{CH}_3)_3\text{OH}$ R14: Optimized against the experimental profile of $\text{OSi}(\text{CH}_3)_3$ R20, R21: Optimized against the experimental profile of $\text{Si}(\text{OH})_3$ R22 and R26: Optimized against the experimental profile of $\text{Si}(\text{OH})_4$ R23 and R27: Optimized against the experimental profile of SiO_2 R24: Optimized against the experimental profiles of SiO_2 and $\text{Si}(\text{OH})_4$ R25 and R28: Optimized against the experimental profile of $\text{Si}_4\text{O}_{10}\text{H}_4$

7.5.3 Comparison with different loads of TMS

The developed mechanism was further compared to new measurements performed in this study for other initial TMS mole fractions in flames C and D to substantiate the development of the present TMS mechanism. Figure 7-14 shows the measured and calculated mole-fraction profiles of the major species O_2 , H_2 , H_2O , CO , and CO_2 as well as TMS. The experimental and simulated mole fractions of flame B (600 ppm TMS) are also given in this figure for the sake of comparison. The mole fractions in the legend indicate which molar percentage of precursor is doped into the flames. The uncertainties of mole fraction measurements for the 400 ppm and 800 ppm case are the same as for the 600 ppm case, which is discussed in the previous sections of this work. The colored areas that represent the uncertainty ranges of the experiments in the previous figures are not included in Figure 7-14. Simulated mole fractions of major species and Si-containing intermediates are also sensitive to the uncertainties of the prescribed experimental temperatures. The sensitivity of predicted mole fractions to the measured temperature is shown in supplemental material for 400 ppm case and 800 ppm case (see appendix B). The simulations are performed with shifted ± 100 K temperature and the simulated mole fractions are compared to the measured mole fractions in Figure B-9.

The measured mole fractions of H_2 , O_2 , and H_2O as well as simulations are showing similar response to the change of initial TMS mole fractions. The slight shifts of species profiles toward the burner surface are due to the temperature differences caused by the presence of precursor in the flames. Simulations predict measured CO and CO_2 mole fractions within the uncertainty ranges. In Figure 7-14, the simulations predict consumption of TMS at earlier HAB than the experimental observations. As discussed in the previous section, the deviation can be due to sampling effects. The experimental observations demonstrate that TMS decomposes and oxidizes almost independent from the load of precursor for all three cases at almost 8 mm HAB. This behavior is well captured by simulations but only shifted 2 mm closer to the burner surface. It is worth to mention that the rate coefficients of H-atom abstractions of TMS (R1-R5) are either taken from literature or estimated by analogy to hydrocarbons chemistry and not optimized against the experimental profile of TMS. The reason for not optimizing the initial oxidation reactions of TMS is that the peak locations of Si-intermediates are perfectly captured by simulation results. Optimizing the rate constants of R1–R5 to catch the measured TMS slows the total consumption of TMS and all the simulated Si-intermediates shift farther from the burner surface.

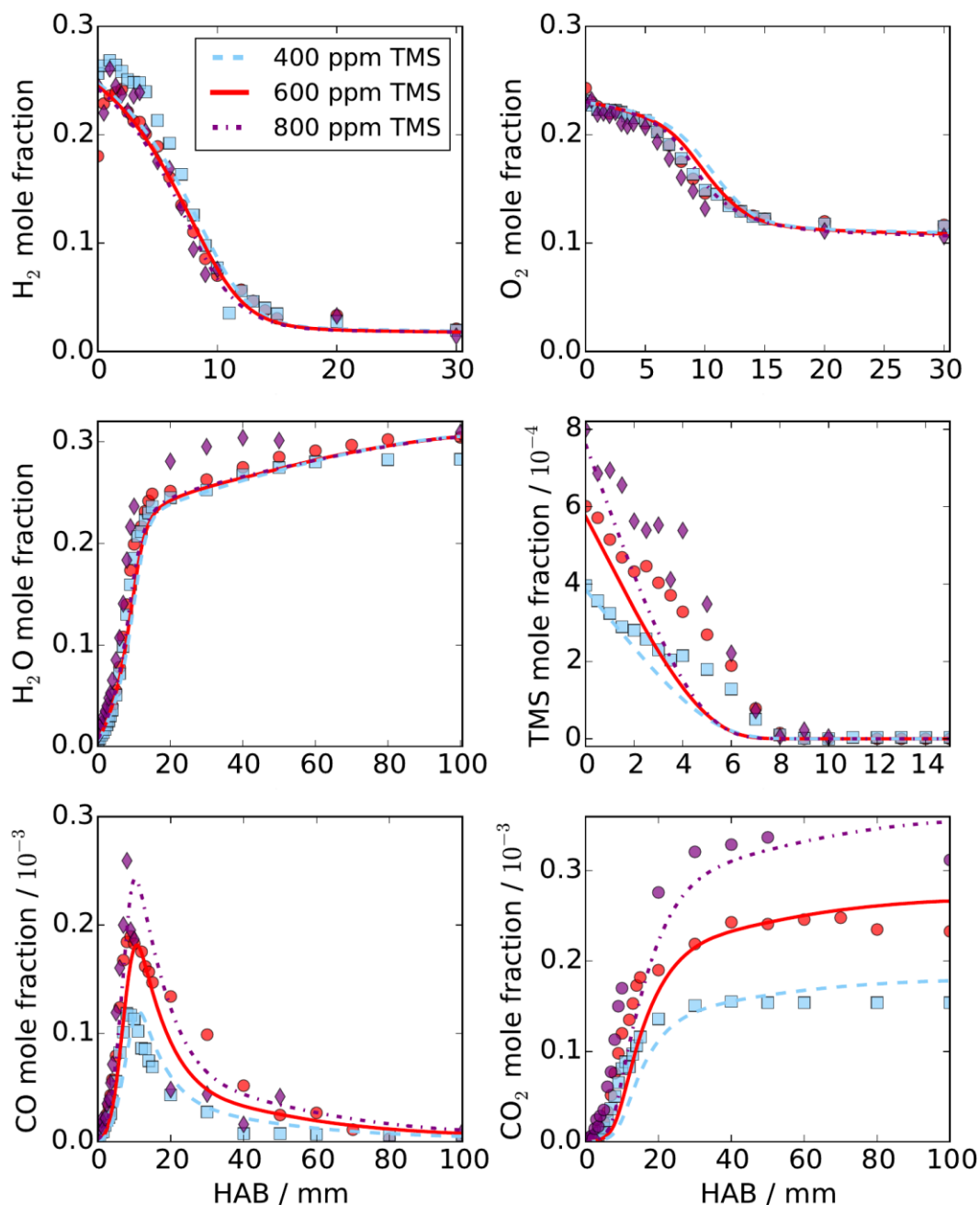


Figure 7-14. Measured and simulated mole-fraction profiles of major species as a function of HAB for a series of TMS doping concentrations: 400 ppm (flame C), 600 ppm (flame B), and 800 ppm (flame D). Symbols: experiments, lines: simulations.

Figure 7-15 shows the comparison of simulated Si-containing intermediates with experimental values from measurements in flames with different TMS load. The TMS mechanism is developed based on experimental observation for the 600 ppm case and evaluated for the other two concentrations of precursor. For all species shown in Figure 7-15, simulations predict the peak mole fractions for 600 ppm case very well. The simulation results are all within the uncertainty ranges of measurements. The uncertainty ranges are not shown in Figure 7-15 due to an overlap of the ranges, which makes it difficult to interpret the results. The uncertainty of mole fraction measurements as well as sensitivity of results to the prescribed measured temperature are shown in the supplementary material (see

appendix B, Figure B-8 and Figure B-9). The measured mole fractions demonstrate that $(\text{CH}_3)_3\text{SiCH}_2\text{O}_2$, $\text{OSi}(\text{CH}_3)_3$, and $\text{Si}(\text{CH}_3)_3\text{OH}$ as major Si-containing species are completely consumed at almost 8 mm HAB where the precursor is also completely consumed. The measured mole fractions of all Si-containing species indicate that the peak locations of intermediates do not shift toward the burner surface in contrast to the base flame major species. Simulated SiO_2 mole fraction overpredict the experiment for the 400-ppm case and underpredict for 800-ppm case, but the simulated SiO_2 profiles are in the uncertainty ranges of the corresponding measurements.

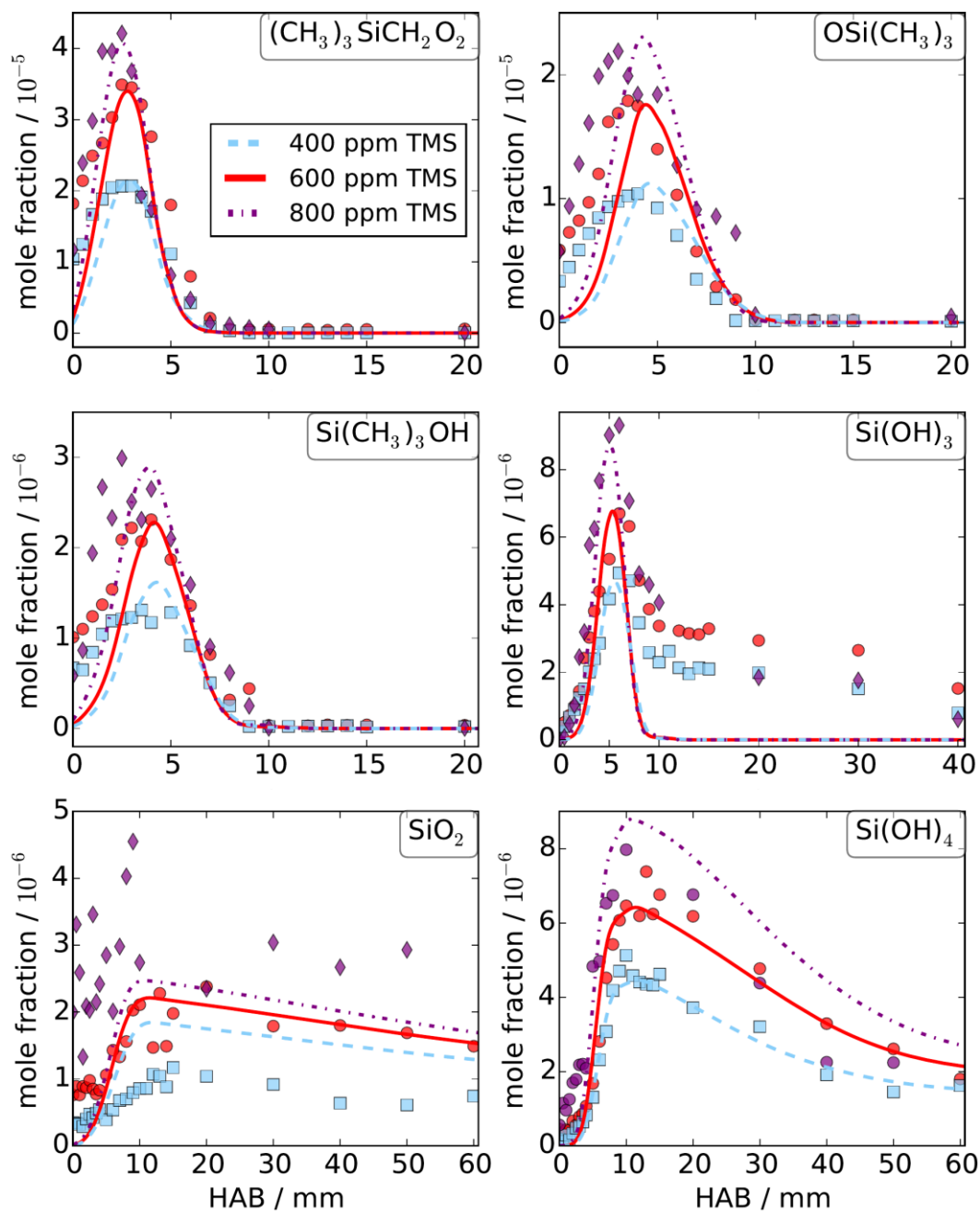


Figure 7-15. Measured and simulated mole-fraction profiles of Si-containing species along the HAB for a series of TMS doping concentrations: 400 ppm (flame C), 600 ppm (flame B), and 800 ppm (flame D). Symbols: experiments, lines: simulations.

The substantially reduced signal-to-noise ratio of the SiO_2 mole-fraction profile in the flame doped with 800 ppm is tentatively interpreted as an indication that condensation processes to solid SiO_2 occur. Figure 7-16 shows measured and simulated mole fractions of $\text{Si}_4\text{O}_{10}\text{H}_4$ along the HAB. Peak locations shift toward the burner surface and the formation of $\text{Si}_4\text{O}_{10}\text{H}_4$ increases rapidly by increasing the initial mole fraction of precursor.

As discussed earlier in this work, aggregation processes involving $\text{Si}_4\text{O}_{10}\text{H}_4$ are assumed to mainly contribute to the formation of larger silicon oxide clusters with the structure $(\text{SiO}_2)_{4n}\text{O}_2\text{H}_4$. Figure 7-16 shows that the mole fraction of clusters decreases around $\text{HAB} = 50\text{--}60$ mm. It can only be hypothesized that the transformation from pure gas-phase clusters to nanoparticles takes place from 60 mm HAB and beyond. Unfortunately, there are no particle measurements for these TMS-doped low-pressure flames available yet, which are needed to further implement particle formations models in our mechanism.

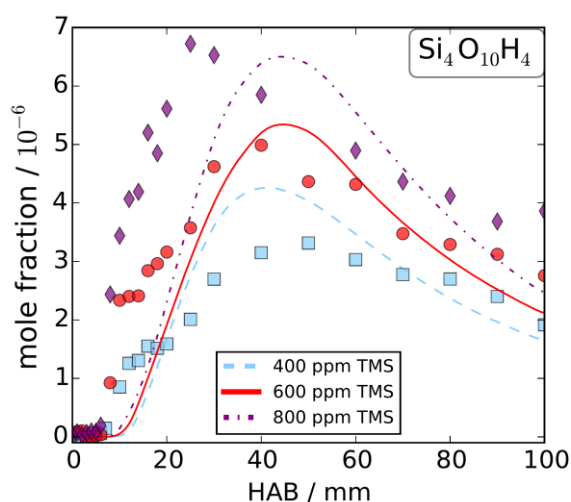


Figure 7-16. Measured and simulated mole-fraction profiles of $\text{Si}_4\text{O}_{10}\text{H}_4$ along the HAB for a series of TMS doping concentrations: 400 ppm (flame C), 600 ppm (flame B), and 800 ppm (flame D). Symbols: experiments, lines: simulations.

It was not possible to detect nanoparticles in this work, because the mass spectrometric setup is designed and optimized for measuring small molecules up to mass-to-charge ratio $m/z = 400$, limiting detection to gaseous Si-containing clusters with up to six silicon atoms. The burner chamber was lightly coated by white particles from the synthesis flames. Measuring the solid state of the silicon dioxide particles by means of a quartz crystal microbalance is future work.

SiO could also not be detected in the experiments of this work because its signal could not be resolved from the signal of CO_2 . As discussed earlier in this work, SiO is assumed to be involved in the early cluster formation in the preheating zone and already consumed completely in the reacting zone. Consequently, SiO is assumed not to be responsible for the formation of silica-nanoparticles. Quantitative measurements for SiO would be appreciated for further work as another potentially important speciation target for mechanism validation. The evaluation of the developed mechanism for other equivalence ratios is subject of future work.

7.6 Conclusions

This work presents a reaction mechanism, which was developed to model the oxidation of TMS in a low pressure H₂/O₂/Ar flame. To the best of our knowledge, this is the first attempt to develop a reaction mechanism that is validated against a dataset of quantitative measurements made via molecular-beam mass spectrometry. Rate coefficients of the reactions included in this mechanism were derived by (1) using a genetic algorithm with experimentally determined mole-fraction profiles as target data for optimization, (2) by applying reactivity analogies, and (3) by using RRKM theory. As part of the mechanism development, also thermochemical and transport data have been calculated and estimated. The G4 composite method is used to calculate the thermodynamic data of Si-containing species. The present reaction mechanism contains 24 species and 28 reactions, and the small number of reactions in this mechanism will facilitate its application in chemical kinetics simulations for analyzing other TMS-doped synthesis flames. The present results suggest that important issues of TMS oxidation chemistry are still not understood and that the development of a detailed reaction mechanism for TMS oxidation requires much more effort regarding future quantum chemical and/or experimental kinetics investigations. In particular, quantitative measurements of SiO and SiO₂ are needed. The need to employ global reactions in this reaction mechanism clearly indicates that reaction pathways are missing. Consequently, future work should target reactions connecting Si(OH)₃ and Si(OH)₄ as well as reaction sequences that can convert Si(OH)₄ to SiO₂ or SiO and vice versa. Open questions also remain for example with respect to other detailed reaction pathways but also the major intermediates contributing to particle formation need to be better identified. It is important to extend the database to other fundamental experimental configurations, e.g., flow reactors that are less influenced by deviations from one-dimensionality. For future work, the combination of MBMS data and new optimization targets, the genetic algorithm has the potential to improve the mechanism.

8 Experimental and numerical study on the influence of equivalence ratio on key intermediates and silica nanoparticles in flame synthesis

The content of this chapter was published in *Proceedings of the Combustion Institute* 38, Issue 1, 1375-1383 (2021), *Y. Karakaya, H. Janbazi, I. Wlokas, A. Levish, M. Winterer and T. Kasper, Experimental and numerical study on the influence of equivalence ratio on key intermediates and silica nanoparticles in flame synthesis*, and is reprinted with permission from Elsevier.

CRedit³ author statement: Y. Karakaya performed the experiments, chose the evaporator and flame conditions, evaluated and discussed the experimental data and wrote the manuscript. H. Janbazi contributed to setting up the reaction mechanism. A. Levish characterized the particle powder and contributed to the interpretation. M. Winterer provided discussions of the results of the particle characterization. T. Kasper provided discussions of the results and helped to shape the manuscript.

8.1 Abstract

Tetramethylsilane is a precursor often used for the production of flame-synthesized silica nanoparticles or coatings. This study investigates the chemical reaction mechanism of tetramethylsilane in a series of H₂/O₂/Ar low-pressure ($p = 30$ mbar) flames from fuel-lean to slightly fuel-rich flame conditions ($\varphi = 0.8, 1.0$ and 1.2). Mole fraction profiles are obtained by molecular-beam mass spectrometry. The experimental data are compared to simulations using a recently published reaction mechanism. The present study reveals the influence of the flame composition on the depletion of the precursor TMS, the formation of its main carbon-containing products (e.g. CO₂ and CO) and the main silicon-containing intermediates (e.g. Si(CH₃)₃(CH₂)OO), Si(OH)₄, SiO₂, Si₄O₁₀H₄) appearing along the routes of particle formation. TEM images of synthesized particles reveal that the nanoparticles obtained from the gas-phase synthesis are spheres with a low degree of agglomeration. The particle size distribution appears to be dependent on the equivalence ratio of the synthesis flames and the changes can tentatively be traced to different particle formation pathways. The data set provided in this work can serve a basis for improvements to the reaction mechanisms of the Si/C/H/O system that are urgently needed to improve particle synthesis processes.

8.2 Introduction

Silica nanoparticles are useful materials for advanced medical and pharmaceutical applications e.g. biosensing, or drug delivery [183]. To enable the synthesis of nanoparticles

³ CRedit (Contributor Roles Taxonomy)

with properties, e.g. size distributions, adequate for the respective application, the fundamentals of the synthesis process must be understood. They include the precursor decomposition in the flame, interaction of precursor and intermediates with flame species and the influence of the flame conditions on the particle properties. Although, many studies were carried out with different silicon containing precursors, the exact reaction mechanisms leading to the formation of silica nanoparticles from the intermediates are still unclear. Britten et al. [137] developed one of the first reaction mechanisms for silane combustion consisting of 25 species and 70 reactions. Miller et al. [184] extended the reaction mechanism to 58 Si-containing species and 201 reactions. These include a reaction path for silane combustion starting from SiH_3+O_2 and the first steps towards silica cluster formation from SiO.

Feroughi et al. [19] studied hexamethyldisiloxane (HMDSO) doped flames by measuring SiO profiles via laser-induced fluorescence and postulated SiO as an important species for the silica cluster formation in flames. Chrystie et al. [16, 17] investigated the impact of precursor load on the SiO concentrations. Shekar et al. [41] emphasized the relevance of $\text{Si}(\text{OH})_4$ monomers in the gas-phase for the formation of nanoparticles and based a detailed population balance model for the aerosol synthesis of silica nanoparticles from tetraethylorthosilicate (TEOS) on this hypothesis.

Nurkowski et al. [138] proposed a detailed chemical reaction mechanism for the pyrolysis of TEOS, reduced it to a skeletal chemical mechanism [139] and validated it for a hydrogen-oxygen flame. Various computational studies on high-temperature oxidation of TEOS postulate $\text{Si}(\text{OH})_4$ as one of the most relevant silicon species over a wide range of the temperatures [40, 139].

Recently, a detailed reaction mechanism for the destruction of tetramethylsilane (TMS) combustion was developed by Janbazi et al. [185]. Based on numerous experimental data [16, 17, 86, 185] and in particular on molecular-beam mass spectrometry data of TMS oxidation in hydrogen flames [86], a TMS submechanism consisting of 28 reactions and 24 Si-containing species was incorporated into the C1 mechanism proposed by Li et al. [124]. The transport data and thermodynamic properties of Si-C-H- and Si-C-O-H-containing species are taken from literature [153, 185]. Rate coefficients were estimated either by analogy to the hydrocarbon chemistry, by Rice-Ramsperger-Kassel-Marcus calculations or by an optimization engine based on genetic algorithms [155, 156] with the flame data as optimization targets. The performance of the mechanism was further evaluated with flames of the same equivalence ratio doped with 400 and 800 ppm of TMS, which show that different doping leads to different mole fractions of intermediates in the experiments without changing the overall reaction pathways in the flames. The next step to improve the reaction mechanism further, is the evaluation if it can reproduce the interaction between precursor and flame chemistry correctly. One way to test the influence of different oxygen, water, and radical mole fractions on the reaction pathways of TMS oxidation, is to change the equivalence ratio of the flames. The work reported here provides the validation data necessary for this development step and compares new experimental data with simulations of the different flame conditions using the mechanism of Janbazi et al. [185].

8.3 Experiment and flame conditions

The formation of main flame species (H_2 , O_2 , H_2O , Ar, O) and the decomposition of the precursor to intermediate species e.g. TMS, $\text{Si}(\text{CH}_3)_3(\text{CH}_2)\text{OO}$, SiO_2 , $\text{Si}(\text{OH})_4$, $\text{Si}_4\text{O}_{10}\text{H}_4$, CO_2 , CO are monitored in laminar $\text{H}_2/\text{O}_2/\text{Ar}$ low-pressure flames by means of molecular-beam mass spectrometry (MBMS). Details on the experiment, the data analysis and uncertainties of the mole fractions can be found in Karakaya et al. [86] and only a brief description is given here. All low-pressure flames are stabilized on a matrix burner with a diameter of 36 mm installed in a reactor with a pressure of 30 ± 0.03 mbar. Flame conditions are listed in Table 8-1. The burner position can be changed in upwards flow direction relative to the quartz sampling probe between $\text{HAB} = 0 - 100$ mm (HAB, height above burner) with an accuracy of ± 0.01 mm. A throttle valve maintains the pressure in the reactor chamber at 30 mbar with an accuracy of $\pm 0.1\%$. A molecular beam is formed by extraction of a gas sample from the reactor chamber through a $90 \mu\text{m}$ orifice in the tip of a conical quartz sampling probe into a second vacuum stage with a pressure of 10^{-3} mbar. The molecular-beam passes through a skimmer with an orifice diameter of 1.2 mm into the ionization chamber of an orthogonal time-of-flight mass spectrometer (TOF). The nominal kinetic energy of the electrons used for electron ionization is 17 eV in order to detect the major species products (e.g. H_2 , O_2 , H_2O , TMS, CO_2 , CO, O, Si-species) and 70 eV to see silicon-containing clusters (e.g. $\text{Si}_4\text{O}_{10}\text{H}_4$) with low concentrations in the flames. 10^7 mass spectra are summed to obtain sufficient sensitivity for the detection of mole fractions in the $x=10^{-6}$ range. Each integrated mass peak is proportional to the mole fraction of the respective species in the gas sample weighted by the ionization efficiency of the substance. The TOF has a resolution of $m/\Delta m = 3000$ at a mass-to-charge ratio of $m/z = 28$, which is useful for of peaks with near-identical m/z . The settings were optimized to see the decomposition of the precursor and the subsequent formation of the most relevant small gaseous clusters below $m/z = 400$.

TMS was metered with a syringe pump with an accuracy of ± 2 vol.% and evaporated at 333 K. Thermal mass flow controllers regulate the gas flows with an accuracy of $\pm 5\%$.

The inside and the outside of the burner matrix were not coated significantly with SiO_2 , so it can be concluded that TMS starts to decompose in the flame and a significant change in burner porosity is not expected.

The errors of the presented mole fractions depend on the calibration procedure and range between 15% for major species (O_2 , H_2 , H_2O), 30-60% for minor intermediate species and TMS, and a factor of two for flame radicals (e.g. O) and silicon-containing intermediates.

The temperature profiles of flames A-H were measured with a thermocouple and are radiation corrected according to the method of Bahlawane et al. [93]. The uncertainty of the temperature measurement is evaluated to be ± 100 K. Additionally, the relative perturbed temperature profile is evaluated from the temperature dependence of the argon signal as described by Struckmeier et al. [82]. These temperature profiles includes the influence of the nozzle and will be used for the simulations of flames A-H.

Synthesized particles are collected from a filter in the exhaust line of the flame reactor under ambient conditions after a sequence of experiments with different equivalence ratio in order to characterize the particle morphology. Nanoparticles are mechanically deposited onto

copper TEM-grids with lacey carbon films without any solvents. Investigations are performed using a JEOL JEM-2200FS TEM instrument and ImageJ software to obtain the nanoparticle size distribution by analysis of measured diameters of more than 500 particles from the sample. The x-ray diffraction pattern is obtained using a Panalytical X'Pert Pro diffractometer.

Table 8-1. Initial flow rates of the flame gases are given in standard liter per minute (slm). Chamber pressure was 30 mbar. Flame A and B are taken from Karakaya et al. [86]. Flames C-H are new data from this work.

Unit	H ₂ [slm]	O ₂ [slm]	Ar	φ -	TMS [ppm]
A	0.545	0.455	1	0.6	0
B					600
C	0.615	0.385	1	0.8	0
D					600
E	0.667	0.333	1	1.0	0
F					600
G	0.706	0.294	1	1.2	0
H					600

8.4 Numerical modeling and setup

For the simulations of flames A-H, the detailed reaction mechanism together with transport and thermodynamic properties published by Janbazi et al. [185] is used for one-dimensional simulations of the low-pressure laminar flames with the measured perturbed temperature profiles (see Fig. 1a) using Cantera [157] and ChemKin Pro 19.2 [186]. ChemKin Pro 19.2 [186] is used for the detailed reaction flow analyses.

8.5 Results and discussion

8.5.1 Temperatures and main flame species

Figure 8-1a compares the temperature profiles of the doped and the undoped flames with different equivalence ratios. The maximum temperature is almost identical in the neat and doped flames of identical equivalence ratio, but the temperatures in the reaction zone are about 100 K higher. The temperature decrease in the exhaust gas is less pronounced in the doped flames. Both observations, can be explained by exothermic reactions of TMS oxidation close to the burner and exothermic hydrolysis reactions of silicon-containing intermediates in the exhaust gas. Figure 8-1(b,c,d,e,f) show measured and simulated main species profiles for the systematic change of equivalence ratios (φ) between $\varphi = 0.6, 0.8, 1.0, 1.2$. For sake of comparison, the equivalence ratio $\varphi = 0.6$ from the previous work of Karakaya et al. [86] is included. The simulated and measured mole fraction profiles of the main species H₂, O₂, H₂O are in a very good agreement. Small deviations occur close to the burner surface. These can be traced for all species to the influence of the burner surface and the quartz-probe on the flame structure as discussed before, e.g., in a study of Deng et al.

[173]. The hydrogen and oxygen are consumed in the reaction zone of the flame and reach equilibrium values around $HAB = 15$ mm in all flames. Water also reaches an equilibrium value at the same HAB . TMS is consumed completely at $HAB = 10$ mm (see Figure 8-1f). As a consequence, the TMS consumption occurs at very different flame conditions for the flames of different equivalence ratios. The oxygen mole fraction is approximately 50% higher, the hydrogen mole fraction is 30% lower, and the water mole fraction differs by 40% between the flames with $\phi = 0.6$ and $\phi = 1.2$ in the TMS destruction region. The profiles of the other equivalence ratios fall between the profiles of the flames with the largest and smallest equivalence ratio. The flame temperatures rise at $HAB = 10$ mm to 1000 K for all doped flames. It can be observed that the addition of TMS shifts all main species profiles closer to the burner surface as a result of the temperature rise in the reaction zone.

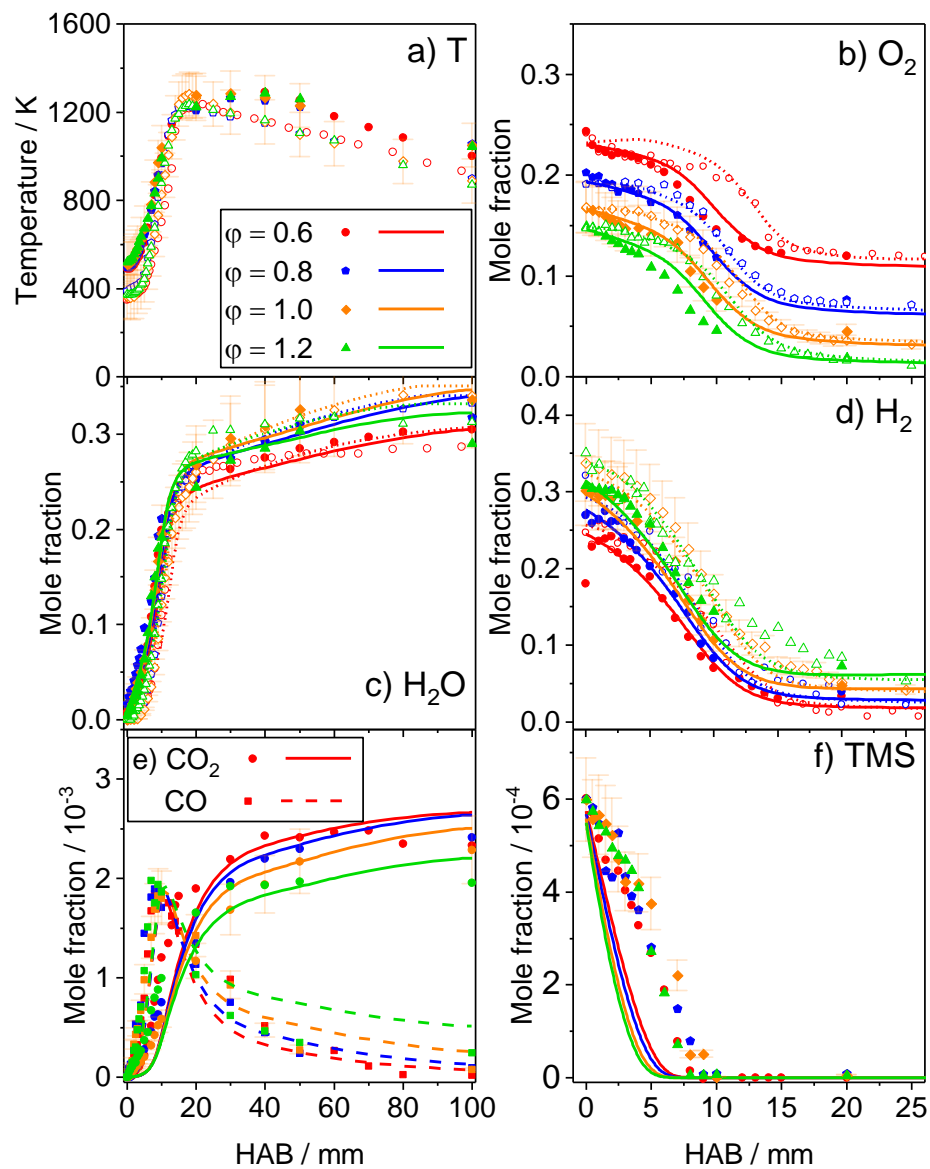


Figure 8-1. Measured (symbols) and simulated (lines) mole fraction profiles of main species (e.g. H_2 , H_2O , TMS, O_2 , CO , CO_2) and temperature profiles in neat (open symbols) and doped (closed symbols) $H_2/O_2/Ar/TMS$ -flames. Error bars show the uncertainties of measured temperature and mole fractions.

Deviations between simulation and experiment concerning TMS are extensively discussed in the work of Janbazi et al. [185]. In summary, the decomposition steps of TMS are estimated by analogy to the hydrocarbon chemistry of neopentane and were not optimized against the experimental profiles during model development. Also, probing effects can affect the flow field and temperature field. This results in widening the flame front and cooling the flame close to the sampling-probe. The effect of the sampling-probe on the flame temperature and the resulting changes to the flame structure are tentatively shown in the supplementary material Figure C-3 (see appendix C). Figure 8-2 shows the measured and simulated mole fraction profiles of the oxygen radicals in the reported flames. The measured O-radical profiles have comparatively large uncertainties and exhibit more noise than the profiles of other intermediates because the small radicals OH and O are often lost in the sampling process [84]. According to the simulation the oxygen radical is involved in many reactions with intermediate species of TMS. As expected, the mole fraction of the O-radical is higher-at lean than at rich flame conditions. Compared to flame B it decreases by 20%, 38%, 55% in the exhaust gas of flames D, F, and H, respectively. For all equivalence ratios, the maximum O-radical mole fraction is reached downstream of the point of complete decomposition of TMS and is followed by a slow consumption of O-radicals in the exhaust gas. The deviations in the O consumption rates between doped and undoped flames can be traced by reaction path analyses and sensitivity analyses to the reaction between CO and O forming CO₂. The model overpredicts this difference for the lean conditions.

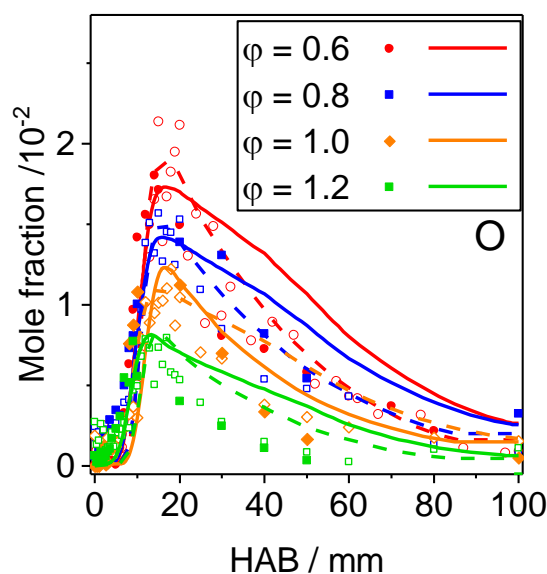


Figure 8-2. Measured (symbols, scaled) and simulated (lines) mole fraction profiles of O-radicals in neat (open symbols) and TMS-doped (closed symbols) H₂/O₂/Ar-flames.

Most likely, either the dependence of this reaction on the equivalence ratio is not accurately captured in the model or reactions with silicon-containing species, which are not included in the model, contribute markedly to the consumption of O radicals under lean conditions.

8.5.2 TMS and carbon-containing composition products

The comparison of measured and simulated TMS profiles in Figure 8-1f reveals significant deviations. The simulated mole fraction profiles show a convex-down behavior and the experiments a convex-up behavior, for all equivalence ratios. The difference in profile shape can be explained by the effect of the sampling-probe on the flow- and temperature field of the flame. In addition, the simulations predict a much faster TMS destruction than observed in the experiments, that was also observed in the original reaction mechanism development work [185]. TMS destruction is dominated by hydrogen abstraction reactions from TMS by O, H and OH radicals as can be seen from the rate of production analysis (ROP) in Figure 8-3. ROP analyses were performed at HAB = 1 mm, 2.5 mm and 6 mm. The rate coefficient for the hydrogen abstraction from TMS by H radicals is among the few rate coefficients in the Si/C/H/O system that has been accurately measured by Peukert et al. [169]. The rate coefficients for the hydrogen abstraction by other radicals have been estimated with reasonable accuracy based on analogies of H-abstraction from neopentane. These reaction rates were not changed in the reaction mechanism optimization. The reactions with OH and H radicals contribute strongly to the decomposition of TMS for equivalence ratios investigated here, while the reaction with O radicals plays only a minor role. The importance of the H-abstraction by H radicals increases with increasing equivalence ratios in agreement with the larger H radical mole fractions, while importance of the reaction with OH radicals is unaffected. The fact that the overestimation of the reaction rate of TMS in the experiments is also independent of the flame conditions, e.g., independent of mole fractions of O, H and OH radicals, suggests that the discrepancies in the TMS consumption rate are most likely linked to the H-abstraction reaction by OH radicals.

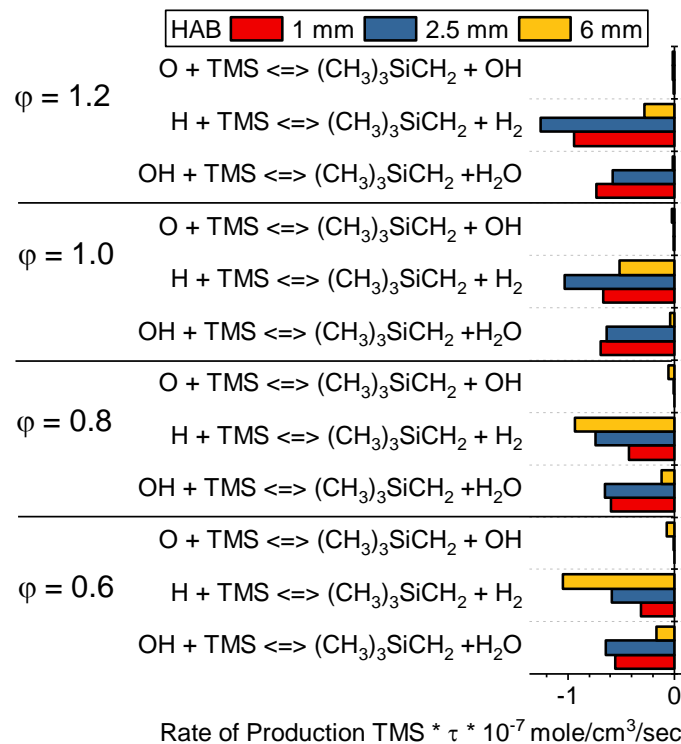


Figure 8-3. Reaction flow analyses of the three most important reactions for the decomposition of TMS.

Figure 8-1e presents measured and simulated mole fraction profiles of the CO₂ and CO formed during oxidation of the TMS. The carbon monoxide profiles peak around HAB = 10 mm, so at the same HAB where all TMS is consumed. In all flames, the CO is further oxidized to CO₂ reaching equilibrium values close to 2400 ppm. Carbon is only introduced into the gas mixture by the TMS addition (2400 ppm). From the carbon balance, it is evident that all carbon is converted to CO and subsequently CO₂ at high HAB, which is desirable in the synthesis of ultrapure silicon-oxide particles. The simulation reproduces the measured CO₂ and CO mole fraction profiles quite well, but deviations appear close to the burner due probe perturbations. Deviations between measured and simulated CO₂ mole fractions at higher distances are slightly larger than the expected error limit of 15%. They can be explained by a stream stall of the one-dimensional flow field leading to a source for further perturbations.

The comparison of the experimental and simulated mole fraction values demonstrates that the reaction mechanism reproduces the overall flame chemistry with and without addition of TMS well. This is a prerequisite for further analysis and interpretation of observations using the simulations.

8.5.3 Initial intermediates of TMS

Figure 8-4 shows two reaction path analyses at HAB = 10 mm and HAB = 20 mm for $\phi = 1$ at temperatures of 1013 K and 1250 K. They show that only the relative importance of the reaction pathways changes with HAB, while the active pathways are identical. Similar reaction pathways were found for all equivalence ratios.

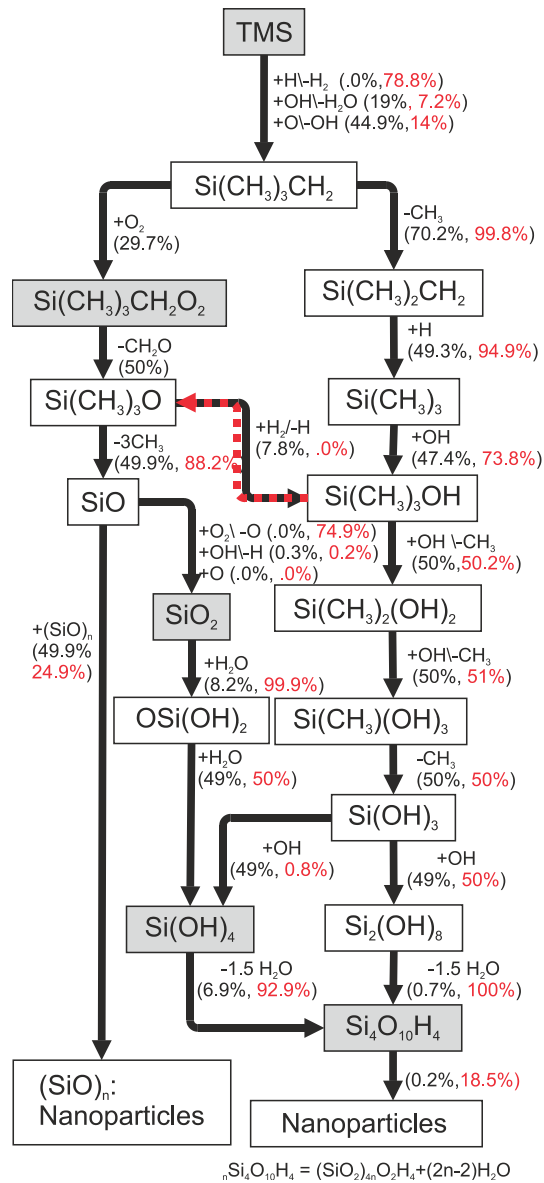


Figure 8-4. Reaction pathways of silicon-species at $\phi = 1$ at HAB = 10 mm, T = 1013 K (black) and at HAB = 20 mm, T = 1250 K (red). Experimentally detected silicon-species are shaded in grey.

Since $\text{Si}(\text{CH}_3)_3\text{CH}_2$ could not be detected, the first experimentally observed silicon-containing intermediate at all equivalence ratios is $\text{Si}(\text{CH}_3)_3\text{CH}_2\text{OO}$. This species may be a peroxide or one of its more stable isomers. In the reaction mechanism the peroxide $\text{Si}(\text{CH}_3)_3\text{CH}_2\text{OO}$ is produced by O_2 addition to the initially formed TMS radical. The maxima of the mole fraction profiles of $\text{Si}(\text{CH}_3)_3\text{CH}_2\text{OO}$ move to slightly larger distances from the burner with decreasing equivalence ratio. This trend and the absolute mole fraction

profiles shown in Figure 8-5 are in good agreement between experiment and simulation, and in accord with the shifts in the temperature profiles (Figure 8-1a). Also, the mole fraction of $\text{Si}(\text{CH}_3)_3\text{CH}_2\text{OO}$ increases with increasing amount of O_2 . For all equivalence ratios, $\text{Si}(\text{CH}_3)_3\text{CH}_2\text{OO}$ is completely consumed at around 700 K. Other silicon intermediate species, e.g., $\text{OSi}(\text{CH}_3)_3$, $\text{Si}(\text{CH}_3)_3\text{OH}$, $\text{Si}(\text{OH})_3$ appear in the reaction zone as it is postulated in the reaction pathway in Figure 8-4.

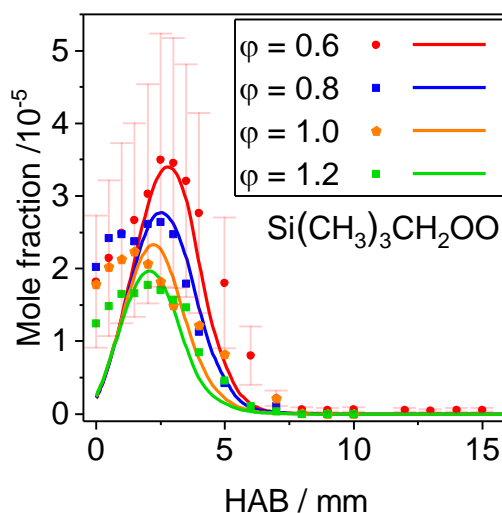


Figure 8-5. Measured (symbols) and simulated (lines) mole fraction profiles of $(\text{CH}_3)_3\text{Si}(\text{CH}_2)\text{OO}$ in TMS-doped $\text{H}_2/\text{O}_2/\text{Ar}$ - flames.

8.5.4 Cluster and particle formation pathways

Figure 8-6a reports measured and simulated mole fraction profiles of SiO_2 , $\text{Si}(\text{OH})_4$, $\text{Si}_4\text{O}_{10}\text{H}_4$ that are important intermediates of particle formation in the reaction pathway in Figure 8-4. These species are formed from the initial intermediates and peak at $\text{HAB} \geq 10$ mm. According to the reaction mechanism, two distinct pathways lead to the formation of silica nanoparticles. The first pathway forms SiO , which condenses to SiO_2 nanoparticles. Condensation of $\text{Si}(\text{OH})_4$ to larger clusters such as $\text{Si}_4\text{O}_{10}\text{H}_4$ which in turn form silica nanoparticles constitutes the second pathway.

The measured and simulated mole fraction profiles of SiO_2 in Figure 8-6a have their maxima near $\text{HAB} = 10$ mm at 1000 K. SiO_2 is consumed slowly in the exhaust gas. The maximum mole fractions of SiO_2 decrease with increasing equivalence ratio and reach the detection limit in the richest flame H. The simulations predict the measured profiles within the accuracy of the data. According to the reaction path analysis at $\varphi = 1$ and $\text{HAB} = 10$ mm SiO_2 is mainly formed by the reaction $\text{SiO} + \text{O}_2 = \text{SiO}_2 + \text{O}$, so consequently less SiO_2 is formed with increasing equivalence ratio because less oxygen is available in the exhaust. It is conceivable that as a consequence more SiO could react to nanoparticles.

Figure 8-6b presents measured and simulated mole fraction profiles of $\text{Si}(\text{OH})_4$. The simulation captures the measurements within the absolute uncertainties of the data. Species like $\text{Si}(\text{OH})_4$ are quantified using estimated ionization efficiencies and have large absolute uncertainties of a factor of two. In addition, the model was optimized in the work of Janbazi et al. [185], to fit the absolute mole fractions in flame B, so that a good match of experiment

and simulation is expected. When comparing profiles from different equivalence ratios, the uncertainties in the ionization efficiency can be neglected because they will shift the mole fraction values in the same direction.

Figure 8-6c shows measured and simulated mole fraction profiles of $\text{Si}_4\text{O}_{10}\text{H}_4$. According to the reaction pathways in Figure 8-4 for $\text{HAB} = 10$ mm and $\text{HAB} = 20$ mm, the first cluster $\text{Si}_4\text{O}_{10}\text{H}_4$ is formed through $\text{Si}(\text{OH})_3 + \text{OH} = 0.5 \text{ Si}_2(\text{OH})_8$, followed by a dehydration sequence $\text{Si}_2(\text{OH})_8 = 0.5 \text{ Si}_4\text{O}_{10}\text{H}_4 + 3.0 \text{ H}_2\text{O}$ or by $\text{Si}(\text{OH})_4 = 0.25 \text{ Si}_4\text{O}_{10}\text{H}_4 + 1.5 \text{ H}_2\text{O}$.

At the maximum of the $\text{Si}(\text{OH})_4$ profiles at approximately $\text{HAB} = 10$ mm, the experimental mole fractions of the cluster $\text{Si}_4\text{O}_{10}\text{H}_4$ are about 40% lower in flame B ($\varphi = 0.6$) compared to flame H ($\varphi = 1.2$), reflecting the decrease in the respective $\text{Si}(\text{OH})_4$ profiles quantitatively. This observation confirms, that independent of the equivalence ratio of the flame the formation of $\text{Si}_4\text{O}_{10}\text{H}_4$ is linked directly to $\text{Si}(\text{OH})_4$.

In conclusion, the model describes the effect of equivalence ratio on important species in the particle formation path correctly and can be used to estimate the relative importance of both pathways as a function of equivalence ratio.

The nanoparticles can be formed either via the SiO or via the $\text{Si}_4\text{H}_{10}\text{O}_4$ -cluster route shown in Figure 8-4. According to a rate of production analysis at $\varphi = 1$ at $\text{HAB} = 10$ mm, the ROP of nanoparticles by the SiO pathway is 10^5 time higher than the ROP by the cluster pathway. At $\text{HAB} = 20$ mm the cluster pathway is more important with a 10^4 times higher ROP. This observation indicates that the pathway for the formation of nanoparticles changes within the flame with increasing HAB . The relative importance of both pathways in the complete synthesis process is estimated by comparison of the integrated ROP for both routes over all HAB . This analysis shows that 97% of the particles are formed via the SiO route and 3% are formed via the $\text{Si}_4\text{O}_{10}\text{H}_4$ cluster route.

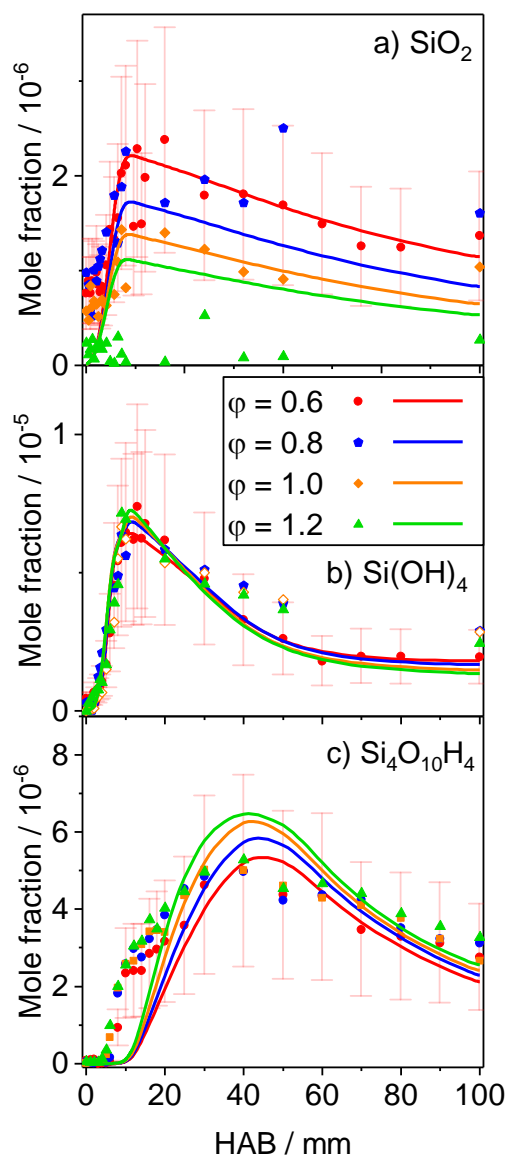


Figure 8-6. Measured (symbols) and simulated (lines) mole fraction profiles of (a) SiO_2 , (b) Si(OH)_4 , (c) $\text{Si}_4\text{O}_{10}\text{H}_4$ in TMS-doped $\text{H}_2/\text{O}_2/\text{Ar}$ -flames.

Compared to the study of hydrocarbon systems the investigation of inorganic nanoparticle formation in flames is considerably more difficult, e.g., due to the lack of any prior knowledge of the species occurring in these flames, unknown species properties and the more rapid particle formation which presents a technical challenge. Consequently, the presented data are state-of-the-art but do not reach the accuracy that can be achieved in hydrocarbon systems. The study presented here is the only systematic speciation study of the Si/H/O system reaching this level of chemical detail in the literature. As a result, the chemical reaction mechanism trained on these data is currently an “engineering model” with a majority of optimized rate constants [185]. However, the change in nanoparticle formation pathways observed is significant and outside the error margin.

8.5.5 Particle characterization

If a change in particle formation pathways occurs as function of equivalence ratio, this effect should be evident in the synthesized nanoparticles. The particle sizes could not be determined online in the experiment described here, but the particle properties were investigated with offline techniques. Silica powders are collected after a series of measurements with the three flames D, F and H of different equivalence ratio. Consequently, the powders are a mixture of the nanoparticles produced with different oxygen flows. 8 TEM images are used and 511 particles are counted to obtain a representative and statistically significant nanoparticle size distribution. Figure 8-7 shows a particle size distribution of silica nanoparticles. A log-normal fit of the data clearly shows a bimodal size distribution with two fractions of particles with mean diameters of 46.7 nm and 158 nm.

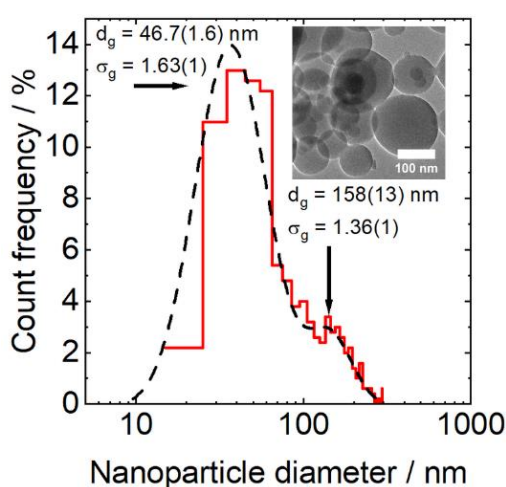


Figure 8-7. Particle size distribution with log-normal fit of data (dashed line) and separate contributions for each size mode (blue and green), the inset shows a part of a TEM micrograph.

Changes to the size distribution have previously been observed in flame synthesis by Akurati et al. [187] who measured the BET based nanoparticle diameter of silicon oxides depending on the oxygen flow rate. The inset of Figure 8-7 shows a representative TEM micrograph of the spherical particles. The amorphous lattice of the particles is supported by a X-ray diffraction investigation with a broad feature at $\sim 25^\circ 2\theta$ typically for amorphous SiO_2 (see Figure C-1 and Figure C-2 in appendix C).

The data support the observation that the equivalence ratio seems to affect the final particle size but not the particle structure. The flame data offer several possible explanations for the observed effect. On the one hand, the different particle sizes may be related to the different particle formation pathways. On the other hand, the changes in the mole fractions of the radicals in the exhaust gas may lead to different growth patterns of the initially formed nanoparticles. These open questions will be addressed in future research.

8.6 Conclusion

This work investigates the influence of the equivalence ratio of H₂/O₂/Ar synthesis flames on the reaction pathways of tetramethylsilane, intermediates and nanoparticles. Mole fraction profiles of the most important species are compared to simulations with a reaction mechanism for TMS combustion from literature. The results demonstrate that the reaction mechanism can be improved by more accurate rate coefficients for the hydrogen abstraction by OH radicals from TMS, and by inclusion of reactions of silicon-containing species with the flame radicals in the exhaust gas. Nevertheless, the reaction mechanism reproduces the experimental data with satisfactory accuracy for all equivalence ratios. In particular, it is shown that two nanoparticle formation pathways are active at all equivalence ratios and that they may lead to different particle size distributions. The data set can be further used to improve reaction kinetics in the Si/C/H/O system.

9 New insights into methane-oxygen ion chemistry

The content of this chapter was published in *Proceedings of the Combustion Institute 36, 1213-1221 (2017)*, A. B. S. Alquaity, C. Bingjie, H. Jie, H. Selim, M. Belhi, Y. Karakaya, T. Kasper, S. M. Sarathy, F. Bisetti, A. Farooq, *New insights into methane-oxygen ion chemistry* and is reprinted with permission from Elsevier.

CRedit⁴ author statement: Y. Karakaya performed the experiments and the data analysis. T. Kasper conceptualized the experiments and was responsible for the funding acquisition. A. B. S. Alquaity conceptualized, designed and performed the experiments, carried out the data collection and analysis, and prepared the original draft. C. Bingjie contributed to the data collection and analysis. H. Jie developed the reaction model for the simulation of the ion chemistry, performed simulations and prepared the original draft. H. Selim did the data analysis. M. Belhi performed the simulations. S. M. Sarathy contributed to the manuscript review and was responsible for the funding acquisition. F. Bisetti developed the reaction model. A. Farooq conceptualized the experiments and did the funding acquisition. All authors contributed to the manuscript review.

9.1 Abstract

External electric fields may reduce emissions and improve combustion efficiency by active control of combustion processes. In-depth, quantitative understanding of ion chemistry in flames enables predictive models to describe the effect of external electric fields on combustion plasma. This study presents detailed cation profile measurements in low-pressure, burner-stabilized, methane/oxygen/argon flames. A quadrupole molecular beam mass spectrometer (MBMS) coupled to a low-pressure ($p = 30$ Torr) combustion chamber was utilized to measure ion signals as a function of height above the burner. Lean, stoichiometric and rich flames were examined to evaluate the dependence of ion chemistry on flame stoichiometry. Additionally, for the first time, cataloging of flame cations is performed using a high mass resolution time-of-flight mass spectrometer (TOF-MS) to distinguish ions with the same nominal mass. In the lean and stoichiometric flames, the dominant ions were H_3O^+ , CH_3O_2^+ , $\text{C}_2\text{H}_7\text{O}^+$, $\text{C}_2\text{H}_3\text{O}^+$ and CH_5O^+ , whereas large signals were measured for H_3O^+ , C_3H_3^+ and $\text{C}_2\text{H}_3\text{O}^+$ in the rich flame. The spatial distribution of cations was compared with results from numerical simulations constrained by thermocouple-measured flame temperatures. Across all flames, the predicted H_3O^+ decay rate was noticeably faster than observed experimentally. Sensitivity analysis showed that the mole fraction of H_3O^+ is most sensitive to the rate of chemi-ionization $\text{CH} + \text{O} \leftrightarrow \text{CHO}^+ + \text{e}^-$. To our knowledge, this work represents the first detailed measurements of positive ions in canonical low-pressure methane flames.

⁴ CRedit (Contributor Roles Taxonomy)

9.2 Introduction

Flame chemi-ionization produces ions in trace quantities, with typical mole fractions varying from 10^{-9} to 10^{-7} [61]. Ion current sensors have been used to control spark advance timing [188], knock [189] and in-cylinder pressure [190]. In addition to these applications, there has been an increasing interest in understanding ion chemistry to enable effective application of external electric fields for active control of combustion processes. Electric fields have been shown to reduce emissions [191], extend the operability of combustion devices and improve combustion efficiency [192, 193]. Nevertheless, progress has been hampered by the limited characterization of flame ionization processes, rudimentary ion chemistry models and the lack of experimental data on the distribution of ions in flames. Detailed knowledge of ion chemistry is required to accurately predict the total density of positive and negative charges, which are essential to model the interaction of flames with external electric fields [194]. Consequently, experimental and modeling efforts towards a thorough characterization of flame ion chemistry are needed.

Owing to the extremely small concentrations of ions in flames, it is very challenging to implement non-intrusive laser-based diagnostics to measure ion mole fractions. Compared to other diagnostic techniques, molecular beam mass spectrometry (MBMS) provides high sensitivity and the ability to differentiate between ions and neutrals. MBMS has previously been used to carry out ion measurements in flames [195-202]. Deckers and Van Tiggelen [195-197] utilized a mass spectrometer to measure ions primarily in low-pressure acetylene-oxygen flames. Calcote and Reuter [198] used MBMS to measure cations in low-pressure ethylene-oxygen flames. Goodings et al. [199, 200] performed a detailed study of methane ion chemistry by measuring relative cation and anion signals in lean and rich premixed atmospheric Bunsen-type flames, although temperature profiles were not reported. The lack of temperature information and the inherent two-dimensional conical flame structure make it difficult to compare their experimental data with one-dimensional flame simulations [203]. Recently, Alqaity et al. [204, 205] used a quadrupole mass spectrometer to measure positive ions and flame temperature in atmospheric premixed methane-oxygen flat flames. However, the flame structure was not fully resolved due to the relatively small flame thickness (~ 1 mm) at 1 atm.

The predicted ion concentration profiles in previous modeling studies [203, 206] were significantly narrower compared to the experimental data for atmospheric flames. Modeling studies attributed the disagreement to the lack of temperature information and insufficient spatial resolution due to the thin flame front at 1 atm. Therefore, additional experiments, which circumvent the aforementioned limitations are critical to address these remaining issues.

The present effort seeks to provide a comprehensive dataset to aid the development and validation of predictive ion chemistry models for methane flames. Burner-stabilized laminar premixed low-pressure flat flames are selected to achieve high spatial resolution for cation measurements carried out using a quadrupole MBMS. Additionally, a high mass resolution TOF-MS is utilized to identify and distinguish ions with the same nominal mass. Firstly, we give a brief description of the MBMS experimental setup and the numerical framework used to carry out simulations. We then present the detailed cation measurements for methane-

oxygen flames and compare against numerical simulations carried out using an established ion chemistry model [203]. Lastly, we present a sensitivity analysis to highlight critical ion-molecule reactions and suggest possible areas of improvement to the ion chemistry mechanism.

9.3 Experimental details and ion chemistry model

9.3.1 Experimental setup and method

A stainless-steel water-cooled 6 cm diameter McKenna burner (Holthuis & Associates) was used to establish burner-stabilized premixed methane-oxygen-argon flat flames at 30 Torr. The flow rates and equivalence ratios used in this study are reported in Table 9-1. The flow rates were controlled via mass flow controllers (MKS, 1179B), which have an uncertainty of $\pm 1\%$ of the full range (5 SLPM). The McKenna burner was mounted on a motorized translation stage (SMC, LEY-25RC-350G-S5) with a positioning repeatability of ± 0.02 mm. Measurements carried out on different days showed that the spatial location of ion profiles was repeatable within ± 0.5 mm. A modified Hiden HPR-60 MBMS system equipped with a triple-filter quadrupole mass spectrometer (EQP, 300 m/z range) was used to measure ion profiles as a function of height from the burner surface. A 24 mm long nickel cone of 57° angle and 0.4 mm aperture was used for sampling the gases along the centerline of the flat flame. Three stages of differential pumping were used, where the first and second stage skimmer cones had orifice sizes of 0.3 mm and 2 mm, respectively. In order to detect naturally occurring ions in flames, electrical potentials of -33 V and -51 V were applied to the first stage and second stage skimmer cones, respectively. The negative potentials applied to the skimmer cones aid in funneling the positive ions into the sampling system, however, the transmission of molecules through the two skimmer cones is primarily due to physical gas expansion and differential pumping via molecular beam sampling, resulting in transmission efficiencies that are similar for ions and neutrals [205]. The flame temperature was measured in the absence of the sampling cone using an SiO₂ coated Type-B (Omega) thermocouple with a bead of 0.38 mm diameter. Thermocouple readings were corrected for radiation effects [92] with corrections ranging from 83 to 195 K for flame temperatures between 1521 and 2091 K. The burner surface temperature was measured using a laser thermometer gun (Traceable, Model # 4483) and found to be between 328.15 and 331.15 K depending on the stoichiometry of the flame.

Table 9-1. Flame conditions. The reactant mixture entered the burner at 23 °C for all flames. The cooling water temperature was 25 °C. Chamber pressure was 30 Torr. Flow rates are given in SLPM.

Flame	Equivalence ratio	CH ₄ flow rate	O ₂ flow rate	Ar flow rate	Total flow rate
1	0.5	0.75	3	1.25	5
2	1	1.25	2.5	1.25	5
3	1.5	1.61	2.14	1.25	5

The procedure used for obtaining relative ion profiles has been detailed previously [205], so only a brief description is given here. Firstly, mass scans were performed at various heights above the burner to identify dominant ions. Next, energy scans were performed for each ion to obtain its total signal. The area under the energy distribution curve is a good representation of the ion density and was found to be repeatable within 10%. The integrated ion signal for each ion was then scaled with the overall mass discrimination factor (MDF) of the MBMS system. The MDF was measured by flowing various gas mixtures of known mole fractions through the MBMS while ensuring that the pressure in the first pressure reduction stage remained the same as in flame measurements. The MDF corrected signal was scaled with the instrument sampling function (FKT) [146] to yield relative ion mole fractions across the flame. Hydrates of flame ions formed during the sampling process were lumped together with the parent ion, as is the norm in experimental ion studies [202]. The contribution of hydrates to the total signal of the parent ion is discussed in the Supplementary Material (see appendix D). Additionally, a high mass resolution ($m/\Delta m \approx 4000$ at $m/z = 28$) time-of-flight mass spectrometer (TOF-MS, Kaesdorf) at the University of Duisburg-Essen [207] was used to facilitate the identification of ions with the same nominal mass-to-charge ratios, which cannot be separated using the quadrupole mass spectrometer.

9.3.2 Numerical methods and model

Low-pressure flames were modeled as one-dimensional burner-stabilized premixed flat flames using the PREMIX [208] code. Two modifications were implemented in the code to account for the transport of charged species. Firstly, the electric potential was added as an additional variable and the Poisson equation for the potential was solved. Secondly, the drift diffusion flux was included in the mass flux for charged species [209]. Ion transport was modeled according to a mixture-averaged approach with suitable potentials [209] and the electron mobility was set to $0.4 \text{ m}^2/\text{V}^{-1}\text{s}^{-1}$ [210]. In the present work, a modified AramcoMech 1.3 C₀ – C₂ mechanism [211] was used for neutral species. The modification was carried out to improve the prediction of CH radical, which is responsible for the generation of electrons and ions via chemi-ionization [212].

The ion mechanism assembled by Prager et al. [203] was added to the base ARAMCO 1.3 mechanism to predict cation profiles. The ion chemistry mechanism contains 4 cations (H_3O^+ , $\text{C}_2\text{H}_3\text{O}^+$, CH_5O^+ and CHO^+), 6 anions (O_2^- , O^- , OH^- , CHO_2^- , CHO_3^- and CO_3^-), electron e^- , and 67 elementary reactions. This mechanism, however, does not contain C_3H_3^+ , which appears in small amounts in lean and stoichiometric flames, but is abundant in rich flames. Rate parameters for most reactions in the ion chemistry mechanism [203] were updated according to the most recent data available in the UMIST 2012 database [213]. Although alternative rate parameters for chemi-ionization and recombination reactions are available from the UMIST database, we retained the parameters given in [203] as they were determined experimentally and found to be most appropriate [209, 212]. This updated version of the ion chemistry mechanism is available as supplementary material.

9.4 Results and discussion

9.4.1 Neutral species

Validation of the experimental setup was first carried out by measuring neutral species in the same flames (Table 9-1) used for ion measurements. Flame neutrals were ionized by an electron gun operating at ~ 20 eV. Figure 9-1 compares the measured mole fraction profiles of major neutral species (CH_4 , O_2 , CO , CO_2 and Ar) with model predictions as a function of the height above the burner (HAB) for the three flames studied here. As commonly done in probe-based flame measurements [107], the experimental data have been shifted towards the burner by 1, 2 and 4 mm for lean, stoichiometric and rich premixed flames, respectively, to match with the predicted species profiles. A relatively large cone angle (57°) was used here to get adequate cation signals. The larger than usual cone angle resulted in perturbation of the flame front, and, consequently, relatively large axial shifting of experimental data. The rates of species formation and decay were markedly slower in the rich flame as compared to other flames. Overall, simulated mole fractions reproduced the experimental data adequately across all flames. Disagreement in methane and oxygen mole fractions near the reaction zone of rich flame may be attributed to probe effects, as discussed previously. Reasonable agreement between the measured and simulated neutral species validates the experimental setup and methodology.

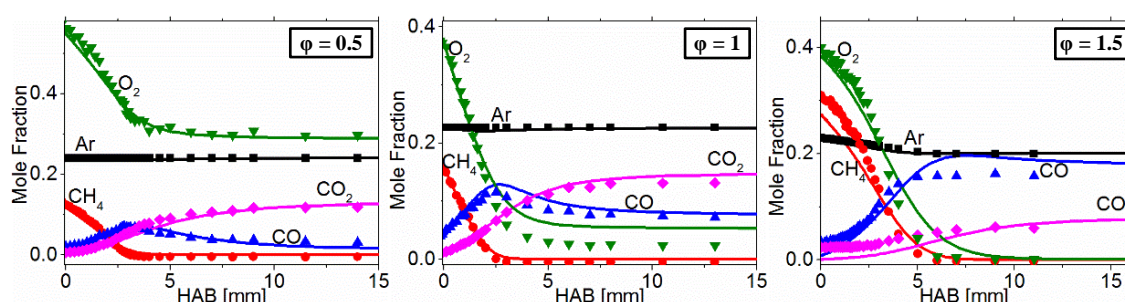


Figure 9-1. Measured neutral species (symbols) and simulations (lines). Measurements are shifted towards the burner surface by 1, 2 and 4 mm for lean, stoichiometric and rich flames, respectively.

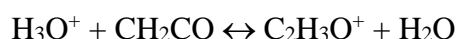
9.4.2 Cation Measurements

Figure 9-2, Figure 9-3 and Figure 9-4 report cation profiles as a function of the height above the burner for the three flames together with model predictions. The experimental ion profiles have been scaled to match the peak mole fraction of H_3O^+ from simulations. Furthermore, the experimental data have been shifted towards the burner by 1 to 4 mm, as mentioned previously for neutral species.

9.4.2.1 Lean Flame

In the lean flame (Figure 9-2), the most abundant flame ions, in the order of high to low signals, are H_3O^+ ($m/z = 19 + 37 + 55 + 73$), ions at m/z of 47 (+ 65), CH_5O^+ ($m/z = 33 + 51$

+ 69), and $C_2H_3O^+$ ($m/z = 43 + 61 + 79$). The m/z values in parentheses indicate the mass of the parent ion and its hydrates. Although other pathways to form ions have been proposed, protonation of neutrals/intermediates is considered to be the dominant mechanism [199]. Hydronium (H_3O^+) is formed by the protonation of water, CH_5O^+ is formed by the protonation of methanol, and $C_2H_3O^+$ is formed by the protonation of ketene (CH_2CO). The protonation reactions mainly responsible for the formation of the above ions are shown below [203]:



High-resolution measurements via TOF-MS in a similar lean ($\phi = 0.8$) methane/oxygen flame carried out at the University of Duisburg-Essen indicate that the large signal at $m/z = 47 (+ 65)$ reflects contributions from $CH_3O_2^+$ and $C_2H_7O^+$. Proton transfer from CHO^+ to formic acid (CH_2O_2) can form $CH_3O_2^+$ [202], while $C_2H_7O^+$ may be formed by the proton transfer from CHO^+ to structural isomers, ethanol and dimethyl ether [202]. Numerical simulations of neutral species in the lean flame showed negligible amounts of ethanol compared to formic acid and dimethyl ether, which suggests that the signal at $m/z = 47 (+ 65)$ is primarily due to the protonation of formic acid and dimethyl ether.

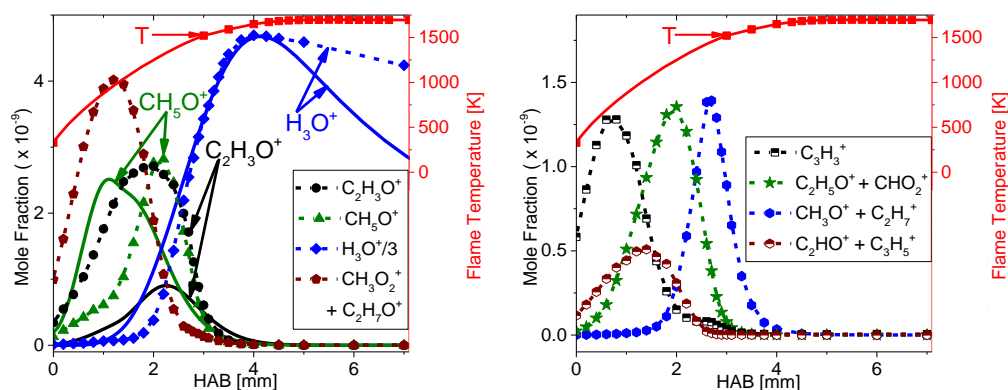


Figure 9-2. Ion mole fractions from experiments (symbols with dashed lines) and simulations (solid lines in corresponding color) for the lean premixed flame ($\phi = 0.5$). Measured flame temperature (red symbols with red line) also shown. Experimental relative ion profiles have been scaled to match the peak mole fraction of simulated H_3O^+ . Simulation data include results for $C_2H_3O^+$, CH_5O^+ and H_3O^+ .

Positive ions found in smaller amounts include $C_3H_3^+$ ($m/z = 39 + 57 + 75$) and ions with $m/z = 45 (+ 63)$ reflecting contributions from $C_2H_5O^+$ and CHO_2^+ , $m/z = 31 (+ 49)$ from CH_3O^+ and $C_2H_7^+$, and $m/z = 59 (+ 77)$ due to $C_2HO^+ \cdot H_2O$, $C_3H_5^+ \cdot H_2O$ and $C_3H_7O^+$. We remark that, in the lean flame, the maximum signal for $C_3H_3^+$ is at $m/z = 75$, which could be identified as a hydrate of $C_3H_3^+$ or a hydrate of $C_3H_5O^+$ (protonated methyl ketene). Cataloging of flame cations using high mass resolution TOF-MS allowed for the correct

identification of targets having very similar m/z values. However, this device cannot differentiate between isomers and ions having equal number of C/H/O, for example, $C_3H_5O^+ \cdot H_2O$ and $C_3H_3^+ \cdot (H_2O)_2$. Hydronium (H_3O^+) is the most dominant ion and reaches its peak downstream of the peak of other ions. Its rate of increase is quite rapid as it rises from 75% its peak value to the peak over an axial distance of about 0.95 mm. The rapid rise can be attributed to the fact that chemi-ionization occurs only in the thin reaction zone and protonation of H_2O accelerates when H_2O mole fraction rises sharply. Hydronium decays rather slowly, going from peak to 75% of the peak in about 7.5 mm, because of the relatively slow recombination reaction rates.

9.4.2.2 Stoichiometric Flame

For the stoichiometric flame (Figure 9-3), the most abundant ions, in the order of high to low signals, are H_3O^+ , $C_2H_3O^+$, $CH_3O^+ + C_2H_7O^+$ and CH_5O^+ . As observed in the lean flame, H_3O^+ is the most dominant ion and persists over a broad region of the flame. Compared to the lean flame, additional ions at $m/z = 53$ (+ 71) with contribution from C_3HO^+ and $C_4H_5^+$ have been observed. These ions were not reported in previous studies [199, 201, 202]. Two distinct peaks are observed for $m/z = 39 + 57 + 75$, where the first peak is dominated by $m/z = 75$ and the second peak by $m/z = 39$. These two peaks most likely indicate that the signal at $m/z = 75$ is due to the $C_3H_5O^+$ hydrate with some contribution from $C_3H_3^+$, while the second peak corresponds solely to the $C_3H_3^+$ ion.

The hydronium signal increases from 75% of its peak value to the peak in about 0.8 mm and decays to 75% of its peak over an axial distance of about 5.7 mm. The decay in the stoichiometric flame is faster than in the lean flame. Additionally, the experimental peak H_3O^+ signal is almost a factor of two higher than in the lean flame. Increased H_3O^+ mole fraction is ascribed to higher CH densities in the stoichiometric flame, which play a key role in the formation of H_3O^+ [212]. Faster H_3O^+ decay in stoichiometric flames is due to the recombination being faster for larger H_3O^+ concentrations [212].

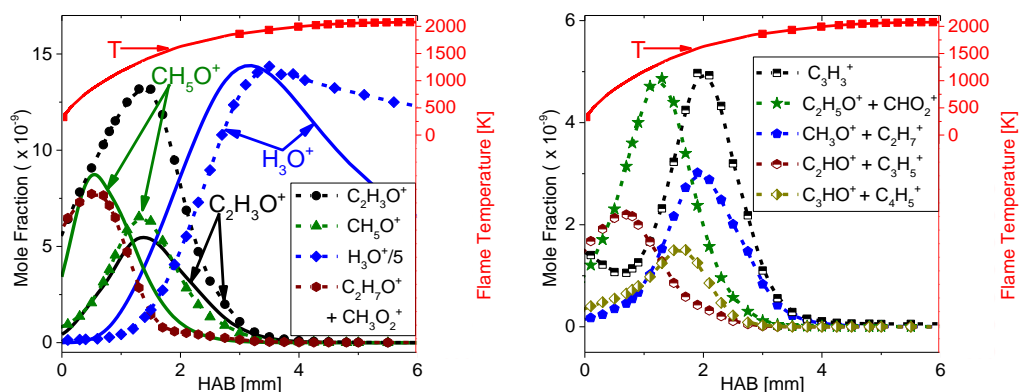


Figure 9-3. Ion mole fractions from experiments (symbols with dashed lines) and simulations (solid lines in corresponding color) for the stoichiometric premixed flame ($\phi = 1$). Experimental relative ion profiles have been scaled to match the peak mole fraction of simulated H_3O^+ . Simulation data include results for $C_2H_3O^+$, CH_5O^+ and H_3O^+ .

9.4.2.3 Rich flame

Figure 9-4 shows measured ion profiles, flame temperature and comparison with simulations for the rich flame (Flame 3 in Table 9-1). Compared to the stoichiometric flame, no additional ions were observed. However, the relative abundance of the ions was different. Major flame ions, in the order of high to low signals, are H_3O^+ , C_3H_3^+ , $\text{C}_2\text{H}_3\text{O}^+$ and CH_3O_2^+ + $\text{C}_2\text{H}_7\text{O}^+$. The relative cumulative signal from C_3HO^+ and C_4H_5^+ is higher than the corresponding signal for the stoichiometric flame. Once more, C_3H_3^+ ($m/z = 39 + 57 + 75$) has two distinct peaks with first peak dominated by $m/z = 75$ and second peak by $m/z = 39$, leading to the same conclusions as in stoichiometric flame.

It is interesting to note that the formation and consumption rates of all major ions in the rich flame are slower than their corresponding rates in the lean and stoichiometric flames. This trend is similar to the slow decay and formation rates of neutrals in the rich flame. Hydronium is produced and consumed rather slowly in the rich flame. Its signal increases from 75% of its peak value to the peak in about 4.5 mm and decays to 75% of its peak over a very large axial distance of ~ 14 mm. Experimental measurements show that despite decaying slowly, hydronium signal in rich flame is about 2 times smaller than in the stoichiometric flame. Presence of considerable amounts of C_3H_3^+ near the H_3O^+ peak hints at the possible existence of an indirect reaction pathway between the two ions. Eraslan et al. [214] had proposed the formation of C_3H_3^+ by an ion-molecule reaction between C_2H_2 and CH_3^+ . An earlier numerical work [206] had proposed the formation of CH_3^+ through proton transfer from either H_3O^+ or CHO^+ to CH_2 . Moreover, simulated profiles of neutral species in rich flame (see appendix D) show CH_2 and C_2H_2 reaching a maximum where C_3H_3^+ peaks. The most probably pathway linking H_3O^+ to C_3H_3^+ is: $\text{H}_3\text{O}^+ + \text{CH}_2 \leftrightarrow \text{CH}_3^+ + \text{H}_2\text{O}$ followed by $\text{CH}_3^+ + \text{C}_2\text{H}_2 \leftrightarrow \text{C}_3\text{H}_3^+ + \text{H}_2$. Our analysis suggests that ion chemistry mechanisms should include both CH_3^+ and C_3H_3^+ in order to simulate rich flames adequately.

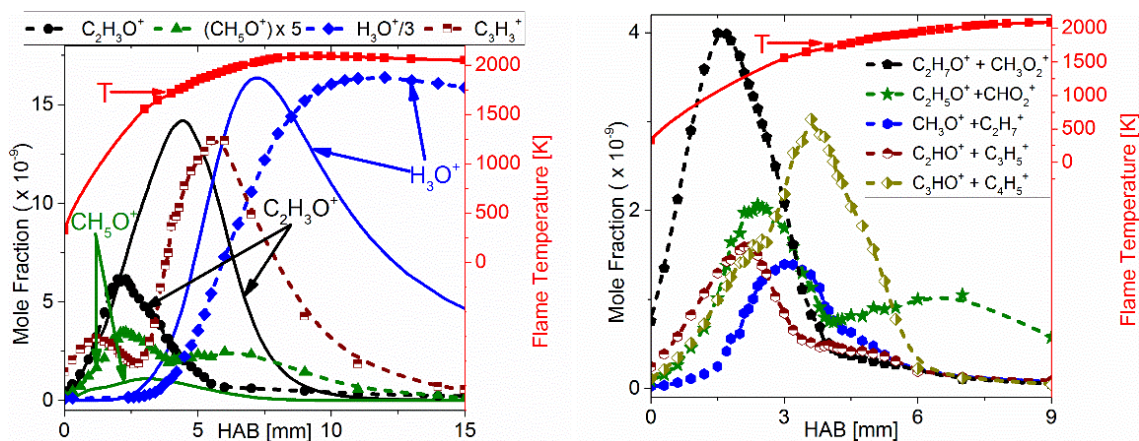


Figure 9-4. Ion mole fractions from experiments (symbols with dashed lines) and simulations (solid lines in corresponding color) for the rich premixed flame ($\phi = 1.5$). Experimental relative ion profiles have been scaled to match the peak mole fraction of simulated H_3O^+ . Simulation data include results for $\text{C}_2\text{H}_3\text{O}^+$, CH_5O^+ and H_3O^+ .

9.4.3 Modeling Results

9.4.3.1 Cation Predictions

Figure 9-2, Figure 9-3, Figure 9-4 report the data from simulations and a comparison with measured cation profiles. It should be noted that the ion chemistry model does not include CH_3O_2^+ and $\text{C}_2\text{H}_7\text{O}^+$ which are abundant across all flames. Additionally, the model does not contain pathways for C_3H_3^+ which is quite large in the rich flame. Since only relative ion densities are available from the experimental data, the mole fractions of all ions are scaled with respect to the predicted peak mole fraction of H_3O^+ .

The peak of $\text{C}_2\text{H}_3\text{O}^+$ relative to H_3O^+ is under-estimated in lean and stoichiometric flames and over-estimated in the rich flame. However, the location of the $\text{C}_2\text{H}_3\text{O}^+$ peak relative to that of H_3O^+ is captured correctly by the model. The predicted CH_5O^+ peak value relative to H_3O^+ is within 12% of the experimental data for the lean flame, while the CH_5O^+ peak value is over-estimated in the stoichiometric flame and under-estimated in the rich flame. The predicted CH_5O^+ peaks too early relative to the peak of $\text{C}_2\text{H}_3\text{O}^+$ for all three flames. Furthermore, for all flames, the sum of all simulated ions excluding H_3O^+ is under-estimated which suggests that the H_3O^+ mole fraction may be over-estimated in the ion mechanism. This is seen clearly in Figure 9-5 for the stoichiometric flame. Based on the disagreements observed, it may be argued that there are missing cation species and reaction pathways that must be added to the ion chemistry model to reconcile the differences between experimental data and simulations.

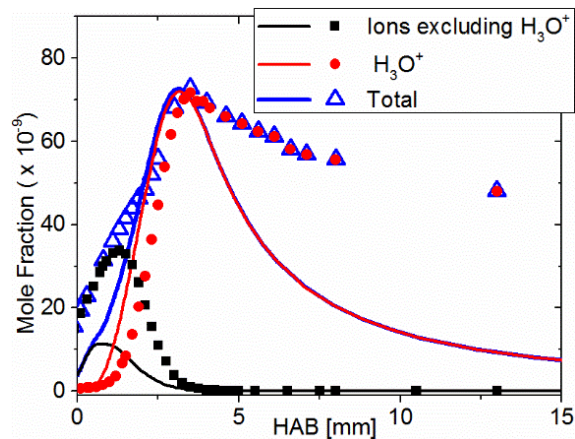


Figure 9-5. Ion mole fractions from experiments (symbols) and simulations (lines) for the stoichiometric flame ($\phi = 1$). Experimental ion profiles have been scaled to match the peak total ion mole fraction from simulation.

For all the flames studied here, the simulated decay rate of H_3O^+ is more rapid than measured experimentally. This observation is consistent with results from previous modeling studies [203, 206], wherein simulated decay rates were faster than those in experiments [199]. The discrepancy in decay rate was attributed to the limitations in spatial resolution and lack of temperature information in the experimental data. In the present work, the flame temperature profile has been measured carefully and used to constrain the simulations. Additionally, a sensitivity analysis was performed to study the effect of uncertainty (maximum 65 K) in

thermocouple-based temperature measurements on the H_3O^+ profile, and it was found to be negligible. Furthermore, reasonable agreement in the prediction of neutral species (Figure 9-1) implies that the current experimental data do not suffer from spatial resolution issues.

9.4.3.2 Hydronium Sensitivity Analysis

Figure 9-6 shows the sensitivity of H_3O^+ to the rate constants of key reactions. A positive sensitivity coefficient indicates reactions that increase the formation of H_3O^+ , while reactions with a negative coefficient increase its consumption. Sensitivity analysis was carried out at the peak of H_3O^+ and at 75% and 50% of the peak during the decay. It is interesting to note that the sensitivity coefficients of all reactions are almost independent of flame stoichiometry. At or near the peak, H_3O^+ is most sensitive to the chemi-ionization reaction $\text{CH} + \text{O} \leftrightarrow \text{CHO}^+ + \text{E}^-$ across all three flames. However, during the decay (at 50% of the peak), H_3O^+ is sensitive to its recombination with electrons. The hydronium recombination rate depends significantly on its peak mole fraction and an over-estimation of the peak value can lead to significantly faster decay [212]. We conclude that, in view of the important discrepancies in the predicted H_3O^+ decay rate, the rate constant of chemi-ionization reaction merits further scrutiny.

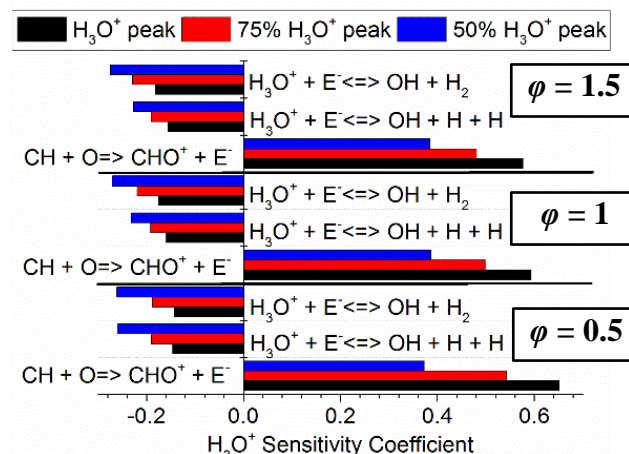


Figure 9-6. Sensitivity analysis of H_3O^+ at the peak and during the decay in lean, stoichiometric and rich flames.

9.5 Conclusions

Detailed relative cation mole fraction measurements were carried out in premixed 30 Torr flat flames of methane. Relative ion mole fraction profiles show strong dependence of the identity of dominant ions and their spatial distribution on the flame equivalence ratio. In lean and stoichiometric flames, the five most dominant ions are H_3O^+ , CH_3O_2^+ , $\text{C}_2\text{H}_7\text{O}^+$, $\text{C}_2\text{H}_3\text{O}^+$ and CH_5O^+ . In rich flame, H_3O^+ , C_3H_3^+ and $\text{C}_2\text{H}_3\text{O}^+$ appear in large quantities. For all flames, H_3O^+ is the most dominant ion. Simulated H_3O^+ decay rate is found to be much faster than observed experimentally, most-likely due to the over-estimation of the peak value of H_3O^+ . Sensitivity analysis showed that near the peak location, H_3O^+ is most sensitive to the chemi-ionization reaction $\text{CH} + \text{O} \leftrightarrow \text{CHO}^+ + \text{E}^-$, and its rate constant may need to be revisited.

In summary, our data provide the following new insights into the methane oxygen ion chemistry:

The current study showed that the prediction of notably faster H_3O^+ decay was due to inadequacies in the ion chemistry model and not due to experimental issues as previously postulated [203, 206]. Cataloging of ions facilitated using a high mass resolution TOF-MS allowed the conclusive identification of selected ions with very similar m/z values. CH_3O_2^+ and $\text{C}_2\text{H}_7\text{O}^+$ were found to be among the major ions in lean flame and need to be included in future ion chemistry models. We highlighted the possibility of an indirect reaction pathway between C_3H_3^+ and H_3O^+ in rich flames, proceeding through CH_3^+ . This new route suggests that both CH_3^+ and C_3H_3^+ and related reactions should be included in ion chemistry models to simulate rich flame conditions. For the first time, ions at $m/z = 53$ (+ 71) reflecting contributions from C_3HO^+ and C_4H_5^+ were observed in stoichiometric and rich flames. To the best of our knowledge, the present effort represents the first detailed measurements of cations in canonical low-pressure methane-oxygen-argon flames. It is expected that the database presented in this work will be used to develop and validate detailed and skeletal ion mechanisms for methane oxidation.

10 Investigation of the combustion of iron pentacarbonyl and the formation of key intermediates in iron oxide synthesis flames

The content of this chapter was published in *Chemical Engineering Science* 230, 116169 (2021), *Y. Karakaya, S. Kluge, H. Wiggers, C. Schulz and T. Kasper, Investigation of the combustion of iron pentacarbonyl and the formation of key intermediates in iron oxide synthesis flames* and is reprinted with permission from Elsevier.

CRedit⁵ author statement: Y. Karakaya performed the ion measurements, chose the precursor- and flame conditions, evaluated and discussed the experimental data, wrote the original draft of the manuscript. S. Kluge and T. Kasper performed the measurements at the Advanced Light Source. C. Schulz, H. Wiggers and S. Kluge provided discussions of the results. T. Kasper provided discussions of the results and contributed to the manuscript.

10.1 Abstract

The information of the gas phase kinetics are relevant for the development of detailed reaction mechanisms as well as for process design and control in flame synthesis. In this study, the decomposition of iron pentacarbonyl and the reaction pathways towards iron oxide clusters and particles in laminar H₂/O₂/Ar low-pressure synthesis flames are investigated. Gas-phase species are analyzed by photoionization and electron ionization mass spectrometry. The extraction of a representative sample from the particle-laden flow of a synthesis flame by an intrusive sampling technique for the analysis is challenging, because iron-intermediate species can condense easily. Cations can be extracted from the flame with a high efficient ion sampling technique that results in high sensitivity. Iron-containing cations provide evidence of the presence of key intermediates, e.g., Fe(OH)₂, Fe(OH)₃, Fe₂O₃, and larger Fe-O-clusters which are the dominant intermediates with respect to particle formation and need to be considered in future gas-phase reaction mechanisms.

10.2 Introduction

Every year millions of tons of nanoparticles are produced as functional materials from, e.g., iron oxide [32, 57], silicon dioxide [42, 48, 86], tungsten oxide [23], and titanium dioxide [102, 215, 216] in flame-based synthesis processes. Application fields for iron oxide nanoparticles are, e.g., oxidation catalysis, magnetic hyperthermia, magnetic resonance imaging, or magnetic data storage. To extend the applicability of nanoparticles to more fields, processes for targeted synthesis of particles with various properties such as size, crystal phase, and magnetic properties are demanded. These properties are set by an intricate

⁵ CRedit (Contributor Roles Taxonomy)

interaction of the precursor chemistry, the environmental conditions (e.g., flame chemistry) and the concentration–temperature history of the reactive gas mixture on their path through the reactor. For optimal process design and control, the fundamentals of the gas-phase kinetics must be fully understood [1].

Iron pentacarbonyl ($\text{Fe}(\text{CO})_5$) is often used as a precursor for flame-based iron oxide nanomaterials. There are several studies on the decomposition kinetics of $\text{Fe}(\text{CO})_5$ [1, 21, 50-52, 55, 217] as well as studies on the condensed phase of iron oxide nanoparticles [1, 58, 218-220]. But there are few experimental data describing the gaseous species during the oxidation of $\text{Fe}(\text{CO})_5$ in flames [21, 52, 53, 57, 98]. The work of Gerasimov et al. [21] reports the decomposition of $\text{Fe}(\text{CO})_5$ in a premixed, laminar, atmospheric $\text{H}_2/\text{O}_2/\text{N}_2$ flame. Gas-phase species were detected using molecular beam mass spectrometry coupled to electron ionization. The study belongs to the few investigations that determined spatially-resolved mole fraction profiles of intermediate species formed from $\text{Fe}(\text{CO})_5$. The database includes both atomic iron and oxidized iron-containing intermediates such as FeO_2 , FeOH , $\text{Fe}(\text{OH})_2$. The authors report that the underlying measurements were challenging due to the tendency of particle buildup on the nozzle and the very low concentrations of the iron-containing species. To the best of our knowledge, this study is the only one that successfully characterized gas-phase intermediates with more than five atoms in systems for iron oxide nanoparticle flame synthesis. Smaller intermediates like Fe and FeO can be detected by optical methods. In several studies [57, 221] the initial reaction steps of $\text{Fe}(\text{CO})_5$ and the formation of FeO in a laminar low-pressure flame is investigated by laser spectroscopy and the formation of condensed phase using a particle mass spectrometer (PMS) and a quartz microbalance. They showed a transient particle growth of atomic iron particles in the cold part of the flame followed by a second zone of particle formation at a later stage of the flame. Kluge et al. [57] conclude that Fe and FeO only contribute to the particle forming zone at an early stage of the flame, while particle growth further downstream in the synthesis flame is probably due to molecules such as FeOOH and $\text{Fe}(\text{OH})_2$. Wen et al. [220] showed with aid of a thermodynamic analysis and equilibrium calculations that iron oxides (FeO and Fe_2O_3) and iron hydroxides ($\text{Fe}(\text{OH})_2$ and $\text{Fe}(\text{OH})_3$) are relevant precursors for particle formation in flames. Kluge et al. [57] also observed an iron oxide formation pathway by means of laser spectroscopic measurements in a pilot plant nanoparticle synthesis reactor via the formation of primary iron clusters and the formation of iron oxide in a subsequent oxidation step under fuel-rich flame conditions. Wlokas et al. [52] proposed an updated reaction mechanism for iron oxide formation from $\text{Fe}(\text{CO})_5$ in laminar low-pressure hydrogen flames, which is based on the kinetic model of Rumminger et al. [50] and is evaluated with the results of Kluge et al. [57] and Feroughi et al. [53].

Molecular beam mass spectrometry is an established technique for the investigation of combustion processes [25, 26, 28, 29, 31, 82] and synthesis processes [21, 23, 57, 86, 216]. During the intrusive sampling process, condensing material can block the nozzle and reduce the sampling efficiency making molecules in a certain mass range hard to detect in synthesis flames. Sampling cations from flames improves sampling efficiency and allows the measurement of species, which often elude detection in neutral sampling mode. The study by Chen et al. [222] showed that only very few reactions lead to the formation of cations so that the relationship between cation and the corresponding neutral molecule are often well

defined. This observation is the basis of our hypothesis that ions can be used as indicators for their neutral counterparts. This study reports the mass spectrometric detection of decomposition products of $\text{Fe}(\text{CO})_5$ and charged iron-containing intermediates in synthesis flames and compares the results to simulations.

10.3 Experiment and flame conditions

10.3.1 Flame conditions

Experiments are carried out with photoionization (PI) and electron ionization (EI) molecular beam mass spectrometry in Berkeley and in Duisburg, respectively. The flame conditions of the investigated H_2/O_2 or $\text{H}_2/\text{C}_2\text{H}_4/\text{O}_2$ flames are shown in Table 10-1. They were chosen to be similar to the work of Kluge et al. [57] to facilitate comparison and discussion.

Table 10-1. Flame conditions in standard cubic centimeter per minute (sccm).

Flame	ϕ	P / mbar	H_2 / sccm	O_2 / sccm	Ar / sccm	C_2H_4 / sccm	$\text{Fe}(\text{CO})_5$ / ppm
A	0.5	33.3	1000	1000	2000	-	0
B	0.5	33.3	1000	1000	2000	-	200
C	0.6	120	545	455	1000	25	0
D	0.6	120	545	455	1000	25	300

For flame B, the precursor concentration was set by creating a mixture of 200 ppm of $\text{Fe}(\text{CO})_5$ in argon in a 0.05 m^3 stainless steel vessel with an accuracy of $\pm 5\%$. In flame D, liquid $\text{Fe}(\text{CO})_5$ was metered with a syringe pump with an accuracy of $\pm 2\%$ of the delivered volume and was evaporated. Schematics of both precursor delivery systems are shown in detail in the supplementary material Figure E-4 (see appendix E). The argon flow in flame B and D carries the gaseous $\text{Fe}(\text{CO})_5$ and is mixed with the hydrogen and oxygen before the combustion synthesis. Calibrated mass flow controllers regulate the gas flows with an accuracy of $\pm 5\%$. Direct calibration measurements of flame species (H_2 , O_2 , C_2H_4 , CO , CO_2) are performed under the same instrumental settings as the measurements. For H_2O the elemental balance was used for determination of the mole fraction. In accord with previous work, e.g. Kasper et al. [24], the uncertainties of all major species mole fractions were within 20 %.

10.3.2 Photoionization molecular beam mass spectrometry (PI-MBMS)

Flame structures including major flame radicals, e.g., O, OH, main species and $\text{Fe}(\text{CO})_5$ from flame A and B are analyzed using the flame-sampling photoionization MBMS instrument at the Chemical Dynamics beamline of the Advanced Light Source in Berkeley, USA. A schematic of the sampling interface attached to the linear time-of-flight mass

spectrometer system coupled to synchrotron photoionization (PI) is shown in Figure 10-1a and specifics of the instrument are detailed in Refs. [107, 223]. In this experiment, a McKenna burner with a water-cooled steel burner matrix with a diameter of 60 mm is used. The burner is arranged in a horizontal flow direction. A molecular beam is formed by expanding the flame gases through an 80- μm quartz probe and a 2-mm skimmer located 23 mm downstream of the probe. The sampling probe is made of quartz, which reduces catalytic effects regarding the recombination of highly reactive species (e.g., radicals) and improves their detection. The pressures in the two expansion stages are 1×10^{-4} and 1×10^{-6} mbar, respectively. The rapid pressure drop effectively quenches reactions between neutral species. The energy of the vacuum ultraviolet (VUV) radiation can be precisely tuned between 7.8–17 eV to minimize fragmentation during photoionization.

Fragmentation during the ionization of molecules with excess photon energy often produces species with the same mass-to-charge ratios as those that naturally occur in flames (see Figure E-1 in appendix E). For this reason, it is important to avoid fragmentation and to ionize the species with photon energies below the fragmentation energy of the parent ion. For iron pentacarbonyl $\text{Fe}(\text{CO})_5$ and its decomposition products, an energy above the fragmentation threshold needs to be used due to lack of sensitivity at lower photon energies. The measured fragmentation pattern of $\text{Fe}(\text{CO})_5$ has been taken into account in the analysis of the profiles of the fragment ions. Measured and estimated photoionization cross-sections of commonly used components like H_2 [224, 225], O_2 [226], Ar [227], H_2O [228], Kr [227], Xe [227], CH_4 [229], C_2H_2 [230], CO [231], CO_2 [232] and well-studied intermediates (O, [233] OH [234]) are taken from the literature. The ionization cross sections are needed to quantify the signals for the mass-to-charge ratios.

TOF-spectra are recorded at various locations in the flame with this setup. Each peak in the TOF-spectra was automatically fitted by a Gaussian profile. Using a cold gas flow of a commercial mixture with a known composition of gaseous components (hydrogen, methane, acetylene, carbon monoxide, carbon dioxide, krypton, xenon, argon) one can derive both a calibration for the conversion between time-of-flight and respective mass-to-charge ratio and the mass discrimination factor of the setup. The latter accounts for the depletion of lighter species compared to heavier components due to pressure diffusion and Mach-number focusing during the formation of the molecular beam [223]. The area of the fit was plotted either against the height above the burner (HAB) or the energy of the photons. Data evaluation is described in more detail in the study of Schenk et al. [235].

10.3.3 Electron ionization molecular beam mass spectrometry (EI-MBMS)

Samples from flames C and D are analyzed by a molecular beam mass spectrometer system combined with electron ionization (EI). Data evaluation and the setup are described in several studies of Karakaya et al. [86, 236]. Schematics of the experimental sampling setup are shown in Figure 10-1a.

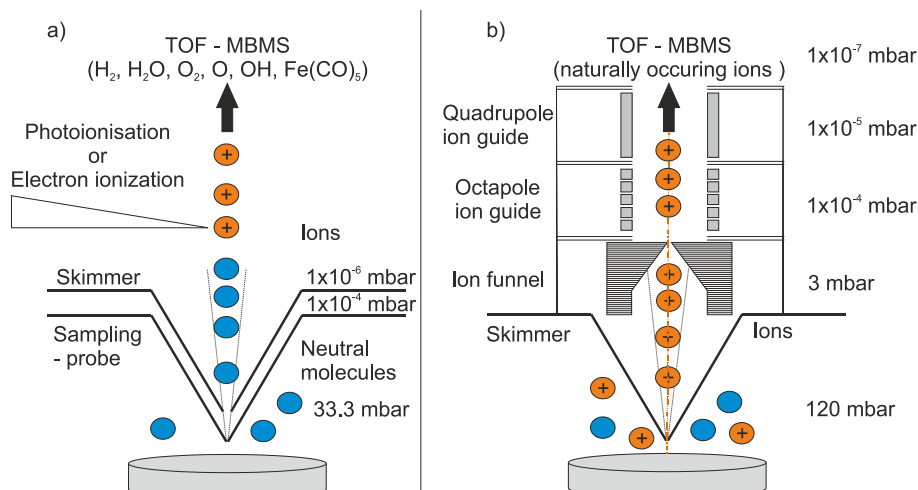


Figure 10-1. Schematics of the gas/particle inlet systems for a) PI-MBMS (experiment 1), EI-MBMS (experiment 2) and b) ion sampling (experiment 3).

The flame is stabilized on a similar burner as in the work of Kluge et al. [57]. This burner is water-cooled and has a burner matrix with a diameter of 36 mm. It is arranged in upwards flow direction. The burner position can be changed in upwards flow direction relative to the sampling probe between $HAB = 0\text{--}100$ mm (HAB , height above burner) with an accuracy of ± 0.01 mm. The pressure in the burner chamber was regulated with a throttle valve to 120 mbar with an accuracy of ± 0.1 %. A sample from the flame is extracted through a quartz probe from the flame with a pressure drop from 120 mbar to 10^{-3} mbar. Here, the diameter of the quartz probe was 90 μm . The core of the molecular beam is extracted by a skimmer with an orifice diameter of 1.2 mm and guided into the ionization chamber of the orthogonal time-of-flight mass spectrometer. As a compromise between good signal-to-noise and short acquisition times, the nominal kinetic energy of the electrons is selected to be 27 eV. 2×10^6 spectra were averaged at each point to determine the concentration of the major gaseous product species (H_2 , C_2H_4 , O_2 , H_2O , CO_2 , CO). For these conditions, each integrated mass peak in the accumulated spectra is proportional to the mole fraction of the respective species in the gas sample weighted by the ionization efficiency of the substance. Time-of-flight (TOF) values are converted to mass-to-charge ratio (m/z) by fitting a quadratic equation to known tuples of TOF and m/z . The orthogonal TOF mass analyzer has a resolution of $m/\Delta m = 3000$ at $m/z = 28$, which is useful for a precise mass determination and separation of peaks with near-identical m/z .

10.3.4 Ion sampling

Figure 10-1b shows the inlet system used for the measurement of ions. The aim of the ion sampling measurements is to identify iron-containing intermediates which elude detection in the previously described experiments, e.g., due to the fragmentation tendency or condensation on the sampling-probe. Quantification of the ion signals is in principle possible using a Faraday cup to measure charge behind the sampling probe and then calculate mole fractions from the sampling rate through the sampling-probe. The mole fractions of ionic species cannot be related to simulations of the flames because they are not included in most chemical reaction mechanisms. Instead, this work focusses on likely formation pathways of

these ions in the flames and what can be deduced from the ion signal profiles about the particle or cluster formation process.

Since ion formation in hydrogen/oxygen flames is limited [61, 237] ethene has been added to the flames investigated here to enhance ion formation. Decomposition of ethene to yield CH radicals initiates the reaction sequence of ion formation. These CH radicals react with O and generate the first chemi-ion CHO^+ by charge separation according to $\text{CH} + \text{O} \rightarrow \text{CHO}^+ + \text{e}^-$ (R 10-1). Water can react with CHO^+ to form H_3O^+ by a proton-transfer reaction according to $\text{CHO}^+ + \text{H}_2\text{O} \leftrightarrow \text{H}_3\text{O}^+ + \text{CO}$ (R 10-2). In order to detect ions, we used a novel ion-sampling system (Figure 10-1b) that is coupled to the same orthogonal time-of-flight mass spectrometer described above for the EI-MBMS system. This setup has already been used to identify species composition in a joint study with Alquaity et al. [30]. The ions in the flame are sampled directly by a metal (Hastelloy) sampling probe with an orifice diameter of 550 μm , by applying a 300 V positive potential to the probe. To avoid an inhomogeneous electrical field between burner and sampling probe the same potential (300 V) is applied to the burner. The pressure in the burner chamber is kept at 120 mbar. The pressure is reduced in three differentially pumped vacuum stages. During operation a typical pressure in the first stage is 3 mbar, 1×10^{-4} mbar in the second stage and 1×10^{-5} mbar in the third stage. The orthogonal TOF mass analyzer is kept at 1×10^{-7} mbar.

Ion transmission in the first stage is ensured by a low-capacitance pcb (printed circuit board) ion funnel to which a DC potential gradient is applied to transport the ions in the flow direction of the ion funnel. The second stage is equipped with a segmented octapole ion guide and in the third stage a quadrupole ion guide is used to reduce the kinetic energy of the ions. Finally, the ions pass through several apertures and beam forming Einzel lenses into the extraction region of the orthogonal TOF. Further analysis proceeds as described above. 5×10^6 spectra were averaged to obtain mass spectra of the naturally occurring ions with good signal-to-noise ratios. Compared to the EI and PI experiments, the sampling probe has a larger diameter so that it clogs less, but the larger diameter results in a reduced spatial resolution of the measurements. In addition, higher Mach numbers are obtained in the ion sampling system leading to more cooling and better parallelization of the molecular beam. Due to the high background pressure in the second stage, gases pass through the shock structure of the Mach disk while in the EI and PI experiments, the skimmer is placed in front of the Mach disk in the zone of silence. We expect that in agreement with previous studies on MBMS systems, reactions are quenched in both systems during the molecular beam expansion but that in the ion sampling interface an order of magnitude more collisions occur and that the gases are heated again. The appearance of water clusters (Figure 10-5: $\text{H}_3\text{O}^+(\text{H}_2\text{O})$, $\text{H}_3\text{O}^+(\text{H}_2\text{O})_2$, $\text{H}_3\text{O}^+(\text{H}_2\text{O})_3$, (R 10-3)) is an indication that very fast ion–molecule reactions with reaction rates close to the collision limit are typically not quenched in most molecular beam ion extractions [30, 61, 205, 238] even in systems with lower pressures in the second vacuum stage than reported here. These clusters also occur in other ion sampling systems, e.g., from electro-spray sources [239] or atmospheric pressure ionization sources [240]. The water clusters are typically stable at low temperatures and low pressures [241]. Both effects cannot be avoided and need to be considered when interpreting the data.

10.3.5 Flame temperature

Flame temperature measurements are obtained with a silicon dioxide coated thermocouple (type R) with a thickness of 160 μm . A radiation correction for the heat losses of the thermocouple is performed by the method described in the study of [93]. The uncertainty of the temperature measurement is evaluated to be ± 100 K. The temperature profile used in the simulation was generated by adjusting the exhaust gas temperature of the temperature dependent sampling function obtained in the mass spectrometric measurements to the exhaust gas temperatures measured by the thermocouple. This procedure takes the influence of the sampling probe on the flame temperature into account and is well described in previous publications [82, 146].

10.4 Numerical setup

The precursor decomposition and the flame structures in this study are simulated with a merged reaction model consisting of the reaction model for $\text{Fe}(\text{CO})_5$ which was published in the studies of Wlokas et al. [52] and Feroughi et al. [53], and second the GRI-Mech 3.0 by [242] for flame species. Both kinetic reaction mechanisms are used without any modification. ChemkinPro 19.2 [186] is used to simulate the one-dimensional flames with the measured temperature profiles as input.

10.5 Results and discussion

10.5.1 Influence of $\text{Fe}(\text{CO})_5$ on temperature, and product and radical species

The addition of $\text{Fe}(\text{CO})_5$ changes the temperature and main species profiles of the flames and also has an impact on the concentrations of important flame radicals, e.g., O, OH, and H. These findings agree with other studies [21, 23, 54, 56] and are discussed below.

10.5.1.1 Temperature

The measured temperature profiles of the neat flame A and $\text{Fe}(\text{CO})_5$ doped flame B are shown in Figure 10-2. The temperature close to the burner surface is between 400 and 450 K for both flames followed by a sharp increase in temperature as the height above the burner (HAB) increases. The maximum temperature is around 1300 K for the neat flame. Doping the flame with 200 ppm $\text{Fe}(\text{CO})_5$ increases the maximum temperature to 1550 K. The exhaust gas temperature was measured to be around 1300 K in both cases. The increase of temperature in the flame front near the burner is caused by a promotion of heat-releasing reactions, while in the exhaust gas temperatures drop faster as radicals are removed by catalytic cycles involving iron [51, 52]. Both effects can be traced in the temperature profiles in these flames.

10.5.1.2 Major flame species

Datasets of flame A and B will be presented here because it was possible to measure the radicals O and OH using the PI-MBMS system. Main species mole fraction profiles for the neat (empty symbols, dashed lines) flame A and the doped (filled symbols, solid lines) flame B are shown in Figure 10-2. Symbols indicate the experimental values and lines the simulations. The profiles of the stable components Ar, H₂, O₂, and H₂O are nearly the same for both flames. H₂ as the fuel is consumed within the first 10 mm. The O₂ mole fraction profile reaches its final value at around HAB = 10 mm. At the same position, the final mole fraction of the only product H₂O is also reached indicating complete reaction within the first 10 mm of the neat flame. Despite the difference in flame temperature, the main species mole fraction profiles agree almost quantitatively in the experiments and the simulations.

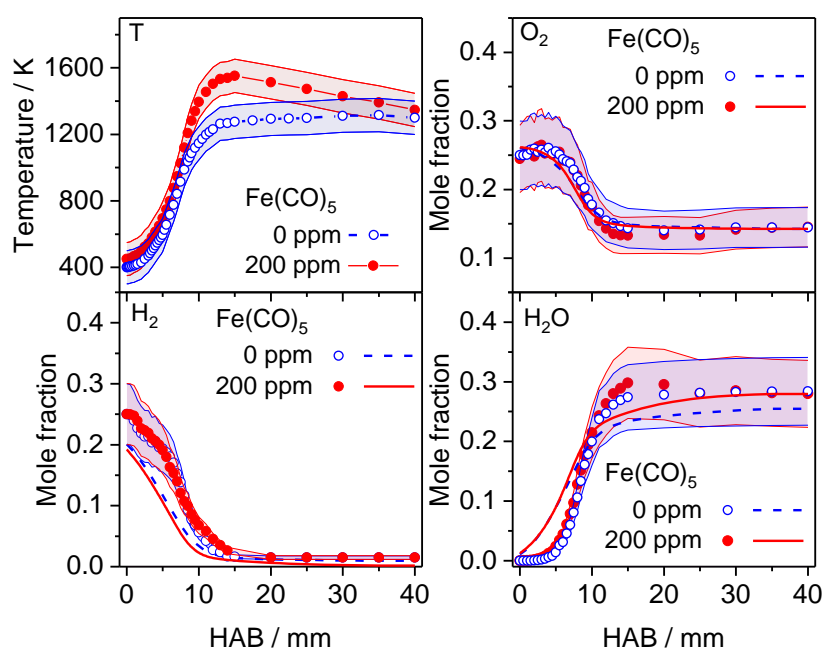


Figure 10-2. Mole fraction profiles of major species for the neat flame A (dashed lines, 0 ppm Fe(CO)₅) and doped flame B (solid lines, 200 ppm Fe(CO)₅) analyzed with PI-MBMS (experiment 1). Measured temperature profiles of flames A, B. Empty symbols and dashed lines indicates neat flame and filled symbols and filled lines indicates doped flame. The uncertainty of the measurement is indicated by the shaded area between the thin lines for each experimental mole fraction profile.

10.5.1.3 Radical species

For flames A and B it was possible to measure the mole fraction profiles of the O and OH radicals. The H radical could not be detected in these measurements because the instrument settings were tuned for the expected iron-containing species at higher m/z . The OH and O mole fraction profiles in Figure 10-3 corroborate the simulation results with the mechanism of [52]. The qualitative agreement between the measured and the simulated profiles is acceptable. The main difference between the neat and the doped flame is that the mole fractions of the O radicals are below the detection limit in the doped flame indicating reactions with iron-containing species acting as a sink for the flame radicals. Also, the mole

fraction of the OH radicals is smaller in the $\text{Fe}(\text{CO})_5$ -doped flame at higher heights above burner.

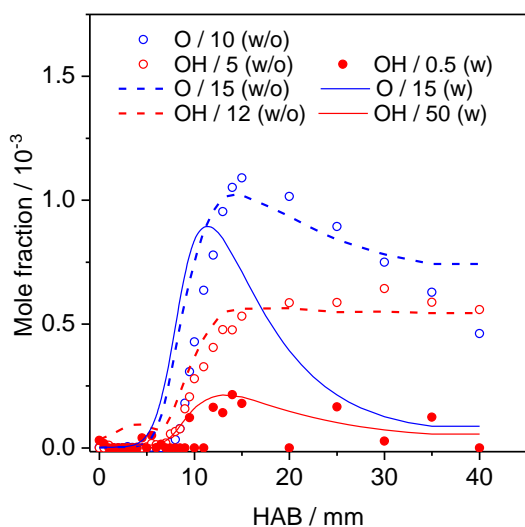


Figure 10-3. Mole fraction profiles of flame radicals O and OH in the neat flame A (dashed lines, empty symbols) without (w/o) $\text{Fe}(\text{CO})_5$ doping and flame B (filled lines, symbols) with (w) $\text{Fe}(\text{CO})_5$ doping analyzed with PI-MBMS (experiment 1).

Quantitative deviations between experiments and simulations can be attributed to sampling artifacts [173], e.g. cooling of the flame by the sampling probe and the distortion of radical diffusion. In particular, for the OH radical it could be shown in a similar flame-sampling molecular beam experiment that the raw signals of the OH radical obtained from the measurement are approximately a factor of 10 too small because the OH radicals collide with bath gas during sampling and do not survive these collisions [84]. These sampling losses are often compensated in the data analysis by determining the radical mole fractions of O, H, and OH from partial-equilibrium calculations in the exhaust gas [107, 243] rather than the use of uncertain ionization cross-sections. Given that the effect of the iron-containing species on the reactions in the recombination zone of the doped flame is not as well characterized as the equilibrating reactions in neat H_2/O_2 flames this procedure is not applied here.

In summary, the change of the flame structure induced by adding $\text{Fe}(\text{CO})_5$ can be explained due to the involvement of iron species that most likely participate in catalytic radical recombination cycles [51] between the metal oxides and hydroxides and the flame radicals such as H, O, and OH. These reactions lead to lower radical mole fractions at all positions in the flames investigated here.

10.5.2 Thermal decomposition of $\text{Fe}(\text{CO})_5$

Figure 10-4 shows the mole fraction profiles of iron pentacarbonyl and its decomposition products $\text{Fe}(\text{CO})_4$, $\text{Fe}(\text{CO})_3$ and $\text{Fe}(\text{CO})_2$ in flame B.

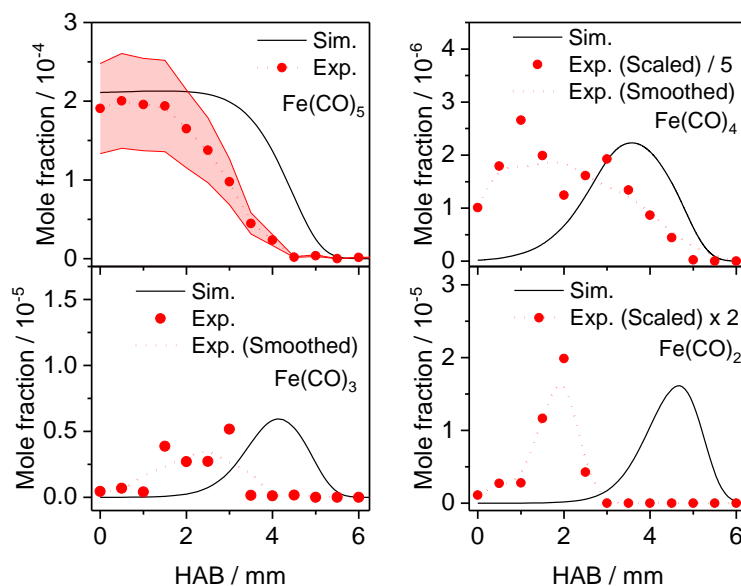


Figure 10-4. Measured (symbols) and simulated (lines) mole fraction profiles of the decomposition products of $\text{Fe}(\text{CO})_5$ in flame B (experiment 1). Experimental signal intensity profiles of the decomposition products $\text{Fe}(\text{CO})_n$ with $n = 2 - 4$ are scaled to the simulation.

The measured mole fraction profiles are corrected for fragmentation. Symbols represent the measured data while the lines are simulation results. The simulated species mole fraction profiles of the decomposition products of $\text{Fe}(\text{CO})_5$ in Figure 10-4 seem to be shifted to higher heights above burner. The axial deviation between experiment and simulation is in line with the findings of [173], who report in their numerical study that for very small distances between sampling probe and burner there can be a compression of the flame regions in the direction of the burner. Another explanation could be that the reaction rates for the initial decomposition step do not capture the reactions in the flame correctly. Species mole fraction profiles of these decomposition products have not been available for model development previously. $\text{Fe}(\text{CO})_4$ as the first decomposition product has a maximum simulated mole fraction of 2.23×10^{-6} at 3.5 mm HAB. Downstream, the simulation shows that $\text{Fe}(\text{CO})_3$ and $\text{Fe}(\text{CO})_2$ have a mole fraction of 5.94×10^{-6} at 4.125 mm and a mole fraction of 1.61×10^{-5} at 4.75 mm, respectively. The mole fraction of $\text{Fe}(\text{CO})_5$ in the measurements is based on a measured calibration factor and reliable within 20%. The mole fractions of the decomposition products could not be calibrated. The quantification is based on the relative signal strength of $\text{Fe}(\text{CO})_4$ - $\text{Fe}(\text{CO})_2$ and the assumption that only these species contain iron, so that the iron balance can be used to convert the relative signals to mole fractions. The fragmentation of $\text{Fe}(\text{CO})_5$ during ionization is rather high in these measurements because a large photon energy of 11 eV was used. Using photon energies lower than 11 eV to reduce fragmentation of $\text{Fe}(\text{CO})_5$ is crucial but reduces photon flux at the ALS compared to higher photon energies, so that the detection limit is reached. Most importantly, the sampling probe slowly clogged over the 9-hour duration of the experiment. This fact illustrates one of the greatest challenges in the investigation of particle-laden reacting flows: While typically signal-to-noise ratios can be improved by extensive averaging (limited only by the availability of beam-time at synchrotron light sources), the measurement time in particle-laden flows is restricted by the time it takes for the sampling probe to clog.

10.5.3 Cationic flame structure

Figure 10-5 gives an overview of the charged species up to $m/z = 400$ that are formed in flame D with increasing height above the burner between $HAB = 1$ and 32.5 mm. The charged species can be classified into several groups, e.g., H_3O^+ , hydrocarbon ions from the hydrocarbon combustion of added C_2H_4 , iron hydroxide and iron oxides with one iron atom, and iron hydroxides and iron oxide ions with more than one Fe atom. Each group is discussed in more detail.

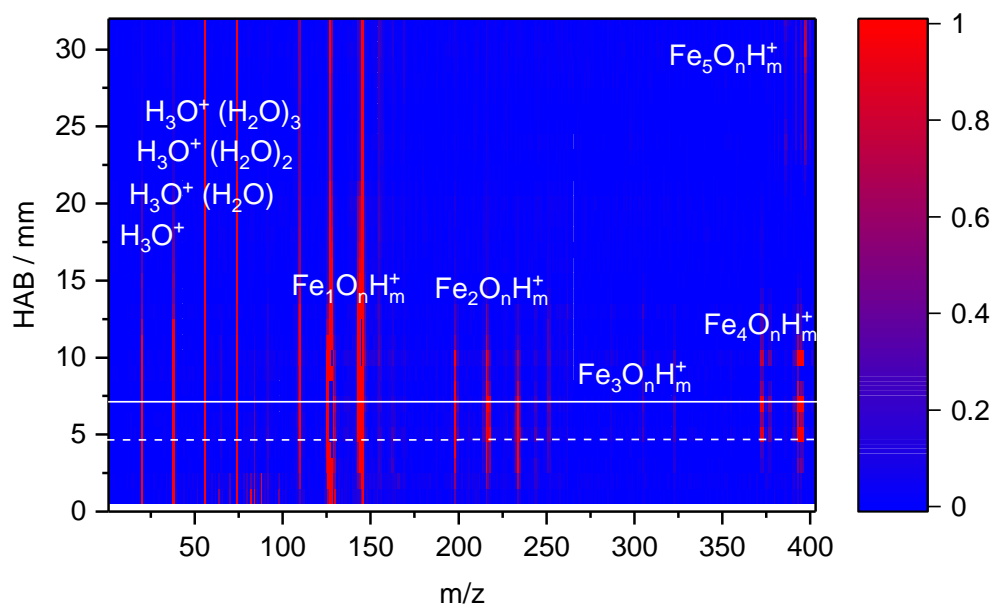


Figure 10-5. Ions in flame D measured with the ion sampling system. Iron hydroxide or oxide structures with $n, m \neq 0$ appear. The dashed line indicates the end of the flame front in the $C_2H_4/H_2/O_2/Ar$ -flames. The filled line indicates the maximum concentration of the iron-containing cations.

The comparison of the results of the PI- and EI-experiments to simulations reveals that the decomposition of $Fe(CO)_5$ and the formation of iron intermediates requires speciation data to determine and improve the reaction sequences for the formation of relevant key intermediates in synthesis flames. If the appearance of cationic iron-containing intermediates can be linked to neutral iron-containing components by elucidating the formation reactions, they can provide information on missing key intermediates that often elude detection in neutral mode.

The initial requirement is that the iron-containing ions are detected and their formation reactions deduced – this task is attempted below by first screening the much better investigated ion formation reactions of hydrocarbons [222] and then discussing likely formation reactions of iron-containing ions.

10.5.3.1 H₃O⁺ and hydrocarbon ions

The mole fraction profiles of neutral species in this section were measured with the EI-MBMS in flames C and D. The cation ion signal profiles were measured with the ion sampling interface and can be interpreted as relative concentration profiles. In the C₂H₄/H₂/O₂/Ar-flames C and D H₃O⁺ is probably formed according to $\text{CHO}^+ + \text{H}_2\text{O} \leftrightarrow \text{H}_3\text{O}^+ + \text{CO}$. The CHO⁺ could not be detected. The steep slope of the H₃O⁺ ion signal profile with its maximum at HAB = 2 mm coincides with the steeply increasing slope in the water mole fraction profile but the H₃O⁺ ion signal profile exhibits a maximum at HAB = 3 mm and then decreases as shown in Figure 10-6a. The continuous decrease in the H₃O⁺ ion signal profile is most likely caused by proton transfer to other species in the exhaust gas and by recombination reactions. The ion signal profiles of H₃O⁺ and its hydrates are lumped. The hydrates with chemical structures (H₃O)⁺(H₂O)_n with n = 1, 2, 3 and m/z = 37, m/z = 55, m/z = 73 form in the molecular beam expansion in reactions with water according to $\text{H}_3\text{O}^+ (\text{H}_2\text{O})_{n-1} + \text{H}_2\text{O} \leftrightarrow \text{H}_3\text{O}^+(\text{H}_2\text{O})_n$. These water clusters have been observed in several studies [30, 222, 244] and the stability of the water clusters, the equilibrium constants [241] for the reactions and the rate constants have been investigated in some detail [245]. From these studies it follows that the formation of the water hydrates does not occur at flame temperatures and that the equilibrium favors the formation of larger hydrates only at low temperatures and small partial pressures of water, e.g., at the conditions encountered by the gas sample during the molecular beam expansion. For a systematic evaluation of the mass spectrometric data, the characteristic hydrate formation during the sampling of ions needs to be considered in detail because it may occur for all ions and has an impact on the observed mass spectra.

H₃O⁺ can transfer a proton to all species with larger proton affinities in the flame, e.g., almost all hydrocarbons. The dominant oxygenated ions in decreasing order of signal strength in flame C are: CH₅O⁺ (m/z = 33 + 51 + 69 + 87), C₂H₅O⁺ (m/z = 45 + 63 + 81 + 99), C₂H₃O⁺ (m/z = 43 + 61 + 79 + 97). All of these ions are formed in the reaction zones of the flame C and D and also form artificial hydrates similar to H₃O⁺ during sampling. The values in brackets correspond to the mass-to-charge ratios of the core ion species and their hydrates. The evaluation revealed that the ion signal profile shapes of H₃O⁺ and its water clusters and the ion signal profiles of the above mentioned hydrocarbon ions and their hydrates are similar and the second hydrate (H₃O)⁺(H₂O)₂ is the dominant water cluster in the series of hydrates of H₃O⁺. For flame D, the ion signal profiles of the most abundant hydrocarbon ions and the mole fraction profiles of their neutral compounds from the simulations, e.g., methanol for the CH₅O⁺ ion and CH₂CO for the ion C₂H₃O⁺ are shown in Figure 10-6c. At flame conditions, proton transfer from H₃O⁺ to the hydrocarbons is the most likely formation route of these ions in agreement with the proton affinities of all compounds and previous work, e.g., the recent study of Chen et al [222]. C₂H₃O⁺ is formed by the protonation of CH₂CO according to $\text{H}_3\text{O}^+ + \text{CH}_2\text{CO} \leftrightarrow \text{C}_2\text{H}_3\text{O}^+ + \text{H}_2\text{O}$ (R 10-4), C₂H₅O⁺ is formed by the protonation of C₂H₄O according to $\text{H}_3\text{O}^+ + \text{C}_2\text{H}_4\text{O} \leftrightarrow \text{C}_2\text{H}_5\text{O}^+ + \text{H}_2\text{O}$ (R 10-5), and CH₅O⁺ is formed by the protonation of methanol CH₄O according to $\text{H}_3\text{O}^+ + \text{CH}_3\text{OH} \leftrightarrow \text{CH}_5\text{O}^+ + \text{H}_2\text{O}$ (R 10-6). Proton transfer may also occur from hydrocarbon species with lower proton affinities than the core ions.

From Figure 10-6c it is evident that the mole fraction profiles of the corresponding neutral species peak closer to the burner than the respective ion signal profiles and the ion signal profiles are much broader. This observation can be explained in two ways. First, the simulation does not capture the perturbation of the flame by the sampling probe. This effect is also evident from the larger discrepancies between the experimental data of the major species mole fraction profiles and the simulation in Figure 10-2 and the comparison of measured neutral species mole fraction profiles and simulations in Figure 10-6b. Unfortunately, the perturbation can only tentatively be included in an one-dimensional simulation by a measured temperature profile [82, 83] and cannot be modeled correctly. The orifice size of the sampling probe influences the deviations between simulated and measured mole fraction profiles (e.g., [82, 246]). Consequently, the smaller deviations in Figure 10-6b compared to Figure 10-6c can be explained partly by the smaller orifice size used in the EI-MBMS measurements than in the ion sampling measurements. Second, the proton transfers between H_3O^+ and the oxygenated hydrocarbon species is most effective when both species are present in large quantities, e.g., when the overlap between the H_3O^+ ion signal profile and the hydrocarbon ion signal profile is large. This effect can also lead to a broadening of the ion signal profiles. In contrast to H_3O^+ , the signals of the hydrocarbon ions disappear around $\text{HAB} = 4$ mm and it can be concluded that they will not make a significant contribution to the formation of iron-containing ions further downstream.

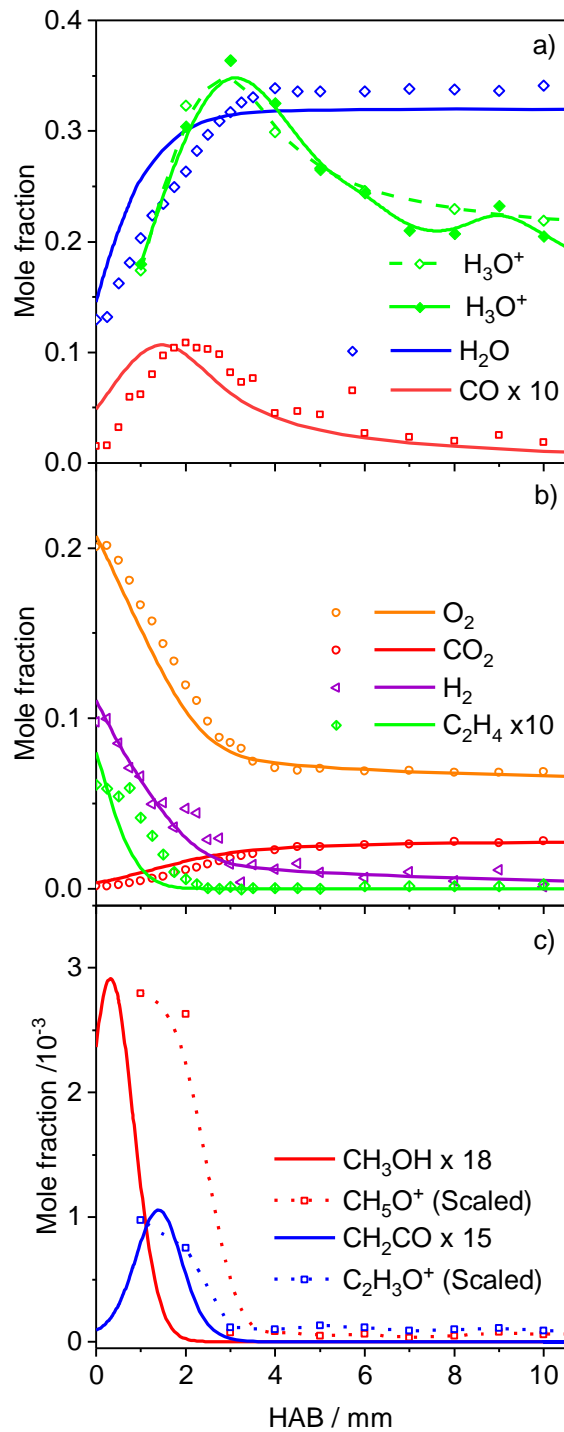


Figure 10-6. Species mole fraction profiles of a) CO, H₂O in flame C and H₃O⁺ in flame C and D, b) C₂H₄, H₂, O₂, CO₂ in flame C, c) CH₅O⁺, C₂H₃O⁺ in flame D. Points are experimental data (experiment 2 and 3) and solid lines are simulations.

10.5.3.2 Iron-containing ions

The identification of iron-containing ions is accomplished by comparing the mass-to-charge ratios (m/z) from the flame with the exact theoretical mass of potentially present species containing the elements Fe, O, H and C. Additionally, the iron has a characteristic four-peak isotope pattern consisting of ^{54}Fe : ^{56}Fe : ^{57}Fe : ^{58}Fe with abundances of 5.82 %: 91.18 %: 2.1 %: 0.28 % [247], respectively. The isotope pattern is used to identify signals of iron-containing species in the flames (Figure E-2 in appendix E). Isomeric species cannot be distinguished by the m/z ratios so that for most observed signals, assignment to several isomers is possible. In particular, the signals of ions formed in the flame can overlap with strong signals resulting from the formation of hydrates during molecular beam sampling. Because of these complications, only the most abundant ions are discussed here and only a suggestion of the most likely assignments are given. Table 10-2 contains a list of the cationic iron-containing species with increasing nominal mass from $m/z = 19$, the lowest detected signal, up to $m/z = 145$. Signal intensity ratios from intermediate iron-containing ions relative to H_3O^+ at the point of maximum iron species signal in flame D at HAB = 7 are also listed. The most abundant non-iron-containing cation is H_3O^+ ($m/z = 19$). The original ion at the core of a water cluster will be called core ion in the following. Ions with one iron atom up to $m/z = 145$ were found with the highest intensity in the reaction zone at HAB = 7 mm, while larger iron-containing ions were found in the post-flame zone at HAB = 28 mm. The reasons for the tentative assignment of species will be discussed in the following section.

10.5.3.3 Ion signal profiles of major iron-containing hydroxides

Figure 10-7 shows expanded mass spectra in the reaction zone at HAB = 7 mm where the iron-containing cations reach their maximum ion signal. It is likely that iron-containing ions are formed by proton-transfer reactions in analogy to the formation of oxygenated hydrocarbon ions, since the proton affinities (PA) of iron-containing compounds, e.g., $\text{PA}(\text{Fe}(\text{CO})_5) = 833 \text{ kJ/mol}$ [248], $\text{PA}(\text{Fe}) = 761 \text{ kJ/mol}$ [249], are greater than the proton affinity of water $\text{PA}(\text{H}_2\text{O}) = 691 \text{ kJ/mol}$ [248]. Iron-containing species have also larger proton affinities than most oxygenated species, e.g., $\text{PA}(\text{CH}_4\text{O}) = 754.3 \text{ kJ/mol}$ [248], $\text{PA}(\text{CH}_3\text{CHO}) = 768.5 \text{ kJ/mol}$ [248]. No protonation of $\text{Fe}(\text{CO})_{0-5}$ was observed in the mass spectra (Figure 10-7). In preliminary experiments with very high precursor loading, cationic atomic Fe^+ was observed. A systematic study under those conditions proved impossible and in the flame D, Fe^+ is most likely below the detection limit of the MBMS system. The artificial hydration of Fe^+ ($m/z = 56$) can be excluded, because $\text{Fe}^+(\text{H}_2\text{O})$ ($m/z = 74$) is not observed in the mass spectra. The simulation of flame D predicted FeO and FeO_2 as intermediates of the oxidation of the precursor (Figure E-3 in appendix E). Signals of ions of these species are expected on $m/z = 72$ and 88, respectively, but do not appear in the spectra. According to the simulation, the expected mole fraction of FeO and FeO_2 are low, which might be the reason that the ions are not observed.

Table 10-2. Mass-to-charge ratios (m/z), empirical cation formula and possible structures of ions with $m/z \leq 145$ in flame D. The designation $\cdot(\text{H}_2\text{O})_n$ indicates a hydrate. Bold structures are suggested to be the dominant isomers. $[\text{S}_i/\text{S}_{\text{H}_3\text{O}^+}]$ ratios are calculated from integrated ion signal intensities at $\text{HAB} = 7$ mm. An ion signal ratio of zero indicates that the species is expected to be present but was not found in this experiment.

m/z	Empirical formula	Ion structural formulas	$[\text{S}_i/\text{S}_{\text{H}_3\text{O}^+}]$	Ref.
19	H_3O^+	H_3O^+	1	-
56	Fe^+	-	0	[250]
57	FeH^+	-	0	-
72	FeO^+	-	0	-
73	FeOH^+	FeO^+ , FeOH^+	≈ 0	-
74	FeOH_2^+	$(\text{FeOH})\text{H}^+$	0	[250]
88	FeO_2^+	FeO_2^+	0	-
89	FeO_2H^+	FeO_2H^+ , $\text{FeO}(\text{OH})^+$	0	-
90	FeO_2H_2^+	$\text{FeO}^+\cdot(\text{H}_2\text{O})$, $\text{FeO}(\text{OH})\text{H}^+$, $\text{Fe}(\text{OH})_2^+$	0.07	[250]
91	FeO_2H_3^+	$\text{FeOH}^+\cdot(\text{H}_2\text{O})$, $\text{Fe}(\text{OH})_2\text{H}^+$	0.08	[250]
107	FeO_3H_3^+	$\text{FeO}_2\text{H}^+\cdot(\text{H}_2\text{O})$, $\text{Fe}(\text{OH})_3^+$, $\text{FeO}(\text{OH})^+\cdot\text{H}_2\text{O}$, $^{54}\text{FeO}_3\text{H}_5^+$	0.05	[250]
108	FeO_3H_4^+	$\text{FeO}\cdot(\text{H}_2\text{O})_2$, $\text{FeO}(\text{OH})\text{H}^+\cdot\text{H}_2\text{O}$, $\text{Fe}(\text{OH})_3\text{H}^+$, $\text{Fe}(\text{OH})_2^+\cdot(\text{H}_2\text{O})$	0.37	[250]
109	FeO_3H_5^+	$\text{FeOH}^+\cdot(\text{H}_2\text{O})_2$, $\text{Fe}(\text{OH})_2\text{H}^+\cdot\text{H}_2\text{O}$	0.86	[250]
125	FeO_4H_5^+	$\text{FeO}_2\text{H}^+\cdot(\text{H}_2\text{O})_2$, $\text{Fe}(\text{OH})_4\text{H}^+$, $\text{FeO}(\text{OH})^+\cdot(\text{H}_2\text{O})_2$, $\text{Fe}(\text{OH})_3^+\cdot(\text{H}_2\text{O})$, $^{54}\text{FeO}_4\text{H}_7^+$	1.27	-
126	FeO_4H_6^+	$\text{FeO}\cdot(\text{H}_2\text{O})_3$, $\text{FeO}(\text{OH})\text{H}^+\cdot(\text{H}_2\text{O})_2$, $\text{Fe}(\text{OH})_3\text{H}^+\cdot\text{H}_2\text{O}^+$, $\text{Fe}(\text{OH})_2^+\cdot(\text{H}_2\text{O})_2$, $^{54}\text{FeO}_4\text{H}_8^+$	12.57	-
127	FeO_4H_7^+	$\text{FeOH}^+\cdot(\text{H}_2\text{O})_3$, $\text{Fe}(\text{OH})_2\text{H}^+\cdot(\text{H}_2\text{O})_2$, $^{54}\text{FeO}_4\text{H}_9^+$	16.07	-
143	FeO_5H_7^+	$\text{FeO}_2\text{H}^+\cdot(\text{H}_2\text{O})_3$, $\text{Fe}(\text{OH})_3^+\cdot(\text{H}_2\text{O})_2$, $\text{FeO}(\text{OH})^+\cdot(\text{H}_2\text{O})_3$, $^{54}\text{FeO}_5\text{H}_9^+$	1.52	-
144	FeO_5H_8^+	$\text{FeO}\cdot(\text{H}_2\text{O})_4$, $\text{FeO}(\text{OH})\text{H}^+\cdot(\text{H}_2\text{O})_3$, $\text{Fe}(\text{OH})_3\text{H}^+\cdot(\text{H}_2\text{O})_2$, $\text{Fe}(\text{OH})_2^+\cdot(\text{H}_2\text{O})_3$	6.04	-
145	FeO_5H_9^+	$\text{FeOH}^+\cdot(\text{H}_2\text{O})_4$, $\text{Fe}(\text{OH})_2\text{H}^+\cdot(\text{H}_2\text{O})_3$	3.17	-

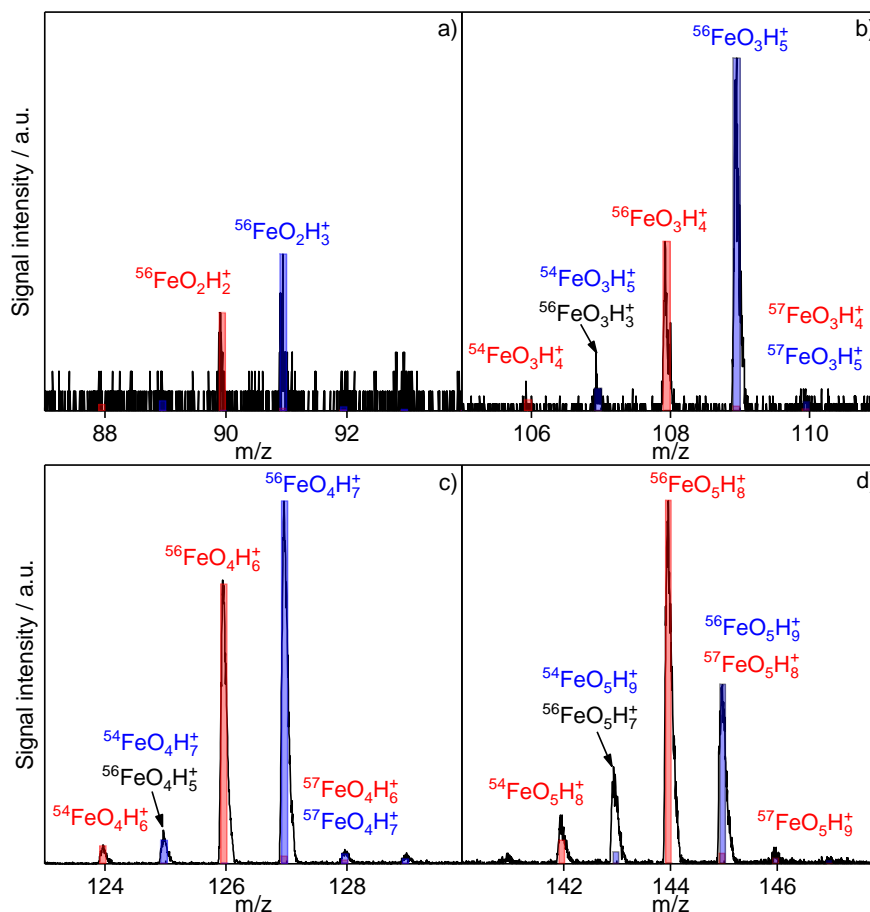
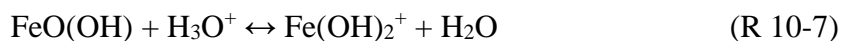


Figure 10-7. Expanded parts of the mass spectrum at HAB = 7 mm in Fe(CO)₅-doped C₂H₄/H₂/O₂/Ar-flames (flame D, experiment 3) show ions and the hydrate series. Red and blue bars indicate the isotopic pattern of iron with four stable isotopes ⁵⁴Fe, ⁵⁶Fe, ⁵⁷Fe, ⁵⁸Fe. Labels indicate species of the same series with the same core ion.

In Figure 10-7, the signals of the first iron-containing species with $m/z = 90$ (FeO₂H₂⁺) and $m/z = 91$ (FeO₂H₃⁺) are clearly visible. Since at smaller mass-to-charge ratios no ion signal for, e.g., FeO⁺, Fe(OH)⁺ were detected in significant amounts, we conclude that $m/z = 90$ (FeO₂H₂⁺) and $m/z = 91$ (FeO₂H₃⁺) do not arise as artifacts by hydration reactions. Both observed ion signals can result from either proton transfer or from charge transfer reactions. The formation of Fe(OH)₂⁺ from the neutral species included in the reaction mechanism is possible by proton transfer to FeO(OH) (R 10-7) or by charge transfer to Fe(OH)₂ (R 10-8):



If it is assumed that always both types of reaction occur, two additional ionic species are expected. FeO(OH)⁺ would be the product of a charge transfer reaction between FeO(OH) and H₃O⁺. A signal with $m/z = 89$, corresponding to FeO(OH)⁺ was not observed. The product of a proton transfer reaction between Fe(OH)₂ and H₃O⁺ would be Fe(OH)₂H⁺, so that this reaction could explain the signal on $m/z = 91$.

Both $m/z = 90$ (FeO_2H_2^+) and $m/z = 91$ (FeO_2H_3^+) are also reported in the study by Ham and McAllister [250] as a dominant cation species. Ham and McAllister discuss the probability of the reactions forming iron-containing ions based on their own measurements and the observations of Hayhurst and Telford [251], e.g., reactions (R 10-9) to (R 10-11). Hayhurst and Telford [251] discuss formation pathways of only neutral Fe atoms, FeOH and FeO in the formation of iron-containing ions, and neglect ion formation from all other iron-containing intermediates.

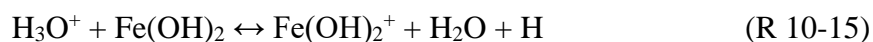
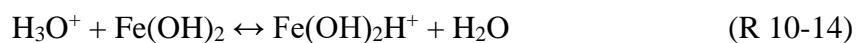


Because of the endothermicity, they exclude all reactions, which form an iron water cluster from consideration. According to Ham and McAllister [250] the charge transfer reaction (R 10-11) is endothermic for Fe but it is possible that it is driven towards the products by the exothermic recombination of the hydrogen atoms in the exhaust gas of the flame.

Hayhurst and Telford [251] determine the proton transfer reactions below to be the most important:



As discussed above, none of these intermediates are observed in flame D. The identical ion signal profiles of the ions $m/z = 90$ ($\text{Fe}(\text{OH})_2^+$) and $m/z = 91$ ($\text{Fe}(\text{OH})_2\text{H}^+$) shown in Figure 10-8 could be an indication that they originate from the same iron-containing neutral species in the flame. In this case, the proton-transfer reaction (R 10-14) and the charge-transfer reaction (R 10-15) would be responsible for the production of these ions.



This tentative mechanism of ion production agrees with the simulation of the neutral Fe-species in flame D. Here, the predicted mole fraction for $\text{Fe}(\text{OH})_2$ is about one order of magnitude higher than the mole fraction of $\text{FeO}(\text{OH})$, thus it seems permissible to neglect the formation of $\text{Fe}(\text{OH})_2^+$ from $\text{FeO}(\text{OH})$. The ratio of $\text{FeO}_2\text{H}_3^+/\text{FeO}_2\text{H}_2^+$ is around 1.3, which could indicate that in flame D the formation of ions of $\text{Fe}(\text{OH})_2$ by protonation reaction (R 10-14) is slightly higher than by charge exchange reaction (R 10-15).

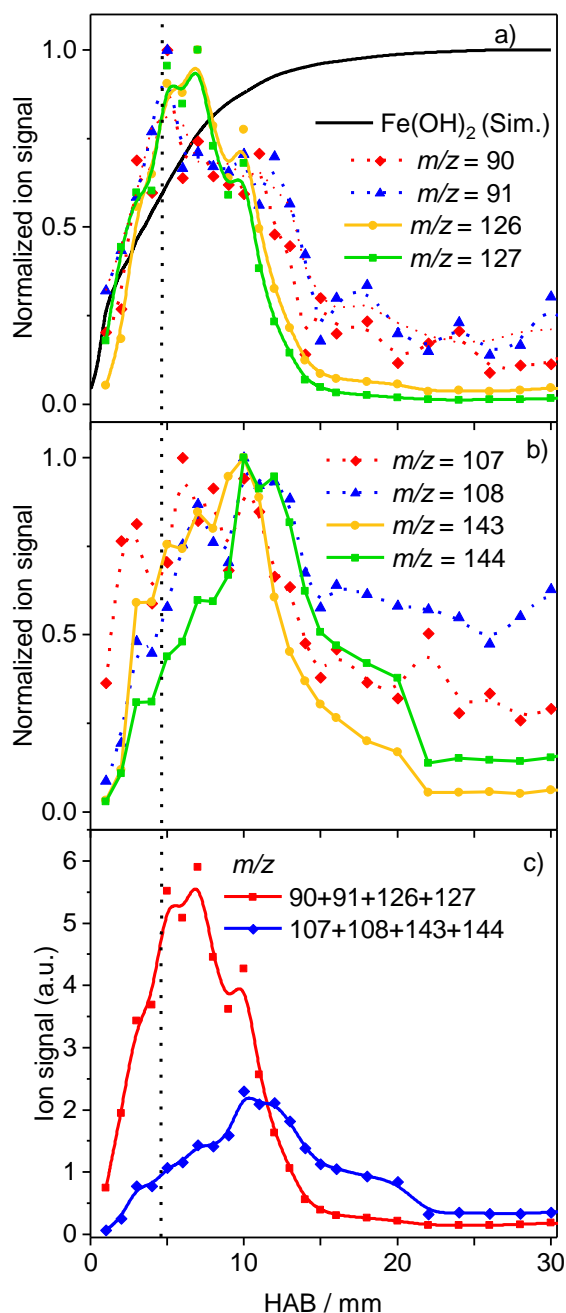
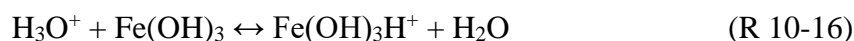


Figure 10-8. Ion signal profiles in $\text{Fe}(\text{CO})_5$ -doped $\text{C}_2\text{H}_4/\text{H}_2/\text{O}_2/\text{Ar}$ -flames (flame D, experiment 3) of a) $m/z = 90$ ($\text{Fe}(\text{OH})_2^+$) and $m/z = 91$ ($\text{Fe}(\text{OH})_2\text{H}^+$) and their sampling induced hydrates on $m/z = 126$ ($\text{Fe}(\text{OH})_2^+(\text{H}_2\text{O})_2$) and $m/z = 127$ ($\text{Fe}(\text{OH})_2\text{H}^+(\text{H}_2\text{O})_2$), b) on $m/z = 107$ ($\text{Fe}(\text{OH})_3^+$) and $m/z = 108$ ($\text{Fe}(\text{OH})_3\text{H}^+$) with the hydrates on $m/z = 143$ ($\text{Fe}(\text{OH})_3^+(\text{H}_2\text{O})_2$) and $m/z = 144$ ($\text{Fe}(\text{OH})_3\text{H}^+(\text{H}_2\text{O})_2$), c) spatial variation of the oxidation states of iron species in flame D. Vertical dashed line indicates the end of the flame front.

Similar to H_3O^+ , $\text{Fe}(\text{OH})_2^+$ and $\text{Fe}(\text{OH})_2\text{H}^+$ appear to function as core ions for the formation of water clusters. The core ion $m/z = 90$ $\text{Fe}(\text{OH})_2^+$ forms hydrates on $m/z = 108$ (FeO_3H_4^+), $m/z = 126$ (FeO_4H_6^+), and $m/z = 144$ (FeO_5H_8^+) and the core ion $m/z = 91$ (FeO_2H_3^+) forms hydrates on $m/z = 109$ (FeO_3H_5^+), $m/z = 127$ (FeO_4H_7^+), $m/z = 145$ (FeO_5H_9^+). While other assignments of the observed ion signals are possible, the interpretation as two series of

hydrates with $\text{Fe}(\text{OH})_2^+(\text{H}_2\text{O})_n$ and $\text{Fe}(\text{OH})_2\text{H}^+(\text{H}_2\text{O})_n$ with $n \leq 3$ is the most conclusive and supported by the similar ion signal profile shapes and the characteristic isotopic patterns.

Following the same pattern of ion formation, another two series of species can be identified with core ions with $m/z = 107$ ($\text{Fe}(\text{OH})_3^+$) and $m/z = 108$ ($\text{Fe}(\text{OH})_3\text{H}^+$). The ion signals from these series overlap with the isotopic pattern of the series starting at $m/z = 90$ ($\text{Fe}(\text{OH})_2^+$) and $m/z = 91$ ($\text{Fe}(\text{OH})_2\text{H}^+$) (Figure 10-8a). It seems likely that the core ions $m/z = 107$ ($\text{Fe}(\text{OH})_3^+$) and $m/z = 108$ ($\text{Fe}(\text{OH})_3\text{H}^+$) (Figure 10-8b) are formed by (R 10-16) and (R 10-17):



The ratio of $\text{FeO}_3\text{H}_4^+/\text{FeO}_3\text{H}_3^+$ is approximately 11 and does not change significantly with distance from the burner, which indicates that the proton-transfer reaction is favored for these ions at all positions in the flame. Tran et al. [249] revealed that (R 10-17) is endothermic for $\text{Fe}(\text{OH})_2^+$ and $\text{Fe}(\text{OH})_3^+$. They suggest an alternative reaction sequence to form these hydroxide ions in a two-step mechanism. First a proton transfer takes place by the reaction $\text{H}_3\text{O}^+ + \text{Fe}(\text{OH})_n \rightarrow \text{Fe}(\text{OH})_n\text{H}^+ + \text{H}_2\text{O}$ and then a charge-transfer reaction leads to the hydroxide $\text{Fe}(\text{OH})_n\text{H}^+ + \text{H}_2\text{O} \rightarrow \text{Fe}(\text{OH})_n^+ + \text{H}_2\text{O}$. The reaction pathways are tentatively assigned here. It is evident from the simulation in Figure 10-9a, that the flame radicals H and OH are still present with mole fractions in range of 10^{-4} to 10^{-5} . These mole fractions are large enough to enable reactions with $\text{Fe}(\text{OH})_2$ species according to the postulated alternative reaction pathway. Even though the concentration of the cations are very small, the fact that the radicals are consumed in these reactions, may contribute to the disappearance of radicals in the exhaust gas of $\text{Fe}(\text{CO})_5$ -doped flames.

The ion signal profile shape of the water cluster and the core ion differ substantially for $\text{Fe}(\text{OH})_3^+$ and $\text{Fe}(\text{OH})_3\text{H}^+$. A reason for the different profiles may be the high convolution of the isotope patterns of the core ions and the water clusters, which cannot be separated.

In summary, because H_3O^+ is the main ion formed by the known ion-formation reactions of hydrocarbons in the flame and there is no indication of a direct ion formation involving iron-containing flame species, the assumption was made that the reactions occur predominantly with H_3O^+ . In principle, charge transfer reactions with iron-containing intermediates can be present in the studied flames. Proton transfer between intermediates was neglected. With these assumptions, the observed ion signals of iron species in the flame can be linked to a limited number of reactions to the neutral iron-containing intermediates. The ion signal profiles will be used in the following paragraph to deduce information on the neutral Fe-species. It should be noted that many ion reactions produce or consume radicals and interact in this way with the neutral Fe-species in the flame. The effect on the overall radical pool in the flame is expected to be minor due to the low ion concentrations. Gaseous iron compounds are known as a potent catalysts in the selective oxidation of hydrocarbons according to, e.g., $\text{CH}_4 + \text{FeO}^+ \rightarrow \text{Fe}^+ + \text{CH}_3\text{OH}$ [252].

We conclude that most of the iron-containing ions seem to be formed by hydration reactions in analogy to $\text{H}_3\text{O}^+(\text{H}_2\text{O})_n$ with $n \leq 3$ and the oxygenated hydrocarbon species. The ions shown in Table 10-2 can be classified into four series, namely $\text{Fe}(\text{OH})_2^+(\text{H}_2\text{O})_{0-3}$, $\text{Fe}(\text{OH})_3^+(\text{H}_2\text{O})_{0-3}$ and $\text{Fe}(\text{OH})_2\text{H}^+(\text{H}_2\text{O})_{0-3}$, $\text{Fe}(\text{OH})_3\text{H}^+(\text{H}_2\text{O})_{0-3}$. The listed signal ratios of $\text{Fe}(\text{OH})_2^+$, $\text{Fe}(\text{OH})_2\text{H}^+$ and $\text{Fe}(\text{OH})_3^+$, $\text{Fe}(\text{OH})_3\text{H}^+$ are smaller than one and their raw signals are much smaller than the signal of H_3O^+ . This observation supports the assumption that H_3O^+ is the main proton donor for iron-containing species.

10.5.3.4 Evolution of the oxidation state of iron compounds

$\text{Fe}(\text{OH})_2$ and $\text{Fe}(\text{OH})_3$ differ in their oxidation states. In $\text{Fe}(\text{OH})_2$, iron has the oxidation state +2 and in $\text{Fe}(\text{OH})_3$ it has +3. To understand the oxidation from +2 to +3 the ion signals of $\text{Fe}(\text{OH})_2^+$ and $\text{Fe}(\text{OH})_2\text{H}^+$ and their hydrates, on the one hand, and $\text{Fe}(\text{OH})_3^+$ and $\text{Fe}(\text{OH})_3\text{H}^+$ and their hydrates on the other hand were summed up and the comparison of the resulting ion signal profiles of +2 and +3 are shown in Figure 10-8c. $\text{Fe}(\text{OH})_2^+$ and $\text{Fe}(\text{OH})_2\text{H}^+$ and their hydrates reach their maximum ion signal intensities at $\text{HAB} = 7$ mm. They are completely decomposed at $\text{HAB} = 12$ mm. $\text{Fe}(\text{OH})_3^+$, $\text{Fe}(\text{OH})_3\text{H}^+$ and their hydrates reach their maximum ion signal intensities at $\text{HAB} = 12$ mm and are completely decomposed at $\text{HAB} = 22.5$ mm. Likely the ion signal profiles in Figure 10-8c give a good representation of the neutral mole fraction profiles of $\text{Fe}(\text{OH})_2$ and $\text{Fe}(\text{OH})_3$. Gerasimov et al. [22] did not detect $\text{Fe}(\text{OH})_3$, but they have postulated that the formation of $\text{Fe}(\text{OH})_3$ is a possible missing reaction in the reaction mechanism of $\text{Fe}(\text{CO})_5$ in flames.

The oxidation from $\text{Fe}(2+)$ to $\text{Fe}(3+)$ can be described by, e.g., the hydrolysis reaction $\text{Fe}(\text{OH})_2 + \text{H}_2\text{O} \leftrightarrow \text{Fe}(\text{OH})_3 + \text{H}$ according to Jensen and Jones [253]. Since water is the most abundant species in the flame at higher HAB, hydrolysis reactions are likely at large distances from the burner.

As shown in Figure 10-9, the oxygen mole fraction remains almost constant at larger distances from the burner than $\text{HAB} = 5$ mm and the radical mole fraction profiles of O, H, and OH simulated in the doped flame D peak at $\text{HAB} = 2$ mm and reach a low equilibrium value at $\text{HAB} = 15$ mm. The radical mole fractions are orders of magnitude smaller than the mole fractions of oxygen and water. Consequently, the oxidation of $\text{Fe}(2+)$ to $\text{Fe}(3+)$ in these flames is most likely mediated by water and by oxygen. It can be concluded that different oxidation states of iron coexist in the reaction zone of the flame D, while in the exhaust the oxidation state 3 dominates. For material synthesis in any flame this means that reactions with water must be suppressed or avoided in order to preserve the oxidation state 2. This task seems difficult in any flame.

10.5.3.5 Larger iron-containing ions

Larger iron-containing ions with mass-to-charge ratios at $m/z = 197$ ($\text{Fe}_2\text{O}_5\text{H}_5^+$), $m/z = 215$ ($\text{Fe}_2\text{O}_6\text{H}_7^+$), $m/z = 233$ ($\text{Fe}_2\text{O}_7\text{H}_9^+$), $m/z = 251$ ($\text{Fe}_2\text{O}_8\text{H}_{11}^+$) are also observed in flame D. Only the core ion of the series ($m/z = 197$) is shown here, without the hydrates of the series ($m/z = 215$, $m/z = 233$, $m/z = 251$). Their maximum ion signal intensities are reached at $\text{HAB} = 5$ mm (Figure 10-9b). The peak shape of all peaks is similar and exemplary shown in Figure 10-9b by the ion signal profile of $m/z = 197$ ($\text{Fe}_2\text{O}_5\text{H}_5^+$). For comparison, Figure

10-9b also includes the ion signal profiles of $\text{Fe}(\text{OH})_2^+$, $\text{Fe}(\text{OH})_2\text{H}^+$ ($m/z = 90, 91$) and $\text{Fe}(\text{OH})_3^+$, $\text{Fe}(\text{OH})_3\text{H}^+$ ($m/z = 107, 108$).

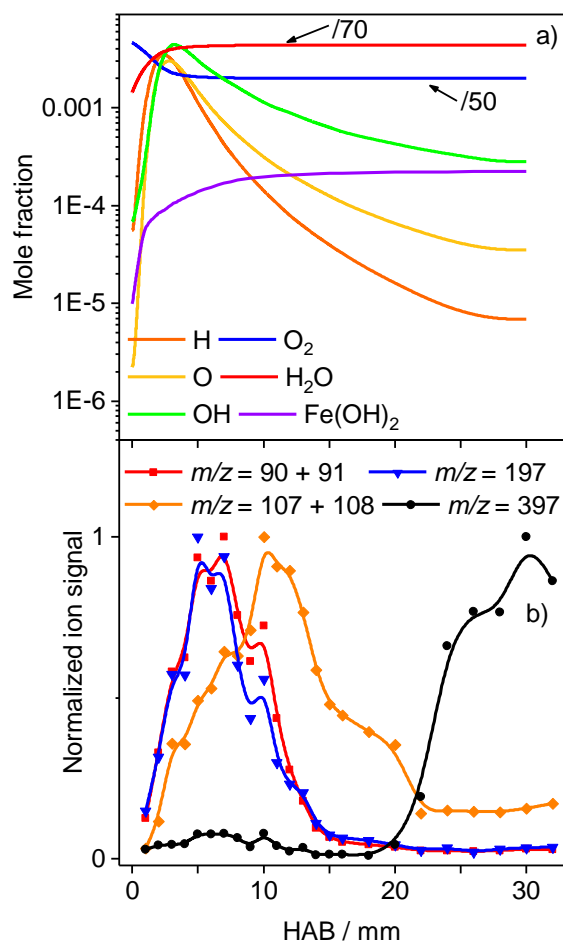
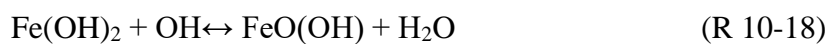


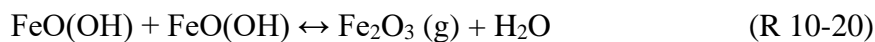
Figure 10-9. a) Simulated concentration profiles in flame D. b) Ion signal profiles of larger iron-containing ions in the $\text{Fe}(\text{CO})_5$ -doped $\text{H}_2/\text{C}_2\text{H}_4/\text{O}_2/\text{Ar}$ flame (flame D, experiment 3). Symbols with lines indicate experimental data and lines indicate simulations.

A likely reaction route that leads to the formation of the first ion containing two iron atoms with the structure $\text{Fe}_2\text{O}_3\text{H}^+(\text{H}_2\text{O})_2$ ($m/z = 197$) is explained as follows: Rumminger et al. [50] propose that $\text{Fe}(\text{OH})_2$ can react with OH and forms $\text{FeO}(\text{OH})$ under elimination of water according to (R 10-18), which is also part of the reaction mechanism of Wlokas et al. [52].

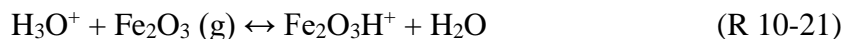


Chemistry textbooks [254] suggest sequential dehydration reactions of iron hydroxides to iron oxides for the conversion of freshly precipitated hydroxides in the presence of hot water vapor. Analogous reactions could occur in the gas phase (R 10-19) and (R 10-20).

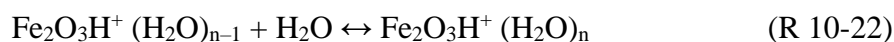




followed by the protonation of gaseous Fe_2O_3 according to (R 10-21):



The hydration pattern of water, hydrocarbons and smaller iron-containing ions revealed that the second hydrate ($n = 2$) is dominant in the series and makes the hydration of $\text{Fe}_2\text{O}_3\text{H}^+$ plausible:



A comparison of the ion signal profiles in Figure 10-9 shows an evident correlation in the shape of the ion signal profile of $m/z = 197$ ($\text{Fe}_2\text{O}_3\text{H}^+(\text{H}_2\text{O})_2$) to the ion signal profile of $\text{Fe}(\text{OH})_2\text{H}^+/\text{Fe}(\text{OH})_2^+$. We assume that the reactions (R 10-18) to (R 10-22) are relevant for the formation of $m/z = 197$ ($\text{Fe}_2\text{O}_3\text{H}^+ (\text{H}_2\text{O})_2$).

It is evident from Figure 10-9 that the larger iron-containing cluster with higher mass-to-charge ratios (e.g., $m/z = 397$) increase from $\text{HAB} = 20$ mm and reach their maximum further downstream in the flame at $\text{HAB} = 32.5$ mm. Overlapping isotopic patterns and the formation of water clusters make it difficult to discern reaction patterns for these large molecules so that the likely formation reactions cannot be discussed. The ion signal profile shape of the larger clusters is similar to the particle deposition profile shape of the solid particle phase measured under similar conditions in the study by Kluge et al. [57]. We speculate that iron-containing hydroxides may be the main precursors for nascent particles at a late stage in the flame and that in particular condensation reactions lead to particle formation. More investigations of ion chemistry in nanoparticle synthesis flames are required in future work to support this speculation.

10.6 Conclusions

In this work, reactions of $\text{Fe}(\text{CO})_5$ in H_2/O_2 and $\text{H}_2/\text{C}_2\text{H}_4/\text{O}_2$ flames are investigated that were analyzed with multiple mass spectrometric diagnostic tools, e.g., PI-MBMS, EI-MBMS and ion sampling coupled to MBMS. Addition of $\text{Fe}(\text{CO})_5$ results in a change of the flame structure. Major species mole fraction profiles, e.g., H_2O , O_2 , H_2 , were shifted slightly towards the burner surface. Major influences are visible on the maximum flame temperature and the radical flame species, e.g., O , OH . In the reaction zone, the maximum temperature in the flame increased with addition of $\text{Fe}(\text{CO})_5$ by approximately 250 K. The mole fractions of the radicals OH and O decrease significantly with the addition of $\text{Fe}(\text{CO})_5$. The increasing temperature and the decreasing mole fractions of the flame radicals suggest that recombination of radical species with Fe species in exothermal reactions occurs. The dissociation of $\text{Fe}(\text{CO})_5$ by sequential loss of carbon monoxide was detected for the first

time and could be compared with the latest reaction mechanism for $\text{Fe}(\text{CO})_5$ with a good qualitative agreement. Other Fe-species could not be detected using the PI-MBMS or EI-MBMS techniques due to the high tendency of fragmentation of $\text{Fe}(\text{CO})_5$ and its intermediates and condensation of particles on the probe.

To learn more about the gas-phase intermediates in the synthesis flames a new sampling technique is used. It samples charged species from the flame and exhibits a much higher detection efficiency than the PI- and EI-MBMS systems. The charged species indicate the presence of iron hydroxide species, e.g., $\text{Fe}(\text{OH})_2$ and $\text{Fe}(\text{OH})_3$, iron oxide species with two to five iron atoms. An assignment of the larger iron clusters to a definite species or molecular structure is complicated by overlapping isotope patterns and cluster formation with water.

To understand the evolution of the oxidation states of the neutral species we looked at the ion signal profiles of the charged iron hydroxides $\text{Fe}(\text{OH})_2$ and $\text{Fe}(\text{OH})_3$ with the oxidation states $\text{Fe}(2+)$ and $\text{Fe}(3+)$, respectively. $\text{Fe}(2+)$ is formed upstream of the oxidation state $\text{Fe}(3+)$. The isotopic patterns of the iron hydroxides suggest that they are formed in hydrolysis reactions with water. These hydrolysis reactions are still missing in the most recent reaction kinetic models of $\text{Fe}(\text{CO})_5$. We hypothesize that the iron hydroxides play a key role as gaseous growth species during particle formation at the later stage of the flame. In the flame, charged species with two to four iron atoms are formed below $\text{HAB} = 12$ mm, while charged species with five iron atoms start to form at $\text{HAB} > 20$ mm. The ion signal profile shapes of the larger iron clusters with five iron atoms in their structure are similar to the profiles reported for solid particle phase in previous studies. They appear to be likely precursors of the solid phase.

Data sets with ion signal profiles and mole fraction profiles of key intermediates of cationic and neutral iron-containing intermediates from the investigated synthesis flames for iron oxide particles are provided. They help to close the gap between precursor decomposition and particle formation by growth species in the gas phase at early stages of iron oxide forming flames

11 Influence of the sampling probe on flame temperature, species, residence times and on the interpretation of ion signals of methane/oxygen flames in molecular beam mass spectrometry measurements

The content of this chapter was published in *Combustion and Flame* 209, 111388 (2021), Y. Karakaya, J. Sellmann, I. Wlokas, T. Kasper, Influence of the sampling probe on flame temperature, species, residence times and on the interpretation of ion signals of methane/oxygen flames in molecular beam mass spectrometry measurements and is reprinted with permission from Elsevier.

CRedit⁶ author statement: Y. Karakaya performed the experiments, chose the precursor- and flame conditions, evaluated and discussed the numerical and experimental data, wrote the original draft of the manuscript. J. Sellmann and I. Wlokas provided numerical simulations and interpretations of the results. All authors provided discussions of the results and contributed to the manuscript.

11.1 Abstract

Laminar flames are widely used to analyze the fundamentals of combustion processes using molecular beam mass spectrometry. The extraction of a representative sample from a flame by an intrusive sampling technique is challenging because of two main issues. First, the sampling probe itself perturbs the flow and temperature field, affecting the species profiles. These effects need to be characterized by 2-D fluid dynamic simulations to reveal sources of perturbations that are in particular suction and flame cooling. Second, some intermediate species interact with the sampling probe and are removed from the gas sample before analysis. The concentrations of these intermediates in the flames are often low and close to the detection limit. Naturally occurring ions can also be extracted from the flame by molecular beam sampling. Coupled with modern ion optical devices for ion transfer to the mass analyzer very high sensitivity can be reached in the detection of ionic species in flames. Similarities in the shape of measured relative concentration profiles indicate a connection between neutrals and the corresponding protonated molecules by proton transfer reactions. A quantification method of neutral flame species based on signals of the flame-sampled ions is presented and evaluated for the intermediate methanol in methane/oxygen/argon flames. The proposed method is based on equilibrium calculations that depend on temperature. To characterize the sampling process and demonstrate the validity of the quantification approach for ion measurements, the influence of the sampling probe on flame temperature and mole fraction profiles of the main species and the intermediate methanol are investigated by a combined experimental and simulation study. A comparison of the methanol profiles measured by conventional molecular beam sampling and the novel ion sampling technique

⁶ CRedit, Contributor Roles Taxonomy

reveal acceptable agreement. This work shows that if all aspects of sampling are considered as well as possible, the ion sampling technique allows access to kinetic data of neutral intermediates.

11.2 Introduction

Low-pressure flames are particularly well suited for the investigation of the flame structure due to their axial one-dimensionality [24, 82, 255]. The information on as many interacting flame species as possible is needed to create detailed kinetic reaction mechanisms for the combustion process. A large number of species can be detected by means of mass spectrometry and the flame structure can be spatially resolved in detail [24, 28, 82, 108, 256]. The operation of the flames at low pressure allows high spatial resolution of the preheating, reaction and recombination zones. But the introduction of a probe perturbs the temperature field and may block diffusion pathways in the flame [257]. Consequently, changes in the local composition of the flame are observed.

The impact of the sampling probe on the flow, temperature and concentration fields of laminar flames have been studied by various groups, e.g. by Hayhurst et al. [238, 244, 258-261], Biordi et al. [262], Korobeinichev et al. [263, 264], Struckmeier et al. [82], Hartlieb et al. [172]. A complete overview of perturbation sources was given by Egolfopoulos et al. [255, 265], Deng et al. [173]. Recently, Hansen et al. [266, 267] investigated the flame perturbation and the drop in temperature due to the presence of the sampling probe in a $C_2H_4/O_2/Kr/Ar$ low pressure flame at 30 torr using x-ray fluorescence and highlighted the deformation of the temperature iso-lines. As confirmed by many studies, the temperature and velocity field deviate from the presumed flatness and the flames lose their one-dimensionality in the vicinity of the sampling probe [57, 82, 172, 173, 238, 255, 258, 261, 263-266]. Still the ideal and steady, one-dimensional, laminar flame model is in general used for reaction mechanism development in the reaction kinetics community. In order to bridge the disparity of model and experiment, corrections have to be applied, as suggested in the past [82, 172, 263]. Unfortunately, the magnitude of the perturbation is difficult to determine experimentally and differs depending on the setup of the flame and the probing system. Since the reliability of kinetic models has increased and computational fluid dynamic simulations with detailed finite rate reaction kinetics mechanisms are affordable, these simulations are widely used for the quantification of probing effects and other sources of perturbation [57, 98, 173, 268, 269]. Multidimensional simulations of premixed flames were presented by Skovorodko et al. [264], Faravelli et al. [270], and Sellmann et al. [98]. Gururajan et al. [265] investigated a 50 mbar rich propene/oxygen/argon flame and examined the influence of sampling, flange, non-adiabaticity, sampling point and compressibility during the suction through the probe on the flame by means of 2D-simulations. Deng et al. [173] have conducted 2D and 3D numerical studies of atmospheric laminar $CH_4/O_2/Ar$ and $H_2/O_2/N_2$ flames considering the burner structure and sampling probe and were able to reproduce the measurements, previously inaccessible to one-dimensional simulations. As a coarse estimate, Deng et al. [173] proposed a spatial probe shift of 3 probe orifice diameters in the upstream direction. They could show that the temperature drop towards the probe inlet could be estimated by a simple one-dimensional energy balance presuming constant total enthalpy,

as formerly stated by Hayhurst [261, 271]. The thermal perturbation of the flame's reaction zone cannot be estimated from a simplified rule as it strongly depends on the material and structure of the probe. The tools and work flow developed by Deng et al. [173] were applied since then in various fundamental studies complementary to the experiments [57, 98, 268, 272].

During the sampling process of particle-laden flows, i.e., fuel-rich flames used in the investigation of soot formation, condensing material can block the probe and reduce the sampling efficiency to the point of complete loss of signal. In addition, the neutral molecules in the gas sample must be ionized to allow for mass analysis in a mass spectrometer. Most commonly electron ionization [82, 86], and photoionization [83, 84] are used. Even though threshold-photoionization leads to less fragmentation of the molecules during the ionization process than electron ionization, the fragmentation of molecules can still be substantial [24]. Consequently, in combustion analysis polycyclic aromatic hydrocarbons (PAH) in a certain mass range are hard to detect. Due to their role in soot formation as precursors and the health hazards they pose in combustion emissions, their formation mechanisms in fuel-rich flames are of great interest [61, 273]. Sampling charged species from flames improves sampling efficiency for PAH. Further it allows the measurement of species, which often elude detection in molecular beam sampling systems. Gerhardt and Homann [274] have experimentally determined ionic species in hydrocarbon flames without fragmentation issues. They have shown that ionic species often differ from related neutral molecules only by an additional proton. The related neutral molecules can be identified and quantified, when the connection to the ionic species is fully understood. According to Weilmünster et al. [60] the mass spectra of the flame ions already give an insight into PAH growth in flames. Jander and Wagner [275] have also shown that the concentration profiles of neutrals and their corresponding protonated charged counterparts in flames have similar shapes. Formation of ions by proton exchange reactions is fast and in equilibrium on the time scale of the flame experiment. Morley [276] has shown that the equilibrium shifts, due to temperature decreases, which results in a change of the mole fractions of charged species. The precursor CHO^+ of most naturally occurring ions in hydrocarbon flames is produced by chemi-ionization according to reaction (R 11-1) $\text{CH} + \text{O} \rightleftharpoons \text{CHO}^+ + \text{e}^-$ [61, 199]. Through fast proton exchange reactions protonated flame species are formed by the protonation of water according to reaction (R 11-2) $\text{CHO}^+ + \text{H}_2\text{O} \rightleftharpoons \text{H}_3\text{O}^+ + \text{CO}$ [199]. Ions are formed by proton-transfer reactions of the form (R 11-3) $\text{H}_3\text{O}^+ + \text{A} \rightleftharpoons \text{AH}^+ + \text{H}_2\text{O}$, where species A has a higher proton affinity than water and can be almost any intermediate species in combustion processes. Artificial ions (here defined as ions not formed in the flame but in the sampling process) are formed during sampling according to reaction (R 11-4) $\text{AH}^+ + \text{H}_2\text{O} \rightleftharpoons \text{AH}^+(\text{H}_2\text{O})$. Reactions (R 11-1) - (R 11-4) present the most common ion reactions in flames in a simplified scheme.

A method is presented here to obtain the mole fractions of the neutral species (A) from the protonated corresponding species (AH^+) produced by proton transfer reactions as shown in reaction (R 11-3). Because of similarities in the shapes of ionic and corresponding neutral species profiles, a connection can be assumed. The fast reaction rates of proton transfer reactions support the assumption that the reactions are in equilibrium at each point in the flame. This equilibrium is affected by temperature and can shift during flame sampling.

Previous studies [82, 265] have shown that the temperature close to the sampling probe is substantially smaller than in the unperturbed region of the flame downstream of the sampling location. Hayhurst and Kittelson [238] have specified a residence time of species in the perturbed region of about 10 μ s. Few reactions involving neutral, stable, or radical species are fast enough to noticeably change the composition of the gas sample in this time. Ionic reactions are much faster than most reactions of neutral species. For example, the flame reaction $\text{CO} + \text{OH} \rightleftharpoons \text{CO}_2 + \text{H}$ has a reaction rate of $4 \cdot 10^9$ [277] mol/cm³s at 1500 K and a relaxation time of $8 \cdot 10^{-6}$ ms. The proton transfer reaction $\text{H}_3\text{O}^+ + \text{CH}_3\text{OH} \rightleftharpoons (\text{CH}_3\text{OH}) \cdot \text{H}^+ + \text{H}_2\text{O}$ has a reaction rate of $1.51 \cdot 10^{15}$ mol/cm³s [203] at 1500 K and a relaxation time of $1 \cdot 10^{-11}$ ms. Consequently, the position of the equilibrium of reaction (R 11-3) changes when the sample passes through the perturbed region of the flame in front of the sampling probe. In addition, reactions of ions are quenched later in the molecular beam expansion in comparison to the reactions of neutral species because they require fewer collisions so that some new species are formed in the molecular beam. For example, for ions formed in the flame, the equilibrium temperature is equal to the perturbed flame temperature, while the reactions forming protonated water clusters mainly freeze out in the molecular beam expansion in the sampling probe. Identification of equilibrium temperatures helps to differentiate between probe-induced ions and flame ions. Consequently, an accurate determination of the sampling-induced perturbation of temperatures in the flame and the temperatures in the molecular beam is of importance. Once the equilibrium temperature is known, the mole fraction of the neutral species A can be obtained from the equilibrium constant $K_x(x_{\text{reactants}}, x_{\text{products}}, p, T, \Delta G(T))$ calculated from thermodynamic data, measured ion signals of H_3O^+ and AH^+ and the measured water mole fraction according to:

$$x(\text{A}) = \frac{S(\text{AH}^+)}{S(\text{H}_3\text{O}^+)} \cdot x(\text{H}_2\text{O}) \cdot \frac{1}{K_x} \quad (11-1)$$

Here, $x(\text{A})$ and $x(\text{H}_2\text{O})$ are the mole fractions of species A and water, respectively. $S(\text{AH}^+)$ and $S(\text{H}_3\text{O}^+)$ are the measured ion signals of AH^+ and H_3O^+ . It is important to mention that K_x depends on the ion formation temperature, consequently flame perturbations affect it a lot. In this work, the quantification approach based on equilibrium calculations is applied to methanol in methane flames and compared to simulated methanol mole fractions. As a prerequisite for the analysis, the perturbation of the flame temperature by the probe has been analyzed and methods for identifying the formation temperature of the ions have been tested.

11.3 Experiment and flame conditions

11.3.1 Flame conditions

Methane flames with the same flame conditions were studied with three different sampling techniques. The burner feed was composed of a $\text{CH}_4/\text{O}_2/\text{Ar}$ mixture and the composition is shown in Table 11-1. Flame conditions are chosen to be similar to the work of Alqaity et

al. [30]. A McKenna-type burner is mounted in a vertical flow configuration on an axial-translation system, which allows sampling with a sampling probe at different heights above the burner (HAB) between $HAB = 0$ and 50 mm. The pressure in the burner chamber is measured by a capacitance manometer and held constant at 160 mbar by a throttle valve, which is connected to the vacuum pump. The burner and the mounting flange for the sampling probe are water-cooled. The gas flows are regulated by mass flow controllers and mixed before they enter the burner.

Table 11-1. Flame conditions in standard cubic centimeter per minute. Flame A is analyzed with the aid of electron ionization MBMS, flame B is analyzed with the aid of electron ionization expansion sampling, flame C is analyzed by ion sampling. For flame B) and C) the same experimental setup is switched from expansion sampling with electron ionization to ion sampling.

Flame	A	B	C
ϕ	1		
p / mbar	160		
CH ₄ / sccm	670		
O ₂ / sccm	1330		
Ar / sccm	2000		
Orifice Diameter / μm	90	550	550
Sampling Probe Material	Quartz	Metal	Metal
Ionization method	EI	EI	Ion sampling

The flame structure of flames A, B and C, are analyzed, on the one hand with the aid of electron ionization molecular beam mass spectrometry (EI-MBMS) and on the other hand with the aid of an ion sampling interface coupled to the same mass spectrometer (i-MBMS). Both systems have already been used in different studies. Identification and measurements of ions were performed in collaborative work with Alquaity et al. [30] and measurements with the aid of EI-MBMS are described by Karakaya et al. [86, 236], Janbazi et al. [185], and Gonchikzhapov [85]. A short summary of both systems is given below.

11.3.2 Ion sampling (Flame C)

To analyze ions the reactor chamber which contains the burner with flame C is coupled to an orthogonal time-of-flight mass spectrometer (TOF) by three differentially pumped vacuum stages. In the first stage an operational pressure of 3 mbar, in the second stage 10^{-3} mbar and in the third stage $1 \cdot 10^{-6}$ mbar is maintained, while the TOF is kept at $1 \cdot 10^{-7}$ mbar. The charged species from the flame are sampled by a metallic sampling probe with an orifice diameter of 550 μm . A 300 V positive potential is applied to the probe and to the burner to avoid an inhomogeneous electric field between both. The transmission of the ions in the first stage is ensured by a low capacitance printed circuit board ion funnel to which a DC potential gradient is applied to transport the ions through the funnel. The second stage is equipped with a segmented octapole ion guide and in the third stage a quadrupole ion guide is used to

reduce the kinetic energy of the ions. Subsequently, the ions pass through several apertures and beam forming Einzel lenses and are guided into the ionization chamber of the TOF.

11.3.3 Electron ionization TOF analysis with expansion sampling (Flame B) and with molecular beam sampling (Flame A)

To obtain the mole fractions of neutral species under identical sampling conditions as the ions, the ion optics of the ion interface can be grounded, so that the pumping stages serve as low efficiency molecular beam inlet. It is here referred to as expansion inlet. The neutral species are ionized by electron ionization and analyzed in the TOF. This analysis was performed for flame B. In addition, neutral species were measured using a dedicated molecular beam inlet in flame A. The probe in this experiment is made from quartz. Here, the probe diameter was reduced to 90 μm to allow expansion of the sample into a second vacuum stage kept at 10^{-3} mbar with acceptable gas load on the turbo molecular pump. The core of the molecular beam was extracted by a skimmer with an orifice diameter of 1.2 mm to the ionization chamber of the TOF. The gas sample was ionized by electron ionization (EI). The nominal kinetic energy of the electrons was chosen to be 14.5 eV to obtain a good compromise between signal-to-noise, short acquisition times and dissociative ionization. For both sampling procedures, the ions pass between a repeller and extractor electrode and are accelerated into the flight tube of the TOF before they impact a multichannel plate. The orthogonal TOF mass analyser has a resolution of $m/\Delta m = 3000$, which is useful for a precise mass determination and separation of near mass overlaps, e.g. C_2H_4 and CO . The signals of the main and intermediate species obtained in the neutral mode using the ion transfer interface with expansion sampling, and the molecular beam system were converted to mole fractions using the procedures described in [24].

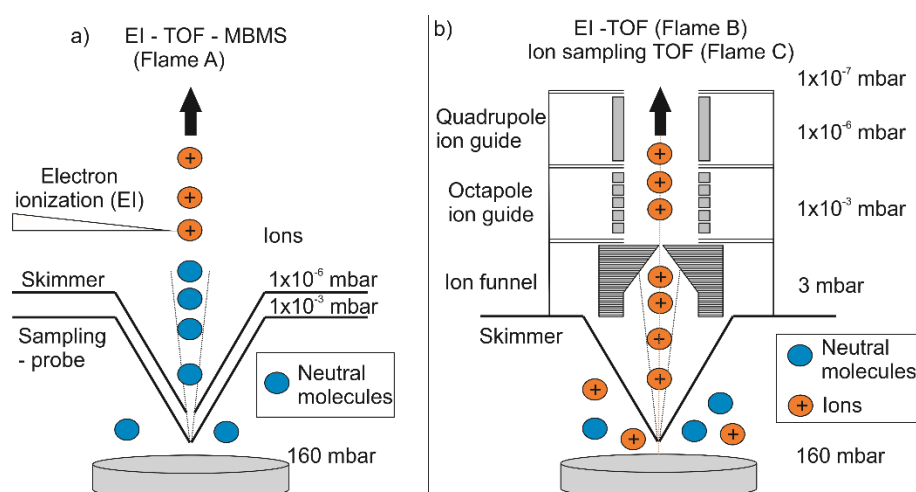


Figure 11-1. Schematics of the experimental setup for a) TOF-MBMS with electron ionization (flame A) and b) TOF with electron ionization and expansion sampling (flame B) and ion sampling TOF (flame C). For flame B) and C) the same experimental setup is used and can be switched from expansion sampling with electron ionization to ion sampling. Reprinted from [62] with permission from Elsevier.

11.3.4 Temperature measurements

The temperature of the flames is measured with a type R thermocouple coated with SiO₂ with a diameter of 200 μm. The thermocouple is positioned one mm in front of the sampling probe. A radiation correction is performed following the procedure described in the study by Bahlawane et al. [93] to obtain the flame temperature. Additionally, the temperature dependence of the argon signal is evaluated to get a relative perturbed temperature profile as shown in the work of Struckmeier et al. [82]. The surface temperature of the metal sampling probe is estimated from a measurement with a thermocouple (type K) touching the inside of the sampling probe close to the tip. The surface temperature on the cold side of the probe was measured to avoid the influence of the thermocouple on the flame structure. The temperature of the molecular beam is measured with a thermocouple (type K) in a distance of one mm behind the orifice inlet. The temperature measurement of the molecular beam and sampling probe surface were carried out at 3 mbar without radiation correction. Temperature values were allowed to stabilize until thermal equilibrium between the gas phase and the thermometer was achieved. The error of the thermocouple measurements was within ± 0.75% (supplier's data sheet). Positioning errors are approximately 1 mm. Temperature measurements were performed independently from the species measurements and thermocouples were removed prior species measurements.

11.4 Simulations

One-dimensional simulations are performed to gain insight into the flame structure. The flame perturbation in one-dimensional simulations is in general tentatively considered as input by the perturbed temperature profile. In order to get a deeper insight into the probe induced perturbation of the flame structure, two-dimensional simulations were performed, which include the sampling probe geometry and use specific experimentally accessible boundary conditions as input to describe the heat losses. The numerical setups of the simulations are briefly summarized.

11.4.1 One-dimensional simulation

ChemkinPro 19.2 [186] is used to simulate the flame structure for a 1D burner stabilized flame using a detailed chemical-kinetic reaction mechanism AramcoMech 2.0 [278] and a measured perturbed temperature profile as input variables.

11.4.2 Two-dimensional simulation

The two-dimensional simulations of the flame sampling were carried out in a rotationally symmetric computational domain, sketched in Figure 11-2. At the probe, the simulation domain ends at the sampling probe inlet where the flow reaches a critical state. Simulation of the flow inside the sampling probe was beyond the scope of this study. Sampling probes with two different orifice diameters ($D = 90 \mu\text{m}$, flame A and $D = 550 \mu\text{m}$, flame B) were

investigated, each at four different heights above burner (HAB = 1, 2.25, 3.25 and 25 mm). The chosen HAB are in particular locations relative to the flame front, which reflect the beginning, middle, end of flame front and the exhaust region. At least 12 cells represented the diameter of the probe inlet. The flow through the sampling probe orifice is choked due to the large pressure ratio between the burner chamber and the sampling system, providing the critical pressure p^* as an outlet boundary condition. With an estimated, average specific heat ratio of the sampled gases $\kappa = 1.3$, the relation $p^* = p \cdot \left(\frac{2}{\kappa+1}\right)^{\frac{\kappa}{\kappa-1}}$ results in an outlet pressure of $p = 85$ mbar [63]. The pressure at the far field boundaries was set to the chamber pressure $p = 160$ mbar. Due to a lack of detailed information on the thermal conductivity of the probe material, limiting boundary conditions were applied: adiabatic and isothermal probe walls, each. The temperature for the isothermal boundary condition for the metal sampling probe ($D = 550 \mu\text{m}$, $T = 1036$ K) was measured in the experiments and used for the quartz sampling probe ($D = 90 \mu\text{m}$) as well. A measurement of the surface temperature of the quartz sampling probe was not possible because the skimmer blocked access to the inside of the sampling probe. The burner inlet temperature is presumed to be fixed at $T = 400$ K. This configuration was chosen in order to keep both, 1D and 2D simulations consistent at the model level. To ensure this consistency is essential for the work-flow of mixed 1D and 2D simulations as it was introduced by Deng et al. [173]. This configuration of boundary conditions is robust for water-cooled burners (like here) and sufficiently lifted flames.

The simulation framework used for the investigation accounts for detailed molecular transport models, and corrects for the species diffusion at the inlet, consistent with the models implemented in the popular 1D kinetics tool-boxes ChemkinPro [186] and Cantera [157]. The Fickian diffusion was treated as mixture averaged. Detailed description of the model implementation in OpenFOAM [279] was provided by Deng et al. [173] and has been successfully used in previous studies [98, 100, 268]. The computational effort required a skeletal, reduced reaction scheme. In this work the DRM22 reaction mechanism was used [280]. All simulations were performed on a hexahedral mesh with 26580 to 47750 cells and the maximum runtime of the large setup was 120 hours on 48 cores (Intel E5-2650 v4 Broadwell CPUs). Axial, radial profiles, contour diagrams and isolated streamlines of fluid elements are analyzed in more depth for a detailed investigation of the flame structure perturbation caused by the sampling probe.

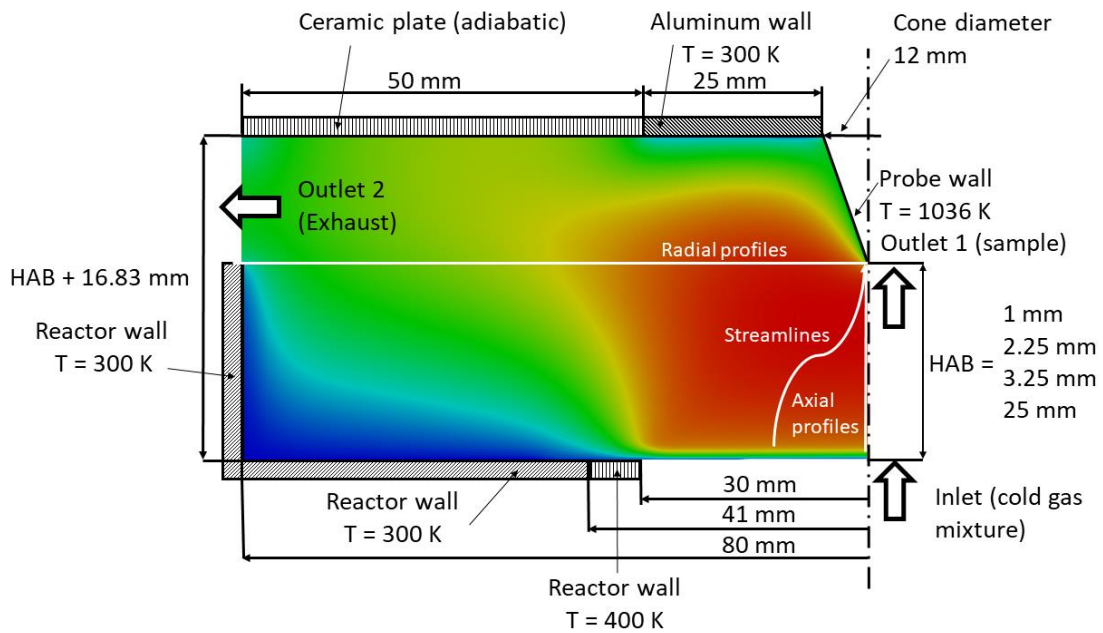


Figure 11-2. Computational two-dimensional domain and the boundary conditions for the simulation, exemplarily shown for flame B. White lines schematically show the profiles analyzed in the post processing evaluation of the 2D-Simulation.

11.5 Results and discussion

11.5.1 Influence of the sampling probe on flame temperature, species and residence times

11.5.1.1 Centerline flame temperature

Two-dimensional simulations of flames A and B were carried out to determine the impact of the probe on the temperature field at various heights above the burner ($HAB = 1, 2.25, 3.25$ and 25 mm). The measured and simulated flame temperature at the centerline of flame A and B with the presence of an isothermal sampling probe are shown in Figure 11-3. The measurements with the thermocouple slightly upstream of the probe reveal that flame A reaches its maximum temperature of 1450 K at $HAB = 3$ mm and in the exhaust at $HAB = 25$ mm the temperature decreases to 1200 K. The 2D-simulations show higher temperatures in the undisturbed case compared to the measurements, but in the vicinity of the sampling probe, the temperature drops and agrees well with the measurements. In the reaction zone, the endpoints of the simulated values coincide with the measured temperature profile, while in the preheat zone at $HAB = 1$ mm deviations to the 2D-simulation are visible. The 2D-simulations reveal the strong decrease of the flame temperature caused by the sampling probe. With the presence of the probe at each sampling point, different intermediate temperature profiles upstream of the sampling probe are present.

In flame A, the intermediate temperature profile for a probe position of $HAB = 1$ mm, 2.25 mm, 3.25 mm increases less steeply compared to the unperturbed case with the probe at $HAB = 25$ mm.

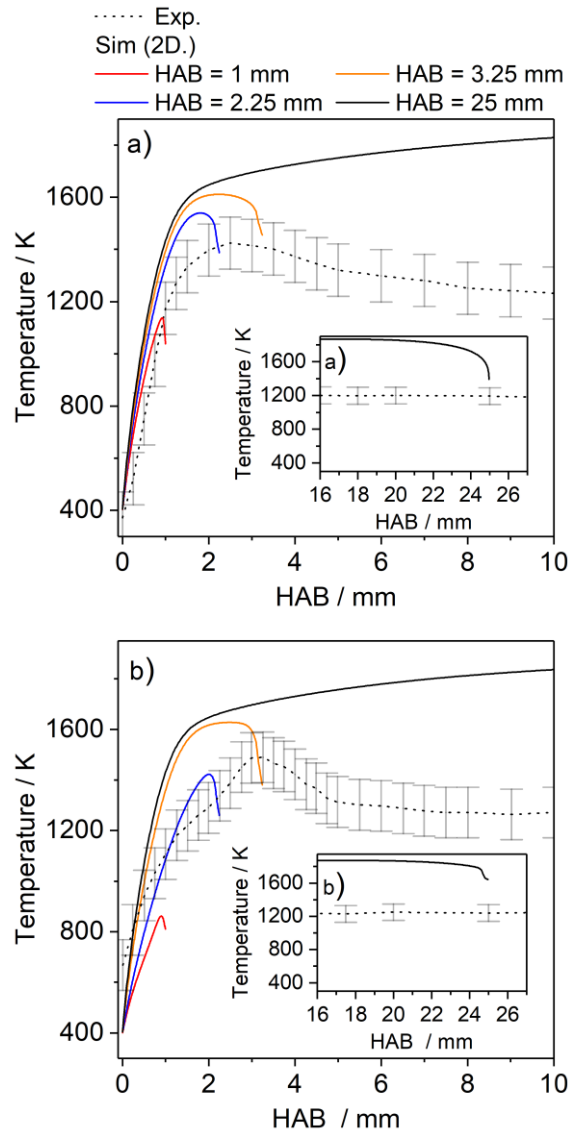


Figure 11-3. Measured (dotted lines) and simulated temperature profiles on the centerline (2D simulations, isothermal sampling probe, solid lines) in a) flame A, and b) flame B for various heights above the burner (HAB = 1, 2.25, 3.25, 25 mm).

As comparative data for the undisturbed flames the 2D-simulation with the sampling probe at HAB = 25 mm is used, as it represents the least perturbation near the burner surface. The temperature profiles for the probe at HAB close to the burner form intermediate maximum plateaus which subsequently decrease in temperature. Compared to the unperturbed profile (HAB = 25 mm), the temperatures at HAB = 1 mm, 2.25 mm, 3.25 mm perturbed by the sampling probe are significantly smaller. For flame A, this results in a flame front that is moving in downstream direction compared to the unperturbed profile (HAB = 25 mm).

The maximum measured temperature of flame B is 1500 K at HAB = 3 mm. In the exhaust gas at HAB = 25 mm the temperature decreases to 1250 K. For flame B, the effect of flame cooling by the probe is less pronounced, but also clearly visible in Figure 11-3. The deviations in the preheat zone and exhaust are on the same order as the experimental uncertainties. In addition, it should be mentioned that the measured temperature is compared

to the centerline temperature, radial temperature gradients can increase the temperature of the sampled volume.

The temperatures at HAB = 1 mm, 2.25 mm, 3.25 mm are significantly smaller compared to the respective HAB in the unperturbed profile with the probe position at HAB = 25 mm. The ending point of the centerline temperature at HAB = 1 mm, 2.25 mm, 3.25 mm is reached further downstream compared to the unperturbed case with the probe position HAB = 25 mm in flame B indicating the widening of the flame front of flame B in downstream direction.

Summarizing, both experiments and simulation show plausible results with good agreement at the inlet of the sampling probe. This gives confidence in simulation and experiment. It is still to be emphasized how important the assumption of an isothermal probe is for the simulations. The simulations with an adiabatic sampling probe have shown significantly higher temperatures at the sample inlet and therefore not such a good agreement with the experiments. These simulations are not discussed further but are included in the supplementary material.

11.5.1.2 Two-dimensional temperature field

The two-dimensional temperature field helps to visualize the effect of flame perturbation by the sampling probe more clearly and can provide information about the differences between measurements and ideal 1D-simulations. The temperature fields are shown in Figure 11-4 for flame A (Figure 11-4 a-d) and flame B (Figure 11-4 e-h).

The sampling at HAB = 1 mm for flame A and B are shown in Figure 11-4 a) and e). The probe is located in the center of the reaction zone, which is characterized by a rapid temperature rise (strong gradient), but the maximum has not yet been reached. Since the body of the sampling probe is positioned upstream in the hot flame, an isothermal boundary condition for the probe wall is used for the 2D-simulation, and consequently the probe wall has a higher temperature compared to the gas at the tip of the probe. This assumption is based on the measured temperature of the metal probe that is approximately 1200 K at all positions in the flame (see Figure 11-11). In principle, the probe causes the gas to heat up upstream of the inlet and the unperturbed 1D assumption is violated. This effect of gas heating (and cooling at larger HAB) by the probe was also reported by Deng et al. [173]. The second pronounced perturbation of the flame at this position is caused by the aspiration of the sample itself and is clearly visible in Figure 11-4 a) and e). Perturbation of the one-dimensional temperature field of flame A is smaller than that of flame B. The reason can be traced to the orifice diameter of the probe. In flame A ($D = 90 \mu\text{m}$) the orifice is smaller than in flame B ($D = 550 \mu\text{m}$) and consequently a smaller sample volume is aspirated, including less cold gas from the preheat zone and more hot gas from the sampling point. The temperature field also reveals that gas fractions with various temperature history are sampled at the same time. The temperature and time histories of each fraction of sampled gas cannot be determined from the mass spectrometric measurements where an averaged signal of all fractions appears. Ideal one-dimensional models do not consider the various time and intermediate temperature histories of the sampled species, which may have an impact on the analysis of the flames. Further numerical investigations are needed at this point.

Near $HAB = 2.25$ mm, the gas has not reached the position of maximum flame temperature. Compared to the position $HAB = 1$ mm the temperature of the probe is lower than the gas temperature and has from this position on a cooling effect on the aspirated gas. A stretching of the flame structure towards the probe can be observed, which is stronger with increasing probe diameter (Figure 11-4 b, f). The distortion results in less steep temperature gradients close to the burner surface than in the unperturbed flame. This effect is evident from the comparison of the simulated intermediate temperature profiles in Figure 11-3 which are less steep than for the unperturbed case.

At $HAB = 3.25$ mm (see Figure 11-4 c, g), close to the end of the flame front where the temperature gradients are less pronounced, stretching of the flame structure cannot be detected. Instead, the perturbation of the temperature field in front of the probe due to its cooling effect is now clearly visible.

At $HAB = 25$ mm the iso-lines show that the hot exhaust gas streams along the sample probe and cools down. At the tip of both probes (flame A and B) it can be observed that the cooled gas is sucked in from the side and mixed with the hot exhaust gas on the centerline.

To quantify the extent of perturbation in radial direction in the sampling region, radial temperature profiles are evaluated. Two regions must be distinguished. The first region is inside of the sampling probe in the cross section of the probe orifice. The second region is the flame beside and upstream of the probe. Radial temperature profiles inside of the probe inlet for the respective probe positions $HAB = 1, 2.25, 3.25, 25$ mm are shown in Figure 11-5 a) for flame A using a probe with $90 \mu\text{m}$ orifice diameter and b) for flame B using a probe with $550 \mu\text{m}$ orifice diameter. Figure 11-5c) explores how far upstream the radial temperatures are perturbed. It shows the radial temperature 0 mm, 1 mm, 2 mm, and 3 mm in front of the probe orifice when the probe is positioned at $HAB = 25$ mm.

The profiles at the probe cross section in Figure 11-5 a) and b) show a temperature profile which is most pronounced for $HAB = 1$ mm with 810 K (1038 K) on the centerline to 1200 K (1134 K) near the probe wall for flame A (B). The temperature gradient towards the probe wall illustrates the heating effect of the probe on the gas for both probes. For flame B and the probe with the larger orifice, at $HAB = 1$ mm suction seems to be the dominating distorting effect on the temperature of the gas sample, because hot gas from the areas around the sampling point is mixed with cold gas from the centerline. The effect is still apparent in the exhaust gas but its influence on the temperature decreases with increasing HAB due to the decreasing temperature gradients. For probe positions larger than $HAB = 1$ mm the probe cools the gas. In Figure 11-5 c) the cooling of the gas by the cold surface of the sampling probe is illustrated for a probe position of $HAB = 25$ mm. The closer the gas is to the probe, the more it is cooled down. The minimum temperatures are reached at the probe wall at $R = 0.09$ mm ($R = 0.55$ mm) for flame A (B). In the center of the probe, however, a rise in temperature can be observed, as hot gas is drawn in from a hotter environment. The suction has two effects. Firstly, it accelerates the gas and reduces its residence time on the centerline. The second effect is still cooling but as an aerodynamic effect on the acceleration in its critical state.

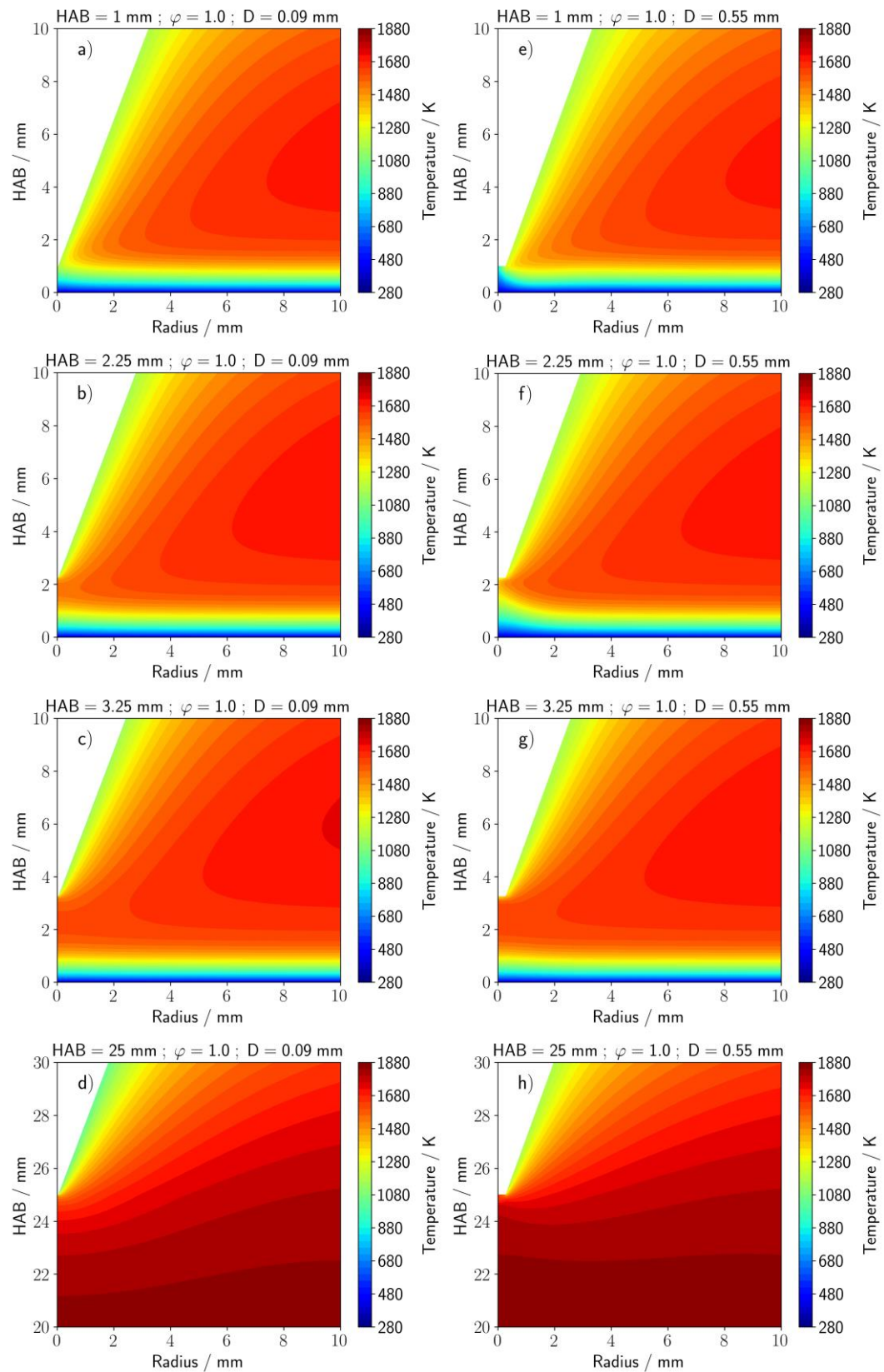


Figure 11-4. Two-dimensional simulation of the temperature field in flame A (4 a-d) and flame B (4 e-h) and isothermal probes for various heights above the burner (HAB = 1, 2.25, 3.25, 25 mm).

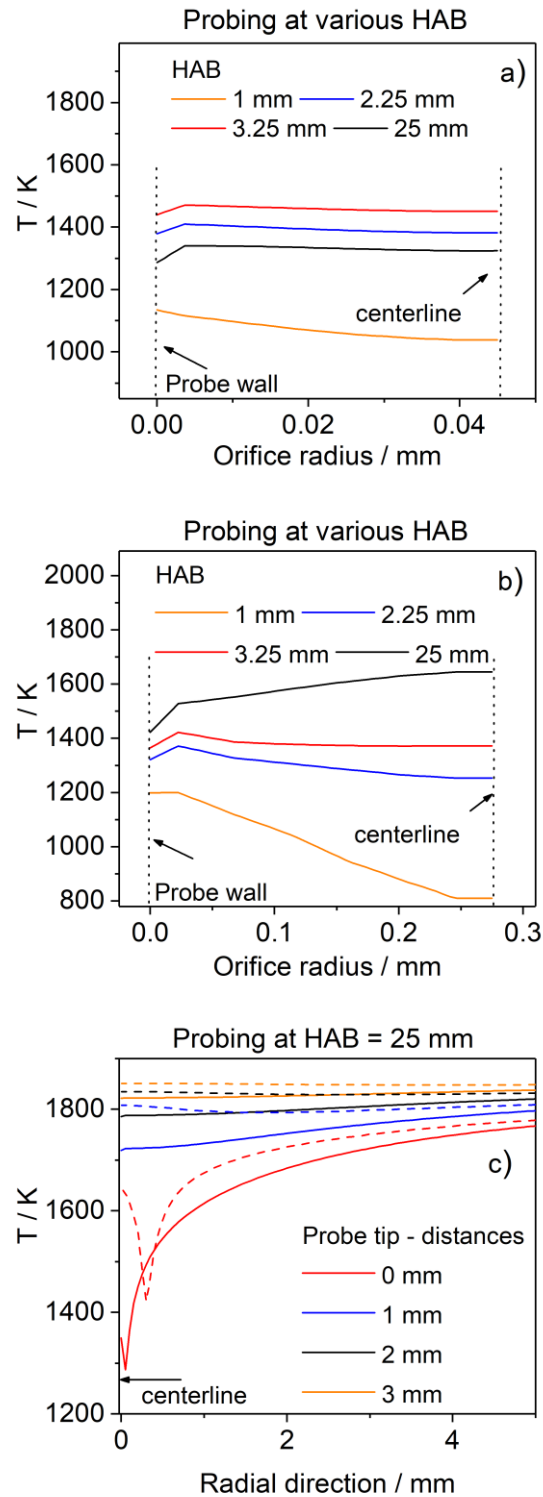


Figure 11-5. Two-dimensional simulation of the radial temperature profiles along the orifice diameter in a) flame A (probe diameter $D = 90 \mu\text{m}$), b) and flame B, C, (probe diameter $D = 550 \mu\text{m}$) at various HAB and c) at various distances parallel to the probe inlet with a distance of 0 mm, 1 mm, 2 mm, 3 mm (solid line for probe diameter $D = 90 \mu\text{m}$ and dashed line for probe diameter $D = 550 \mu\text{m}$).

11.5.1.3 Major species

In the following, the influence of the sampling probe on the major species in flame A and B is investigated. In the first part, each measurement is compared with a 1D-simulation, which was performed with the previously measured temperature profiles shown in Figure 11-3. In the second part, the measurements are compared to 2D-simulations to capture the influence of the probe and the resulting deviation from the measured mole fraction profiles.

Measured and 1D-simulations of the species mole fraction profiles in flame A are shown in Figure 11-6. Flame A has an equivalence ratio of $\varphi = 1$. The main species O_2 , CO_2 and H_2O reach equilibrium mole fractions between $HAB = 2-3$ mm. The dominant intermediate species is CO . It has a maximum mole fraction of 0.06 at $HAB = 2.5$ mm and decays until $HAB = 5$ mm to its equilibrium mole fraction with a value of 0.02. H_2 has a maximum at $HAB = 2$ mm and reaches the baseline at $HAB = 5$ mm. The simulated mole fraction profile of CH_3OH peaks 1 mm earlier than the measured mole fraction profile. The deviation can be explained by suction of gas fractions from cold and hot regions at the same sampling point. The quantitative agreement of the simulated and measured CH_3OH mole fraction is very good. Overall, experiment and one-dimensional simulation show a good agreement.

2D-simulations of the species mole fraction profiles up to the sampling points at $HAB = 1$ mm, 2.25 mm, 3.25 mm and 25 mm in flame A are also shown in Figure 11-6. The end points of the 2D-simulations coincide with the measured mole fractions with reasonable agreement. In the 2D simulation at $HAB = 25$ mm the reaction zone is almost unperturbed, while at the other HAB significant perturbation occurs. A comparison of these perturbed O_2 profiles of the 2D simulations to the almost unperturbed case reveals, that O_2 is consumed less rapidly and reaches a higher mole fraction in the reaction zone when the flame is perturbed (Figure 11-6). This behavior can also be observed for CH_4 decomposition. Consequently, the mole fraction profiles of the intermediate species CO , C_2H_4 , H_2 and the main product species CO_2 and H_2O are less steep and the flame front widens by about 1 mm compared to the unperturbed case and it seems as if the profiles are shifted in downstream flow direction.

Measured and 1D-simulations of the species mole fraction profiles in flame B are presented in Figure 11-7. Flame B has an equivalence ratio of $\varphi = 1$. Here, the main species reach equilibrium mole fractions between $HAB = 3-4$ mm. In this measurement CO does not exhibit a typical intermediate profile. From this observation it can be concluded that the flame is perturbed strongly by the sampling probe.

Despite the perturbation, experiment and the 1D-simulation show reasonable agreement in the exhaust gas. Close to the burner surface up to $HAB = 2$ mm larger deviations are observed for the 1D-Simulations. Only the 2D-simulations can capture the suction-effect at very close distances to the burner. The radial 2D effects cannot be captured accurately by the 1D-simulations, because only the perturbed temperature profile is used. The 2D-simulations show that for flame B the widening of the flame front is between $HAB = 1 - 3$ mm and is more pronounced than in flame A. The reason is the larger diameter of the probe orifice used in flame B that is associated with more suction and more mixing of gas fractions from different positions relative to the probe orifice. As discussed for the temperatures this ultimately results in an apparent widening of the flame front.

Overall, the measured temperature profile approximates the end of the temperature history of the sampled gas well and the 2D-simulation shows that a 1D flame simulation with a measured temperature profile as input is a suited method that achieves acceptable results and can give meaningful insight into the flame structure for small probe diameters.

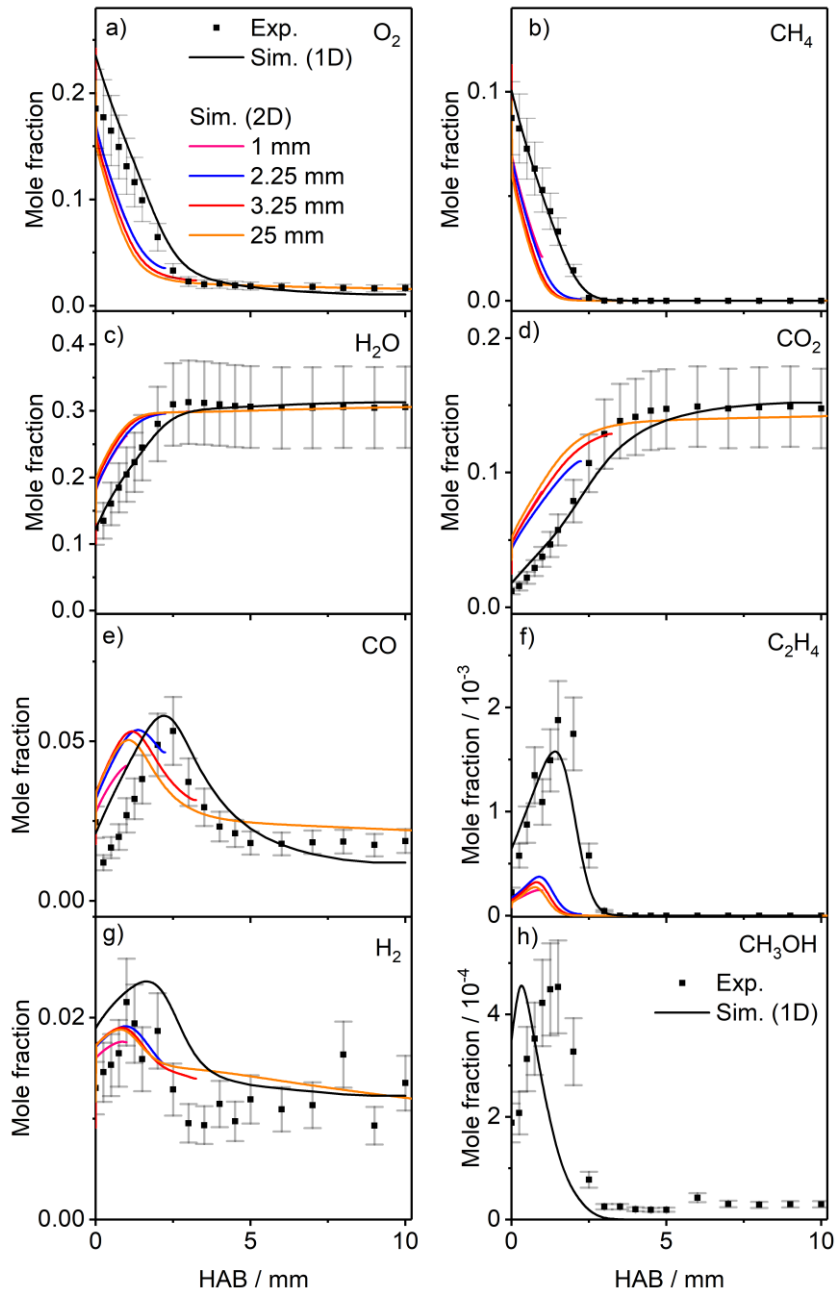


Figure 11-6. Measured (probe diameter $D = 90 \mu\text{m}$, symbols) and simulated (1D- and 2D-simulation, lines) mole fraction profiles of major species on the centerline in flame A. 2D-Simulations are done for an isothermal sampling probe and at various HAB = 1 mm, 2.25 mm, 3.25 mm, 25 mm.

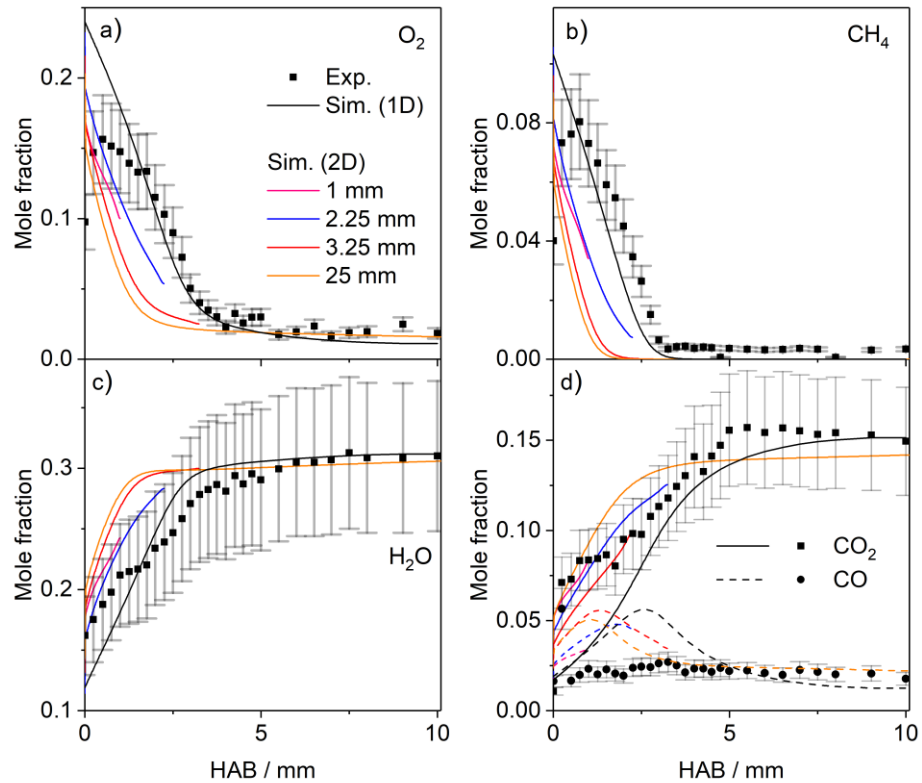


Figure 11-7. Measured (probe diameter $D = 550 \mu\text{m}$, symbols) and simulated (1D- and 2D-simulation, lines) mole fraction profiles of major species on the centerline in flame B. 2D-Simulations are done for an isothermal sampling probe and various $\text{HAB} = 1 \text{ mm}, 2.25 \text{ mm}, 3.25 \text{ mm}, 25 \text{ mm}$.

11.5.1.4 Radical species

CH_3 radicals were measured in flame A and are shown in Figure 11-8. The reduced mechanism has already been used in previous work with promising results [173]. A comparison of the reduced mechanism with the full GRI mechanism [242] is shown in the supplementary material, which shows that it is capable to predict the flame species (see supplemental Figure F-1). The maximum CH_3 mole fraction of $1 \cdot 10^{-3}$ is reached at $\text{HAB} = 1.5 \text{ mm}$ and it is completely consumed at $\text{HAB} = 3 \text{ mm}$. The CH_3 radical profile matches the 1D-simulation results. The ending points of the 2D-simulations are in reasonable agreement with the measured CH_3 radical profile. In the following, the intermediate maximum mole fraction profiles of CH_3 for the simulations with the presence of the sampling probe at $\text{HAB} = 1 \text{ mm}, 2.25 \text{ mm}$ and 3.25 mm are compared to the CH_3 mole fraction profile with the presence of the sampling probe at $\text{HAB} = 25 \text{ mm}$. The maximum mole fraction of CH_3 in the simulation with the presence of the sampling probe at $\text{HAB} = 25 \text{ mm}$ is $x_{\text{CH}_3, \text{max}} = 1.4 \cdot 10^{-3}$. When the sampling probe is located at $\text{HAB} = 1 \text{ mm}$, a lower maximum mole fraction of CH_3 is present ($x_{\text{CH}_3, \text{max}} = 1.1 \cdot 10^{-3}$), while for sampling positions at $\text{HAB} = 2.25 \text{ mm}$ ($x_{\text{CH}_3, \text{max}} = 1.7 \cdot 10^{-3}$) and 3.25 mm ($x_{\text{CH}_3, \text{max}} = 1.6 \cdot 10^{-3}$) the intermediate mole fractions of CH_3 exceed the value in the unperturbed flame. The higher maximum mole fraction of the CH_3 radical at probe position $\text{HAB} = 2.25 \text{ mm}$ can be explained by the presence of the probe which draws the precursors CH_4 and O_2 to higher temperatures and consequently changes

the methyl concentration in comparison to the unperturbed flame. The 2D-simulation in Figure 11-9, shows how the intermediate mole fractions of the methyl radicals are increased at the probe positions $HAB = 2.25$ mm and $HAB = 3.25$ mm compared to the simulation of the probe position at $HAB = 25$ mm which coincides with the unperturbed flame as can be seen in Figure 11-9d.

It should be mentioned that for each probe position the maximum mole fraction is different and also the position of the maximum varies slightly. The major source of error for methyl radical mole fractions typically reported in MBMS studies is the uncertainty in the ionization cross section, which is quoted as 15 % [281]. The increase by probe perturbation is on the order of 10-20 % of the expected mole fraction and has a similar magnitude as the uncertainty of the cross section. It is also dependent on the probing position. At the maximum of the CH_3 peak the probe has a cooling effect on the flame and drastically reduces the CH_3 mole fraction (here 30 %), but if the probe is positioned upstream of the maximum it leads to a moderate increase in the mole fraction (here 10-20 %). As a consequence, the methyl radical mole fraction is probably more uncertain than expected. In particular, the peak shape is affected: the increase in mole fraction is less steep, a lower maximum mole fraction is observed, and the decay of the mole fraction occurs at higher HAB and is also less steep. It is clear that the effect can be observed for other species too and will likely be even more pronounced for more reactive species than methyl radicals, i.e. the naturally occurring flame ions.

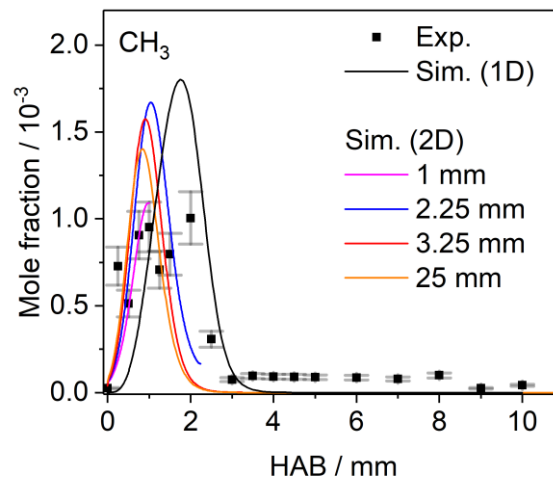


Figure 11-8. Measured (Flame A, Probe diameter $D = 90$ μm , symbols) and simulated (1D- and 2D-simulations, lines) mole fraction profiles of CH_3 on the centerline in flame A. 2D-Simulations are done for an isothermal sampling probe and various $HAB = 1$ mm, 2.25 mm, 3.25 mm, 25 mm.

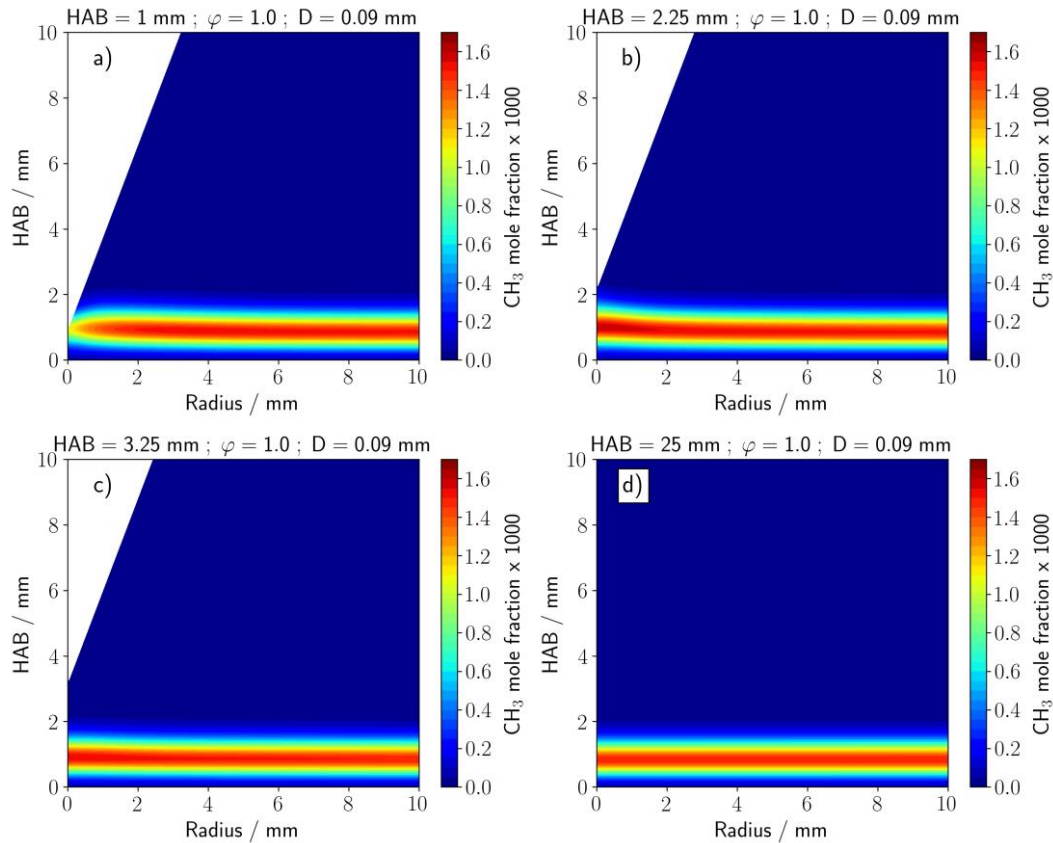


Figure 11-9. Two-dimensional simulations of the CH_3 mole fraction field in flame A) are done for an isothermal sampling probe and various HAB = 1 mm, 2.25 mm, 3.25 mm, 25 mm).

11.5.1.5 Residence time profiles

The contour plots of the flame in Figure 11-4 and Figure 11-9 have shown, that the area of the flame that is affected by suction of the probe has a larger diameter than the probe itself. As a result the residence time (τ) of the gas fractions from different positions and the distance (z) that these gas fractions have traveled in the flame vary. The magnitude and effect of this difference is discussed below by comparing the distance (z) and the residence time (τ) of a gas sample on the centerline (shortest τ and z) and a gas sample at the outer edge of the intake area (longest z and τ). Residence time profiles of these two fluid elements on a streamline drawn from the centerline (r_1) and from the maximum radial point (r_2) are presented in Figure 11-10. The maximum radial point describes the streamline that exits the burner at a radial distance from the centerline and is drawn in by the sampling probe.

For flame A, the values of radius r_{2A} from the centerline are $r_{2A} = 0.89 / 0.81 / 0.79 / 0.79$ mm for sampling at HAB = 1 / 2.25 / 3.25 / 25 mm, respectively. For flame B, the radii are $r_{2B} = 5.4 / 5.21 / 5.13 / 5.1$ mm for the same probing positions as in flame A.

The radii are higher for smaller HAB (due to a compression of the flame front towards the burner surface) and decrease with increasing HAB. The higher radius at small HAB also indicates that a higher mass flow of fresh gas is sampled than at high HAB. Comparing the ratio of the two probe diameters of flame A and flame B ($D_B/D_A=6.1$) to the diameter of the intake surface at the different positions ($r_{2B}/r_{2A} = 6.1 / 6.4 / 6.5 / 6.5$) the intake surface has

increased roughly by the ratio of the probe diameter. The intake surface area is roughly a factor of 20 larger than the probe orifice, for each probe and for the flame conditions investigated here, so that it covers between 0.1 % and 3 % of the burner surface area.

Most of the gas flow in the experiment bypasses the sampling orifice and is pumped out of the chamber via 4 KF40-flanges. The outlets are outside of the simulation domain. The burner has a diameter of 6 cm, and only an area with a diameter of less than 12 mm interacts with the probe. The ratio of orifice/exhaust gas is roughly equal to the ratio of the areas (~ 0.04). As consistency check we calculated the relative change in the ratio of the probe-burner interaction areas and compared them to the relative density change of the flame gases calculated based on simulated and measured temperatures.

In the contour plot in Figure 11-10 a) and e) the radii r_1 and r_2 are illustrated for the probe position $HAB = 1$ mm by streamlines. For the small probe orifice used in flame A, all streamlines go from the burner directly to the probe. For flame B, some of the streamlines apparently pass behind the probe through a region of higher temperature than the temperatures downstream of the probe. As a result, the average temperature encountered by the gas sampled with the larger orifice can be expected to be substantially higher than the temperature encountered by the gas sampled with the smaller orifice at the same position in the flame, even though the cooling effect of the probe on the flame is comparable as can be seen in Figure 11-4. This conclusion is true for all positions because the general form of the streamlines is similar at $HAB = 25$ mm as demonstrated in Figure 11-10 a, b) and e, f). For both probes and larger HAB (Figure 11-10b and Figure 11-10f), the streamlines remain parallel to the centerline over a relatively long distance in the flame compared to small HAB . So, the gas samples experience a temperature history for a longer fraction of their residence time in the flame that resembles to a 1D assumption (direct streamline from the burner to the probe).

Even though the cooling effect of the probe on the flame and the effect of suction are convoluted in the flame, it helps to think of them as two separate effects to rationalize why 1D-simulations with the perturbed temperature profile match the experimental results better at larger HAB than at smaller HAB . At small HAB , the distortion of the streamlines by suction affects the gas sample during its entire residence time in the flame. At larger HAB , a significant distortion of the streamlines only occurs for a fraction of the residence time of the gas sample in the flame. The cooling effect of the probe on the flame is similar at all positions and in part taken into account in a 1D-simulation when using the perturbed temperature profile. Our results and also the results by [25-27, 82, 83] demonstrate that 1D-simulations with the perturbed temperature profile lead to very good agreement between experimental and simulation results except for the data points closest to the burner. Given our observations in this work, it seems likely that the concentration distortions induced by the sampling process are dominated by the effect of suction close to the burner and by the effect of cooling at larger HAB .

To substantiate this reasoning, Figure 11-10 a-h compare the path length that a fluid element with a streamline with r_1 and r_2 experiences, and the respective residence times. Comparing the residence times in flame A for the two streamlines with radius r_1 and r_2 , the following ratios of the residence times are found: $\tau_{2A}/\tau_{1A} = 1.9 / 1.2 / 1.1 / 1.02$ for a sampling position of $HAB = 1 / 2.25 / 3.25 / 25$ mm, respectively. The values for calculating the ratio can be

found either in Figure 11-10 or in the Table F-1 and Table F-2 in the supplementary material. The ratio of the two residence times shows how great the influence of the probe is, especially in the vicinity of the burner (probe located at $HAB = 1$ mm). Near the burner, the residence time of a fluid element on the centerline in the flame is about 2 times shorter than at the limiting radius r_2 . With larger distance to the burner, the ratio decreases as the area affected by suction remains comparable and the streamlines are parallel to the centerline for a substantial distance between probe and burner. For flame B, the ratio of the residence times is considerably larger $\tau_{2B}/\tau_{1B} = 17.23 / 5.2 / 3.8 / 1.13$ and illustrates the immense influence of the larger probe orifice diameter on the individual time histories of the sampled gas.

It is conceivable that gas passing for a longer residence time along the streamline with r_2 will have also reacted for a longer time. Consequently, it can be expected for the larger probe diameter that the concentration of product species is higher in these fractions of the sampled gas. The effect will be enhanced if the gas sample passes through a region of higher temperature behind the probe. The analyzed gas sample will consequently contain comparatively more product gases and less fuel and oxidizer. This effect is clearly visible in the main species profiles in Figure 11-6 and Figure 11-7. The measured oxygen and methane mole fractions at the first data point are approximately 20 % lower in flame B measured with the sampling probe with the larger orifice diameter ($x_{O_2,A}=0.19$, $x_{CH_4,A}=0.09$, $x_{O_2,B}=0.15$, $x_{CH_4,B}=0.08$), and the mole fractions of water and carbon dioxide are about 25 % smaller in flame A than in flame B ($x_{H_2O,A}=0.12$, $x_{CO_2,A}=0.03$, $x_{H_2O,B}=0.16$, $x_{CO_2,B}=0.04$). If compared to the 1D-simulation results, the experimental mole fraction values appear to be an average of the 1D simulated values at different HAB.

The effect on species profiles that are expected to show an intermediate profile with a mole fraction maximum at some distance from the burner is difficult to predict. On the one hand, the CO mole fraction profile in flame B measured with the probe with larger orifice diameter has become flat, which can be expected if the difference between the mole fraction at the maximum and the equilibrium mole fraction in the exhaust gas is small. Near the burner, gas fractions traveling along streamline r_2 have a 17 times longer residence (and probably reaction) time in the flame and reach the equilibrium value of 0.025. On the other hand, when sampling an intermediate species that is consumed completely in the exhaust gas with a probe with a large orifice diameter it may be expected that the intermediate profile shifts towards the burner because a fraction of the sampled gas has experienced a higher temperature and longer residence time than expected for a 1D flame. In addition, the profile will likely increase less steeply, and decay less rapidly as discussed for the methyl radical in flame A. In light of these insights, it is clear that a smaller sampling probe will lead to more accurate results because the effect of suction is less pronounced.

In summary, the path and the residence time that the sample passes prior to reaching the probe inlet can be different even for the same sampling location, as shown by the different residence time profiles for each HAB. The effect of suction is immense and increases with a larger orifice diameter of the probe. The previously described measured “perturbed” temperature profiles do not track the path the sample has passed accurately but they are able to lead to good 1D-simulation results in areas of the flame where the cooling effect of the probe distorts the species concentrations in the gas sample more than the suction effect, e.g.

at higher HAB. Because the influence of the different experienced paths on the sample cannot be assessed with the measured temperature profile, it can only tentatively describe the perturbation of the flame structure. The 2D simulations were performed because the use of a sampling probe with large orifice diameter caused a suction effect which perturbed the flame structure. By using small orifice diameters the suction effect is kept small and 1D simulations with the input of the perturbed temperature profile become sufficient to predict mole fraction profiles. However, it must be taken into account that even with small orifice diameters, slight deviations between experimental and 1D-simulated mole fraction profiles can still occur due to the suction effect, especially in the regions of high mole fraction gradients.

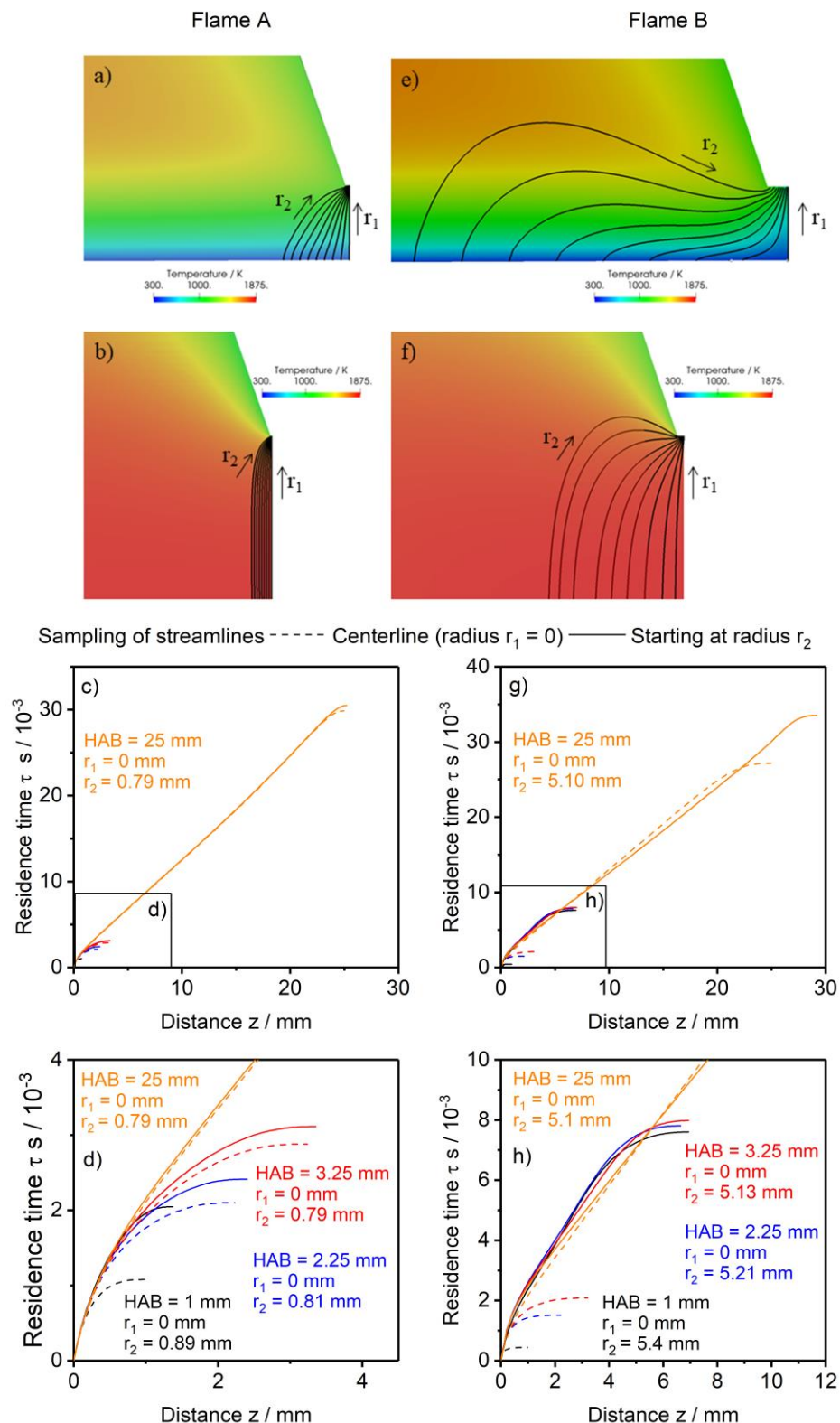


Figure 11-10. Two-dimensional simulation of the temperature field with a streamline pattern and a sampling probe position at HAB = 1 mm and HAB = 25 mm a,b) in flame A and e,f) in flame B. Residence time profiles of gas flows sampled at the centerline (dashed line) and on a streamline suctioned from a radial point of the burner by an isothermal sampling probe and various heights above the burner (HAB = 1, 2.25, 3.25, 25 mm) c,d) in flame A and g,h) in flame B. The distance z indicates the traveled length of the fluid element between burner exit and sampling probe inlet.

Gururajan et al. [265] have numerically investigated the influence of the boundary conditions of the numerical domain of the simulation of the temperature and species mole fraction profiles with the presence of the sampling probe. They have shown how important the boundary conditions are and that they can influence the simulated mole fractions. Deng et al. [173] omitted this question by a conjugate heat transfer computation including the heat transport within the probe. Within the scope of this work, the boundary conditions were experimentally determined from the molecular beam sampling TOF and ion sampling TOF. Struckmeier et al. [82] have experimentally investigated the influence of the sampling probe geometry in particular angle and orifice diameter on the species concentration and the influence of the sampling probe on the flame temperature. By comparison of the perturbed temperature (T_{FKT}) and NO-LIF measurements they have shown how the temperature profile prior to the sampling probe changes compared to the unperturbed flame. The perturbed temperature profile T_{FKT} is frequently used for 1D simulations. In this work, for the first time the perturbed temperature profile (T_{FKT}) was evaluated against 2D simulation for setups used for molecular beam sampling and for setups with ion sampling. Most recently, Hansen et al. [266] investigated the temperature drop due to the presence of the sampling probe experimentally. Under the one-dimensional model assumption, isotherms above the burner no longer run in horizontal order, but form a two-dimensional temperature field. As a result, the temperature curve in the area in front of the sampling probe changes in comparison to the unperturbed flame. Within this work, the 2D simulation reveal how the temperature is perturbed at various distances to the sampling probe and what the gradients are at the orifice of the sampling probe. Skovorodko et al. [264] investigated the flow in the vicinity of the sampling probe and stated a significant effect of radial diffusion on the distribution of concentrations in the plane of the orifice. Deng et al. [173] studied the sampling probe effect on laminar flat flames and found that the suction effect is a dominant mechanism for the perturbation caused by the probe. In this work, 2D simulations show the suction-effect for two different sampling probe apertures under the same flame conditions at various distances from the burner. It could be shown for the first time in experiment and 2D simulation, that the suction effect decreases for smaller orifices and changes the shape of the species mole fraction profiles especially close to the burner surface.

11.6 Interpretation of ion signals

To determine mole fractions of the individual intermediates, the relationship between the signal intensity in the mass spectrometric measurements and the mole fraction of the species in the flame must be known. In neutral sampling mode, the molecules are ionized in a controlled process step by electron or photoionization before detection and the relationship between signal and mole fraction depends mostly on the ionization efficiency and can be accounted for by known ionization cross sections. When sampling naturally occurring ions from the flame the signal strength is dominated by the transfer efficiency. These transfer efficiencies can be very high when modern ion optical devices are used, e.g., in our instrument the transfer efficiency is estimated to be approximately 80 %, and the ions can be measured with high sensitivity.

Since the total ion mole fractions in flames are very small (mole fractions $\ll 10^{-9}$), the chemical reactions of the ions probably play only a minor role in flame chemistry. For a meaningful interpretation of the ion measurements, it is consequently more appropriate to find the connection between the ion signal and the mole fraction of the neutral species in the flame from which the ion was generated. The methane flames contain comparatively few different intermediates and were well suited for a systematic test of a new quantification approach. The methane flames investigated here have in common that the particularly strong ion signals are caused by protonated species of neutral flame components. Our measurements reveal how sensitively these ions can be detected over a large mass range. At higher mass-to-charge ratios (m/z ratios) the signals of protonated polyynes, polyenes and aromatic species are present. Preliminary measurements with this setup suggest that for aromatic molecules mole fractions in the ppt-range can be detected.

In addition to the flame ions, some signals can be attributed to water clusters formed during molecular beam sampling. The strongest ion signals are detected for oxygenated ion species, e.g. $(\text{CH}_3\text{OH})\text{H}^+(\text{H}_2\text{O})_n$, $\text{C}_2\text{H}_3\text{O}^+(\text{H}_2\text{O})_n$, $\text{H}_3\text{O}^+(\text{H}_2\text{O})_n$ with $n = 0$ to 3 and also hydrocarbon ions, e.g. $\text{C}_3\text{H}_3^+(\text{H}_2\text{O})_n$ are identified. The same important ions in methane flames were also identified in previous work [30]. $(\text{CH}_3\text{OH})\text{H}^+$ (here referred to as CH_5O^+) is formed by (R 11-5) and (R 11-6) according to the reaction mechanism proposed by Chen et al. [222]:



Depending on reaction conditions (R 11-6) contributes up to 99% to the formation of the protonated methanol [203].

$\text{C}_2\text{H}_3\text{O}^+$ is formed by (R 11-7) – (R 11-11) [222]:



Because of the comparatively large number of reactions forming $\text{C}_2\text{H}_3\text{O}^+$ only CH_5O^+ is considered for our first attempts at quantifying the ion signals and only reaction (R 11-6) will be used. The main proton donor H_3O^+ and its water clusters $\text{H}_3\text{O}^+(\text{H}_2\text{O})_n$ with $n = 0$ to 3 are considered in the subsequent analysis. The water clusters are artefacts of the flame sampling and also observed in other studies [30, 222, 266]. They are most likely formed in the first couple of μm inside of the probe as a result of the rapid pressure and temperature drop that the gas sample experiences during molecular beam sampling. These clusters are only stable at low temperatures and pressures [241].

Since only signal ratios are used in the following calculations no further attempts at quantifying the ion signals in the form of mole fractions have been performed and it is assumed that all signals are detected with the same efficiency, e.g. mass discrimination effects are neglected.

The omission of mass discrimination effects is justified because only the quadrupole ion guide exhibits mass discrimination effects. With the voltage and RF-settings used in this work ions of molecular mass 0 - 1000 amu are transmitted on stable trajectories by the quadrupole ion guide. The mass discrimination of this device appears to be binary, e.g. the ion is either detected or it is not detected.

Reaction 6 is expected to be dominant for $(\text{CH}_3\text{OH})\text{H}^+$ formation at higher HAB [222] and is chosen as the test reaction for our quantification approach. Proton transfer reactions are very fast. For example, the rate constant of the reaction $\text{H}_3\text{O}^+ + \text{CH}_3\text{OH} \rightleftharpoons (\text{CH}_3\text{OH})\text{H}^+ + \text{H}_2\text{O}$ is $k = 1.51 \cdot 10^{15} \text{ mol/cm}^3\text{s}$ at 1500 K and the reaction has no activation energy [203]. Accordingly, it can be assumed that the equilibrium is set at every point in the flame and to some extent during the sampling process. With known thermodynamic values for reaction enthalpy ($\Delta_r H(T)$) and entropy ($\Delta_r S(T)$), the equilibrium constant (K_x) can be determined as a function of temperature. If the ion under consideration ($(\text{CH}_3\text{OH})\text{H}^+$) is formed mainly from the reaction with H_3O^+ , K_x can then be used together with the ion signals for H_3O^+ , $(\text{CH}_3\text{OH})\text{H}^+$ ($S_{(\text{CH}_3\text{OH})\text{H}^+}$, $S_{\text{H}_3\text{O}^+}$) and the measured parameters pressure p , Temperature T , mole fraction of water ($x_{\text{H}_2\text{O}}$) to determine the mole fraction of neutral methanol ($x_{\text{CH}_3\text{OH}}$) in the flame according to the following equations:

$$K_x = \frac{x_{\text{H}_2\text{O}} \cdot x_{(\text{CH}_3\text{OH})\text{H}^+}}{x_{\text{H}_3\text{O}^+} \cdot x_{\text{CH}_3\text{OH}}} = \left(\frac{p^\circ}{p}\right)^{v_{\text{total}}} \cdot \exp\left(\frac{-\Delta G_r(T)}{RT}\right) = \left(\frac{p^\circ}{p}\right)^{v_{\text{total}}} \cdot K_p \quad (11-2)$$

The sum of the stoichiometric coefficients of the reaction is indicated by ν_{total} , with $\nu_{\text{total}} = 0$ for (R 11-6). Converting equation (11-2) to the methanol mole fraction yields:

$$x_{\text{CH}_3\text{OH}} = x_{\text{H}_2\text{O}} \cdot \frac{S_{(\text{CH}_3\text{OH})\text{H}^+}}{S_{\text{H}_3\text{O}^+}} \cdot \frac{1}{K_x} = x_{\text{H}_2\text{O}} \cdot \frac{S_{(\text{CH}_3\text{OH})\text{H}^+}}{S_{\text{H}_3\text{O}^+}} \cdot \left[\exp\left(\frac{-\Delta G_r(T)}{RT}\right) \right]^{-1} \quad (11-3)$$

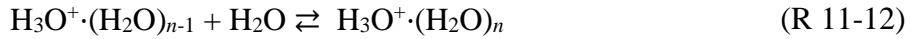
Thermodynamic data are calculated using NASA-Polynomials and NASA-coefficients from [75].

In comparison to the evaluation of measurements with the MBMS interface, the efficiency of the ionization does not have to be explicitly known with this evaluation method. Since ionization efficiencies or cross sections are typically the largest sources of error in the quantitative evaluation of mass spectra with electron or photoionization [24], this is an advantage of measurements with the ion interface. A crucial difficulty in evaluating the equilibrium approach, is to determine the temperature at which the final equilibrium has established; i.e. whether the signal ratio of the ions reflects the equilibrium state at the temperature in the flame, in the boundary layer of the probe, in the molecular beam in front of or behind the Mach disk. The 2D simulations above have shown that the perturbed temperature profile measured by a thermocouple in the flame is a reasonable representation of the temperature of the gas sample in the flame for large distances from the burner. In the following, the temperatures at other positions of the process relevant for the quantification of the ion signals were determined experimentally, e.g. in the perturbed flame, at different positions of the gas dynamic expansion of the molecular beam, in the molecular beam behind the Mach disk, and on the wall of the sampling probe.

11.6.1 Temperatures in the molecular beam

In the flame, the temperature is reduced compared to the unperturbed flame because the sampling probe acts as a heat sink. Inside of the sampling probe, the isentropic expansion further reduces the temperature substantially [282]. The measured signals of the water clusters and their known thermodynamic data are used to deduce the temperature in the molecular beam expansion at which the collision rate in the beam has dropped sufficiently to freeze the reactions. The formation of water clusters is very fast, and the calculated freezing temperatures are an indication of the molecular beam temperature at which the reactions stop. If (R 11-6) proceeds with similar rate constants in the molecular beam as the water cluster formation, the calculated molecular beam temperatures must be used in conjunction with equation (11-3) to calculate the mole fraction of neutral methanol.

Water clusters are observed in all molecular beam sampling systems independent of the method of ion transport from the exit of the sampling probe into the mass spectrometer [283]. This is an indication that the ions are formed in the probe and not in the ion optics of the ion-interface used here. Water clusters are formed according to the reaction:



with $n = 1$ to 3. The thermodynamic properties and the position of the equilibria at different partial pressures of water and at different temperatures have been studied in detail by Kebarle et al. [241, 245]. The studies show that water clusters with $n > 2$ are not stable at flame temperatures. In contrast, in the mass spectra the water cluster with $n = 3$ is observed with the highest intensity. The shapes of the cluster profiles look similar to the profiles of flame ions, because the clusters are formed in reactions with flame-made H_3O^+ . It is reasonable to assume that the equilibrium of water cluster formation shifts at the low molecular beam temperatures from the flame made H_3O^+ as the dominant ion to the larger water clusters. Using the equilibrium approach the temperature at which the water clusters freeze out can be calculated Eq. (11-4) – Eq. (11-6) with the thermodynamic data ($\Delta G_{r,n=1}(T)$, $\Delta G_{r,n=2}(T)$, $\Delta G_{r,n=3}(T)$) from references [241, 245]. The equilibrium temperatures are calculated for different water cluster formation reactions (R 11-12), e.g. for $n = 1$ ($m/z = 19$ and $m/z = 37$, Eq. (11-4) as T_{W37} , $n = 2$ ($m/z = 37$ and $m/z = 55$, Eq. (11-5) as T_{W55} , and $n = 3$ ($m/z = 55$ and $m/z = 73$, Eq. (11-6) as T_{W73} and are shown in Figure 11-11.

$$T_{W37} = \frac{-\Delta G_{r,n=1}(T)}{R} \cdot \frac{1}{\ln \left(\left(\frac{S_{\text{H}_3\text{O}^+\cdot(\text{H}_2\text{O})}}{S_{(\text{H}_3\text{O}^+)} x_{\text{H}_2\text{O}}} \right) / \left(\left(\frac{p^\circ}{p} \right)^{v_{\text{total}}} \right) \right)} \quad (11-4)$$

$$T_{W55} = \frac{-\Delta G_{r,n=2}(T)}{R} \cdot \frac{1}{\ln \left(\left(\frac{S_{\text{H}_3\text{O}^+\cdot(\text{H}_2\text{O})_2}}{S_{(\text{H}_3\text{O}^+\cdot\text{H}_2\text{O})} x_{\text{H}_2\text{O}}} \right) / \left(\left(\frac{p^\circ}{p} \right)^{v_{\text{total}}} \right) \right)} \quad (11-5)$$

$$T_{W73} = \frac{-\Delta G_{r,n=3}(T)}{R} \cdot \frac{1}{\ln \left(\left(\frac{S_{\text{H}_3\text{O}^+\cdot(\text{H}_2\text{O})_3}}{S_{(\text{H}_3\text{O}^+\cdot\text{H}_2\text{O})_2} x_{\text{H}_2\text{O}}} \right) / \left(\left(\frac{p^\circ}{p} \right)^{v_{\text{total}}} \right) \right)} \quad (11-6)$$

The resulting temperature profiles as function of different sampling positions are shown in Figure 11-11. The freezing temperatures do not depend on the sampling position. The lowest temperature is reached for the water cluster $\text{H}_3\text{O}^+\cdot(\text{H}_2\text{O})_3$ and the highest for $\text{H}_3\text{O}^+\cdot(\text{H}_2\text{O})$. The rate constant of (R 11-6) [222] is slightly smaller than the reaction rate of (R 11-12) with $n = 1$ (assuming a base pressure of ~ 3 Pa for this third order reaction) [245], so that it can be expected that the formation of protonated methanol freezes out at temperatures above $T_{W37} \approx 600$ K.

Figure 11-11 also shows a temperature profile measured with a thermocouple in contact with the inside of the probe (T_{probe}) and in the molecular beam at approximately 1 mm distance from the probe orifice (T_{MB}). The gas temperature at 1 mm behind the probe is almost constant at 1000 K for every HAB as indicated by the temperature profile T_{MB} in Figure 11-11. Also, equilibrium temperatures of all water cluster formation reactions are smaller than the measured molecular beam temperatures at 1 mm distance from the probe orifice. Assuming an ideal adiabatic molecular beam expansion the terminal Mach numbers ($Ma =$

8.2-11.5) and lowest temperatures in the molecular beam ($T = 10-90$ K) for the sampling conditions here, are reached in approximately 2-10 mm distance from the probe orifice. The experimentally observed equilibrium temperatures can be rationalized by assuming that the water cluster formation reactions “freeze-out” at distances between 1 and 5 mm behind the orifice. The calculated equilibrium temperatures confirm that the water clusters are formed in the molecular beam. Since the temperatures of the water clusters (T_{W37} , T_{W55} , T_{W73}) determined from ion signals are measured behind the expected position of the Mach disc, the Mach shock is probably not very pronounced in our setup and the equilibrium does not seem to change when passing the position of the Mach disc.

11.6.2 Temperatures of probe and flame

The radiation-corrected temperature profiles measured with a thermocouple in the flame (T_{TC}) is also presented in Figure 11-11. A temperature profile at the probe orifice (T_{MA}) calculated according to [284] from the thermocouple measured temperature profile T_{TC} for an acceleration to a Mach number $Ma = 1$, and a profile determined from the sampling rate (T_{FKT}) in the mass spectrometric measurement complete the set of all available temperature profiles for this flame. The calculation of T_{FKT} is based on the fact that the pressure in the mass spectrometer and the signal strength decrease when the density in front of the probe decreases due to a higher flame temperature [82]. From this temperature dependence, a relative temperature profile is obtained, which is adjusted here to the temperature of T_{MA} . In addition, the temperature profiles obtained in the 2D-simulations for the four different sampling positions ($HAB = 1 / 2.25 / 3.25 / 25$ mm) discussed in detail above are shown as T_{S1} , T_{S2} , T_{S3} and T_{S25} , respectively to visualize the difference between unperturbed and perturbed flame and enable consistency checks between the profiles. The two-dimensional flow simulations of the flame reactor described before were performed in order to better quantify the change in temperature due to the presence of the probe at different probe positions. Since the temperature of the probe hardly changes as a function of HAB (see T_{probe}), an isothermal probe was assumed for the simulations in order to reduce the computing time. Deviations of the simulated temperature in the preheating zone and in the exhaust gas of the flame can become smaller in a three-dimensional simulation and with explicit calculation of the heat transfer between flame and probe. In the reaction zone of the flame, the end points of the simulated values coincide with the profiles T_{Ma} or T_{FKT} . The T_{FKT} profile approximates the temperature history of the analyzed gas sample most accurately and the 2D-simulations explain the observation that a 1D flame simulation with a given T_{FKT} typically shows a good agreement between experiment and simulation [25, 83], because at the inlet of the probe the gas sample has the temperature found by the 2D-simulation. In summary, the temperature profiles in Figure 11-11 cover the complete temperature history of a gas sample from the perturbed flame (T_{TC}) to the boundary layer of the probe (T_{Ma} , T_{FKT}), and during the sampling process (T_{MB} , T_{probe} , T_{W37} , T_{W55} , T_{W73}) obtained from different experimental sources, which can potentially be used to calculate the methanol mole fraction. For the analysis of the ion signals, the T_{FKT} is expected to provide the correct temperature for the quantification of the ion signals by the equilibrium approach, unless the ion is made

in the molecular beam. In this case, the temperature is smaller than the molecular beam temperature T_{MB} as demonstrated for the water cluster in Figure 11-11.

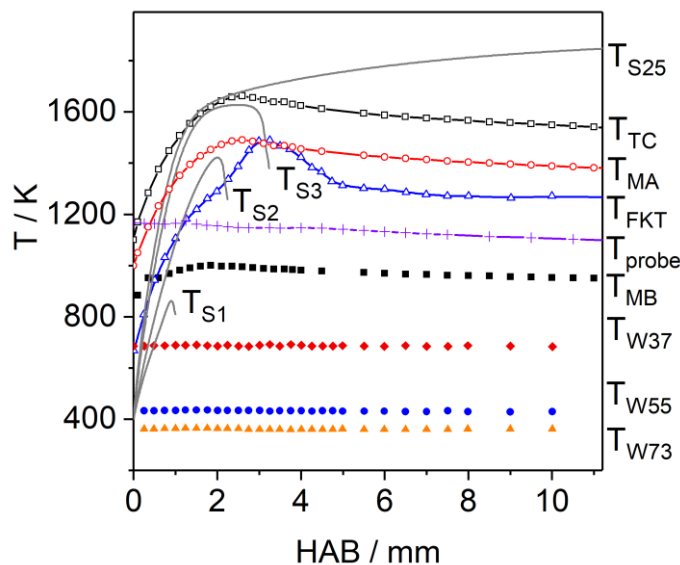


Figure 11-11. Temperature history of a gas sample from the perturbed flame (T_{TC} , T_{Ma} , T_{FKT}), and during the sampling process (T_{MB} , T_{probe} , T_{W37} , T_{W55} , T_{W73}) obtained from different experimental sources. Thermocouple measurement of the perturbed flame (T_{TC}), perturbed flame (T_{Ma} , T_{FKT}), molecular beam temperature in a distance of one mm behind the orifice (T_{MB}). Equilibrium temperatures are calculated by solving Eq. (11-2) for temperature profiles for freezing of the water clusters determined from the equilibrium data for water cluster formation with $m/z = 37$ (T_{W37}), $m/z = 55$ (T_{W55}) and $m/z = 73$ (T_{W73}).

11.6.3 Calculation of mole fraction profile of methanol based on protonated methanol ion signals

According to the study of Chen et al. [222] (R 11-6) is the dominant reaction forming $(CH_3OH)H^+$. Depending on reaction conditions it can contribute up to 99% to the formation of the protonated methanol [203]. Based on the assumption that the proton transfer reaction (R 11-6) is the dominant reaction forming $(CH_3OH)H^+$ and an equilibrium is achieved, the mole fraction of neutral methanol (see Figure 11-12) is calculated according to Eq. (11-2). The inputs for Eq. (11-2) are: Ion signals of $(CH_3OH)H^+$ and H_3O^+ including its hydrates in flame C, water mole fraction of flame B, the temperature at which the equilibrium is achieved, and the equilibrium constant calculated from thermodynamic data ($\Delta H(T)$, $\Delta S(T)$) obtained from database of Goos, Burcat and Ruscic [75] for various temperature profiles. It should be mentioned that it is necessary to use the same sampling probe during species and temperature measurements to maintain the same sampling conditions. Since the equilibrium constant and free reaction enthalpy $\Delta G(T)$ are strongly temperature dependent, the temperature profile used in the calculation has a large impact on the resulting methanol mole fraction. The mole fraction profiles resulting from the use of different temperatures are summarized in Figure 11-12b: The normalized ion signal profile of $(CH_3OH)H^+$ in flame C is shown Figure 11-12b. The ion signal profile of $(CH_3OH)H^+$ peaks very close to the burner

surface at around $HAB = 1$ mm and the baseline is reached at $HAB = 3$ mm. The mole fraction profile of neutral CH_3OH is calculated from the ion signal with Eq. (11-2) using the temperature profiles T_{TC} , T_{FKT} and T_{MB} . These profiles represent the three possible cases: T_{TC} – the ion signal is not affected by cooling in the boundary layer of the probe, T_{FKT} – the ion signal is affected by equilibrium shifts due to cooling by the probe and suction, but not by equilibrium shifts due to cooling in the molecular beam, T_{MB} – the cooling in the molecular beam determines the measured equilibrium composition. The resulting mole fraction profiles are shown in Figure 11-12b. The calculated maximum mole fraction of CH_3OH decreases with the decreasing maximum temperatures of T_{TC} , T_{FKT} and T_{MB} by one order of magnitude. Simultaneously, the profile shape changes. The profile based on T_{FKT} exhibits the most pronounced maximum at the largest HAB . This shape reflects the larger gradients of this temperature profile and the fact that it is not as smooth as the temperature profiles measured by thermocouple.

In order to determine which temperature profile gives the most realistic methanol mole fraction in the flame, the calculated profiles in Figure 11-12b are compared to 1D simulations of the flame (B and C) with the perturbed temperature profile of flame B as input and the experimental and simulated mole fraction profile of methanol in flame A. These profiles are shown in Figure 11-12a. It can be stated that independent of the temperature profile used in the quantitative evaluation of the ion signal the order of magnitude of the methanol mole fraction is correctly obtained. MBMS measurements are of course more accurate for methanol as indicated by the error bars shown for the measurement in flame A because methanol can be calibrated directly, and independent ionization cross sections are reported. For other species, e.g. large PAH, these data are not always readily available and obtaining the correct order of magnitude of a mole fraction can be a step forward. Nevertheless, use of the best temperature profile for data reduction can improve the deviation. In the following we will discuss which temperature profile appears as the most suited.

The methanol mole fraction values calculated using T_{FKT} fit best to values of the mole fraction profile measured by the established EI-MBMS technique (Figure 11-12a).

The shape of the simulated and measured mole fraction profile in flame A are in reasonable agreement, but the simulated maximum mole fraction of CH_3OH is located 1 mm downstream of the measured maximum, which indicates an underestimation of the perturbation in the 1D-simulation. We expect a similar mismatch of the position of the maximum mole fraction in the experiment and simulation for flame C.

The simulated profile of flame C peaks closer to the burner and its mole fraction is approximately a factor of three lower than the value obtained with T_{FKT} . The mole fraction values obtained with T_{MB} fit the simulated values better.

The following arguments need to be considered when deciding which temperature profile to use in the quantification of the ion signal. The profile shapes and the shift between the simulated and experimental mole fraction profiles suggests that T_{FKT} gives the better result. As discussed above, suction by the probe leads to aspiration and analysis of fractions of gas with higher temperature and longer residence time in the flame. From the profiles in Figure 11-12b it is clear that higher temperatures lead to larger methanol mole fraction calculated from the ion measurement. Consequently, the observed discrepancy in the maximum mole fraction value may be attributed to suction. Methanol is an intermediate and as discussed

above the exact changes of intermediate profiles caused by probe perturbation of the flame are difficult to predict in detail based on 1D-simulations. Unfortunately, the reduced chemical reaction mechanism used in the 2D-simulations does not include methanol formation, so a detailed analysis is not possible here.

This result is expected because the dominant formation reaction of $(\text{CH}_3\text{OH})\text{H}^+$, (R 11-6), proceeds mainly in the flame. The reasonable agreement implies that cooling in the molecular beam does not affect the equilibrium substantially. The agreement also suggests that contributions to the $(\text{CH}_3\text{OH})\text{H}^+$ signal by other reactions are indeed negligible.

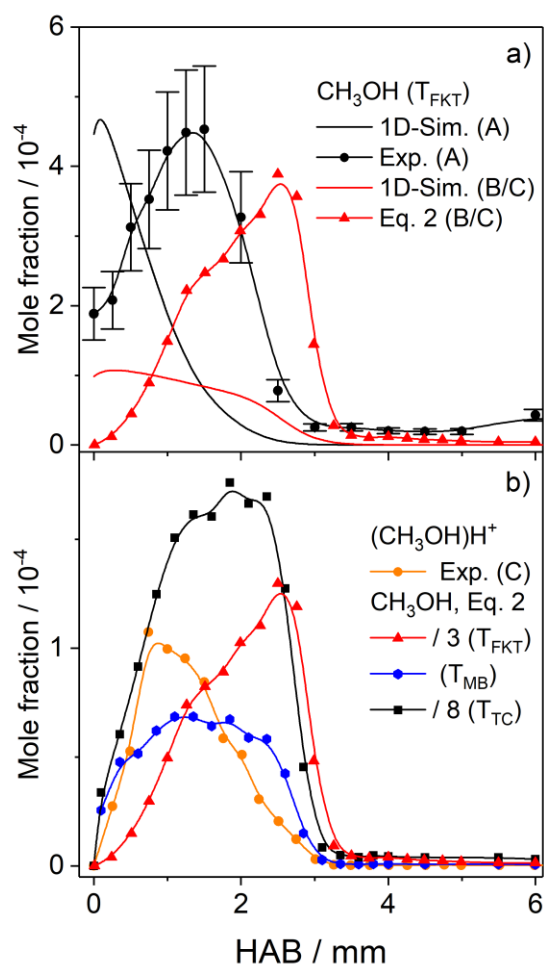


Figure 11-12 a) Measured and simulated mole fraction profile of CH_3OH in flame A, equilibrium mole fraction (Eq. (11-2)) and simulated mole fraction of CH_3OH in flame B, b) Equilibrium mole fraction profile CH_3OH in flame B obtained by equation (Eq. (11-2)) with the measured perturbed temperature profile (T_{FKT} , T_{TC} , T_{MB}) as input. $(\text{CH}_3\text{OH})\text{H}^+$ signal intensities profile is normalized to the maximum of the 1D-Simulation in flame B. The symbol / indicates the divisor.

In summary, a correlation between cations and their neutral counterparts has been demonstrated and points at a strategy to obtain qualitative and quantitative knowledge about the relevant flame species from ion sampling measurements. This technique is particularly interesting for species which often elude detection in neutral mode because of their low concentrations. The rate constants for reactions of ions are often very inaccurate or unknown.

While this is also true for the thermodynamic data of ions, these can in principle be measured much easier. The equilibrium approach demonstrated here for methanol only uses thermodynamic and experimental data for the quantification. It is limited in the respect that it does not take proton transfer from other species than H_3O^+ into account and therefore neglects the different proton affinities of flame molecules. This may be solved in future work by performing an equilibrium calculation using thermodynamic data or the better known proton affinities of different flames species at each point in the flame.

11.7 Conclusions

The work investigates the influence of the sampling probe on the temperature profiles, species profiles and species residence times and interprets ion signals of $\text{CH}_4/\text{O}_2/\text{Ar}$ laminar low-pressure flames in molecular beam measurements. In this study a quartz sampling probe and metal sampling probe were used to transfer a sample from a flat flame to the mass spectrometer. Most importantly, the quartz probe sucked the gas sample through a smaller orifice diameter ($D = 90 \mu\text{m}$) than the metal probe ($D = 550 \mu\text{m}$) into the vacuum system used to transfer a sample to the mass analyzer.

Experimental mole fraction profiles of flame species, e.g., CH_4 , O_2 , H_2O , CO_2 , CO , H_2 , CH_3OH , C_2H_4 , and CH_3 and flame temperature profiles were compared to 2D- and 1D-simulations.

For both sampling probes our results show, that three aspects must be considered when evaluating the effect of the sampling probe on the measured profiles. First, the sampling probe can reach a higher temperature than the gas at the sampling point. As a result, it may heat the flame gases near the burner. Second, the probe sucks in gases from regions upstream and downstream of the probe orifice. As a result, fractions of gas with varying residence times are simultaneously analyzed at each sampling position. These gases can also have higher or lower temperatures. Third, on the centerline in front of the probe suction pulls a gas sample towards the orifice, leading to deformed iso-lines of temperature and varying streamlines.

The results for both sampling probes demonstrate that especially suction is a governing type of perturbation of the flame structure. To get an insight into the suction the residence times of the gas samples along streamlines at various HAB are evaluated. At small HAB, the perturbation of the streamlines by suction affects the gas sample during almost its entire residence time in the flame and can increase the residence times of the sample fractions up to a factor of 2 and 17 for a sampling orifice diameter of $D = 90 \mu\text{m}$ and $D = 550 \mu\text{m}$, respectively. At larger HAB, a significant distortion of the streamlines only occurs for a fraction of the residence time of the gas sample in the flame and the sampled fractions vary by a factor of 1 and 1.13 for a sampling orifice diameter of $D = 90 \mu\text{m}$ and $D = 550 \mu\text{m}$, respectively. Our results show, that the magnitude of suction can be reduced by using a small orifice for the sampling probe aperture. This result can be generalized as a design rule for the sampling probe that helps to minimize the grade of perturbation on the 1D structure of flat flames during flame sampling at low-pressure.

The suction effect overlaps with the cooling effect by the sampling probe during flame-sampling. The perturbed temperature used as input for 1D-simulation takes the flame cooling

by the sampling probe into account. The whole range of experienced path and residence times (reaction times) the sample has passed due to suction are not captured sufficiently enough by the perturbed temperature profile. This also explains why the 1D-simulation with the measured temperature profile as input often fits to experiments better for larger HAB than for the region at small HAB.

Ion species, e.g. H_3O^+ , and $(\text{CH}_3\text{OH})\text{H}^+$ were analyzed by means of ion sampling for the same flame conditions with a new flame sampling experiment with high sensitivity. This detection method is especially valuable for species, which over time block the probe in molecular beam sampling or can only be doped into flames in small concentrations. It is desirable to relate the ion signal to the concentrations of the neutral molecules that produce these ionic species for the validation of chemical kinetic models. The methane flames investigated here have particularly strong ion signals that are caused by protonated species of neutral flame components originating from very fast proton transfer reactions. Assuming that these reactions are in equilibrium at each position in the flame, the mole fraction of the neutral species can be determined from the equilibrium of the proton transfer reaction using thermodynamic data and the ion signals as input. The challenge in evaluating the equilibrium approach is to figure out the temperature at which the final equilibrium is present. Our results have shown that the equilibrium is established at each sampling point. A systematic analyses shows, that the methanol mole fraction values obtained from the ion signals and thermodynamic data by using an equilibrium calculation with the perturbed temperature profile as input fit best to values of the mole fraction profile measured with the aid of EI-MBMS. Deviations in mole fraction and profile shape close to the burner surface can be traced back to the suction effect. Vice versa, the calculation of equilibrium temperatures for the proton transfer reactions can help to determine if an ion was formed in the flame or during sampling and is a useful tool to simplify the analysis of ion sampling mass spectrometry measurements. This study demonstrates one promising approach to access quantitative speciation data that are useful for kinetic studies in laminar flames from the measurement of naturally occurring flame ions. In the future, the ion measurements can potentially be used to determine the mole fraction profiles of those species that are below the detection limit in conventional flame-sampling MBMS studies and they can provide a cross check for quantification because the mole fraction values are affected by different sources of error in both techniques.

12 Summary

Nanomaterials are becoming increasingly important for daily life and their potential for new and unexplored applications is practically unlimited. The control of their composition and particle size enables a new class of nanoparticles to be produced with new properties. The scientific question about the formation of inorganic nanoparticles in the gas phase has been investigated for decades, but the basic principles of particle formation are still not understood completely. The DFG research unit FOR2284 addresses this problem and investigates the entire process from the precursor to the formed particles. The research focuses on the formation of nanomaterials of various structures. The structures are classified as primary particles (particles with a narrow size distribution), secondary particles (agglomerates) and tertiary particles (surface-functionalized complex structures). Understanding the initial decomposition of the precursor and its interaction with the flame is a prerequisite to optimize and scale the synthesis process in order to produce specific nanoparticles. Overall, *this work* deals with the fundamentals of the precursor decomposition, precursor and flame interaction, formation of growth species for particle inception and the effect of flame conditions on the gas phase processes in the flame synthesis. Here, for the production of the two target materials silicon dioxide and iron oxide the precursor tetramethylsilane (TMS) and iron pentacarbonyl ($\text{Fe}(\text{CO})_5$) are used, respectively. Experimental species profiles are measured in premixed, synthesis flames with the aid of a molecular beam mass spectrometer and complementary experimental data are obtained by means of a novel ion sampling technique. In this work species profiles in flames were added to the database of the reaction kinetics data of species containing the elements Fe/O/H/C and Si/O/H/C. Reproduction of speciation data in flames constitutes a stringent test case for reaction mechanism development or improvement.

Tetramethylsilane is a frequently used precursor for the gas phase synthesis of silicon dioxide nanoparticles. The *combustion of TMS* is studied in chapter 6 [86]. It includes the precursor decomposition in $\text{H}_2/\text{O}_2/\text{Ar}$ -flames and its interaction with the flame. The experiments are performed under conditions similar to those in the existing literature. For the first time, Si-C-O-H, Si-O-H and C_1 - C_2 species are detected with the aid of the MBMS technique in synthesis flames. The results show, that TMS (600 ppm) decomposes under fuel-lean flame conditions ($\varphi = 0.6$) according to the following sequence: $\text{TMS} \rightarrow \text{Si}(\text{CH}_3)_3\text{CH}_2 \rightarrow \text{Si}(\text{CH}_3)_3\text{CH}_2\text{O}_2 \rightarrow \text{Si}(\text{CH}_3)_3\text{O} \rightarrow \text{Si}(\text{CH}_3)_3\text{OH} \rightarrow \text{Si}(\text{OH})_3 \rightarrow \text{Si}(\text{OH})_4$. The decomposition can briefly be described as follows: In the initial decomposition step the precursor reacts with flame species and forms a $\text{Si}(\text{CH}_3)_3\text{CH}_2$ radical via H-abstraction from a methyl group. Subsequently the radical reacts with O_2 in order to form a peroxide $\text{Si}(\text{CH}_3)_3\text{CH}_2\text{O}_2$ (or its isomer). The species $\text{Si}(\text{CH}_3)_3\text{CH}_2\text{O}_2$ is the first intermediate in the decomposition sequence of the precursor. With increasing distance from the burner surface, the molecular decomposition of the peroxide yields $\text{Si}(\text{CH}_3)_3\text{O}$ and CH_2O . Subsequent reactions with H_2 form the silanol $\text{Si}(\text{CH}_3)_3\text{OH}$. The oxidation of the precursor occurs in the region of the flame where the flame temperature increases. The monomers SiO_2 and $\text{Si}(\text{OH})_4$

and silicon-containing clusters such as $\text{Si}_4\text{O}_{10}\text{H}_4$, $\text{Si}_5\text{O}_{12}\text{H}_4$ and $\text{Si}_6\text{O}_{14}\text{H}_4$ are present at large distances from the burner in significant amounts. Timoshkin [134] has shown that the silicon-containing cluster $\text{Si}_4\text{O}_{10}\text{H}_4$ is stable at high temperature conditions and can either have a linear or a cage-like structure. One pathway towards the nanoparticles is expected to proceed via the clusters growth sequence $\text{Si}(\text{OH})_4 \rightarrow \text{Si}_4\text{O}_{10}\text{H}_4 \rightarrow \text{Si}_5\text{O}_{12}\text{H}_4 \rightarrow \text{Si}_6\text{O}_{14}\text{H}_4$. These intermediates are likely to be the precursors for particle formation.

The knowledge of the reaction kinetics data in form of mole fraction profiles of intermediate gas phase species is needed for the creation and evaluation of a *chemical reaction kinetics model for TMS*. In the framework of the DFG research unit FOR 2284, the work of this thesis has contributed to reaction mechanism development of tetramethylsilane-doped flames by Janbazi et al. (chapter 7 and/or in publication [185]). The mechanism is evaluated for lean $\text{H}_2/\text{O}_2/\text{Ar}$ flames ($\varphi = 0.6$) with the addition of TMS in the range between 400 – 800 ppm. The reaction rates in the kinetics reaction mechanism of TMS are obtained by using reactivity analogies to hydrocarbon-chemistry (neopentane, C_5H_{12}), by utilizing theoretical calculations and by including a genetic algorithm with experimentally determined mole fraction profiles as target data for optimization by Janbazi et al. [185]. The thermodynamic data and transport data are obtained by Janbazi et al. [153, 185]. Although many gas phase reactions are considered to describe the underlying chemistry of the complete oxidation of TMS, there has been a need to include global reactions to reproduce the experiments. The use of global reactions indicates that still some reactions are missing in the reaction mechanism. Further research is needed that focuses on the missing reactions involving silicon-containing species.

Chapter 8 deals with the scientific question of how the *equivalence ratio* of the flame influences the initial decomposition step of TMS, the formation of the major silicon-containing intermediates and of the production of silicon dioxide nanoparticles. The combustion of TMS is systematically investigated in a numerical and experimental study (chapter 8 and/or in reference [236]). The developed reaction model of TMS oxidation is evaluated for flame equivalence ratios ranging from fuel-lean ($\varphi = 0.6$) to fuel-rich ($\varphi = 1.2$). The results show that addition of TMS into the $\text{H}_2/\text{O}_2/\text{Ar}$ flame leads to an increase in the flame temperature for all equivalence ratios. The increase in the temperature can be explained by the exothermal oxidation reactions of TMS. The addition of TMS into the flame results in a shift of the major flame species (H_2 , O_2 and H_2O) closer to the burner surface in simulation and experiments. The simulation shows that the initial step of the precursor decomposition proceeds via the H-abstraction from a methyl group. A rate of production analysis reveals that the initial reaction proceeds via reactions with $\text{H} + \text{TMS} \leftrightarrow (\text{CH}_3)_3\text{SiCH}_2 + \text{H}_2$ followed by $\text{OH} + \text{TMS} \leftrightarrow (\text{CH}_3)_3\text{SiCH}_2 + \text{H}_2\text{O}$. The reaction of $\text{O} + \text{TMS} \leftrightarrow (\text{CH}_3)_3\text{SiCH}_2 + \text{OH}$ does not significantly contribute to the consumption of TMS. Since the first reaction step from TMS by H is among the few measured rate coefficients in the Si/C/H/O system and the others are based on analogies of H-abstraction from neopentane, further investigation of the reaction rates are necessary to optimize the simulations. The simulation shows that two particle formation routes are distinguishable for all equivalence ratios, which proceed either via the $\text{SiO} \rightarrow (\text{SiO})_n \rightarrow$

particles or through $\text{Si(OH)}_4 \rightarrow \text{Si}_4\text{O}_{10}\text{H}_4 \rightarrow \text{particles}$. The simulation also reveals that the SiO route is more dominant at smaller distances in the flame, while the latter becomes more important at larger distances.

Hexamethyldisiloxane (HMDSO) is another silicon-containing precursor for the silicon dioxide synthesis. Preliminary results of the *combustion of HMDSO* show similarities in the reaction patterns. A detailed description of the combustion of HMDSO can be found in the study of Karakaya et al. [285]. HMDSO decomposes via H-abstraction and forms the peroxide species or its stable monomer. Important gas phase species such as Si(OH)_4 and cluster with the structure $\text{Si}_4\text{O}_{10}\text{H}_4$, $\text{Si}_5\text{O}_{12}\text{H}_4$ and $\text{Si}_6\text{O}_{10}\text{H}_4$ are formed. The future task is to create the kinetics reaction mechanism of HMDSO.

Only a few techniques exist that enable the measurement of molecular species in synthesis flames. Consequently, the development of new measurement methods is urgently needed. Current challenges that present themselves in these efforts are that species elude detection. This is caused due to various reasons like fragmentation of the species by the electron ionization before reaching the detector of the mass spectrometer system, reaching the detection limit of the mass spectrometric system or species condensing on the quartz sampling probe. In this thesis, an analysis method for the gas phase analysis with the aid of ion sampling time-of-flight mass spectrometry is established. The development of the analysis method is divided into three steps.

In the first step, *methane ion chemistry* is studied. The work is performed in collaboration with colleagues from Kaust (chapter 9 and reference [30]). An important objective of this chapter is to develop the ion sampling technique for the analyses of the ion chemistry. Many ions are identified in this study. The experiments are used to evaluate reaction kinetics mechanism for the methane ion chemistry.

In the second part, the *combustion of Fe(CO)_5* and the formation of iron-containing intermediates in iron oxide synthesis flames are investigated (chapter 10 and reference [62]). The decomposition steps of Fe(CO)_5 are analyzed by using photoionization-MBMS (PI-MBMS) at the Advanced Light Source. For the first time, it is experimentally shown that the decomposition of Fe(CO)_5 proceeds stepwise via the sequence $\text{Fe(CO)}_5 \rightarrow \text{Fe(CO)}_4 \rightarrow \text{Fe(CO)}_3 \rightarrow \text{Fe(CO)}_2$. Photoionization has the advantage of avoiding fragmentation during the ionization of the molecules. The decomposition proceeds in the temperature range of 400 K - 700 K in the reaction zone of the flame and the peak maximum of the decomposition product moves in the downstream direction of the flame. Other iron-containing species could not be detected with PI-MBMS. For the first time, experiments show that mole fractions of the flame radicals drastically decrease due to the addition of Fe(CO)_5 . The flame temperature increases with the addition of Fe(CO)_5 . This can be explained by the exothermal oxidation of the precursor. The advancement of the mass spectrometric method is a prerequisite for the investigation of the processes in the gas phase synthesis, since clogging of the sampling probe is an ongoing challenge. The *ion chemistry of Fe(CO)_5 -doped $\text{H}_2/\text{C}_2\text{H}_4/\text{O}_2/\text{Ar}$ flames* is studied with the aid of the ion sampling technique. The addition of C_2H_4 enhances the ion formation in neat hydrogen/oxygen flames. The experiments show that iron-containing ions

are mainly formed at larger HAB. The two dominant reactions are proton transfer reactions like $\text{H}_3\text{O}^+ + \text{Fe}(\text{OH})_2 \leftrightarrow (\text{Fe}(\text{OH})_2)\text{H}^+ + \text{H}_2\text{O}$ and charge transfer by reactions like $\text{H}_3\text{O}^+ + \text{Fe}(\text{OH})_2 \leftrightarrow (\text{Fe}(\text{OH})_2)^+ + \text{H}_2\text{O} + \text{H}$. Both types of reaction lead to the formation of ions of $\text{Fe}(\text{OH})_2$. The same type of reactions are present to form the ions of $\text{Fe}(\text{OH})_3$, Fe_2O_3 , Fe_4O_5 and Fe_5O_5 . The flame structure demonstrates that the oxidation states of iron in the flame appear spatially separated. In the reaction zone, atomic iron with the oxidation state 0 is initially formed. At the end of the reaction zone and at the beginning of the recombination zone of the flame, the iron is present in the form of hydroxides. First, it occurs in the oxidation state +2 and then in the oxidation state +3. The hydroxides finally react in condensation reactions with water release to iron oxide clusters of the form Fe_mO_m with the predominant oxidation state +2. These iron oxides and iron hydroxides are important growth species that are likely to contribute to the particle formation in synthesis flames. The reaction kinetics model of $\text{Fe}(\text{CO})_5$ is evaluated and species are detected which are still missing in the current reaction kinetics model from the literature.

For the understanding of how ions and neutrals are related to each other, first it needs to be understood of how ions are formed. The details of the methane ion chemistry can be found in chapter 9 and the details of iron pentacarbonyl ion chemistry in flames can be found in chapter 10. Our work and studies from the literature show that in the flame ions are present in much smaller concentrations compared to neutrals. So, the kinetics of neutral molecules are more important to describe the flame chemistry. Since the ion chemistry of methane is well understood, the correlation of ions and neutrals in methane flames is studied in chapter 11 in detail. A short description of the ion formation pathways in methane flames is previously given before the results of the equilibrium calculations are described. In hydrocarbon flames ions are produced by chemical ionization with the initial reaction sequence $\text{CH} + \text{O} \leftrightarrow \text{CHO}^+ + \text{e}^-$ followed by $\text{CHO}^+ + \text{H}_2\text{O} \leftrightarrow \text{CO} + \text{H}_3\text{O}^+$. In lean methane flames H_3O^+ , CH_5O^+ and $\text{C}_2\text{H}_3\text{O}^+$ are dominant ions. Methanol (CH_3OH) ions and ketene (CH_2CO) ions are formed according to very fast proton transfer reactions. These are $\text{H}_3\text{O}^+ + \text{CH}_3\text{OH} \leftrightarrow \text{CH}_5\text{O}^+ + \text{H}_2\text{O}$ and $\text{H}_3\text{O}^+ + \text{CH}_2\text{CO} \leftrightarrow \text{C}_2\text{H}_3\text{O}^+ + \text{H}_2\text{O}$, respectively. The correlation is based on the assumptions that the ion formation reactions are mainly proton transfer reactions. The proton transfer reaction is the major path contributing to the formation of 99% of CH_5O^+ [203]. If the contribution of the proton transfer reaction is dominating this approach is also applicable for other species. A rough test whether the approach is applicable is to determine a relative flame temperature profile from the signal ratios, assuming that protonation by H_3O^+ is the main formation reaction. If the resulting profile has the correct shape this is one indication that the approach is reasonable. For $\text{C}_2\text{H}_3\text{O}^+$, the resulting profile does not match with the temperature profile shape. The explanation is that for some ions, e.g. $\text{C}_2\text{H}_3\text{O}^+$, other reactions than the above described proton transfer reactions contribute to the formation of the ion. In the future, the method describing the correlation between the ion and the neutral needs to be extended by the other potential reactions. There is a good chance that also polycyclic aromatic hydrocarbons (PAHs) are protonated by reactions with H_3O^+ because they occur at large distances from the burner where only H_3O^+ is present in high concentrations. The proton affinities of PAH are well known [248]. In chapter 10, the results show that iron-containing species are formed by proton transfer reactions in iron oxide

synthesis flames [62]. In subsequent studies, this quantification approach needs to be applied for the iron-containing ions such as protonated iron hydroxides.

As this work has demonstrated, in the gas phase synthesis of inorganic nanoparticles, the precursor decomposes to smaller molecules by the reactions with flame species. Monomers grow to clusters and subsequently to particles. The results from this work in combination with the data from the literature also show an *intermittent growth of the solid particle* (see Figure 12-1). In iron oxide synthesis, iron atoms contribute to the particle formation close to the burner. Fe-Cluster are formed and decompose behind the flame front. At larger distances, iron oxide particles are formed most probably by the growth species $\text{Fe}(\text{OH})_2$ and $\text{Fe}(\text{OH})_3$. The experiments highlight the importance of hydrolysis reactions at larger distances. For the silicon dioxide synthesis, the experiments show that two flame positions are present where particles are formed. The first position is dominated by the condensation of gaseous SiO_2 . Behind the flame front the particles are formed mainly via the cluster-route of formation with $\text{Si}_4\text{O}_{10}\text{H}_4$ as intermediate. An interesting research target is to extract the particles from the different particle formation positions in a controlled way from the synthesis flame. It is possible to quench the reactions and to stabilize the particles from the different positions in the flame for further processing such as coating. An aim is to use the growth species as intrinsic synthesis parameter to manipulate the properties of the nanoparticles with respect to the chemical composition, oxidation states and chemical structure. The work in this thesis has presented techniques to measure the flame structures, which are needed for controlled manipulations and use of flame conditions.

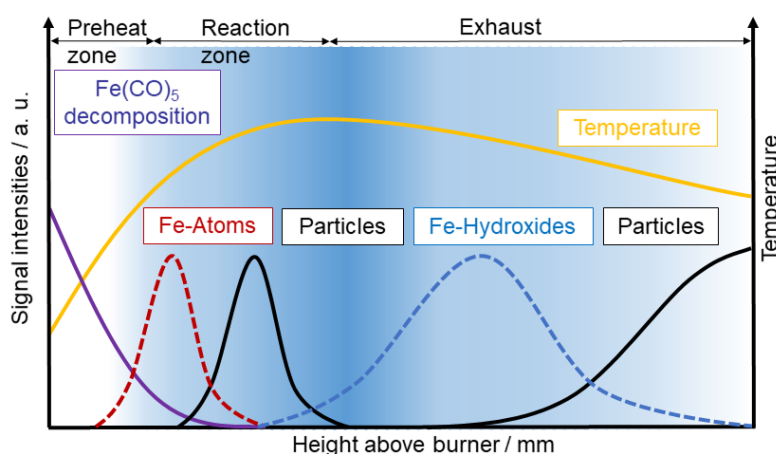


Figure 12-1. Scheme for the particle formation in flame synthesis. The violet curve indicates the decomposition of the precursor. The flame temperature is indicated by the yellow line. The first peak corresponds to gaseous Fe which was measured by Kluge et al. [57] and leads to the formation of solid particles [57] close to the burner surface. The second peak corresponds to the iron hydroxides measured by Karakaya et al. [62] which are present behind the flame front. The solid particle formation at the late stage of the flame was measured by Kluge et al. [57].

13 Outlook

The formation of the particles in synthesis flames can be detected with the aid of a quartz crystal microbalance in the molecular beam. These measurements have been performed for iron oxides by various groups [57, 98, 99, 286] and for silicon dioxide [19]. The results of this thesis and studies from the literature indicate that *different particle formation zones* can be present in the flame. To evaluate this hypothesis further research must be done. For the Si-system, this means that there are two zones for silicon dioxide formation. For the Fe-system, this means that the oxidation states of iron appear in spatially separated zones. This work contributes to the identification of the different particle formation zones by the characterization of the flame structure. Sampling particles from these zones can give further insights into the particle size distribution with which a discontinuous change might be identified. Finding *methods to quench the flame reactions* should be made a primary goal for the future. By quenching the flame reactions, the particles formed in the reaction zone can be stabilized in order to feed them to further processing steps, such as further separation and coating.

A complete database comprising profiles of smaller flame and precursor species and solid particles can be used to evaluate chemical reaction mechanisms of the gas phase synthesis in flames. This work has contributed first results for the understanding of the fundamentals of the gas phase synthesis, which is needed for the optimization of the synthesis process.

Bibliography

- [1] C. Schulz, T. Dreier, M. Fikri, H. Wiggers, Gas-phase synthesis of functional nanomaterials: Challenges to kinetics, diagnostics, and process development, *Proc. Combust. Inst.* 37 (2019) 83-108.
 - [2] S.K. Gupta, M. Talati, P.K. Jha, Shape and size dependent melting point temperature of nanoparticles, *Mater. Sci. Forum* 570 (2008) 132-137.
 - [3] A.A. Minea, A review on electrical conductivity of nanoparticle-enhanced fluids, *Nanomaterials* 9 (2019) 1592.
 - [4] M.I. Sujan, S.D. Sarkar, S. Sultana, L. Bushra, R. Tareq, C.K. Roy, M.S. Azam, Bi-functional silica nanoparticles for simultaneous enhancement of mechanical strength and swelling capacity of hydrogels, *RSC Advances* 10 (2020) 6213-6222.
 - [5] C. Rao, G. Kulkarni, P.J. Thomas, P.P. Edwards, Size-dependent chemistry: properties of nanocrystals, *Chem. Eur. J.* 8 (2002) 28-35.
 - [6] J. Wang, G. Liu, Y. Lin, Electroactive silica nanoparticles for biological labeling, *Small* 2 (2006) 1134-1138.
 - [7] J.-K. Hsiao, M.-F. Tai, Y.-C. Lee, C.-Y. Yang, H.-Y. Wang, H.-M. Liu, J.-S. Fang, S.-T. Chen, Labelling of cultured macrophages with novel magnetic nanoparticles, *J. Magn. Magn. Mater.* 304 (2006) e4-e6.
 - [8] M. Manzano, M. Vallet-Regí, Mesoporous silica nanoparticles for drug delivery, *Adv. Funct. Mater.* 30 (2020) 1902634.
 - [9] A. Aghebati-Maleki, S. Dolati, M. Ahmadi, A. Baghbanzhadeh, M. Asadi, A. Fotouhi, M. Yousefi, L. Aghebati-Maleki, Nanoparticles and cancer therapy: Perspectives for application of nanoparticles in the treatment of cancers, *J. Cell. Physiol.* 235 (2020) 1962-1972.
 - [10] S.A. Noorian, N. Hemmatinejad, J.A. Navarro, Ligand modified cellulose fabrics as support of zinc oxide nanoparticles for UV protection and antimicrobial activities, *Int. J. Biol. Macromol.* 154 (2020) 1215-1226.
 - [11] K.V. Kravchyk, M.V. Kovalenko, M.I. Bodnarchuk, Colloidal Antimony Sulfide Nanoparticles as a High-Performance Anode Material for Li-ion and Na-ion Batteries, *Sci. Rep.* 10 (2020) 1-8.
 - [12] S.L. Mousavi, F. Jamali-Sheini, M. Sabaeian, R. Yousefi, Enhanced solar cell performance of P3HT: PCBM by SnS nanoparticles, *Sol. Energy* 199 (2020) 872-884.
 - [13] C.-J. Zhong, J. Luo, D. Mott, M.M. Maye, N. Kariuki, L. Wang, P. Njoki, M. Schadt, I. Stephanie, Y. Lin, Gold-based nanoparticle catalysts for fuel cell reactions, *Nanotechnology in catalysis*, Springer 2007, pp. 289-307.
 - [14] F.E. Kruis, H. Fissan, A. Peled, Synthesis of nanoparticles in the gas phase for electronic, optical and magnetic applications—a review, *J. Aerosol Sci* 29 (1998) 511-535.
 - [15] W.Y. Teoh, R. Amal, L. Mädler, Flame spray pyrolysis: An enabling technology for nanoparticles design and fabrication, *Nanoscale* 2 (2010) 1324-1347.
 - [16] R.S. Chrystie, H. Janbazi, T. Dreier, H. Wiggers, I. Wlokas, C. Schulz, Comparative study of flame-based SiO₂ nanoparticle synthesis from TMS and HMDSO: SiO-LIF concentration measurement and detailed simulation, *Proc. Combust. Inst.* 37 (2019) 1221-1229.
-

- [17] R.S. Chrystie, O.M. Feroughi, T. Dreier, C. Schulz, SiO multi-line laser-induced fluorescence for quantitative temperature imaging in flame-synthesis of nanoparticles, *Appl. Phys. B* 123 (2017) 104.
- [18] T. Dreier, C. Schulz, Laser-based diagnostics in the gas-phase synthesis of inorganic nanoparticles, *Powder Technol.* 287 (2016) 226-238.
- [19] O.M. Feroughi, L. Deng, S. Kluge, T. Dreier, H. Wiggers, I. Wlokas, C. Schulz, Experimental and numerical study of a HMDSO-seeded premixed laminar low-pressure flame for SiO₂ nanoparticle synthesis, *Proc. Combust. Inst.* 36 (2017) 1045-1053.
- [20] T. Dreier, R. Chrystie, T. Endres, C. Schulz, *Laser-Based Combustion Diagnostics*, Encyclopedia of Analytical Chemistry, 2016.
- [21] I. Gerasimov, D. Knyazkov, A. Shmakov, A. Paletsky, V. Shvartsberg, T. Bolshova, O. Korobeinichev, Inhibition of hydrogen–oxygen flames by iron pentacarbonyl at atmospheric pressure, *Proc. Combust. Inst.* 33 (2011) 2523-2529.
- [22] I. Gerasimov, D. Knyazkov, A. Shmakov, A. Paletsky, V. Shvartsberg, T. Bolshova, O. Korobeinichev, Structure of an atmospheric-pressure H₂/O₂/N₂ flame doped with iron pentacarbonyl, *Combust. Explos. Shock Waves* 47 (2011) 1-11.
- [23] S. Kluge, H. Wiggers, C. Schulz, Mass spectrometric analysis of clusters and nanoparticles during the gas-phase synthesis of tungsten oxide, *Proc. Combust. Inst.* 36 (2017) 1037-1044.
- [24] T. Kasper, P. Oßwald, U. Struckmeier, K. Kohse-Höinghaus, C.A. Taatjes, J. Wang, T. Cool, M. Law, A. Morel, P.R. Westmoreland, Combustion chemistry of the propanol isomers—investigated by electron ionization and VUV-photoionization molecular beam mass spectrometry, *Combust. Flame* 156 (2009) 1181-1201.
- [25] T. Bierkandt, T. Kasper, E. Akyildiz, A. Lucassen, P. Oßwald, M. Köhler, P. Hemberger, Flame structure of a low-pressure laminar premixed and lightly sooting acetylene flame and the effect of ethanol addition, *Proc. Combust. Inst.* 35 (2015) 803-811.
- [26] D. Krüger, P. Oßwald, M. Köhler, P. Hemberger, T. Bierkandt, Y. Karakaya, T. Kasper, Hydrogen abstraction ratios: A systematic iPEPICO spectroscopic investigation in laminar flames, *Combust. Flame* 191 (2018) 343-352.
- [27] N.J. Labbe, V. Seshadri, T. Kasper, N. Hansen, P. Oßwald, P.R. Westmoreland, Flame chemistry of tetrahydropyran as a model heteroatomic biofuel, *Proc. Combust. Inst.* 34 (2013) 259-267.
- [28] P. Oßwald, U. Struckmeier, T. Kasper, K. Kohse-Höinghaus, J. Wang, T.A. Cool, N. Hansen, P.R. Westmoreland, Isomer-specific fuel destruction pathways in rich flames of methyl acetate and ethyl formate and consequences for the combustion chemistry of esters, *J. Phys. Chem. A* 111 (2007) 4093-4101.
- [29] K. Kohse-Höinghaus, P. Oßwald, U. Struckmeier, T. Kasper, N. Hansen, C.A. Taatjes, J. Wang, T.A. Cool, S. Gon, P.R. Westmoreland, The influence of ethanol addition on premixed fuel-rich propene–oxygen–argon flames, *Proc. Combust. Inst.* 31 (2007) 1119-1127.
- [30] A.B. Alqaity, B. Chen, J. Han, H. Selim, M. Belhi, Y. Karakaya, T. Kasper, S.M. Sarathy, F. Bisetti, A. Farooq, New insights into methane-oxygen ion chemistry, *Proc. Combust. Inst.* 36 (2017) 1213-1221.
- [31] T.S. Kasper, P. Oßwald, M. Kamphus, K. Kohse-Höinghaus, Ethanol flame structure investigated by molecular beam mass spectrometry, *Combust. Flame* 150 (2007) 220-231.
- [32] P. Roth, Particle synthesis in flames, *Proc. Combust. Inst.* 31 (2007) 1773-1788.
-

- [33] J.M. Lemieux, J. Zhang, Thermal decomposition of tetramethylsilane and tetramethylgermane by flash pyrolysis vacuum ultraviolet photoionization time-of-flight mass spectrometry, *Int. J. Mass spectrom.* 373 (2014) 50-55.
- [34] P. Sela, S. Peukert, J. Herzler, M. Fikri, C. Schulz, Shock-tube study of the decomposition of tetramethylsilane using gas chromatography and high-repetition-rate time-of-flight mass spectrometry, *Phys. Chem. Chem. Phys.* 20 (2018) 10686-10696.
- [35] A.C. Baldwin, I.M. Davidson, M.D. Reed, Mechanism of thermolysis of tetramethylsilane and trimethylsilane, *J. Chem. Soc., Faraday Trans. 1* 74 (1978) 2171-2178.
- [36] R. Baldwin, C. Everett, R. Walker, Inhibition of the H_2+O_2 reaction by alkyl silanes, *Trans. Faraday Soc.* 64 (1968) 2708-2722.
- [37] M.A. Reed, The thermal reaction between tetramethylsilane and oxygen in the gas phase, PhD thesis. University of Leicester. Available at: <https://ira.le.ac.uk/handle/2381/31988>, (Accessed: 16 November 2017) 1973.
- [38] N.G. Glumac, Formation and consumption of SiO in powder synthesis flames, *Combust. Flame* 124 (2001) 702-711.
- [39] S. Shekar, M. Sander, R.C. Riehl, A.J. Smith, A. Braumann, M. Kraft, Modelling the flame synthesis of silica nanoparticles from tetraethoxysilane, *Chem. Eng. Sci.* 70 (2012) 54-66.
- [40] W. Phadungsukanan, S. Shekar, R. Shirley, M. Sander, R.H. West, M. Kraft, First-principles thermochemistry for silicon species in the decomposition of tetraethoxysilane, *J. Phys. Chem. A* 113 (2009) 9041-9049.
- [41] S. Shekar, A.J. Smith, W.J. Menz, M. Sander, M. Kraft, A multidimensional population balance model to describe the aerosol synthesis of silica nanoparticles, *J. Aerosol Sci* 44 (2012) 83-98.
- [42] D. Lindackers, M. Strecker, P. Roth, C. Janzen, S.E. Pratsinis, Formation and Growth of SiO_2 Particles in Low Pressure $H_2/O_2/Ar$ Flames Doped with SiH_4 , *Combust. Sci. Technol.* 123 (1997) 287-315.
- [43] H. Briesen, S.E. Pratsinis, The effect of precursor in flame synthesis of SiO_2 , *Chem. Eng. Sci.* 53 (1998) 4105-4112.
- [44] G.D. Ulrich, Theory of particle formation and growth in oxide synthesis flames, *Combust. Sci. Technol.* 4 (1971) 47-57.
- [45] G. Ulrich, B. Milnes, N. Subramanian, Particle growth in flames. II: Experimental results for silica particles, *Combust. Sci. Technol.* 14 (1976) 243-249.
- [46] G.D. Ulrich, N. Subramanian, III. Coalescence as a rate-controlling process, *Combust. Sci. Technol.* 17 (1977) 119-126.
- [47] G.D. Ulrich, J.W. Rieh, Aggregation and growth of submicron oxide particles in flames, *J. Colloid Interface Sci.* 87 (1982) 257-265.
- [48] S.-M. Suh, M. Zachariah, S. Girshick, Modeling particle formation during low-pressure silane oxidation: Detailed chemical kinetics and aerosol dynamics, *J. Vac. Sci. Technol. A* 19 (2001) 940-951.
- [49] G.T. Linteris, V.I. Babushok, Promotion or inhibition of hydrogen-air ignition by iron-containing compounds, *Proc. Combust. Inst.* 32 (2009) 2535-2542.
- [50] M. Rumminger, D. Reinelt, V. Babushok, G.T. Linteris, Numerical study of the inhibition of premixed and diffusion flames by iron pentacarbonyl, *Combust. Flame* 116 (1999) 207-219.
- [51] G.T. Linteris, M.D. Rumminger, V.I. Babushok, Catalytic inhibition of laminar flames by transition metal compounds, *Prog. Energy Combust. Sci.* 34 (2008) 288-329.
-

- [52] I. Wlokas, A. Faccinetto, B. Tribalet, C. Schulz, A. Kempf, Mechanism of iron oxide formation from iron pentacarbonyl-doped low-pressure hydrogen/oxygen flames, *Int. J. Chem. Kinet.* 45 (2013) 487-498.
- [53] O.M. Feroughi, S. Hardt, I. Wlokas, T. Huelser, H. Wiggers, T. Dreier, C. Schulz, Laser-based in situ measurement and simulation of gas-phase temperature and iron atom concentration in a pilot-plant nanoparticle synthesis reactor, *Proc. Combust. Inst.* 35 (2015) 2299-2306.
- [54] C. Hecht, H. Kronemayer, T. Dreier, H. Wiggers, C. Schulz, Imaging measurements of atomic iron concentration with laser-induced fluorescence in a nanoparticle synthesis flame reactor, *Appl. Phys. B* 94 (2009) 119.
- [55] J.Z. Wen, C.F. Goldsmith, R.W. Ashcraft, W.H. Green, Detailed kinetic modeling of iron nanoparticle synthesis from the decomposition of $\text{Fe}(\text{CO})_5$, *J. Phys. Chem. C* 111 (2007) 5677-5688.
- [56] S. Staude, C. Hecht, I. Wlokas, C. Schulz, B. Atakan, Experimental and numerical investigation of $\text{Fe}(\text{CO})_5$ addition to a laminar premixed hydrogen/oxygen/argon flame, *Z. Phys. Chem.* 223 (2009) 639-649.
- [57] S. Kluge, L. Deng, O. Feroughi, F. Schneider, M. Poliak, A. Fomin, V. Tsionsky, S. Cheskis, I. Wlokas, I. Rahinov, Initial reaction steps during flame synthesis of iron-oxide nanoparticles, *CrystEngComm* 17 (2015) 6930-6939.
- [58] C. Janzen, P. Roth, B. Rellinghaus, Characteristics of Fe_2O_3 nanoparticles from doped low-pressure $\text{H}_2/\text{O}_2/\text{Ar}$ flames, *J. Nanopart. Res.* 1 (1999) 163-167.
- [59] Y. Karakaya, J. Sellmann, I. Wlokas, T. Kasper, Influence of the sampling probe on flame temperature, species, residence times and on the interpretation of ion signals of methane/oxygen flames in molecular beam mass spectrometry measurements, *Combust. Flame* 229 (2021) 111388.
- [60] P. Weilmünster, A. Keller, K.-H. Homann, Large molecules, radicals, ions, and small soot particles in fuel-rich hydrocarbon flames: Part I: positive ions of polycyclic aromatic hydrocarbons (PAH) in low-pressure premixed flames of acetylene and oxygen, *Combust. Flame* 116 (1999) 62-83.
- [61] A.B. Fialkov, Investigations on ions in flames, *Prog. Energy Combust. Sci.* 23 (1997) 399-528.
- [62] Y. Karakaya, S. Kluge, H. Wiggers, C. Schulz, T. Kasper, Investigation of the combustion of iron pentacarbonyl and the formation of key intermediates in iron oxide synthesis flames, *Chem. Eng. Sci.* 230 (2021) 116169.
- [63] H. Pauly, Atom, molecule, and cluster beams I: Basic theory, production and detection of thermal energy beams, Springer Science & Business Media 2012.
- [64] D.R. Miller, Free jet sources, *Atomic and molecular beam methods* 1 (1988) 14-53.
- [65] M.D. Morse, Supersonic beam sources, *Experimental methods in the physical sciences* 29 (1996) 21-47.
- [66] E. de Hoffmann, V. Stroobant, *Mass spectrometry, Mass spectrometry principles and applications*, 3rd Edition, John Wiley & Sons Ltd., West Sussex, England, (2007).
- [67] J.H. Gross, *Massenspektrometer, Massenspektrometrie*, Springer 2013, pp. 129-244.
- [68] E. Tiesinga, P.J. Mohr, D.B. Newell, B.N. Taylor, J. Baker, M.A. Douma, S.A. Kotochigova, "The 2018 CODATA Recommended Values of the Fundamental Physical Constants" (Web Version 8.1). Available at <http://physics.nist.gov/constants>, National Institute of Standards and Technology, Gaithersburg, MD 20899, (2020).
- [69] W. Wiley, I.H. McLaren, Time-of-flight mass spectrometer with improved resolution, *Rev. Sci. Instrum.* 26 (1955) 1150-1157.
-

- [70] B. Mamyrin, Laser assisted reflectron time-of-flight mass spectrometry, *Int. J. Mass Spectrom. Ion Processes* 131 (1994) 1-19.
- [71] J. Warnatz, Calculation of the structure of laminar flat flames I: Flame velocity of freely propagating ozone decomposition flames, *Berichte der Bunsengesellschaft für physikalische Chemie* 82 (1978) 193-200.
- [72] J. Warnatz, U. Maas, R.W. Dibble, J. Warnatz, *Combustion*, Springer 2006.
- [73] R.J. Kee, M.E. Coltrin, P. Glarborg, H. Zhu, *Chemically Reacting Flow: Theory, Modeling, and Simulation*, John Wiley & Sons 2018.
- [74] R. Gilbert, K. Luther, J. Troe, Theory of thermal unimolecular reactions in the fall-off range. II. Weak collision rate constants, *Berichte der Bunsengesellschaft für physikalische Chemie* 87 (1983) 169-177.
- [75] E. Goos, A. Burcat, B. Ruscic, Extended third millennium ideal gas and condensed phase thermochemical database for combustion with updates from active thermochemical tables, German Aerospace Center, Institute of Combustion Technology, Stuttgart, Germany, accessed Aug 2 (2010) 2018.
- [76] S. Mathur, P. Tondon, S. Saxena, Thermal conductivity of binary, ternary and quaternary mixtures of rare gases, *Mol. Phys.* 12 (1967) 569-579.
- [77] G.-N. Dixon-Lewis, Flame structure and flame reaction kinetics II. Transport phenomena in multicomponent systems, *Proc. R. Soc. London, Ser. A* 307 (1968) 111-135.
- [78] L. Monchick, E. Mason, Transport properties of polar gases, *J. Chem. Phys.* 35 (1961) 1676-1697.
- [79] J. Parker, Rotational and vibrational relaxation in diatomic gases, *Phys. Fluids* 2 (1959) 449-462.
- [80] C. Brau, R. Jonkman, Classical theory of rotational relaxation in diatomic gases, *J. Chem. Phys.* 52 (1970) 477-484.
- [81] G. Irvin, Y. Richard, *Combustion*, Academic Press, 2008.
- [82] U. Struckmeier, P. Oßwald, T. Kasper, L. Böhling, M. Heusing, M. Köhler, A. Brockhinke, K. Kohse-Höinghaus, Sampling probe influences on temperature and species concentrations in molecular beam mass spectroscopic investigations of flat premixed low-pressure flames, *Z. Phys. Chem.* 223 (2009) 503-537.
- [83] T. Bierkandt, P. Hemberger, P. Oßwald, M. Köhler, T. Kasper, Insights in m-xylene decomposition under fuel-rich conditions by imaging photoelectron photoion coincidence spectroscopy, *Proc. Combust. Inst.* 36 (2017) 1223-1232.
- [84] D. Krüger, P. Oßwald, M. Köhler, P. Hemberger, T. Bierkandt, T. Kasper, The fate of the OH radical in molecular beam sampling experiments, *Proc. Combust. Inst.* 37 (2019) 1563-1570.
- [85] M. Gonchikzhapov, T. Kasper, Decomposition reactions of $\text{Fe}(\text{CO})_5$, $\text{Fe}(\text{C}_5\text{H}_5)_2$, and TTIP as precursors for the spray-flame synthesis of nanoparticles in partial spray evaporation at low temperatures, *Ind. Eng. Chem. Res.* 59 (2020) 8551-8561.
- [86] Y. Karakaya, S. Peukert, T. Kasper, Mass spectrometric study on the combustion of tetramethylsilane and the formation of silicon oxide clusters in premixed laminar low-pressure synthesis flames, *J. Phys. Chem. A* 36 (2018) 7131-7141.
- [87] M. Guilhaus, D. Selby, V. Mlynski, Orthogonal acceleration time-of-flight mass spectrometry, *Mass Spectrom. Rev.* 19 (2000) 65-107.
- [88] F. Vietmeyer, Electron transfer rates in coupled semiconductor systems, *Diplomarbeit, Universität Bielefeld, Bielefeld*, 2009.
- [89] J.C. Biordi, Molecular beam mass spectrometry for studying the fundamental chemistry of flames, *Prog. Energy Combust. Sci.* 3 (1977) 151-173.
- [90] P.J. Linstrom, W.G. Mallard, NIST Chemistry WebBook, NIST Standard Reference Database Number 69, National Institute of Standards and Technology,
-

- Gaithersburg MD, 20899, <https://doi.org/10.18434/T4D303>, (retrieved October 1, 2020).
- [91] W.L. Fitch, A.D. Sauter, Calculation of relative electron impact total ionization cross sections for organic molecules, *Anal. Chem.* 55 (1983) 832-835.
- [92] C.R. Shaddix, Correcting thermocouple measurements for radiation loss: a critical review, Sandia National Labs., Livermore, CA (US), 1999.
- [93] N. Bahlawane, U. Struckmeier, T.S. Kasper, P. Oßwald, Noncatalytic thermocouple coatings produced with chemical vapor deposition for flame temperature measurements, *Rev. Sci. Instrum.* 78 (2007) 013905.
- [94] N. Bahlawane, Novel sol-gel process depositing α -Al₂O₃ for the improvement of graphite oxidation-resistance, *Thin Solid Films* 396 (2001) 126-130.
- [95] J. Madson, E. Theby, SiO₂ coated thermocouples, *Combust. Sci. Technol.* 36 (1984) 205-209.
- [96] W. Kaskan, The dependence of flame temperature on mass burning velocity, *Symp. Int. Combust. Proc.* 6 (1957) 134-143.
- [97] L. Papula, *Mathematik für Ingenieure und Naturwissenschaftler Band 3: Vektoranalysis, Wahrscheinlichkeitsrechnung, Mathematische Statistik, Fehler- und Ausgleichsrechnung*, Springer-Verlag 2016.
- [98] J. Sellmann, I. Rahinov, S. Kluge, H. Jünger, A. Fomin, S. Cheskis, C. Schulz, H. Wiggers, A. Kempf, I. Wlokas, Detailed simulation of iron oxide nanoparticle forming flames: Buoyancy and probe effects, *Proc. Combust. Inst.* 37 (2018) 1241-1248.
- [99] I. Rahinov, J. Sellmann, M.R. Lallane, M. Nanjaiah, T. Dreier, S. Cheskis, I. Wlokas, Insights into the Mechanism of Combustion Synthesis of Iron Oxide Nanoparticles Gained by Laser Diagnostics, Mass Spectrometry, and Numerical Simulations: A Mini-Review, *Energy Fuels* 35 (2020) 137-160.
- [100] M. Nanjaiah, A. Pilipodi-Best, M. Lallane, P. Fjodorow, C. Schulz, S. Cheskis, A. Kempf, I. Wlokas, I. Rahinov, Experimental and numerical investigation of iron-doped flames: FeO formation and impact on flame temperature, *Proc. Combust. Inst.* 38 (2020) 1249-1257.
- [101] T. Hirasawa, C.-J. Sung, Z. Yang, A. Joshi, H. Wang, Effect of ferrocene addition on sooting limits in laminar premixed ethylene-oxygen-argon flames, *Combust. Flame* 139 (2004) 288-299.
- [102] S.E. Pratsinis, W. Zhu, S. Vemury, The role of gas mixing in flame synthesis of titania powders, *Powder Technol.* 86 (1996) 87-93.
- [103] S.E. Pratsinis, Flame aerosol synthesis of ceramic powders, *Prog. Energy Combust. Sci.* 24 (1998) 197-219.
- [104] M.R. Zachariah, D.R. Burgess, Strategies for laser excited fluorescence spectroscopy. Measurements of gas phase species during particle formation, *J. Aerosol Sci* 25 (1994) 487-497.
- [105] T. Moore, B. Brady, L.R. Martin, Measurements and modeling of SiCl₄ combustion in a low-pressure H₂/O₂ flame, *Combust. Flame* 146 (2006) 407-418.
- [106] A. Lamprecht, B. Atakan, K. Kohse-Hö, Fuel-rich propene and acetylene flames: a comparison of their flame chemistries, *Combust. Flame* 122 (2000) 483-491.
- [107] N. Hansen, T.A. Cool, P.R. Westmoreland, K. Kohse-Höinghaus, Recent contributions of flame-sampling molecular-beam mass spectrometry to a fundamental understanding of combustion chemistry, *Prog. Energy Combust. Sci.* 35 (2009) 168-191.
- [108] P. Oßwald, K. Kohse-Höinghaus, U. Struckmeier, T. Zeuch, L. Seidel, L. Leon, F. Mauss, Combustion chemistry of the butane isomers in premixed low-pressure flames, *Z. Phys. Chem.* 225 (2011) 1029-1054.
-

- [109] M.S. Wooldridge, Gas-phase combustion synthesis of particles, *Prog. Energy Combust. Sci.* 24 (1998) 63-87.
- [110] R. Clifford, B. Gowenlock, C. Johnson, J. Stevenson, The pyrolysis of organometallic compounds IV. Kinetic studies of the decomposition of tetramethylsilane, *J. Organomet. Chem.* 34 (1972) 53-61.
- [111] G. Fritz, B. Raabe, Bildung siliciumorganischer Verbindungen. V. Die thermische Zersetzung von $\text{Si}(\text{CH}_3)_4$ und $\text{Si}(\text{C}_2\text{H}_5)_4$, *Z. Anorg. Allg. Chem.* 286 (1956) 149-167.
- [112] H. Chagger, D. Hainsworth, P. Patterson, M. Pourkashanian, A. Williams, The formation of SiO_2 from hexamethyldisiloxane combustion in counterflow methane-air flames, *Symp. Int. Combust. Proc.* 26 (1996) 1859-1865.
- [113] C. Pandya, Electron-impact ionization of SiCl , SiCl_2 and SiCl_4 molecules, *J. At. Mol. Sci.* 4 (2013) 41-48.
- [114] K. Joshipura, B. Vaishnav, S. Gangopadhyay, Electron impact ionization cross-sections of plasma relevant and astrophysical silicon compounds: SiH_4 , Si_2H_6 , $\text{Si}(\text{CH}_3)_4$, SiO , SiO_2 , SiN and SiS , *Int. J. Mass Spectrom.* 261 (2007) 146-151.
- [115] W. Hwang, Y.K. Kim, M.E. Rudd, New model for electron-impact ionization cross sections of molecules, *J. Chem. Phys.* 104 (1996) 2956-2966.
- [116] M.J. Frisch, G. Trucks, H.B. Schlegel, G. Scuseria, M. Robb, J. Cheeseman, G. Scalmani, V. Barone, B. Mennucci, G. Petersson, Gaussian 09, revision A. 1, Gaussian Inc. Wallingford CT 27 (2009) 34.
- [117] F. De Proft, P. Geerlings, Calculation of ionization energies, electron affinities, electronegativities, and hardnesses using density functional methods, *J. Chem. Phys.* 106 (1997) 3270-3279.
- [118] O. Kostko, M. Ahmed, R.B. Metz, Vacuum-ultraviolet photoionization measurement and ab initio calculation of the ionization energy of gas-phase SiO_2 , *J. Phys. Chem. A* 113 (2009) 1225-1230.
- [119] V. Khvostenko, B. Zykov, V. Yuriev, V. Mironov, G. Kovel'zon, A. Panasenko, V. Sheludyakov, I. Gailyunas, Study of $d\pi$ - $p\pi$ interaction in vinyl- and alkylsilicon-containing compounds by photoelectron spectroscopy, *J. Organomet. Chem.* 218 (1981) 155-158.
- [120] R. Roberge, C. Sandorfy, J. Matthews, O. Strausz, The far ultraviolet and HeI photoelectron spectra of alkyl and fluorine substituted silane derivatives, *J. Chem. Phys.* 69 (1978) 5105-5112.
- [121] K.H.A.O. Starzewski, W. Richter, H. Schmidbaur, Photoelektronenspektren und Struktur von Arsen-yliden. P versus As: Ein Beitrag zur Problematik der ylidischen Bindung, *Chem. Ber.* 109 (1976) 473-481.
- [122] Computational Chemistry Comparison and Benchmark DataBase (CCCBDB), National Institute of Standards and Technology, Maryland, 20899-8320, Release 19, April 2018, available at: <https://cccbdb.nist.gov/Calcdatab.asp>.
- [123] K.L. Chemical WorkBench® 4.0, available online at <http://www.kintechlab.com/products/chemical-workbench/>.
- [124] J. Li, Z. Zhao, A. Kazakov, F.L. Dryer, An updated comprehensive kinetic model of hydrogen combustion, *Int. J. Chem. Kinet.* 36 (2004) 566-575.
- [125] R. Sivaramakrishnan, J. Michael, L. Harding, S. Klippenstein, Shock tube explorations of roaming radical mechanisms: the decompositions of isobutane and neopentane, *J. Phys. Chem. A* 116 (2012) 5981-5989.
- [126] E.C. Tuazon, S.M. Aschmann, R. Atkinson, Atmospheric degradation of volatile methyl-silicon compounds, *Environ. Sci. Technol.* 34 (2000) 1970-1976.
-

- [127] P. Sela, S. Peukert, J. Herzler, Y. Sakai, M. Fikri, C. Schulz, High-temperature gas-phase kinetics of the thermal decomposition of tetramethoxysilane, *Proc. Combust. Inst.*, (2018).
- [128] L.A. Curtiss, P.C. Redfern, K. Raghavachari, Gaussian-4 theory, *J. Chem. Phys.* 126 (2007) 084108.
- [129] M.J. Almond, R. Becerra, S.J. Bowes, J.P. Cannady, J.S. Ogden, R. Walsh, A mechanistic study of cyclic siloxane pyrolyses at low pressures, *Phys. Chem. Chem. Phys.* 10 (2008) 6856-6861.
- [130] O. Sanogo, M.R. Zachariah, Étude de la décomposition thermique de l'octaméthylcyclosiloxane (D4) dans un réacteur à écoulement rapide, *Comptes Rendus Chimie* 10 (2007) 518-523.
- [131] V. Khabashesku, Z. Kerzina, E. Baskir, A. Maltsev, O. Nefedov, Direct spectroscopic study of unstable molecules with silicon-oxygen multiple bonds: low temperature matrix stabilization of $(\text{CH}_3)_2\text{SiO}$ and $(\text{CD}_3)_2\text{SiO}$ in the gas phase, *J. Organomet. Chem.* 347 (1988) 277-293.
- [132] J. Plane, J.C. Gómez-Martín, W. Feng, D. Janches, Silicon chemistry in the mesosphere and lower thermosphere, *J. Geophys. Res. Atmos.* 121 (2016) 3718-3728.
- [133] C. Xu, W. Wang, W. Zhang, J. Zhuang, L. Liu, Q. Kong, L. Zhao, Y. Long, K. Fan, S. Qian, Magic numbers in silicon dioxide-based clusters, *J. Phys. Chem. A* 104 (2000) 9518-9524.
- [134] A.Y. Timoshkin, Gas Phase Generation of Si-OH Clusters: an Ab Initio Study of Structural and Thermodynamic Properties, *Proc. Electrochem. Soc.* 12 (2001-12) 262.
- [135] K. Wegner, S.E. Pratsinis, Gas-phase synthesis of nanoparticles: scale-up and design of flame reactors, *Powder Technol.* 150 (2005) 117-122.
- [136] M.R. Zachariah, R.G. Joklik, Multiphoton ionization spectroscopy measurements of silicon atoms during vapor-phase synthesis of ceramic particles, *J. Appl. Phys.* 68 (1990) 311-317.
- [137] J.A. Britten, J. Tong, C.K. Westbrook, A numerical study of silane combustion, *Proc. Combust. Inst.* 23 (1991) 195-202.
- [138] D. Nurkowski, P. Buerger, J. Akroyd, M. Kraft, A detailed kinetic study of the thermal decomposition of tetraethoxysilane, *Proc. Combust. Inst.* 35 (2015) 2291-2298.
- [139] D. Nurkowski, P. Buerger, J. Akroyd, S. Mosbach, M. Kraft, Skeletal chemical mechanism of high-temperature TEOS oxidation in hydrogen-oxygen environment, *Combust. Flame* 166 (2016) 243-254.
- [140] J. Chen, Z. Huang, L. Zheng, Detailed OMCTS/ H_2/O_2 chemical kinetics mechanism and its application in the fused silica glass synthesis, *J. Non-Cryst. Solids* 481 (2018) 33-40.
- [141] P. Sela, S. Peukert, J. Herzler, Y. Sakai, M. Fikri, C. Schulz, High-temperature gas-phase kinetics of the thermal decomposition of tetramethoxysilane, *Proc. Combust. Inst.* 37 (2019) 1133-1141.
- [142] J.E. Taylor, T.S. Milazzo, A comparative study of the pyrolyses of the tetramethyl derivatives of silicon, germanium, and tin using a wall-less reactor, *J. Phys. Chem.* 82 (1978) 847-852.
- [143] D. Chaussende, M. Ucar, L. Auvray, F. Baillet, M. Pons, R. Madar, Control of the Supersaturation in the CF₄-PVT Process for the Growth of Silicon Carbide Crystals: Research and Applications, *Cryst. Growth Des.* 5 (2005) 1539-1544.
-

- [144] M. Zachariah, H. Semerjian, Experimental and numerical studies on refractory particle formation in flames: Application to silica growth, *High Temp. Sci.* 28 (1988) 113-125.
- [145] R.S. Chrystie, F.L. Ebertz, T. Dreier, C. Schulz, Absolute SiO concentration imaging in low-pressure nanoparticle-synthesis flames via laser-induced fluorescence, *Appl. Phys. B* 125 (2019) 29.
- [146] T.A. Cool, K. Nakajima, C.A. Taatjes, A. McIlroy, P.R. Westmoreland, M.E. Law, A. Morel, Studies of a fuel-rich propane flame with photoionization mass spectrometry, *Proc. Combust. Inst.* 30 (2005) 1681-1688.
- [147] S. Canneaux, F. Bohr, E. Henon, KiSTheLP: A program to predict thermodynamic properties and rate constants from quantum chemistry results, *J. Comput. Chem.* 35 (2014) 82-93.
- [148] D. Ben-Amotz, K.G. Willis, Molecular hard-sphere volume increments, *J. Phys. Chem.* 97 (1993) 7736-7742.
- [149] R. Kee, F. Rupley, J. Miller, M. Coltrin, J. Grcar, E. Meeks, H. Moffat, A. Lutz, G. Dixon-Lewis, M. Smooke, CHEMKIN Collection, Release 3.6, Reaction Design, Inc., San Diego, CA 20 (2000) 0.
- [150] M. Chase Jr, C. Davies, J. Downey Jr, D. Frurip, R. McDonald, JANAF thermochemical tables. 3rd ed., *J. Phys. Chem. Ref. Data* 14, Suppl. 1 (1985).
- [151] J.W. Ochterski, Thermochemistry in gaussian, Gaussian Inc 1 (2000) 1-19.
- [152] J. Simmie, J. Sheahan, Validation of a database of formation enthalpies and of mid-level model chemistries, *J. Phys. Chem. A* 120 (2016) 7370-7384.
- [153] H. Janbazi, O. Hasemann, C. Schulz, A. Kempf, I. Wlokas, S. Peukert, Response surface and group additivity methodology for estimation of thermodynamic properties of organosilanes, *Int. J. Chem. Kinet.* 50 (2018) 681-690.
- [154] J. Li, Z. Zhao, A. Kazakov, M. Chaos, F.L. Dryer, J.J. Scire Jr, A comprehensive kinetic mechanism for CO, CH₂O, and CH₃OH combustion, *Int. J. Chem. Kinet.* 39 (2007) 109-136.
- [155] N. Sikalo, O. Hasemann, C. Schulz, A. Kempf, I. Wlokas, A genetic algorithm-based method for the automatic reduction of reaction mechanisms, *Int. J. Chem. Kinet.* 46 (2014) 41-59.
- [156] N. Sikalo, O. Hasemann, C. Schulz, A. Kempf, I. Wlokas, A genetic algorithm-based method for the optimization of reduced kinetics mechanisms, *Int. J. Chem. Kinet.* 47 (2015) 695-723.
- [157] D. Goodwin, H. Moffat, R. Speth, Cantera: an object-oriented software toolkit for chemical kinetics, thermodynamics, and transport processes (pasadena, CA: Caltech), (2009).
- [158] Miyoshi, A., 2017. GPOP program suite. GPOP Software, <http://www.frad.t.u-tokyo.ac.jp/~miyoshi/gpop>.
- [159] K.S. Pitzer, W.D. Gwinn, Energy levels and thermodynamic functions for molecules with internal rotation I. Rigid frame with attached tops, *J. Chem. Phys.* 10 (1942) 428-440.
- [160] S.R. Gunn, L.G. Green, The heats of formation of some unstable gaseous hydrides, *J. Phys. Chem.* 65 (1961) 779-783.
- [161] S.R. Gunn, L.G. Green, The heats of formation of trisilane and trigermane, *J. Phys. Chem.* 68 (1964) 946-949.
- [162] A.M. Doncaster, R. Walsh, Thermochemistry of silicon-containing compounds. Part 2.—The enthalpies of formation of the methylsilanes, an experimental study and review, *J. Chem. Soc.* 82 (1986) 707-717.
- [163] T. Brix, N. Arthur, P. Potzinger, Stationary and pulsed photolysis and pyrolysis of 1, 1-dimethylsilacyclobutane, *J. Phys. Chem.* 93 (1989) 8193-8197.
-

- [164] L. Gusel'nikov, N. Nametkin, 1, 1-Dimethyl-1-silaethylene: Heat of formation, ionization potential and the energy of the silicon-carbon π -bond, *J. Organomet. Chem.* 169 (1979) 155-164.
- [165] M.D. Allendorf, C.F. Melius, P. Ho, M.R. Zachariah, Theoretical study of the thermochemistry of molecules in the Si-OH system, *J. Phys. Chem.* 99 (1995) 15285-15293.
- [166] S. Patai, Z. Rappoport, *The chemistry of organic silicon compounds*, 1989.
- [167] M. Ó Conaire, H.J. Curran, J.M. Simmie, W.J. Pitz, C.K. Westbrook, A comprehensive modeling study of hydrogen oxidation, *Int. J. Chem. Kinet.* 36 (2004) 603-622.
- [168] T. Varga, C. Olm, T. Nagy, I.G. Zsély, É. Valkó, R. Pálvölgyi, H.J. Curran, T. Turányi, Development of a joint hydrogen and syngas combustion mechanism based on an optimization approach, *Int. J. Chem. Kinet.* 48 (2016) 407-422.
- [169] S. Peukert, J. Herzler, M. Fikri, C. Schulz, High-Temperature Rate Constants for H + Tetramethylsilane and H + Silane and Implications about Structure–Activity Relationships for Silanes, *Int. J. Chem. Kinet.* 50 (2018) 57-72.
- [170] I.M. Davidson, C.E. Dean, F.T. Lawrence, Kinetics of addition of 2-methyl-2-silapropene to hydrogen chloride, hydrogen bromide, and oxygen, *J. Chem. Soc., Chem. Commun.*, (1981) 52-53.
- [171] E. Ranzi, C. Cavallotti, A. Cuoci, A. Frassoldati, M. Pelucchi, T. Faravelli, New reaction classes in the kinetic modeling of low temperature oxidation of n-alkanes, *Combust. Flame* 162 (2015) 1679-1691.
- [172] A.T. Hartlieb, B. Atakan, K. Kohse-Höinghaus, Effects of a sampling quartz nozzle on the flame structure of a fuel-rich low-pressure propene flame, *Combust. Flame* 121 (2000) 610-624.
- [173] L. Deng, A. Kempf, O. Hasemann, O.P. Korobeinichev, I. Wlokas, Investigation of the sampling nozzle effect on laminar flat flames, *Combust. Flame* 162 (2015) 1737-1747.
- [174] R. Sivaramakrishnan, N. Srinivasan, M.-C. Su, J. Michael, High temperature rate constants for OH+ alkanes, *Proc. Combust. Inst.* 32 (2009) 107-114.
- [175] N. Cohen, K. Westberg, *Chemical Kinetic Data Sheets for High-Temperature Reactions. Part II*, *J. Phys. Chem. Ref. Data* 20 (1991) 1211-1311.
- [176] H.J. Curran, Rate constant estimation for C1 to C4 alkyl and alkoxy radical decomposition, *Int. J. Chem. Kinet.* 38 (2006) 250-275.
- [177] I.M. Davidson, J.F. Thompson, Kinetics of the oxidation of octamethylcyclotetrasiloxane in the gas phase, *J. Chem. Soc., Faraday Trans. 1* 72 (1976) 1088-1095.
- [178] G. Smith, D. Golden, Application of RRKM theory to the reactions $\text{OH} + \text{NO}_2 + \text{N}_2 \rightarrow \text{HONO}_2 + \text{N}_2$ (1) and $\text{ClO} + \text{NO}_2 + \text{N}_2 \rightarrow \text{ClONO}_2 + \text{N}_2$ (2); a modified gorin model transition state, *Int. J. Chem. Kinet.* 10 (1978) 489-501.
- [179] N. Srinivasan, J. Kiefer, R. Tranter, Dissociation, relaxation, and incubation in the pyrolysis of neopentane: heat of formation for tert-butyl radical, *J. Phys. Chem. A* 107 (2003) 1532-1539.
- [180] C. Yeh, E. Zhao, H. Ma, Combustion synthesis of SiO_2 on the aluminum plate, *J. Therm. Sci.* 10 (2001) 92-96.
- [181] H. Ma, E. Zhao, C. Yeh, K. Chung, The formation of nano-size SiO_2 thin film on an aluminum plate with hexamethyldisilazane (HMDSA) and hexamethyldisiloxane (HMDSO), *J. Therm. Sci.* 12 (2003) 89-96.
- [182] M.R. Zachariah, W. Tsang, Theoretical calculation of thermochemistry, energetics, and kinetics of high-temperature $\text{Si}_x\text{H}_y\text{O}_z$ reactions, *J. Phys. Chem.* 99 (1995) 5308-5318.
-

- [183] I.I. Slowing, B.G. Trewyn, S. Giri, V.Y. Lin, Mesoporous silica nanoparticles for drug delivery and biosensing applications, *Adv. Funct. Mater.* 17 (2007) 1225-1236.
- [184] T. Miller, M. Wooldridge, J. Bozzelli, Computational modeling of the $\text{SiH}_3 + \text{O}_2$ reaction and silane combustion, *Combust. Flame* 137 (2004) 73-92.
- [185] H. Janbazi, Y. Karakaya, T. Kasper, C. Schulz, I. Wlokas, S. Peukert, Development and evaluation of a chemical kinetics reaction mechanism for tetramethylsilane-doped flames, *Chem. Eng. Sci.* 209 (2019) 115209.
- [186] CHEMKIN-PRO 19.2, Reaction Design: San Diego, (2018).
- [187] K.K. Akurati, R. Dittmann, A. Vital, U. Klotz, P. Hug, T. Graule, M. Winterer, Silica-based composite and mixed-oxide nanoparticles from atmospheric pressure flame synthesis, *J. Nanopart. Res.* 8 (2006) 379-393.
- [188] M. Hellring, T. Munther, T. Rögnavaldsson, N. Wickström, C. Carlsson, M. Larsson, J. Nytomt, Spark advance control using the ion current and neural soft sensors, *SAE transactions*, (1999) 1590-1595.
- [189] M. Asano, T. Kuma, M. Kajitani, M. Takeuchi, Development of new ion current combustion control system, *SAE transactions*, (1998) 288-293.
- [190] A. Gazis, D. Panousakis, R. Chen, W.-H. Chen, Computationally inexpensive methods of ion current signal manipulation for predicting the characteristics of engine in-cylinder pressure, *Int. J. Engine Res.* 7 (2006) 271-282.
- [191] M. Saito, T. Arai, M. Arai, Control of soot emitted from acetylene diffusion flames by applying an electric field, *Combust. Flame* 119 (1999) 356-366.
- [192] H.F. Calcote, R.N. Pease, Electrical properties of flames. Burner flames in longitudinal electric fields, *Ind. Eng. Chem.* 43 (1951) 2726-2731.
- [193] A. DeFilippo, S. Saxena, V. Rapp, R. Dibble, J.-Y. Chen, A. Nishiyama, Y. Ikeda, Extending the lean stability limits of gasoline using a microwave-assisted spark plug, Report No. 0148-7191, SAE Technical Paper, 2011.
- [194] M. Belhi, P. Domingo, P. Vervisch, Modelling of the effect of DC and AC electric fields on the stability of a lifted diffusion methane/air flame, *Combust. Theory Model* 17 (2013) 749-787.
- [195] Deckers J., T.A. Van, Ion identification in flames, *Symp. Int. Combust. Proc.* 7 (1958) 254-255.
- [196] J. Deckers, A. Van Tiggelen, Ion identification in flames by mass spectrometry, *Nature* 181 (1958) 1460-1460.
- [197] J. Deckers, A. Van Tiggelen, Identity of Ions in Some Flames, *Nature* 182 (1958) 863-863.
- [198] H. Calcote, J. Reuter, Mass-Spectrometric Study of Ion Profiles in Low-Pressure Flames, *J. Chem. Phys.* 38 (1963) 310-317.
- [199] J. Goodings, D. Bohme, C.-W. Ng, Detailed ion chemistry in methane-oxygen flames. I. Positive ions, *Combust. Flame* 36 (1979) 27-43.
- [200] J. Goodings, D. Bohme, C.-W. Ng, Detailed ion chemistry in methane-oxygen flames. II. Negative ions, *Combust. Flame* 36 (1979) 45-62.
- [201] J. Goodings, D. Bohme, T. Sugden, Positive ion probe of methane-oxygen combustion, *Symp. Int. Combust. Proc.* 16 (1977) 891-902.
- [202] D. Bohme, J. Goodings, C.-W. Ng, In situ chemical ionization as a probe for neutral constituents upstream in a methane-oxygen flame, *Int. J. Mass Spectrom. Ion Phys.* 24 (1977) 335-354.
- [203] J. Prager, U. Riedel, J. Warnatz, Modeling ion chemistry and charged species diffusion in lean methane-oxygen flames, *Proc. Combust. Inst.* 31 (2007) 1129-1137.
-

- [204] A.B. Alquaity, N. Hourani, M. Chahine, H.M. Selim, M. Sarathy, A. Farooq. Ion measurements in premixed methane-oxygen flames. 50th AIAA/ASME/SAE/ASEE Joint Propulsion Conference; 2014. p. 3981.
- [205] A.B. Alquaity, J. Han, M. Chahine, H. Selim, M. Belhi, S.M. Sarathy, F. Bisetti, A. Farooq, Measurements of positively charged ions in premixed methane-oxygen atmospheric flames, *Combust. Sci. Technol.* 189 (2017) 575-594.
- [206] T. Pedersen, R.C. Brown, Simulation of electric field effects in premixed methane flames, *Combust. Flame* 94 (1993) 433-448.
- [207] E. Akyildiz, T. Bierkandt, T. Kasper, Detection of naturally occurring flame ions using a high- temperature atmospheric pressure interface coupled to ToF mass spectrometer, *Proceedings of the 6th European Combustion Meeting, Lund, Sweden, (2013).*
- [208] R. Kee, J. Grcar, M. Smooke, J. Miller, E. Meeks, J. Miller, E. Meeks, PREMIX: a Fortran program for modeling steady laminar one-dimensional premixed flames, Sandia Natl, Lab. Rep, (1985).
- [209] J. Han, M. Belhi, F. Bisetti, S. Mani Sarathy, Numerical modelling of ion transport in flames, *Combust. Theory Model* 19 (2015) 744-772.
- [210] F. Bisetti, M. El Morsli, Calculation and analysis of the mobility and diffusion coefficient of thermal electrons in methane/air premixed flames, *Combust. Flame* 159 (2012) 3518-3521.
- [211] W.K. Metcalfe, S.M. Burke, S.S. Ahmed, H.J. Curran, A hierarchical and comparative kinetic modeling study of C1– C2 hydrocarbon and oxygenated fuels, *Int. J. Chem. Kinet.* 45 (2013) 638-675.
- [212] D. Kim, F. Rizzi, K.W. Cheng, J. Han, F. Bisetti, O.M. Knio, Uncertainty quantification of ion chemistry in lean and stoichiometric homogenous mixtures of methane, oxygen, and argon, *Combust. Flame* 162 (2015) 2904-2915.
- [213] D. McElroy, C. Walsh, A. Markwick, M. Cordiner, K. Smith, T. Millar, The UMIST database for astrochemistry 2012, *Astron. Astrophys.* 550 (2013) A36.
- [214] A.N. Eraslan, R.C. Brown, Chemiionization and ion-molecule reactions in fuel-rich acetylene flames, *Combust. Flame* 74 (1988) 19-37.
- [215] J. Fang, Y. Wang, J. Kangasluoma, M. Attoui, H. Junninen, M. Kulmala, T. Petäjä, P. Biswas, Cluster formation mechanisms of titanium dioxide during combustion synthesis: Observation with an APi-TOF, *Aerosol Sci. Technol.* 51 (2017) 1071-1081.
- [216] A. Shmakov, O. Korobeinichev, D. Knyazkov, A. Paletsky, R. Maksutov, I. Gerasimov, T. Bolshova, V. Kiselev, N. Gritsan, Combustion chemistry of $Ti(OC_3H_7)_4$ in premixed flat burner-stabilized $H_2/O_2/Ar$ flame at 1 atm, *Proc. Combust. Inst.* 34 (2013) 1143-1149.
- [217] J.Z. Wen, M. Celnik, H. Richter, M. Treska, J.B. Vander Sande, M. Kraft, Modelling study of single walled carbon nanotube formation in a premixed flame, *J. Mater. Chem.* 18 (2008) 1582-1591.
- [218] B.M. Kumfer, K. Shinoda, B. Jeyadevan, I.M. Kennedy, Gas-phase flame synthesis and properties of magnetic iron oxide nanoparticles with reduced oxidation state, *J. Aerosol Sci* 41 (2010) 257-265.
- [219] R. Strobel, S.E. Pratsinis, Direct synthesis of maghemite, magnetite and wustite nanoparticles by flame spray pyrolysis, *Adv. Powder Technol.* 20 (2009) 190-194.
- [220] J.Z. Wen, H. Richter, W.H. Green, J.B. Howard, M. Treska, P.M. Jardim, J.B. Vander Sande, Experimental study of catalyst nanoparticle and single walled carbon nanotube formation in a controlled premixed combustion, *J. Mater. Chem.* 18 (2008) 1561-1569.
-

- [221] T. Dreier, C. Schulz Laser-based diagnostics in the gas-phase synthesis of inorganic nanoparticles, *Powder Technol.* 287 (2016) 226-238.
- [222] B. Chen, H. Wang, Z. Wang, J. Han, A.B. Alquaity, H. Wang, N. Hansen, S.M. Sarathy, Ion chemistry in premixed rich methane flames, *Combust. Flame* 202 (2019) 208-218.
- [223] T.A. Cool, A. McIlroy, F. Qi, P.R. Westmoreland, L. Poisson, D.S. Peterka, M. Ahmed, Photoionization mass spectrometer for studies of flame chemistry with a synchrotron light source, *Rev. Sci. Instrum.* 76 (2005) 094102.
- [224] C. Backx, G. Wight, M. Van der Wiel, Oscillator strengths (10-70 eV) for absorption, ionization and dissociation in H₂, HD and D₂, obtained by an electron-ion coincidence method, *J. Phys. B* 9 (1976) 315.
- [225] M. Glass-Maujean, S. Klumpp, L. Werner, A. Ehresmann, H. Schmoranzler, Study of the B ¹Σ⁺_u state of H₂: Transition probabilities from the ground state, dissociative widths, and Fano parameters, *J. Chem. Phys.* 126 (2007) 144303.
- [226] D. Holland, D. Shaw, S. McSweeney, M. MacDonald, A. Hopkirk, M. Hayes, A study of the absolute photoabsorption, photoionization and photodissociation cross sections and the photoionization quantum efficiency of oxygen from the ionization threshold to 490 Å, *Chem. Phys.* 173 (1993) 315-331.
- [227] J. Samson, W.C. Stolte, Precision measurements of the total photoionization cross-sections of He, Ne, Ar, Kr, and Xe, *J. Electron. Spectrosc. Relat. Phenom.* 123 (2002) 265-276.
- [228] D. Katayama, R. Huffman, C. O'Bryan, Absorption and photoionization cross sections for H₂O and D₂O in the vacuum ultraviolet, *J. Chem. Phys.* 59 (1973) 4309-4319.
- [229] J. Wang, B. Yang, T.A. Cool, N. Hansen, T. Kasper, Near-threshold absolute photoionization cross-sections of some reaction intermediates in combustion, *Int. J. Mass spectrom.* 269 (2008) 210-220.
- [230] T.A. Cool, J. Wang, K. Nakajima, C.A. Taatjes, A. McIlroy, Photoionization cross sections for reaction intermediates in hydrocarbon combustion, *Int. J. Mass spectrom.* 247 (2005) 18-27.
- [231] J.A. Samson, J. Gardner, Partial photoionization cross-sections and branching ratios of CO from 750 to 304 Å, *J. Electron. Spectrosc. Relat. Phenom.* 8 (1976) 35-44.
- [232] D. Shaw, D. Holland, M. Hayes, M. MacDonald, A. Hopkirk, S. McSweeney, A study of the absolute photoabsorption, photoionisation and photodissociation cross sections and the photoionisation quantum efficiency of carbon dioxide from the ionisation threshold to 345 Å, *Chem. Phys.* 198 (1995) 381-396.
- [233] J.A. Samson, P. Pareek, Absolute photoionization cross sections of atomic oxygen, *Phys. Rev. A* 31 (1985) 1470.
- [234] P.M. Dehmer, Photoionization of OH in the region 750–950 Å, *Chem. Phys. Lett.* 110 (1984) 79-84.
- [235] M. Schenk, L. Leon, K. Moshhammer, P. Oßwald, T. Zeuch, L. Seidel, F. Mauss, K. Kohse-Höinghaus, Detailed mass spectrometric and modeling study of isomeric butene flames, *Combust. Flame* 160 (2013) 487-503.
- [236] Y. Karakaya, H. Janbazi, I. Wlokas, A. Levish, M. Winterer, T. Kasper, Experimental and numerical study on the influence of equivalence ratio on key intermediates and silica nanoparticles in flame synthesis, *Proc. Combust. Inst.* 38 (2020) 1375-1383.
- [237] S. Axford, A.N. Hayhurst, Ionisation in premixed fuel-lean flames of H₂, O₂ and N₂. Part 1.—Naturally occurring positive ions, *J. Chem. Soc., Faraday Trans.* 91 (1995) 827-833.
-

- [238] A. Hayhurst, D. Kittelson, Mass spectrometric sampling of ions from atmospheric pressure flames—III: Boundary layer and other cooling of the sample, *Combust. Flame* 28 (1977) 137-143.
- [239] G. Hulthe, G. Stenhagen, O. Wennerström, C.-H. Ottosson, Water clusters studied by electrospray mass spectrometry, *J. Chromatogr. A* 777 (1997) 155-165.
- [240] D. Zook, E. Grimsrud, Measurement of ion clustering equilibria of proton hydrates by atmospheric pressure ionization mass spectrometry, *J. Phys. Chem.* 92 (1988) 6374-6379.
- [241] P. Kebarle, S.K. Searles, A. Zolla, J. Scarborough, M. Arshadi, Solvation of the hydrogen ion by water molecules in the gas phase. Heats and entropies of solvation of individual reactions $H^+(H_2O)_{n-1}+H_2O \rightarrow H^+(H_2O)_n$, *J. Am. Chem. Soc.* 89 (1967) 6393-6399.
- [242] G.P. Smith, D.M. Golden, M. Frenklach, N.W. Moriarty, B. Eiteneer, M. Goldenberg, C.T. Bowman, R.K. Hanson, S. Song, W.C. Gardiner Jr, V.V. Lissianski, Z. Qin, GRIMech 3.0 reaction mechanism, Berkeley, 2012.
- [243] C.P. Lazzara, J.C. Biordi, J.F. Papp, Concentration profiles for radical species in a methane-oxygen-argon flame, *Combust. Flame* 21 (1973) 371-382.
- [244] A.N. Hayhurst, S.G. Taylor, The stabilities of the gas-phase ions $Li^+ \cdot H_2O$, $Li^+ \cdot (H_2O)_2$ and $Li^+ \cdot CO$ as measured by mass-spectrometric sampling of fuel-rich flames of $C_2H_2+O_2$, *Phys. Chem. Chem. Phys.* 5 (2003) 1610-1618.
- [245] Y. Lau, S. Ikuta, P. Kebarle, Thermodynamics and kinetics of the gas-phase reactions $H_3O^+(H_2O)_{n-1}+water=H_3O^+(H_2O)_n$, *J. Am. Chem. Soc.* 104 (1982) 1462-1469.
- [246] E.L. Knuth, Composition distortion in MBMS sampling, *Combust. Flame* 103 (1995) 171-180.
- [247] J.E. Sansonetti, W.C. Martin, Handbook of basic atomic spectroscopic data, *J. Phys. Chem. Ref. Data* 34 (2005) 1559-2259.
- [248] E.P. Hunter, S.G. Lias, Evaluated gas phase basicities and proton affinities of molecules: an update, *J. Phys. Chem. Ref. Data* 27 (1998) 413-656.
- [249] Q. Tran, N.S. Karellas, J.M. Goodings, Ion chemistry of transition metals in hydrocarbon flames. I. Cations of Fe, Co, Ni, Cu, and Zn, *Can. J. Chem.* 66 (1988) 2210-2218.
- [250] N.S. Ham, T. McAllister, Flame ionization of iron and lead, *Aust. J. Chem.* 36 (1983) 1299-1304.
- [251] A. Hayhurst, N. Telford, Charge exchange reactions of H_3O^+ with metals in flames, *Trans. Faraday Soc.* 66 (1970) 2784-2793.
- [252] D.K. Böhme, H. Schwarz, Gas-phase catalysis by atomic and cluster metal ions: The ultimate single-site catalysts, *Angew. Chem. Int. Ed.* 44 (2005) 2336-2354.
- [253] D.E. Jensen, G.A. Jones, Iron compounds in flames. Relative stabilities of Fe, FeO, FeOH and $Fe(OH)_2$, *J. Chem. Soc., Faraday Trans. 1* 69 (1973) 1448-1454.
- [254] A.F. Hollemann, *Lehrbuch der anorganischen Chemie*, Hollemann-Wiberg, de Gruyter, Berlin 101 (1995) 1118.
- [255] F.N. Egolfopoulos, N. Hansen, Y. Ju, K. Kohse-Höinghaus, C.K. Law, F. Qi, Advances and challenges in laminar flame experiments and implications for combustion chemistry, *Prog. Energy Combust. Sci.* 43 (2014) 36-67.
- [256] L. Ruwe, L. Cai, J. Wullenkord, S.C. Schmitt, D. Felsmann, M. Baroncelli, B. Chen, K. Moshhammer, N. Hansen, H. Pitsch, Low-and high-temperature study of n-heptane combustion chemistry, *Proc. Combust. Inst.* 38 (2020) 405-413.
- [257] O.I. Smith, D.W. Chandler, An experimental study of probe distortions to the structure of one-dimensional flames, *Combust. Flame* 63 (1986) 19-29.
-

- [258] A.N. Hayhurst, J.M. Goodings, S.G. Taylor, The effects of applying electric fields on the mass spectrometric sampling of positive and negative ions from a flame at atmospheric pressure, *Combust. Flame* 161 (2014) 3249-3262.
- [259] A.N. Hayhurst, S.G. Taylor, The ions in fuel-rich hydrogen flames with added ammonia: measurements of the proton affinity of NH_3 and the enthalpy of monohydration of NH_4^+ , *Phys. Chem. Chem. Phys.* 4 (2002) 561-570.
- [260] A. Hayhurst, D. Kittelson, N. Telford, Mass spectrometric sampling of ions from atmospheric pressure flames—II: aerodynamic disturbance of a flame by the sampling system, *Combust. Flame* 28 (1977) 123-135.
- [261] A. Hayhurst, Mass spectrometric sampling of a flame, *Combust. Explos. Shock Waves* 48 (2012) 516-525.
- [262] J.C. Biordi, C.P. Lazzara, J.F. Papp, Molecular beam mass spectrometry applied to determining the kinetics of reactions in flames. I. Empirical characterization of flame perturbation by molecular beam sampling probes, *Combust. Flame* 23 (1974) 73-82.
- [263] O. Korobeinichev, A. Tereshchenko, I. Emel'yanov, A. Rudnitskii, S.Y. Fedorov, L. Kuibida, V. Lotov, Substantiation of the probe mass-spectrometric method for studying the structure of flames with narrow combustion zones, *Combust. Explos. Shock Waves* 21 (1985) 524-530.
- [264] P. Skovorodko, A. Tereshchenko, O. Korobeinichev, D. Knyazkov, A. Shmakov, Experimental and numerical study of probe-induced perturbations of the flame structure, *Combust. Theory Model* 17 (2013) 1-24.
- [265] V. Gururajan, F.N. Egolfopoulos, K. Kohse-Höinghaus, Direct numerical simulations of probe effects in low-pressure flame sampling, *Proc. Combust. Inst.* 35 (2015) 821-829.
- [266] N. Hansen, R.S. Tranter, K. Moshhammer, J.B. Randazzo, J.P. Lockhart, P.G. Fugazzi, T. Tao, A.L. Kastengren, 2D-imaging of sampling-probe perturbations in laminar premixed flames using Kr X-ray fluorescence, *Combust. Flame* 181 (2017) 214-224.
- [267] N. Hansen, R. Tranter, J. Randazzo, J. Lockhart, A. Kastengren, Investigation of sampling-probe distorted temperature fields with x-ray fluorescence spectroscopy, *Proc. Combust. Inst.* 37 (2019) 1401-1408.
- [268] J. Camacho, C. Liu, C. Gu, H. Lin, Z. Huang, Q. Tang, X. You, C. Saggese, Y. Li, H. Jung, Mobility size and mass of nascent soot particles in a benchmark premixed ethylene flame, *Combust. Flame* 162 (2015) 3810-3822.
- [269] C. Weise, A. Faccinetto, S. Kluge, T. Kasper, H. Wiggers, C. Schulz, I. Wlokas, A. Kempf, Buoyancy induced limits for nanoparticle synthesis experiments in horizontal premixed low-pressure flat-flame reactors, *Combust. Theory Model* 17 (2013) 504-521.
- [270] W. Pejpichestakul, A. Cuoci, A. Frassoldati, M. Pelucchi, A. Parente, T. Faravelli, Buoyancy effect in sooting laminar premixed ethylene flame, *Combust. Flame* 205 (2019) 135-146.
- [271] A. Hayhurst, N. Telford, The occurrence of chemical reactions in supersonic expansions of a gas into a vacuum and its relation to mass spectrometric sampling, *Proc. R. Soc. London, Ser. A* 322 (1971) 483-507.
- [272] C. Saggese, A. Cuoci, A. Frassoldati, S. Ferrario, J. Camacho, H. Wang, T. Faravelli, Probe effects in soot sampling from a burner-stabilized stagnation flame, *Combust. Flame* 167 (2016) 184-197.
- [273] D. Keil, R. Gill, D. Olson, H. Calcote, Ionization and soot formation in premixed flames, *Symp. Int. Combust. Proc.* 20 (1985) 1129-1137.
-

- [274] P. Gerhardt, K.d. Homann, Ions and charged soot particles in hydrocarbon flames. 2. Positive aliphatic and aromatic ions in ethyne/oxygen flames, *J. Phys. Chem.* 94 (1990) 5381-5391.
- [275] H. Jander, H.G. Wagner, Formation of flame ions, clusters, nanotubes, and soot in hydrocarbon flames, *Combust. Explos. Shock Waves* 42 (2006) 696-701.
- [276] C. Morley, Sampling of ions from flames, *Vacuum* 24 (1974) 581-584.
- [277] P. Kebarle, R.M. Haynes, J.G. Collins, Competitive solvation of the hydrogen ion by water and methanol molecules studied in the gas phase, *J. Am. Chem. Soc.* 89 (1967) 5753-5757.
- [278] Y. Li, C.-W. Zhou, K.P. Somers, K. Zhang, H.J. Curran, The oxidation of 2-butene: A high pressure ignition delay, kinetic modeling study and reactivity comparison with isobutene and 1-butene, *Proc. Combust. Inst.* 36 (2017) 403-411.
- [279] OpenCFD Release OpenFOAM, 2012 <<http://www.openfoam.org/version2.1.0>>.
- [280] A. Kazakov, M. Frenklach, <http://www.me.berkeley.edu/drm/>.
- [281] V. Tarnovsky, A. Levin, H. Deutsch, K. Becker, Electron impact ionization of (x= 1-4), *J. Phys. B: At., Mol. Opt. Phys.* 29 (1996) 139.
- [282] N. Burdett, A. Hayhurst, Kinetics of formation and removal of atomic halogen ions X^- by $HX + e \rightleftharpoons H + X^-$ in atmospheric pressure flames for chlorine, bromine and iodine, *Proc. R. Soc. London, Ser. A* 355 (1977) 377-405.
- [283] N.A. Burdett, A.N. Hayhurst, Hydration of gas-phase ions and the measurement of boundary-layer cooling during flame sampling into a mass spectrometer, *J. Chem. Soc., Faraday Trans. 1* 78 (1982) 2997-3007.
- [284] N. Burdett, A. Hayhurst, Mass spectrometric sampling of ions from atmospheric pressure flames. IV. Scattering processes in molecular beams from supersonic expansions, *Combust. Flame* 34 (1979) 119-134.
- [285] Y. Karakaya, T. Kasper, Comparative mass spectrometric study of gaseous key intermediates from tetramethylsilane and hexamethyldisiloxane in silica synthesis flames, *Proceedings of the 9th European Combustion Meeting, Lisboa, Portugal* 9 (2019).
- [286] M. Poliak, A. Fomin, V. Tsionsky, S. Cheskis, I. Wlokas, I. Rahinov, On the mechanism of nanoparticle formation in a flame doped by iron pentacarbonyl, *Phys. Chem. Chem. Phys.* 17 (2015) 680-685.
-

Appendix A of chapter 6

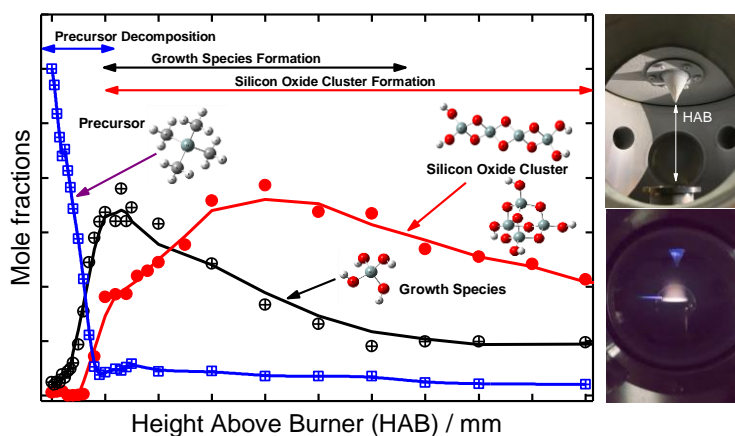


Figure A-1. Table of Contents (TOC) Image

Schematics of the experimental setup

Time-of-Flight Molecular Beam Mass Spectrometer system (ToF-MBMS)

An established technique for identifying and quantifying combustion species, e.g. reactive radicals, in laminar low pressure flames is time-of-flight Molecular-Beam Mass Spectrometry (ToF-MBMS). A schematic of the instrument used in this study is shown in Figure A-1. One of the biggest challenges with this technique is the transfer of a representative sample from the flame to the mass analyzer without influencing the gas composition. With a nozzle-skimmer system, gas is sampled from the flame and the reactions are quenched by a pressure drop. The molecular-beam formed by the sampling system is then ionized in the ionization chamber by electron ionization. The electron beam has an electron energy distribution of FWHM = 0.5 eV that allows many species to be detected simultaneously.

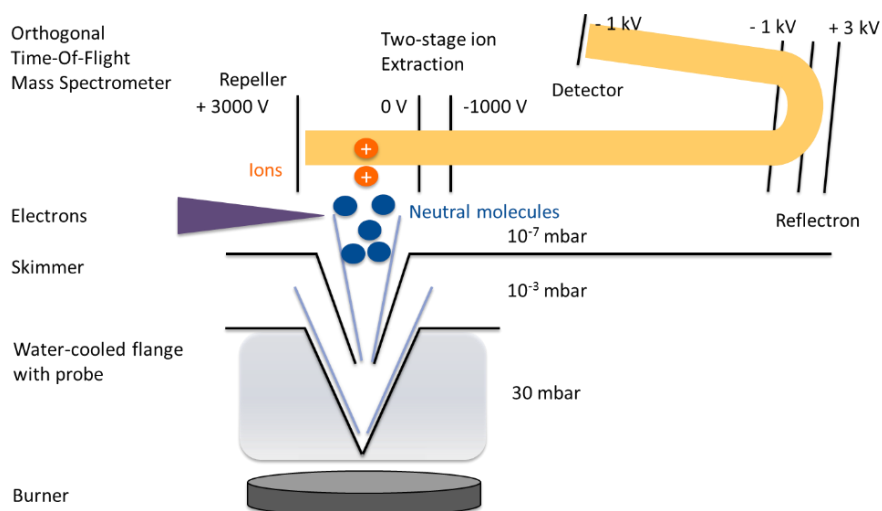


Figure A-2. Experimental schematic of the Time-of-Flight Molecular-Beam Mass Spectrometer system (ToF-MBMS)

Mass spectra of silicon containing species

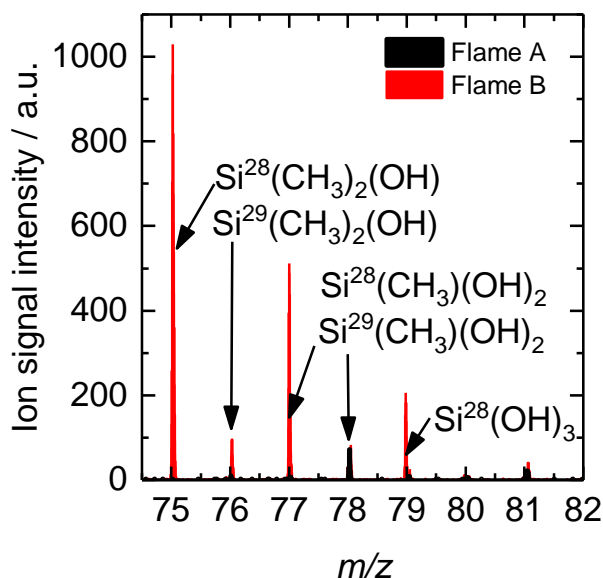


Figure A-3. Mass spectra at HAB = 4 mm without TMS (flame A) and with addition of 600 ppm TMS (flame B) in a $\text{H}_2/\text{O}_2/\text{Ar}$ -Flame at an electron ionization energy of EI = 17.

Figure A-3 shows an excerpt from typical mass spectra in the reaction zones of flames A and B. Upon addition of TMS, signals of Si containing species are detected with the correct isotope patterns. Small signals of hydrocarbons appear on each nominal mass. In conjunction with the exact mass the isotope patterns are used to distinguish between hydrocarbon and silicon species and signals are deconvoluted if the mass separation is sufficient.

Silicon oxide structures

Theoretical calculations by Xu et al. [133] and Timoshkin et al. [134] show that the silicon oxide clusters can have different structures, e.g. a tetrahedral cage structure or a linear chain structure as example for $\text{Si}_4\text{O}_{10}\text{H}_4$ (see Figure A-4). The clusters with $m/z = 336$ ($\text{Si}_5\text{O}_{12}\text{H}_4$) and $m/z = 396$ ($\text{Si}_6\text{O}_{14}\text{H}_4$) cannot form a cage structure in which each silicon atom is coordinated tetrahedrally by oxygen. For these species a chain structure seems more likely.

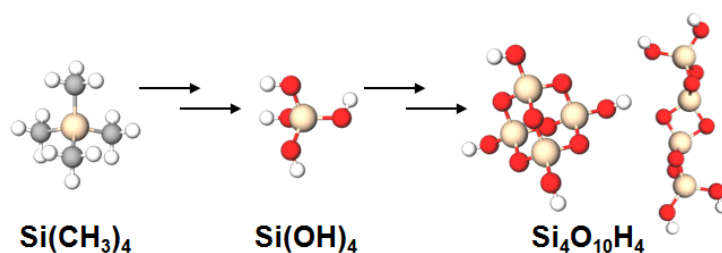


Figure A-4. Silicon oxide cluster growth

Appendix B of chapter 7

Thermochemistry in the form of NASA polynomial coefficients for the Si–C–O–H containing molecules, Lennard-Jones parameters, reaction path diagrams, sensitivity analyses of results to uncertainty of thermodynamic properties, and molecular parameters and energies used for RRKM calculations

Energetics and molecular properties from *ab initio* calculations used for RRKM calculations

Table B-1. Reaction $\text{Si}(\text{CH}_3)_2\text{O} \rightarrow (\text{CH}_3)(\text{OH})\text{SiCH}_2$.

Frequencies (cm^{-1}): Si(CH₃)₂O : 27, 74, 216, 259, 293, 625, 683, 684, 790, 803, 854, 1249, 1280, 1288, 1443, 1448, 1453, 1464, 3031, 3035, 3097, 3101, 3145, 3146 TS(Si(CH₃)₂O→(CH₃)(OH)SiCH₂) : 1767i, 46, 174, 228, 353, 446, 641, 704, 736, 784, 807, 935, 1097, 1212, 1282, 1378, 1444, 1450, 1910, 3038, 3099, 3109, 3144, 3175
Rotational constants (g cm^2): Si(CH₃)₂O : 1.288×10^{-38} , 1.368×10^{-38} , 2.55×10^{-38} TS(Si(CH₃)₂O→(CH₃)(OH)SiCH₂) : 8.959×10^{-39} , 1.679×10^{-38} , 2.473×10^{-38}
Internal energies (G4 calculation; 0 K) E(Si(CH₃)₂O) : -444.349232 hartree E(TS(Si(CH₃)₂O→(CH₃)(OH)SiCH₂)) : -444.258461 hartree
Assumed collision efficiency: $\beta_c = 0.05$
Lennard-Jones parameter: Ar : $\epsilon/\text{K} = 113.5$; $\sigma/\text{\AA} = 3.47$ Si(CH₃)₂O : $\epsilon/\text{K} = 352.3$; $\sigma/\text{\AA} = 4.23$ (estimated to be analog to acetone)
Reaction path degeneracy: 2

Table B-2. Reaction $(\text{CH}_3)(\text{OH})\text{SiCH}_2 \rightarrow \text{Si}(\text{CH}_3)_2\text{O}$.

Frequencies (cm^{-1}): $(\text{CH}_3)(\text{OH})\text{SiCH}_2$: 126, 214, 221, 271, 296, 520, 623, 653, 685, 799, 805, 849, 945, 1066, 1294, 1382, 1453, 1462, 3046, 3119, 3136, 3154, 3240, 3883 TS$(\text{CH}_3)(\text{OH})\text{SiCH}_2 \rightarrow \text{Si}(\text{CH}_3)_2\text{O}$: See Table B-1; same transition state
Rotational constants (g cm^2): $(\text{CH}_3)(\text{OH})\text{SiCH}_2$: 1.184×10^{-38} , 1.393×10^{-38} , 2.524×10^{-38} TS$(\text{Si}(\text{CH}_3)_2\text{O} \rightarrow (\text{CH}_3)(\text{OH})\text{SiCH}_2$: See Table B-1; same transition state
Internal energies (G4 calculation; 0 K) $E((\text{CH}_3)(\text{OH})\text{SiCH}_2)$: -444.329452 hartree $E((\text{CH}_3)(\text{OH})\text{SiCH}_2 \rightarrow \text{Si}(\text{CH}_3)_2\text{O})$: -444.258461 hartree (see Table B-1)
Assumed collision efficiency: $\beta_c = 0.05$
Lennard-Jones parameter: Ar : $\epsilon/\text{K} = 113.5$; $\sigma/\text{\AA} = 3.47$ $(\text{CH}_3)(\text{OH})\text{SiCH}_2$: $\epsilon/\text{K} = 352.3$; $\sigma/\text{\AA} = 4.23$ (also estimated to be analog to acetone)
Reaction path degeneracy: 1

Table B-3. Reaction $\text{Si}(\text{CH}_3)_2\text{O} \rightarrow (\text{CH}_3)\text{SiO} + \text{CH}_3$; in this calculation, a RRKM-Gorin model was applied.

Frequencies (cm^{-1}): $\text{Si}(\text{CH}_3)_2\text{O}$: See Table B-1 $(\text{CH}_3)\text{SiO}$: 41, 242, 589, 652, 774, 1187, 1220, 1431, 1446, 3038, 3129, 3153 CH_3 : 471, 1407, 1407, 3122, 3305, 3305
Moments of inertia (g cm^2): $\text{Si}(\text{CH}_3)_2\text{O}$: 1.288×10^{-38} (This is used as the molecular active moment of inertia for calculation using the RRKM-Gorin model) $(\text{CH}_3)\text{SiO}$: 2.247×10^{-39} , 1.256×10^{-38} , 1.428×10^{-38} CH_3 : 2.935×10^{-40} , 2.935×10^{-40} , 5.871×10^{-40}
Internal energies (G4 calculation; 0 K) $E(\text{Si}(\text{CH}_3)_2\text{O})$: -444.349232 hartree (see Table B-1) $E((\text{CH}_3)\text{SiO})$: -404.416592 hartree $E(\text{CH}_3)$: -39.799951 hartree
$\langle \Delta E \rangle_{\text{down}} = 300 \text{ cm}^{-1}$
Restriction parameter η : $\eta = 1 - (0.01)$ This restriction parameter is estimated, based on values used in literature
Lennard-Jones parameter: Ar : $\epsilon/\text{K} = 113.5$; $\sigma/\text{\AA} = 3.47$ $\text{Si}(\text{CH}_3)_2\text{O}$: $\epsilon/\text{K} = 352.3$; $\sigma/\text{\AA} = 4.23$ (see Table B-1)
Reaction path degeneracy: 2

Table B-4. Reaction $\text{Si}(\text{CH}_3)_3\text{OH} \rightarrow \text{CH}_4 + \text{Si}(\text{CH}_3)_2\text{O}$.

<p>Frequencies (cm^{-1}):</p> <p>$\text{Si}(\text{CH}_3)_3\text{OH}$: 129, 147, 163, 176, 192, 213, 238, 281, 289, 601, 678, 680, 692, 746, 763, 795, 829, 861, 893, 944, 1291, 1292, 1300, 1454, 1457, 1458, 1466, 1468, 1476, 3024, 3026, 3034, 3094, 3097, 3105, 3105, 3108, 3113, 3895</p> <p>$\text{TS}(\text{Si}(\text{CH}_3)_3\text{OH} \rightarrow \text{CH}_4 + \text{Si}(\text{CH}_3)_2\text{O})$: 1475i, 67, 132, 161, 174, 209, 247, 286, 367, 465, 567, 635, 673, 721, 737, 796, 824, 848, 1142, 1208, 1258, 1288, 1295, 1444, 1448, 1450, 1453, 1457, 1469, 1920, 3028, 3031, 3032, 3099, 3099, 3102, 3128, 3130, 3156</p>
<p>Rotational constants (g cm^2):</p> <p>$\text{Si}(\text{CH}_3)_3\text{OH}$: 2.499×10^{-38}, 2.537×10^{-38}, 2.692×10^{-38}</p> <p>$\text{TS}(\text{Si}(\text{CH}_3)_3\text{OH} \rightarrow \text{CH}_4 + \text{Si}(\text{CH}_3)_2\text{O})$: 2.365×10^{-38}, 2.624×10^{-38}, 2.921×10^{-38}</p>
<p>Internal energies (G4 calculation; 0 K)</p> <p>$E(\text{Si}(\text{CH}_3)_3\text{OH})$: -484.875296 hartree</p> <p>$E(\text{Si}(\text{CH}_3)_3\text{OH} \rightarrow \text{CH}_4 + \text{Si}(\text{CH}_3)_2\text{O})$: -484.772328 hartree</p>
<p>Assumed collision efficiency: $\beta_c = 0.05$</p>
<p>Lennard-Jones parameter:</p> <p>Ar: $\epsilon/\text{K} = 113.5$; $\sigma/\text{\AA} = 3.47$</p> <p>$\text{Si}(\text{CH}_3)_3\text{OH}$: $\epsilon/\text{K} = 450.1$; $\sigma/\text{\AA} = 6.69$</p> <p>ϵ was estimated based on the boiling point of $\text{Si}(\text{CH}_3)_3\text{OH}$: b.p. ≈ 372 K (Grubb and Osthoff: <i>J. Am. Chem. Soc.</i> 1953, 75, 2230–2232;</p> <p>σ was estimated based on the volume increments provided in the paper from Ben-Amotz and Willis: <i>J. Phys. Chem.</i> 1993, 97, 7736-7742</p>
<p>Reaction path degeneracy: 1</p>

Table B-5. Reaction $\text{Si}(\text{CH}_3)_3\text{OH} \rightarrow \text{H}_2\text{O} + \text{Si}(\text{CH}_3)_2\text{CH}_2$.

<p>Frequencies (cm^{-1}): Si(CH₃)₃OH: See Table B-4) TS(Si(CH₃)₃OH→H₂O + Si(CH₃)₂CH₂): 375i, 130, 153, 166, 193, 217, 232, 303, 349, 493, 589, 621, 659, 665, 700, 795, 801, 828, 858, 877, 983, 1291, 1296, 1387, 1455, 1457, 1465, 1467, 1508, 2345, 3031, 3037, 3103, 3109, 3111, 3121, 3123, 3198, 3757</p>
<p>Rotational constants (g cm^2): Si(CH₃)₃OH: See Table B-4) TS(Si(CH₃)₃OH→CH₄+Si(CH₃)₂O): 2.472×10^{-38}, 2.589×10^{-38}, 2.895×10^{-38}</p>
<p>Internal energies (G4 calculation; 0 K) E(Si(CH₃)₃OH): -484.875296 hartree (see Table B-4)) E(Si(CH₃)₃OH→H₂O+Si(CH₃)₂CH₂): -484.757462 hartree</p>
<p>Assumed collision efficiency: $\beta_c = 0.05$</p>
<p>Lennard-Jones parameter: Ar: $\epsilon/\text{K} = 113.5$; $\sigma/\text{\AA} = 3.47$ Si(CH₃)₃OH: $\epsilon/\text{K} = 450.3$; $\sigma/\text{\AA} = 6.69$ (see Table B-4)</p>
<p>Reaction path degeneracy: 1</p>

Table B-6. Three-parameter fits, $k(T) = A \times T^n \times \exp(-E_a/RT)$ for reaction
 $\text{Si}(\text{CH}_3)_2\text{O} \rightarrow (\text{CH}_3)(\text{OH})\text{SiCH}_2$.

p / bar	A / s^{-1}	n	$E_a / \text{kJ/mol}$
0.01	8.406×10^{30}	-5.55	259.028
0.03	9.089×10^{24}	-3.70	249.389
0.1	1.727×10^{19}	-1.95	239.661
1.0	5.317×10^{12}	0.04	228.115
10.0	8.278×10^{10}	0.59	224.817
100.0	4.452×10^{10}	0.67	224.321
1000.0	4.162×10^{10}	0.68	224.269

Table B-7. Three-parameter fits, $k(T) = A \times T^n \times \exp(-E_a/RT)$ for reaction
 $(\text{CH}_3)(\text{OH})\text{SiCH}_2 \rightarrow \text{Si}(\text{CH}_3)_2\text{O}$.

p / bar	A / s^{-1}	n	$E_a / \text{kJ/mol}$
0.01	7.690×10^{47}	-10.88	227.528
0.03	7.100×10^{44}	-9.54	223.678
0.1	1.231×10^{38}	-7.68	216.389
1.0	1.628×10^{25}	-3.66	196.505
10.0	8.982×10^{15}	-0.83	180.549
100.0	6.975×10^{12}	0.12	174.953
1000.0	2.169×10^{12}	0.27	174.026

Table B-8. Three-parameter fits, $k(T) = A \times T^n \times \exp(-E_a/RT)$ for reaction
 $\text{Si}(\text{CH}_3)_2\text{O} \rightarrow (\text{CH}_3)\text{SiO} + \text{CH}_3$.

p / bar	A / s^{-1}	n	$E_a / \text{kJ/mol}$
0.01	1.301×10^{78}	-18.97	441.809
0.03	1.938×10^{76}	-18.27	442.851
0.1	2.076×10^{71}	-16.62	437.985
1.0	4.833×10^{55}	-11.71	414.888
10.0	3.245×10^{39}	-6.74	387.586
100.0	3.042×10^{29}	-3.685	369.787
1000.0	6.014×10^{25}	-2.56	363.100

Table B-9. Three-parameter fits, $k(T) = A \times T^n \times \exp(-E_a/RT)$ for reaction
 $\text{Si}(\text{CH}_3)_3\text{OH} \rightarrow \text{CH}_4 + \text{Si}(\text{CH}_3)_2\text{O}$.

p / bar	A / s^{-1}	n	E_a / kJ/mol
0.01	2.964×10^{16}	-1.01	266.494
0.03	1.468×10^{14}	-0.31	262.252
0.1	7.713×10^{12}	0.08	259.878
1.0	1.496×10^{12}	0.29	258.549
10.0	1.217×10^{12}	0.32	258.381
100.0	1.191×10^{12}	0.32	258.364
1000.0	1.189×10^{12}	0.32	258.362

Table B-10. Three-parameter fits, $k(T) = A \times T^n \times \exp(-E_a/RT)$ for reaction
 $\text{Si}(\text{CH}_3)_3\text{OH} \rightarrow \text{H}_2\text{O} + \text{Si}(\text{CH}_3)_2\text{CH}_2$.

p / bar	A / s^{-1}	n	E_a / kJ/mol
0.01	2.639×10^{12}	0.18	301.712
0.03	8.063×10^{11}	0.34	300.750
0.1	4.820×10^{11}	0.41	300.331
1.0	3.843×10^{11}	0.44	300.146
10.0	3.752×10^{11}	0.44	300.126
100.0	3.743×10^{11}	0.44	300.124
1000.0	3.742×10^{11}	0.44	300.124

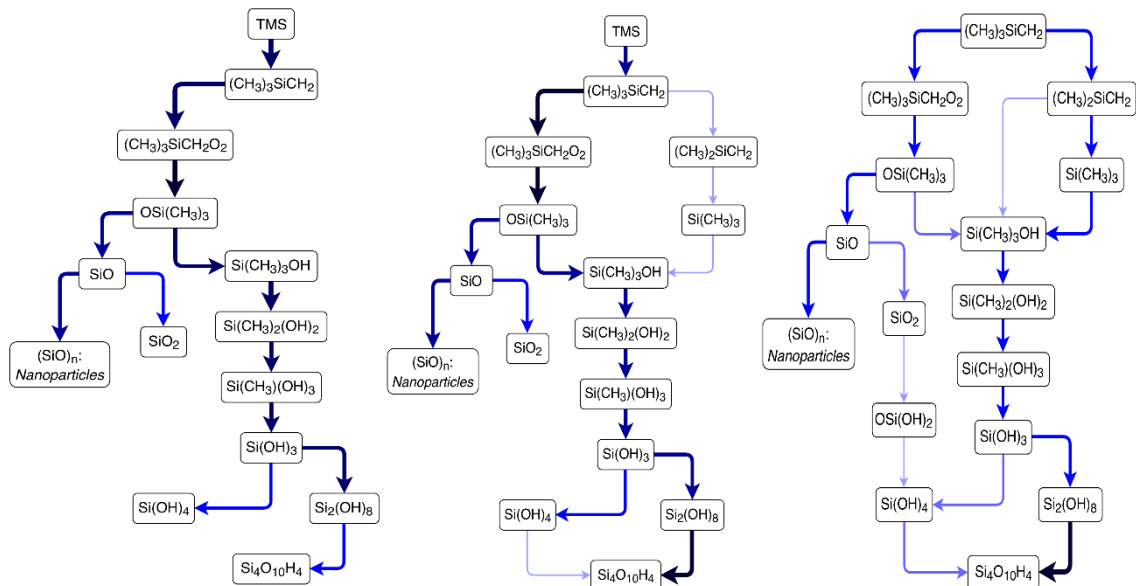


Figure B-1. Reaction pathways of the element Si for gas-phase species at 600, 700, and 1000 K from left to right.

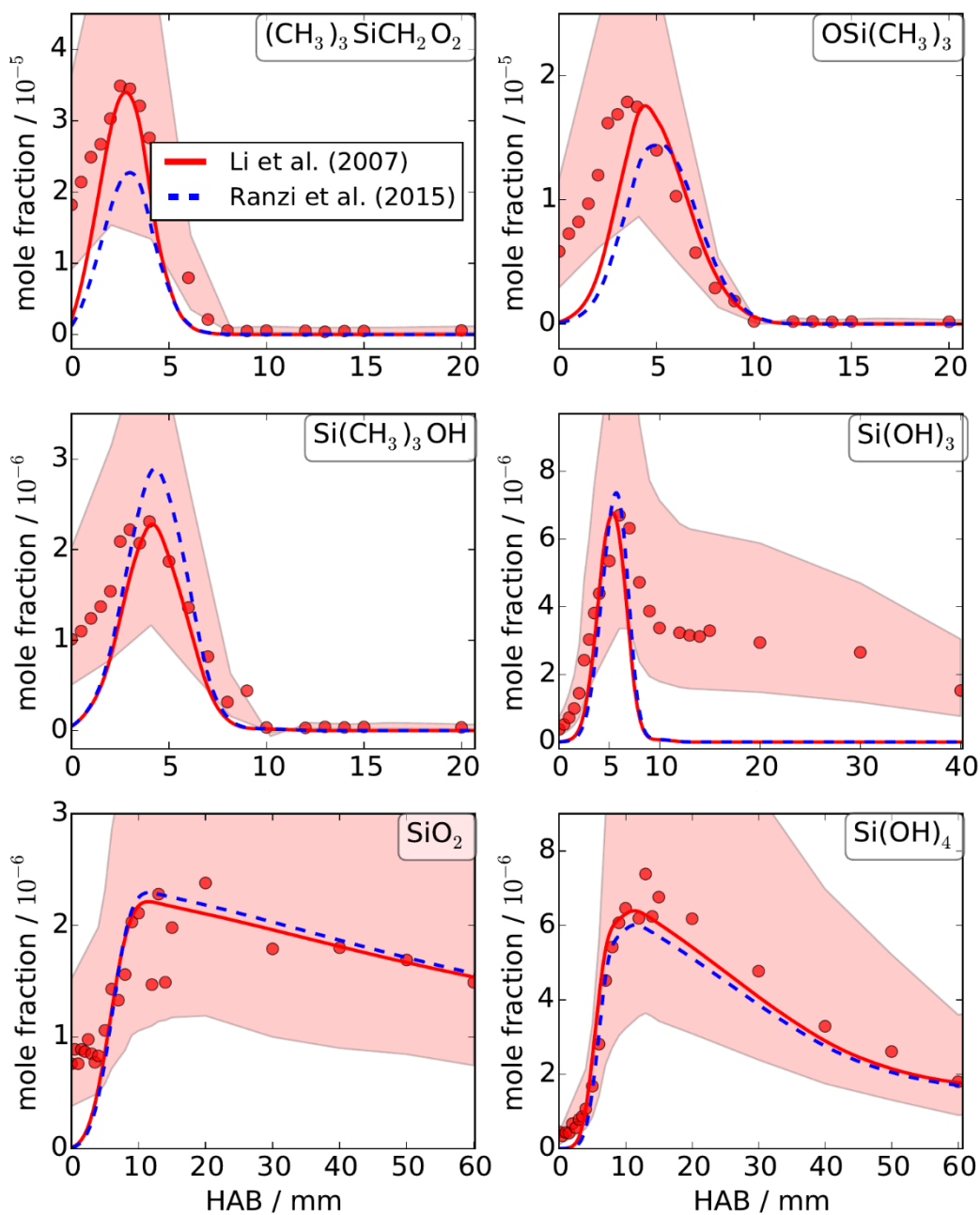


Figure B-2. Measured and simulated mole-fraction profiles of Si-containing species for flame B (600 ppm TMS). Simulations are performed with TMS mechanism merged with (a) Li and (b) Ranzi mechanism. Symbols: experiment, lines: simulation.

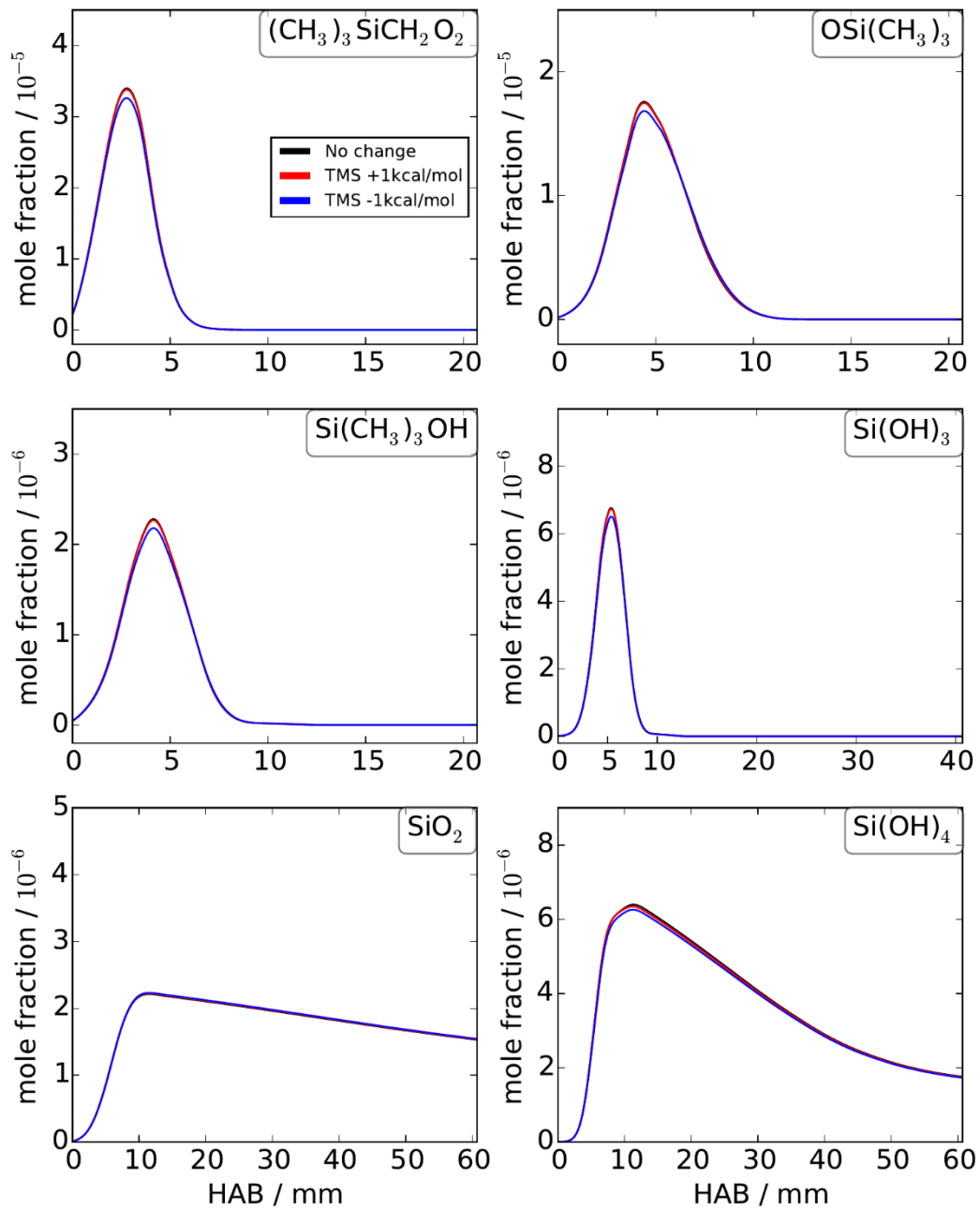


Figure B-3. Sensitivity of the results to the standard enthalpy of formation. Simulated mole-fraction profiles of Si-containing species with ± 4.2 kJ/mol change of standard enthalpy of formation for TMS.

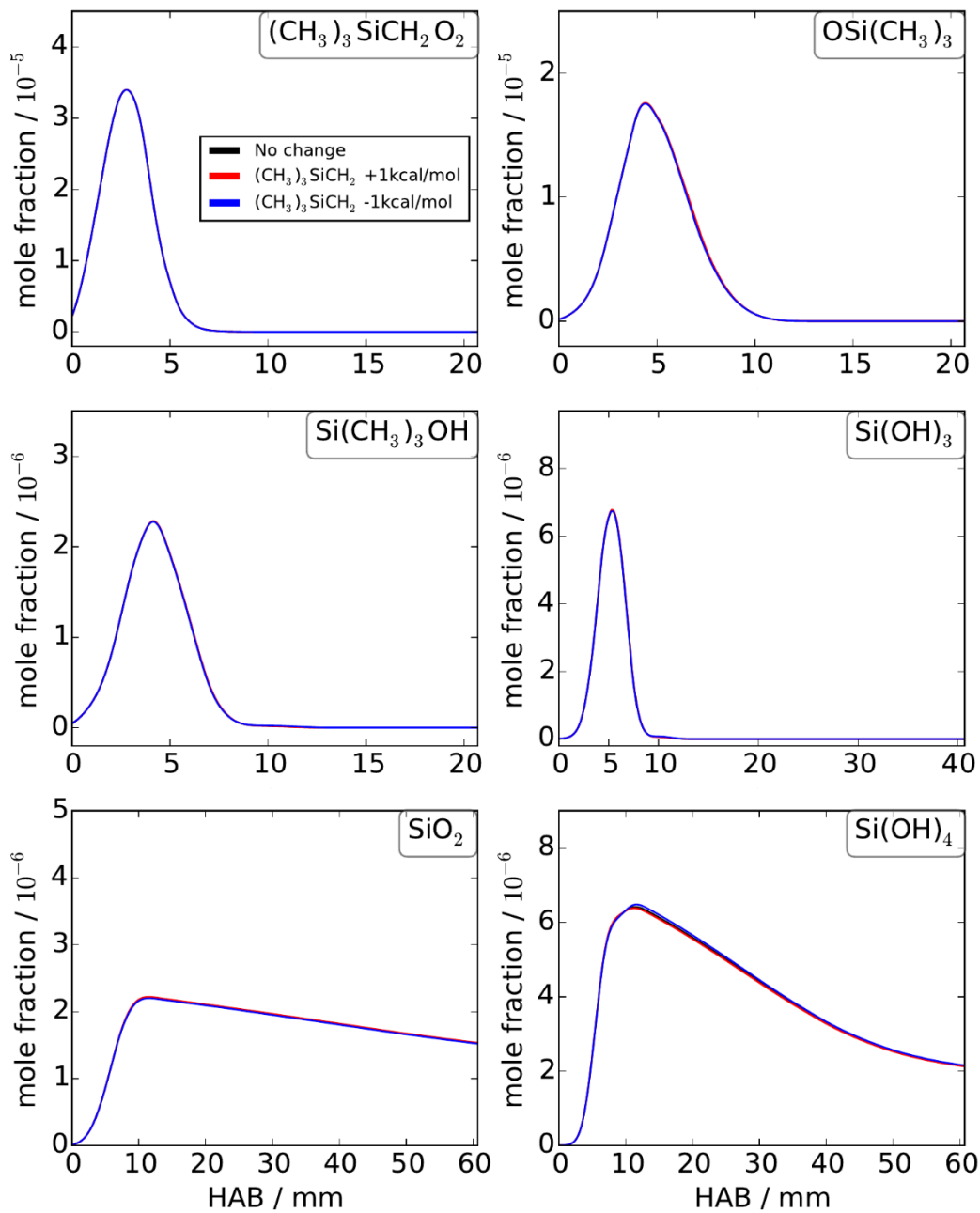


Figure B-4. Sensitivity of the results to the standard enthalpy of formation. Simulated mole-fraction profiles of Si-containing species with ± 4.2 kJ/mol change of standard enthalpy of formation for $(\text{CH}_3)_3\text{SiCH}_2$.

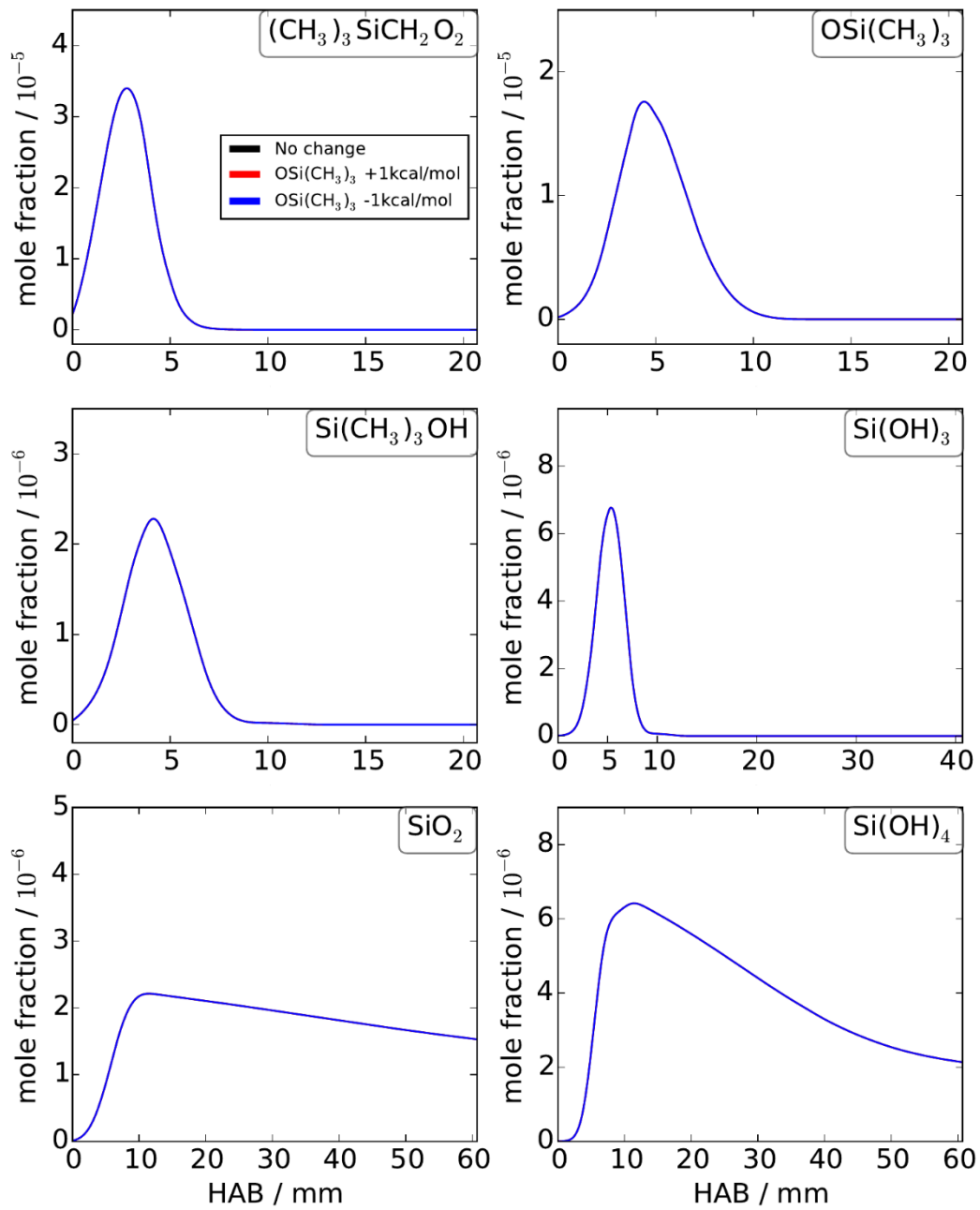


Figure B-5. Sensitivity of the results to the standard enthalpy of formation. Simulated mole-fraction profiles of Si-containing species with ± 4.2 kJ/mol change of standard enthalpy of formation for OSi(CH₃)₃.

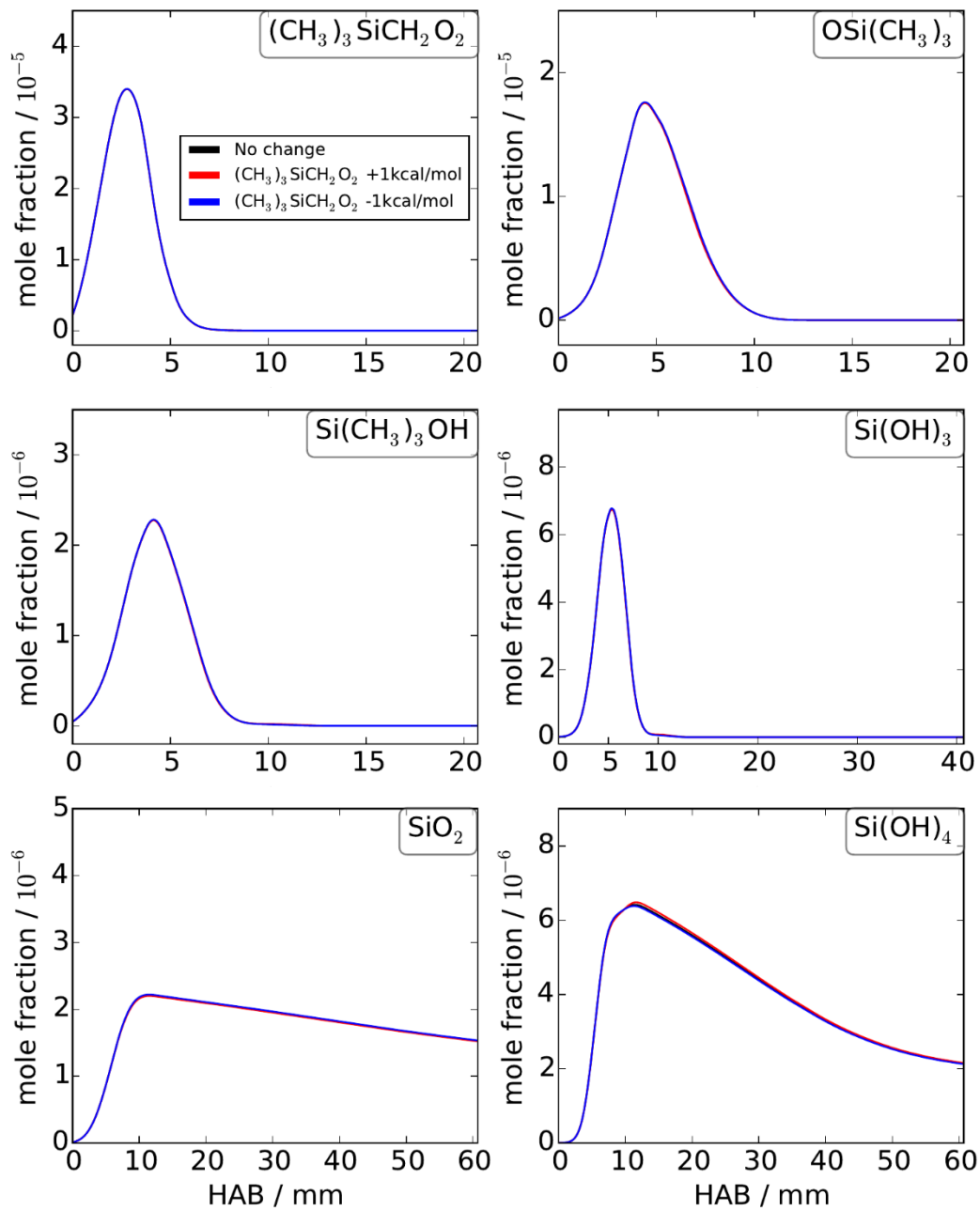


Figure B-6. Sensitivity of the results to the standard enthalpy of formation. Simulated mole-fraction profiles of Si-containing species with ± 4.2 kJ/mol change of standard enthalpy of formation for $(\text{CH}_3)_3\text{SiCH}_2\text{O}_2$.

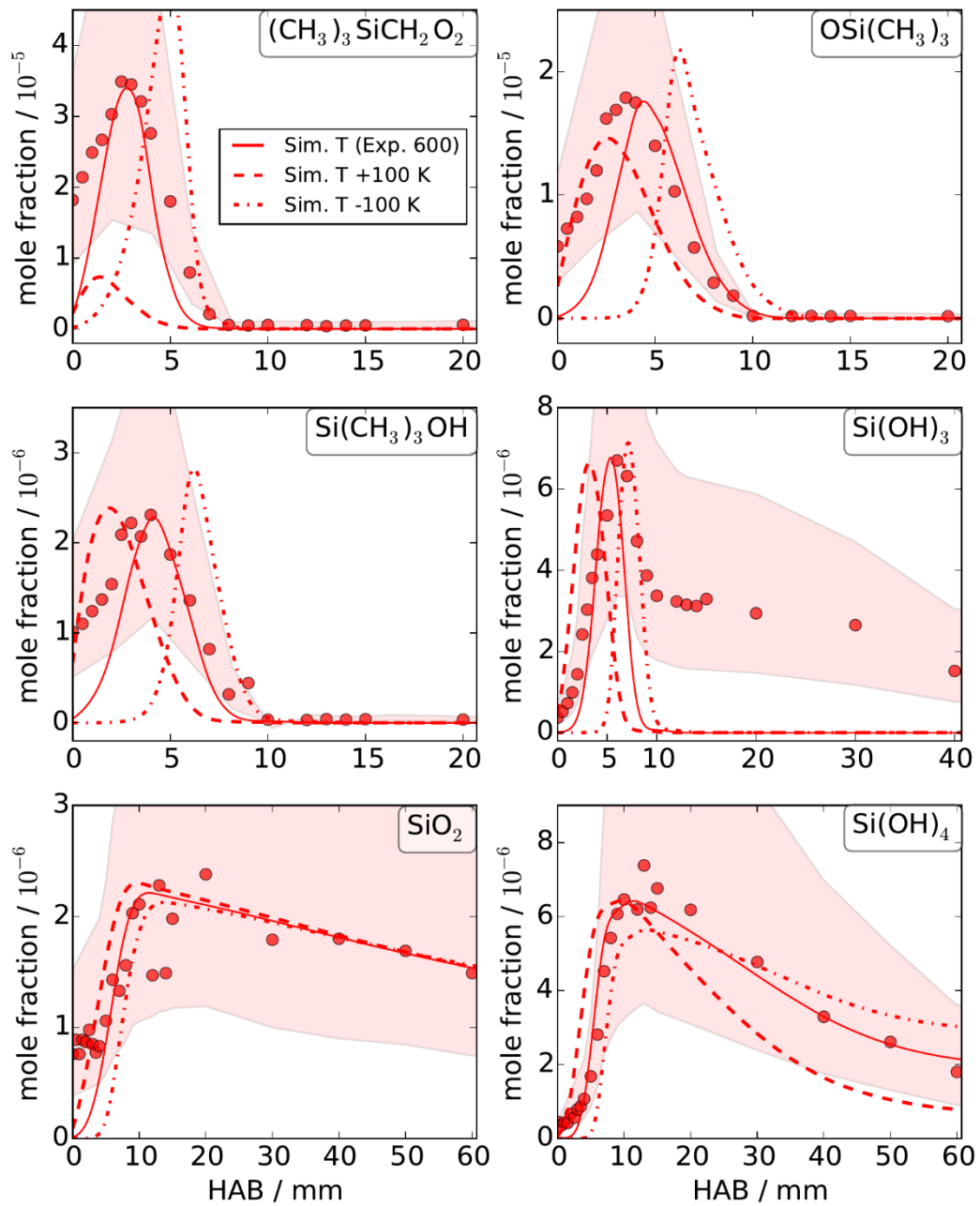


Figure B-7. Sensitivity of the results to the measured temperature for flame B (600 ppm TMS).

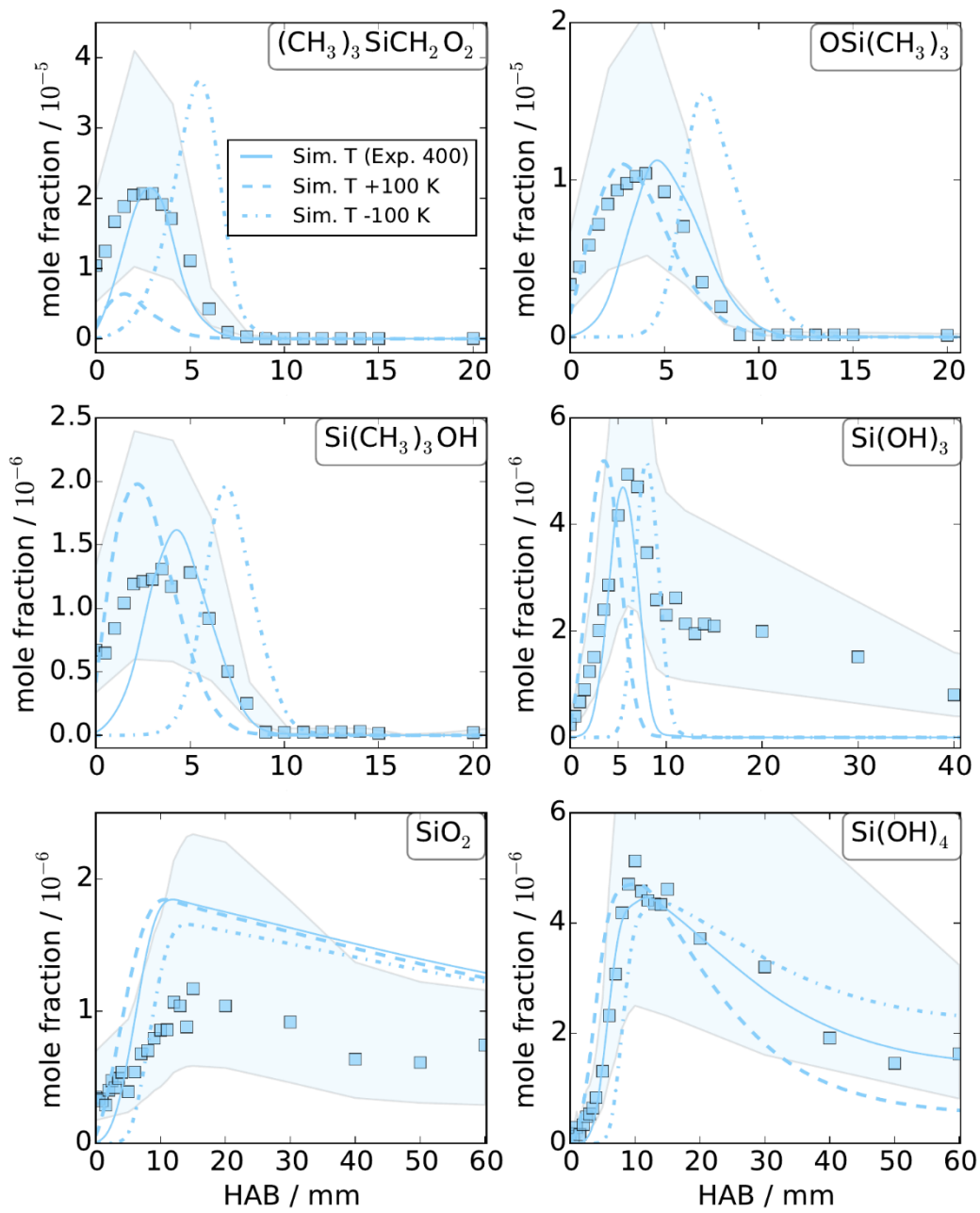


Figure B-8. Sensitivity of the results to the measured temperature for flame C (400 ppm TMS).

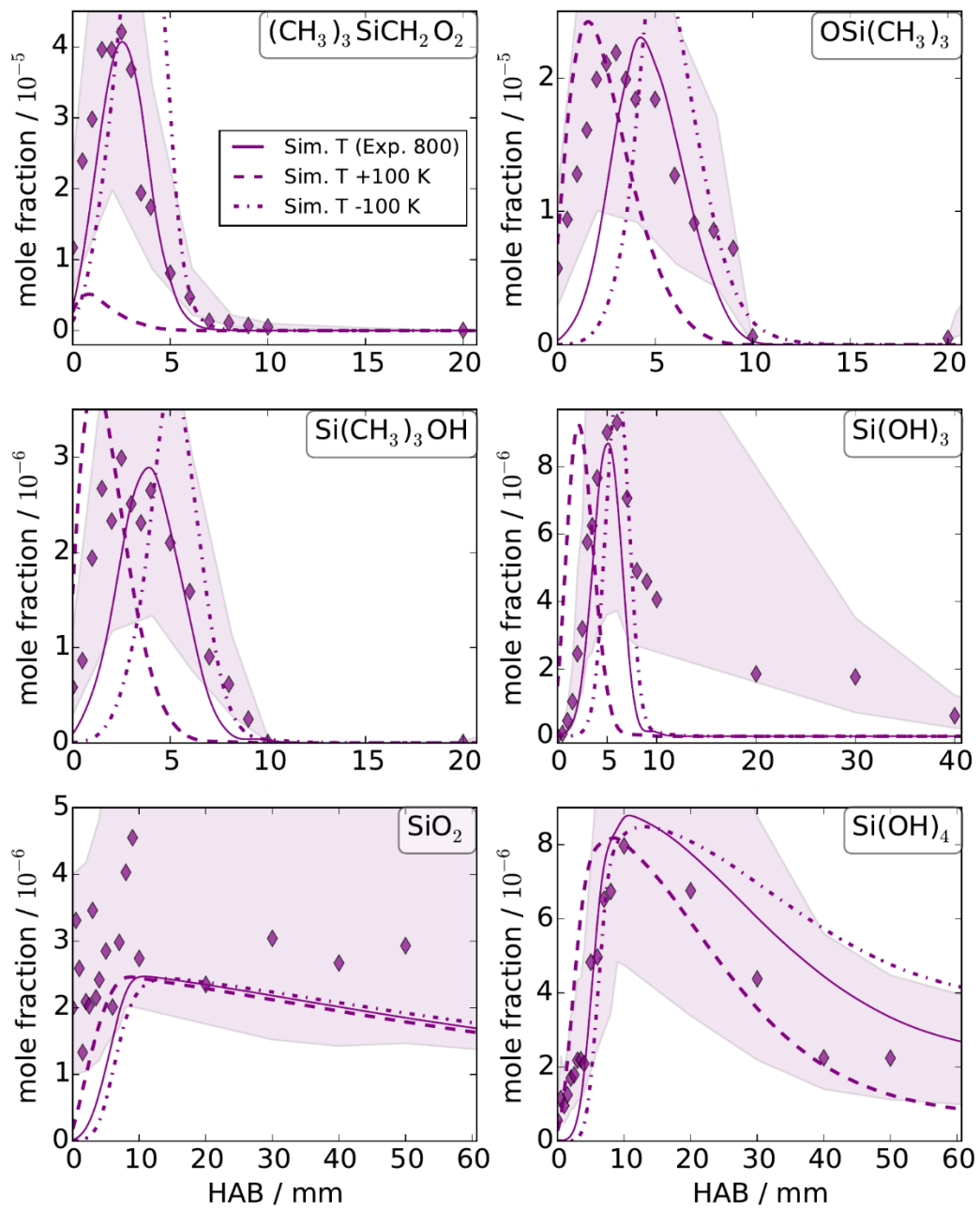


Figure B-9. Sensitivity of the results to the measured temperature for flame D (800 ppm TMS).

Appendix C of chapter 8

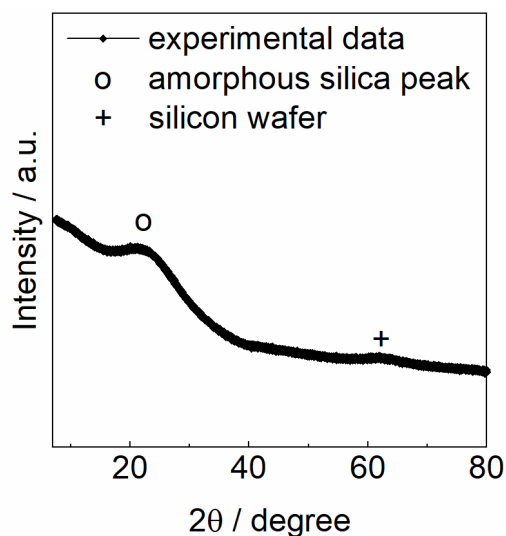


Figure C-1. X-ray diffraction pattern obtained from the silica powder, which is collected after a series of measurements with the three flames D, F and H of the equivalence ratio $\varphi = 0.8$, 1.0 and 1.2, respectively.

Figure C-1 shows a X-ray diffraction pattern obtained from the silica powder with the corresponding peaks for amorphous silica and silicon wafer used as a sample holder.

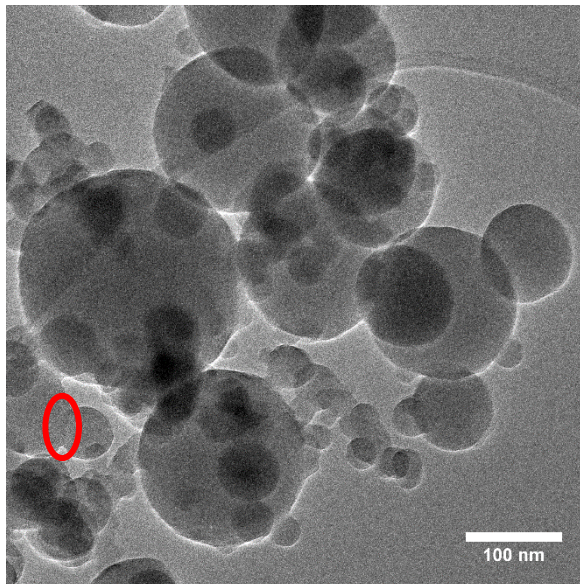


Figure C-2. Micrograph of the synthesized nanoparticles. Silica powder is collected after a series of measurements with the three flames D, F and H of the equivalence ratio $\varphi = 0.8$, 1.0 and 1.2, respectively.

Figure C-2 shows a micrograph of the synthesized nanoparticles. Nanoparticles obtained from the synthesis are round with a low degree of agglomeration. Sintering necks are observed in some nanoparticles as marked in red. The amorphous origin of the nanoparticles could be assumed while no evidence of lattice planes could be observed in the TEM.

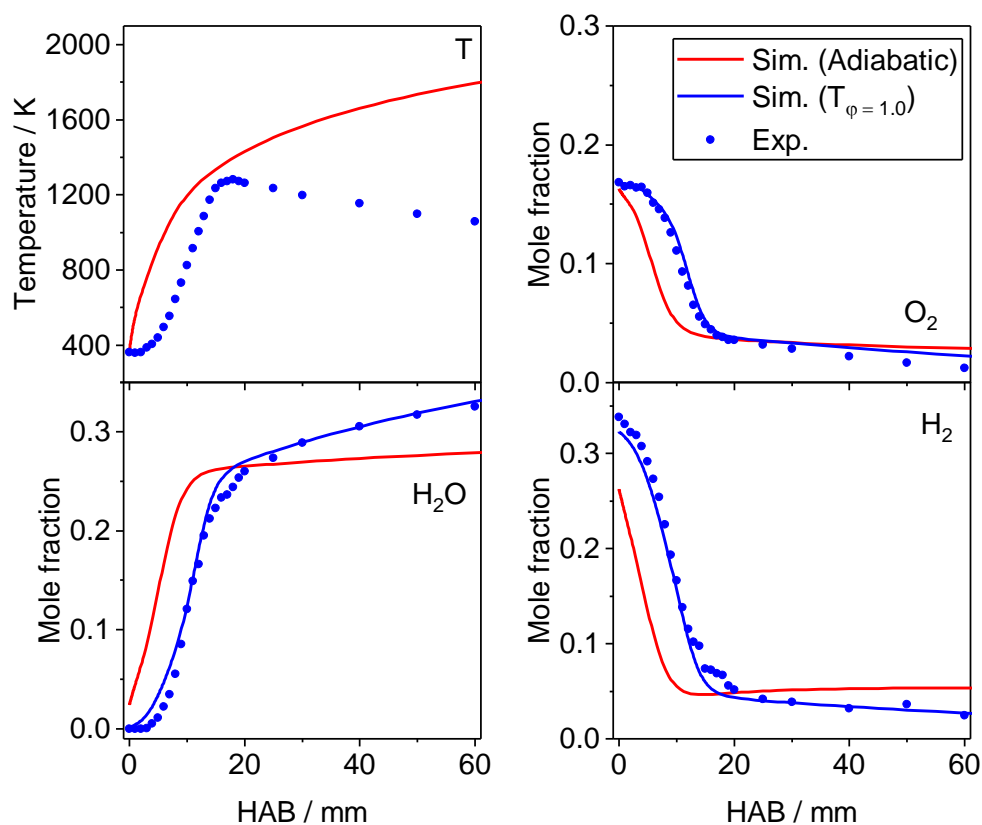


Figure C-3. Sampling-probe effect on the flame structure of a stoichiometric flame.

Figure C-3 shows simulated (lines) and experimental (symbols) temperature and mole fraction profiles of the stoichiometric flame E. Simulation (red line) of the flame structure under adiabatic conditions. Simulation (blue line) of the flame structure with the presence of the sampling-probe for the measured temperature profile. The simulation shows that the discrepancies between experiment and simulation cannot not be resolved by solving the energy equation for the flame. Instead these deviations are most likely caused by uncertainties of the reaction mechanisms.

Appendix D of chapter 9

Predicted minor neutral species in rich flame

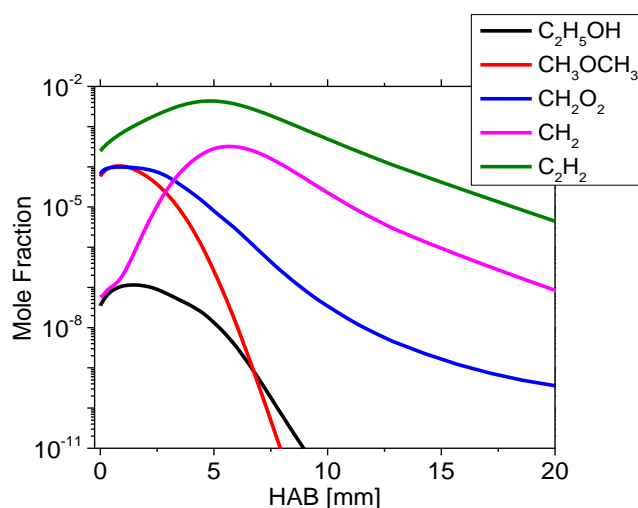


Figure D-1. Simulated minor neutral species in rich flame

Contribution of hydrates

Figure D-2 to Figure D-10 show the ion signals for all the parent ions and their hydrates that were observed in the stoichiometric premixed flame of the current study. The ion signals presented here have been corrected for both the mass discrimination effect and the instrument sampling function FKT. Stoichiometric flame contains all the ions that are observed in lean and rich flames and has thus been selected as a test case to showcase the contribution of hydrates to the total signal for the parent ion. For all ions, the hydrates peak earlier than the parent ions themselves.

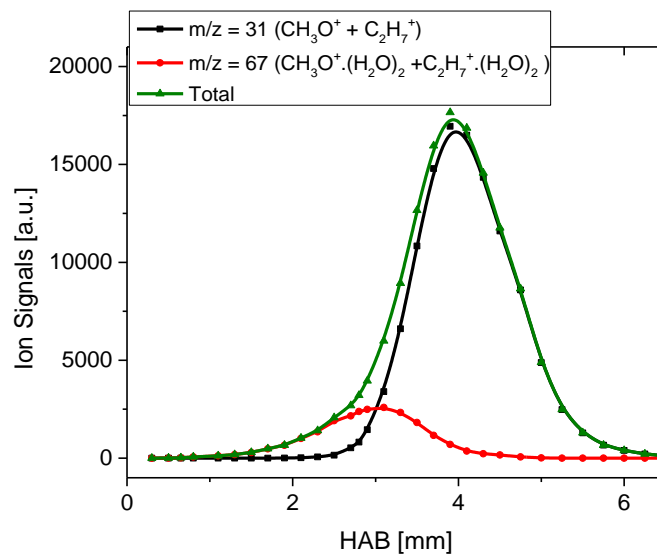


Figure D-2. Ion signal profiles of different hydrates of CH_3O^+ and C_2H_7^+ in the stoichiometric ($\varphi = 1$) premixed flame.

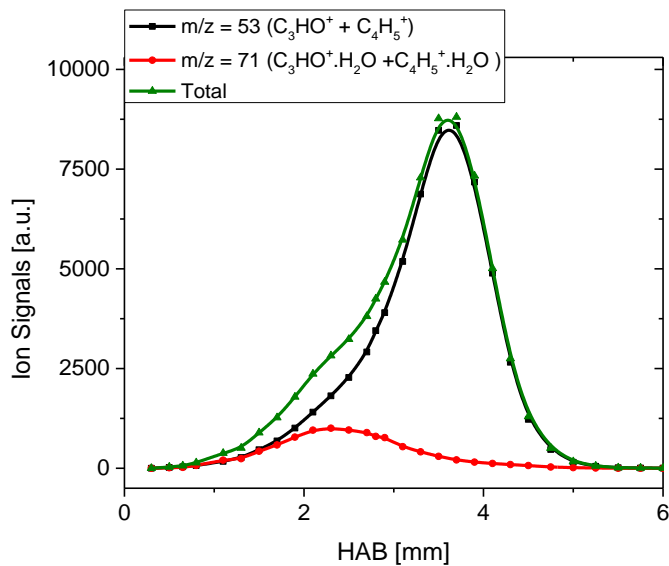


Figure D-3. Ion signal profiles of different hydrates of C_3HO^+ and C_4H_5^+ in the stoichiometric ($\varphi = 1$) premixed flame.

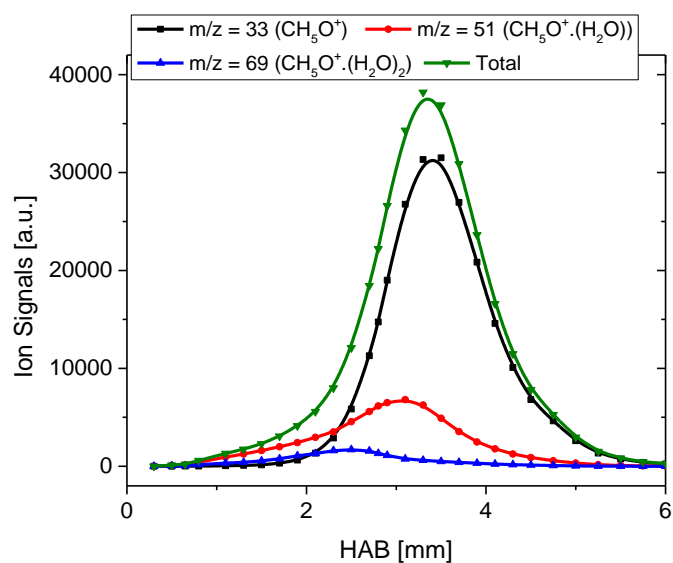


Figure D-4. Ion signal profiles of different hydrates of CH_5O^+ in the stoichiometric ($\varphi = 1$) premixed flame.

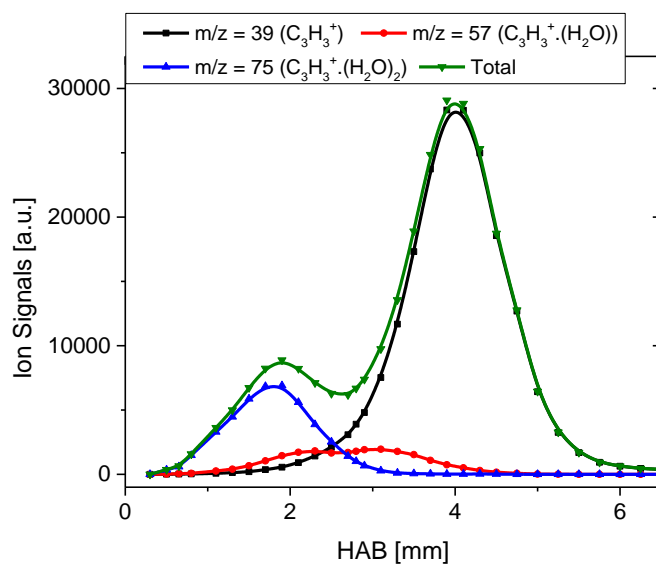


Figure D-5. Ion signal profiles of different hydrates of C_3H_3^+ in the stoichiometric ($\varphi = 1$) premixed flame.

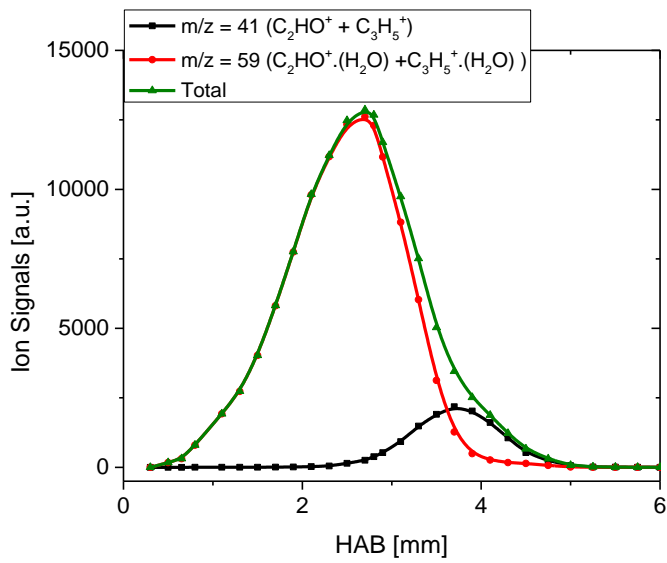


Figure D-6. Ion signal profiles of different hydrates of C_2HO^+ and $C_3H_5^+$ in the stoichiometric ($\varphi = 1$) premixed flame.

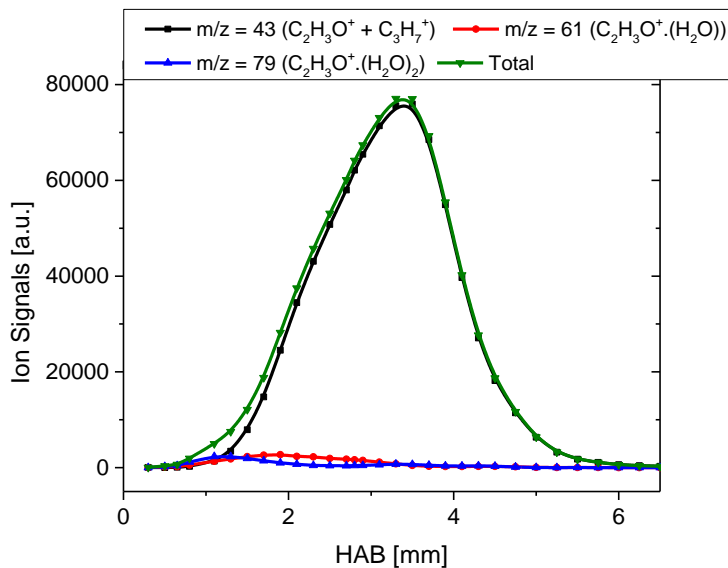


Figure D-7. Ion signal profiles of different hydrates of $C_2H_3O^+$ with small amount of $C_3H_7^+$ in the stoichiometric ($\varphi = 1$) premixed flame.

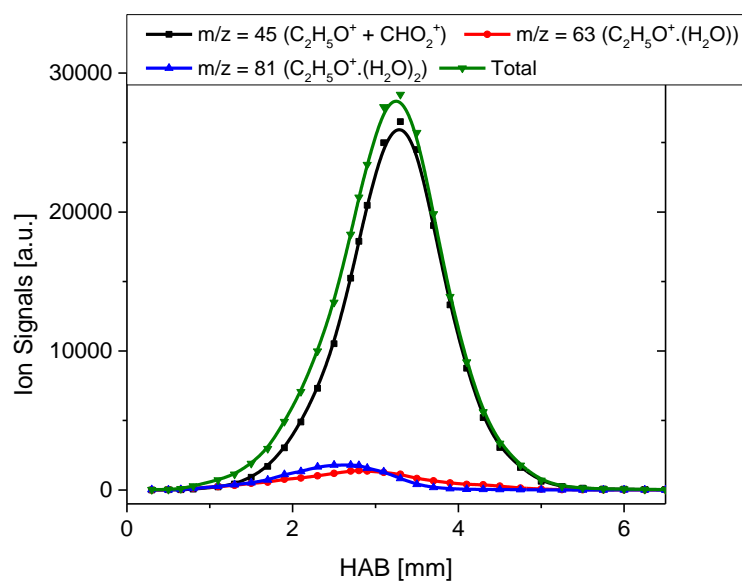


Figure D-8. Ion signal profiles of different hydrates of $C_2H_5O^+$ and CHO_2^+ in the stoichiometric ($\phi = 1$) premixed flame.

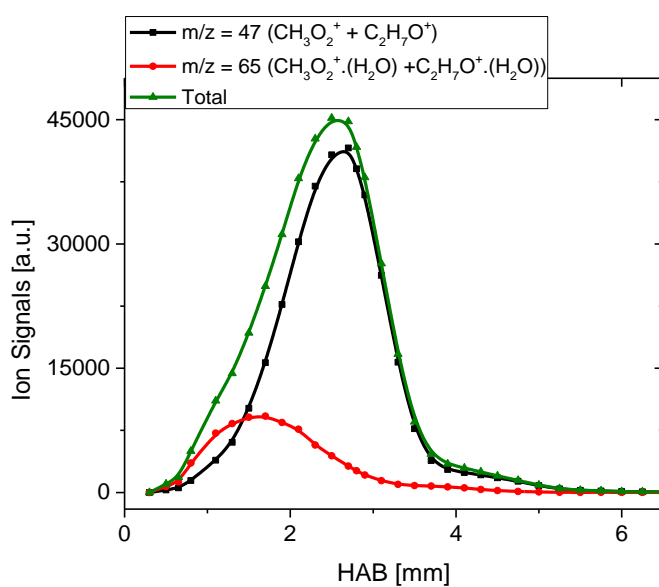


Figure D-9. Ion signal profiles of different hydrates of $CH_3O_2^+$ and $C_2H_7O^+$ in the stoichiometric ($\phi = 1$) premixed flame.

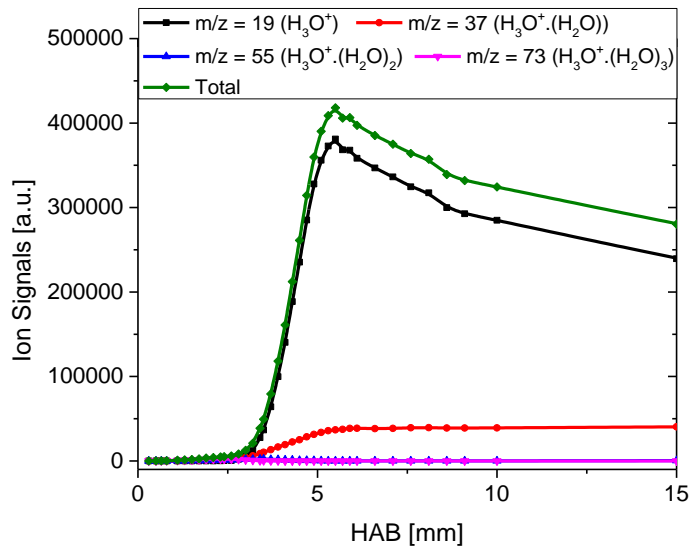
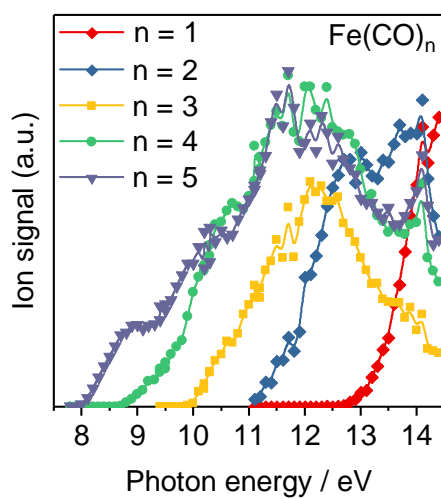
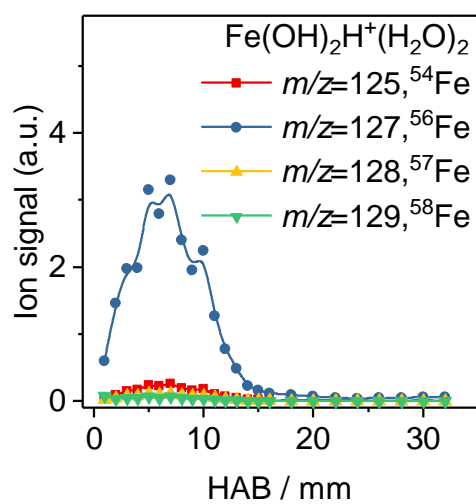


Figure D-10. Ion signal profiles of different hydrates of H_3O^+ in the stoichiometric ($\phi = 1$) premixed flame.

Appendix E of chapter 10

Figure E-1. Photoionization spectrum of $\text{Fe}(\text{CO})_5$ Figure E-2. Ion signal profile of $\text{Fe}(\text{OH})_2\text{H}^+(\text{H}_2\text{O})_2$ and its characteristic isotopes.

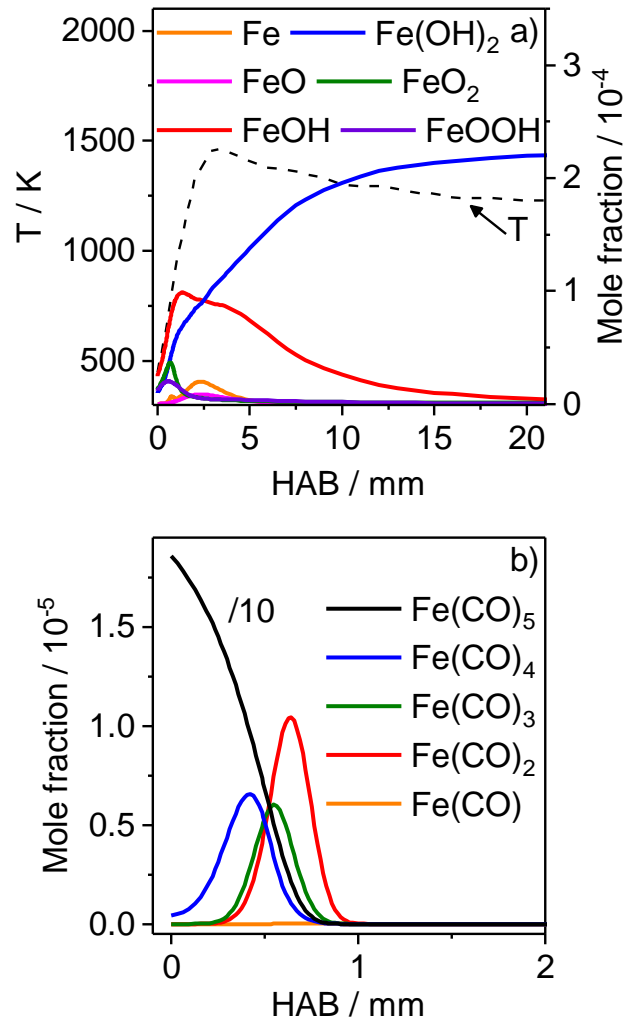


Figure E-3. a) Simulated mole fraction profiles of iron-containing intermediates in flame D (filled lines) and the experimental temperature profile of flame D (dashed line), b) Thermal decomposition of Fe(CO)₅ in flame D.

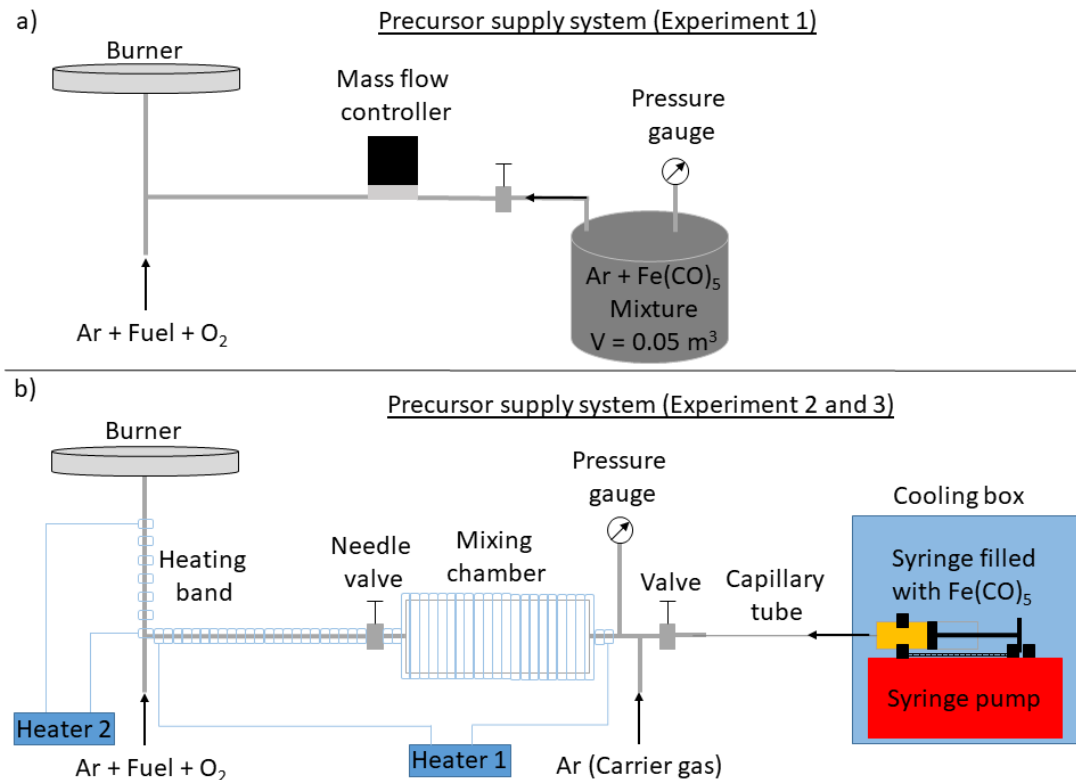


Figure E-4. Schematics of the precursor supplies: a) Experiment 1, b) Experiment 2 and 3.

For flame B, the gas mixture with 200 ppm of Fe(CO)₅ was produced by the partial pressure method (Figure E-4a). First, the species of interest, e.g. Fe(CO)₅ is introduced into an initially evacuated vessel up to a defined pressure. Second, the mixing vessel is filled with argon to the final pressure. With aid of mass flow controller the gas mixture can be regulated and guided to the burner. The total volume of the vessel was 0.05 m³.

In flame D, precooled Fe(CO)₅ was introduced into an evaporator via a syringe pump (Figure E-4b). In the evaporator the gaseous Fe(CO)₅ is mixed with the carrier gas (Ar). In a first step, the mixing chamber is heated up to 313 K with aid of heating bands (Heater 1). In a second step, the carrier gas (Ar+Fe(CO)₅) is mixed with the fuel and oxidizer and heated up to 333 K (Heater 2) for a short distance to avoid condensation before entering the burner matrix.

Appendix F of chapter 11

- Simulation of the methyl radical (DRM22 vs. GRI)

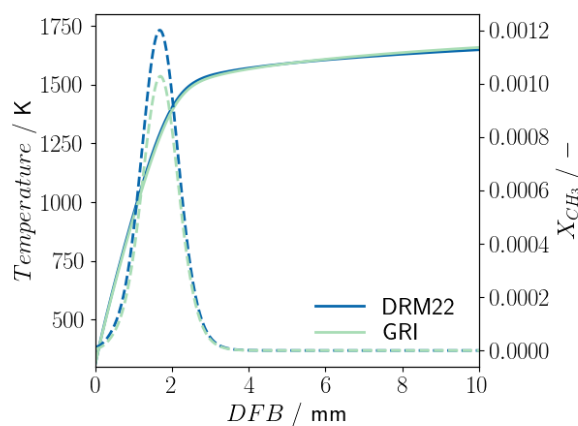


Figure F-1. Simulation of the methyl radical (DRM22 vs. GRI)

- 2D-simulation of the centerline temperature profiles with the presence of an adiabatic and an isothermal sampling probe

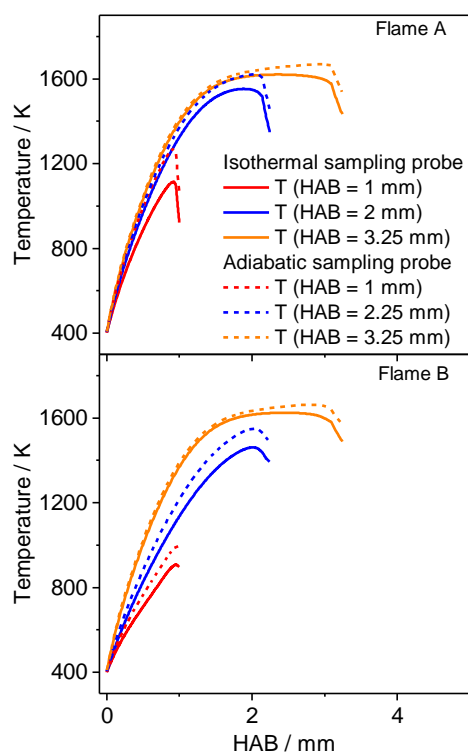


Figure F-2. 2D-simulation of flame A (pressure at orifice 50 mbar) and B (pressure at the orifice 120 mbar) with the presence of an isothermal (filled line) and an adiabatic (dashed line) sampling probe at various HAB.

- 2D simulation of the temperature field and the presence of an adiabatic and an isothermal sampling probe

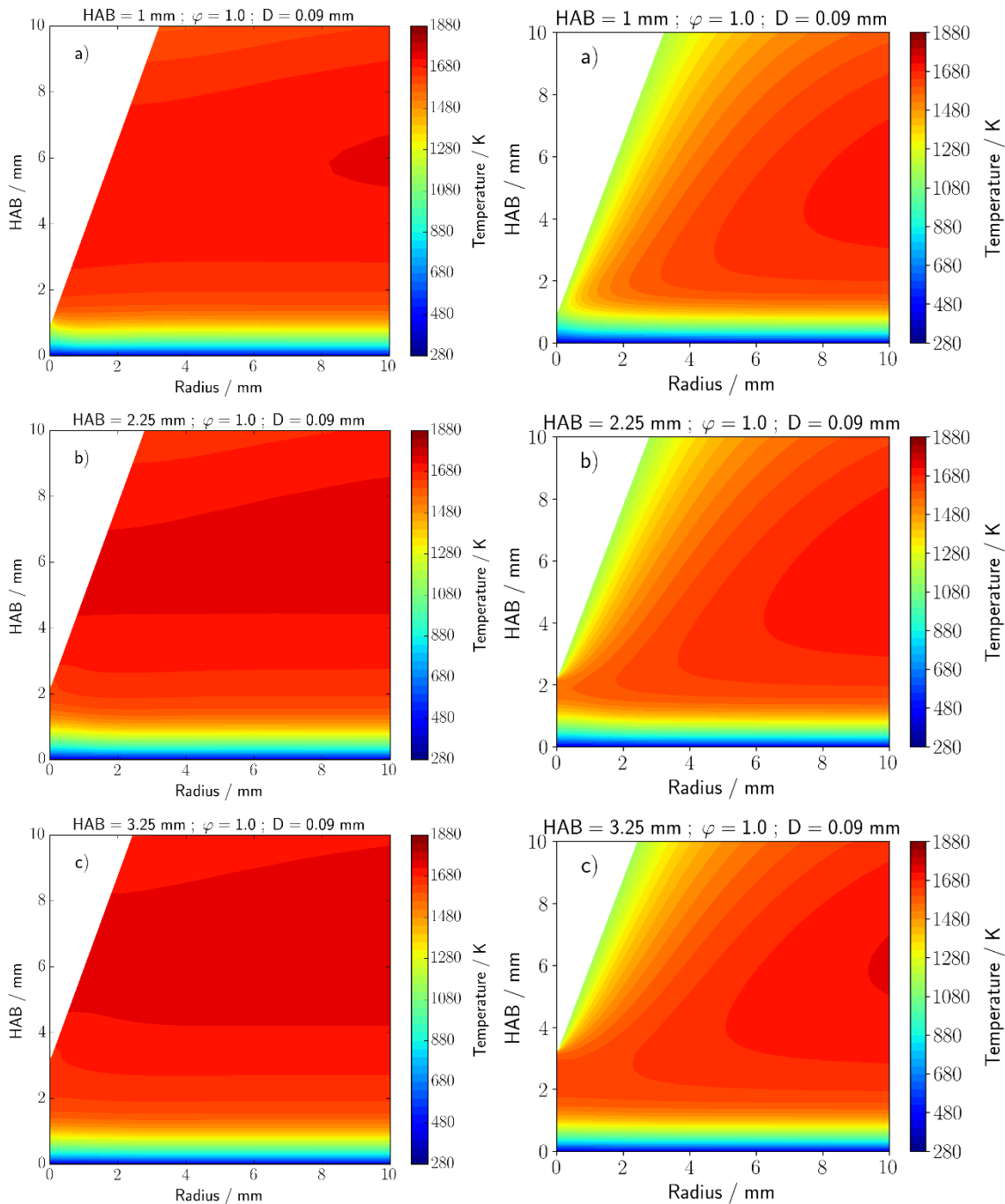


Figure F-3. Two-dimensional simulation of the temperature field in flame A (pressure at the orifice 50 mbar) and the presence of a sampling probe: (left: a)-c)) Adiabatic sampling probe, (right a)-c)) isothermal sampling probe for HAB = 1 mm, 2.25 mm, 3.25 mm.

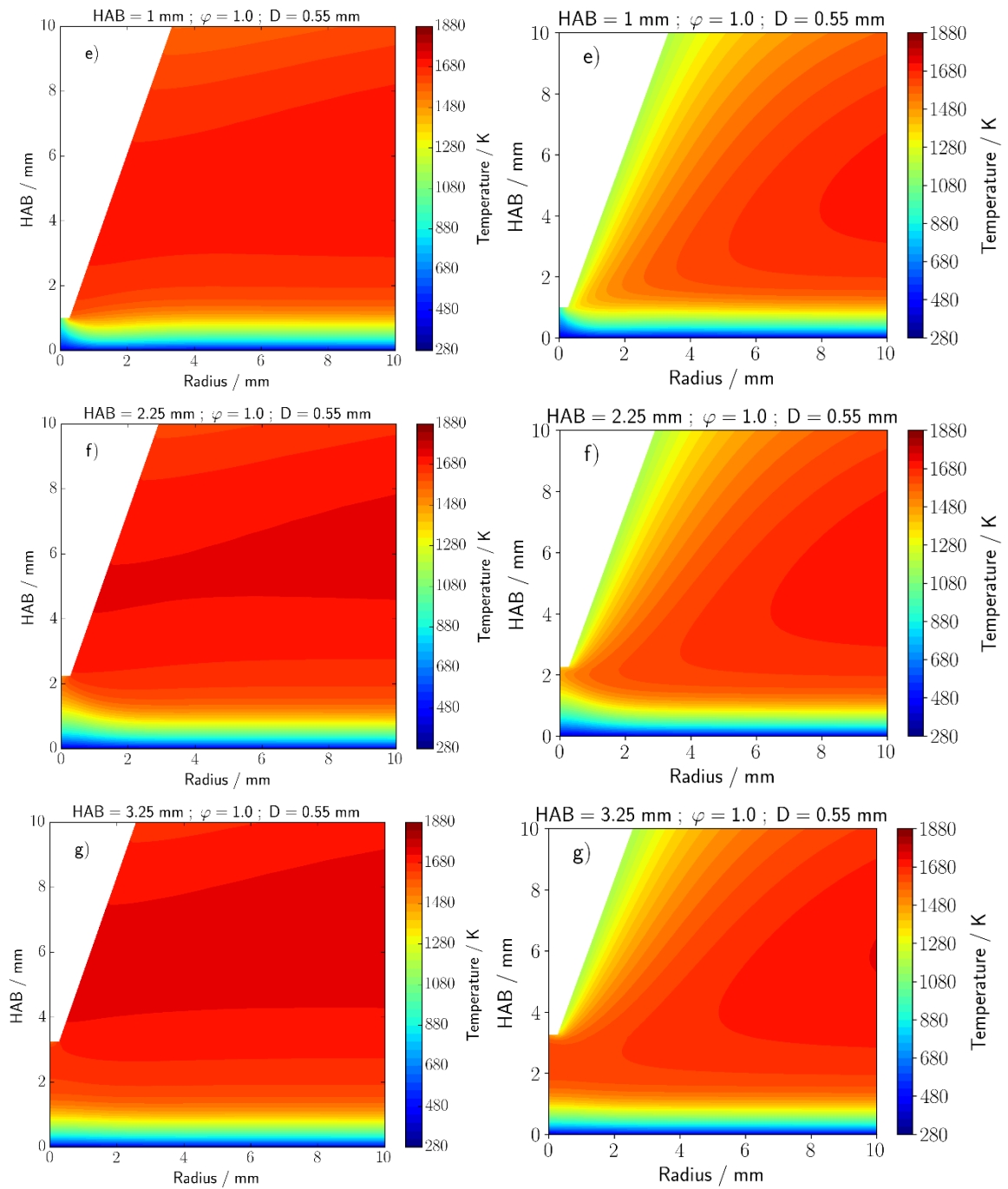


Figure F-4. Two-dimensional simulation of the temperature field in flame B (pressure at the orifice $p = 120$ mbar) and the presence of a sampling probe: (left: e)-g) Adiabatic sampling probe, (right: e)-g) isothermal sampling probe for $HAB = 1$ mm, 2.25 mm, 3.25 mm.

▪ Simulated residence times and distances of gas samples during flame sampling

Table F-1. Residence time τ and distances of gas samples starting at two radial points $r_1 (=0)$ and r_2 in flame A (pressure at the orifice $p = 85$ mbar)

HAB / mm	r / mm	Residence time τ_{1A} / s	Residence time τ_{2A} / s	Ratio residence time τ_{2A} / τ_{1A}	Ratio residence time τ_{1mm} / τ_{25mm}	Distance z_{1A} / mm	Distance z_{2A} / mm	Distance ratio r_{2A}/r_{1A}
1	0	$1.08 \cdot 10^{-3}$	-	-	1.94	1	-	-
1	0.89	-	$2.05 \cdot 10^{-3}$	1.9	-	-	1.3709	1.3709
2.25	0	$2.1 \cdot 10^{-3}$	-	-	1.74	2.25	-	-
2.25	0.81	-	$2.41 \cdot 10^{-3}$	1.15	-	-	2.40387	1.0684
3.25	0	$2.88 \cdot 10^{-3}$	-	-	1.67	3.25	-	-
3.25	0.79	-	$3.11 \cdot 10^{-3}$	1.08	-	-	3.35653	1.03
25	0	$2.985 \cdot 10^{-2}$	-	-	1	25	-	-
25	0.79	-	$3.048 \cdot 10^{-2}$	1.02	-	-	25.22987	1.01

Table F-2. Residence time τ and distances of gas samples at two radial points $r_1 (=0)$ and r_2 in flame B (pressure at the orifice $p = 85$ mbar)

HAB / mm	r / mm	Residence time τ_{1B} / s	Residence time τ_{2B} / s	Ratio residence time τ_{2B} / τ_{1B}	Ratio residence time τ_{1mm} / τ_{25mm}	Distance z_{1B} / mm	Distance z_{2B} / mm	Distance ratio r_{2B}/r_{1B}
1	0	$4.4109 \cdot 10^{-4}$	-	-	3.04	1	-	-
1	5.40	-	$7.6 \cdot 10^{-3}$	17.23	-	-	6.929	6.929
2.25	0	$1.51 \cdot 10^{-3}$	-	-	1.95	2.25	-	-
2.25	5.21	-	$7.81 \cdot 10^{-3}$	5.17	-	-	6.641	2.95
3.25	0	$2.09 \cdot 10^{-3}$	-	-	1.54	3.25	-	-
3.25	5.13	-	$7.99 \cdot 10^{-3}$	3.83	-	-	7.008	2.16
25	0	$2.717 \cdot 10^{-2}$	-	-	1	25	-	-
25	5.10	-	$3.35 \cdot 10^{-2}$	1.13	-	-	29.19	1.17

- Perturbed temperature profile T_{FKT}

The mass spectrometric signal for each ion i is given by

$$S_i(E) = x_i \cdot c \cdot SW \cdot \Phi \cdot MD_i \cdot \text{FKT}(\text{HAB}) \cdot \int \sigma_i(E) f(E) dE, \quad \text{Eq. 1}$$

where x_i is the mole fraction, c is an instrument-dependent proportionality constant, SW is the number of single measurements (sweeps), Φ is the number of electrons which are involved in the electron ionization process, MD_i is a mass discrimination factor, FKT is the temperature and height specific instrument function, $\sigma_i(E)$ the ionization cross section at energy E and $f(E)$ the energy distribution function. The perturbed temperature profile T_{FKT} was determined from the height specific instrument function (see Eq. 1) according to the procedure described by Struckmeier et al. [82]. The molecular flow rate through a sampling probe is defined by

$$\dot{N} = AN_a p_0 \sqrt{\frac{\kappa}{M \cdot R \cdot T}} \cdot \left(\frac{2}{\kappa + 1} \right)^{\frac{\kappa+1}{2(\kappa-1)}}, \quad \text{Eq. 2}$$

where A denotes the area of the sampling probe aperture, N_a is the Avogadro number, p_0 is the pressure, molar mass M , molar gas constant R , temperature T and κ is ratio of the heat capacities.

Constant values or values which can be estimated by a constant factor are combined in the parameter C_1 . The molecular flow rate is proportional to the height specific function FKT of the mass spectrometric signal and is defined by

$$\dot{N} = C_1 \sqrt{\frac{1}{\overline{M} \cdot T}} \propto \text{FKT}(\text{HAB}) \quad \text{Eq. 3}$$

where \propto indicates the proportionality. The FKT -profile can be obtained for each HAB by the ratio of the signal intensity and the corresponding mole fraction of the reference species argon with aid of Eq. 1. The parameter C_1 is calculated for a measured temperature e.g. thermocouple measurement. For the calculation of the other HAB the parameter C_1 is held constant. The perturbed temperature profile T_{FKT} can be calculated by

$$T_{\text{FKT}} = \frac{1}{\overline{M}} \left(\frac{C_1}{\text{FKT}(\text{HAB})} \right)^2. \quad \text{Eq. 4}$$

where \overline{M} is the molar mass of the mixture

List of symbols

Upper case latin symbols

A_0	Low-pressure limit of pre-exponential constant in Arrhenius form	varies
A_∞	High-pressure limit of pre-exponential constant in Arrhenius form	varies
A_i	Pre-exponential factor of a reaction i	varies
A	Instrument factor	-
A	Variable	-
A	Constant	varies
A	Surface	m^2
A	Pre-exponential constant in Arrhenius expression	varies
$C_{k,i}^c$	Normalized consumption contribution of species k in reaction i	-
$C_{k,i}^p$	Normalized production contribution of species k in reaction i	-
C_p	Molar specific heat at constant pressure	J/molK
C_V	Molar specific heat at constant volume	J/molK
C^*	Activated molecule	
C_1	Constant	-
D_k^T	Thermal diffusion coefficient for species k	kg/ms
D_{kj}	Ordinary multicomponent diffusion coefficient	m^2/s
D_{km}	Mixture-averaged diffusion coefficient	m^2/s
D	Diameter	m
D_0	Diameter	m
E_i	Activation energy	V
E	Ionization Energy	eV
E_a	Activation energy in Arrhenius expression	J/mol
E_{el}	Electric potential energy	J
E_{pot}	Potential energy	J
F	Broadening factor	-
F_{cent}	Intersection of the low-pressure and the high-pressure limits of the rate constants	-
G	Critical value for supersonic expansion	-
G	Gibbs free energy	J/mol
H	Enthalpy	J
ΔH_f^0	Standard enthalpy of formation	J/mol
ΔS_f^0	Standard entropy of formation	J/molK
I	Total number of chemical reactions	-
K	Total numbers of chemical species	-
$K_{c,i}$	Equilibrium constants in terms of concentration for reaction i	-
$K_{p,i}$	Equilibrium constant in terms of pressure for reaction i	-
M	Molar mass	kg/mol
M	Molecule	-

M	Collision partner in pressure-dependent reactions	-
M_i	Molar mass of ion i	kg/mol
M_k	Molar mass of a species k	Kg/mol
\overline{M}	Molar mass of a mixture	Kg/mol
R	Mass resolution	-
R	Type of a thermocouple	-
S	Type of a thermocouple	-
S	Sensitivity coefficient	-
S_i	Signal intensity of a species i	-
S_{total}	Total signal intensity	-
T_0	Temperature at the reference point 0	K
T_b	Boiling point	K
U	Potential	kgm ² /s ³ A
V	Volume	m ³
V	Voltage	Kgm ² /s ³ A
V_k	Diffusion velocity of species k	m/s

Physico-chemical constants

N_A	Avogadro number	1/mol
R	Universal gas constant	J/mol K
σ_k	Stefan-Boltzmann constant	W/m ² K ⁴

Dimensionless numbers

Ma	Mach number	-
$Ma(x)$	Mach number in axial direction x	-
p_r	Reduced pressure	-
T^*	Reduced temperature	-

Greek symbols

α_{ki}	Collisional efficiency of species k in reaction i	-
β_0	Low-pressure limit of temperature exponent in modified Arrhenius expression	-
β_∞	High-pressure limit of temperature exponent in modified Arrhenius expression	-
β_i	constant temperature exponent of a reaction i	-
δ_k^*	Reduced dipole moment of species k	-
ε	Constant	-
ϵ	collision efficiency	-
ϵ	Well-depth	-
ϵ_{TC}	Emissivity of the thermocouple	-
θ	Variance in a Gaussian function	-
κ	Isentropic coefficient	-
λ	Thermal conductivity	W/mK
λ_0	length of the mean free path at the reference point 0	m

λ_k	Thermal conductivity of the species k	W/mK
$\bar{\mu}_k$	Dipole moment of species k	C m
μ	Expected value in a Gaussian function	varies
ρ	Density	kg/m ³
σ	Collision diameter	m
σ_i	Electron ionization cross section	cm ²
σ_{ij}	Length-scale in molecular interaction between molecules i and j	m
φ	Equivalence ratio	-
ψ_k	Symbol representing a species	-
\emptyset	Number of electrons involved in the ionization process	-
$[\psi_k]$	Concentration of species k	mol/m ³
Ω_{ij}	Reduced collision integral	-
$\dot{\omega}_k$	Production rate of species k	mol/m ³ s

Acronyms

1D	One-dimensional
1D	One-dimensional
2D	Two-dimensional
BET	Brunauer-Emmett-Teller
CENIDE	Center for Nanointegration Duisburg-Essen
CFD	Computational fluid dynamics
DC	Direct current
DFG	Deutsche Forschungsgemeinschaft
EI	Electron ionization
FKT	Temperature-dependent sampling function
FWHM	Full width at half maximum height
GRI	Gas research institute
HAB	Height-above-burner
HMDSO	Hexamethyldisiloxane
ICLAS	Intracavity laser absorption spectroscopy
IE	Ionization energy
IR	Infrared
KAUST	King Abdullah University of Science and Technology
MBMS	Molecular beam mass spectrometry
MCP	Micro-channel plate
MDF	Mass discrimination factor
MD _i	Mass discrimination factor
NASA	National Aeronautics and space administration
PAH	Polycyclic aromatic hydrocarbon
PES	Potential energy surface
PI	Photoionization
PPM	Parts per million
QCM	Quartz crystal microbalance
RICS	Relative ionization cross section

RRKM	Rice-Ramsperger-Kassel-Marcus
SLM	Standard litre per minute
SLPM	Standard litre per minute
SW	Sweeps, number of time-of-flight mass spectra
TEM	Transmission electron microscopy
TEOS	Tetraethyl orthosilicate
TMS	Tetramethylsilane
TOF-MS	Time of flight-mass spectrometer
VUV	Vacuum ultraviolet

List of figure captions

Figure 2-1.	Principle of silicon dioxide particle formation in a flame. The schematic is based on [32].	5
Figure 2-2.	Schematics of the species and temperature profiles in one-dimensional flames. The red curve indicates the temperature profile, the blue curve indicates the precursor and/or oxygen, the green curve and the black curve indicate the formation of intermediate species along the centerline of the flame. The figure is adapted from [59].	9
Figure 2-3.	Schematic of a supersonic expansion and its characteristic shocks. The streamline indicates the direction of the flow. The schematic is adapted from [63].	11
Figure 2-4.	Schematic representation of an orthogonal time-of-flight mass spectrometer system with a reflectron divided in modular sections: Sample inlet, ionization source and transfer lenses (red section), and accelerator (blue section), mass analyzer (green section). Light ions (red filled and empty spheres) and heavy ions (blue filled and empty spheres) in the orthogonal accelerator and in the drift range with lower (empty spheres) and higher (filled spheres) kinetic energy. The different lengths of the red arrows indicate different kinetic energies of the ionized molecules. Ions with different kinetic energies are time-focused after reflection. The schematic is based on [67].	14
Figure 4-1.	Schematics of the burner types: a) McKenna-type burner, b) Particle synthesis burner. The arrows indicate the direction of the flows.	33
Figure 4-2.	Schematics of the precursor supply system. The schematics is adapted from [62].	34
Figure 4-3.	Schematics of the molecular beam sampling in a low-pressure flame. The blue symbols indicate the molecules, atoms and clusters from the flame. The triangular figure represents the electron beam. The orange symbols indicate their ions after electron ionization. The schematics is adapted from [62].	35
Figure 4-4.	Schematic of the ion sampling TOF. The schematic is adapted from [62].	40
Figure 6-1.	Left: Open symbols show the experimental mole fraction profiles of the major species in a neat hydrogen flame, closed symbols a H ₂ flame doped with 600 ppm TMS and lines indicate the profiles simulated with the mechanism of Li et al. [124] for the neat flame (TMS = 0 ppm), (Profiles evaluated with electron ionization energy EI = 17 eV, flame A and B); Right: Temperature profiles in a laminar low-pressure H ₂ /O ₂ /Ar-flame with addition of TMS (0/600 ppm) measured with a thermocouple.	59
Figure 6-2.	Mole fraction profiles of hydrocarbon species in the H ₂ /O ₂ /Ar-flame with addition of TMS. The carbon balance reveals that all carbon is accounted for in the gas phase species. Solid curves were obtained by	

- fitting experimental data points by a spline function; profiles are evaluated with electron ionization energy $EI = 17$ eV.61
- Figure 6-3. Maximum mole fractions (in ppm) of silicon containing combustion products of TMS in a $H_2/O_2/Ar$ -flame. Maximum mole fractions are evaluated with electron ionization energy $EI = 17$ eV.62
- Figure 6-4. a) First decomposition steps of TMS in a hydrogen flame to form peroxides, b) Formation of $Si(OH)_4$ by a stepwise loss of methyl groups and recombination with a hydroxyl group. Profiles are evaluated with electron ionization energy $EI = 17$ eV.63
- Figure 6-5. Postulation of reaction pathway from precursor to the first silicon oxide clusters (explained in Section 6.6.3 Formation and growth of silicon oxide clusters) based on experimental data (labelled in blue). The schematic of the reaction pathway proposes which species may contribute to particle formation. Numbers in parentheses correspond to reactions from literature.65
- Figure 6-6. Transition state structures for two possible unimolecular reactions of $(CH_3)_3SiOH$ (Calculations at B3LYP/6-31+G(d,p) level of theory): Elimination of H_2O (left) and elimination of CH_4 (right).66
- Figure 6-7. Silicon-intermediates in a $H_2/O_2/Ar$ -flame with addition of 600 ppm TMS (flame B). Profiles are evaluated with electron ionization energy $EI = 17$ eV.67
- Figure 6-8. Formation of silicon oxide clusters with the structure $(SiO_2)_nO_2H_4$ with $n = 4$ and $n = 8$ in a $H_2/O_2/Ar$ -flame with addition of 600 ppm of TMS, Cluster profiles evaluated with electron ionization energy $EI = 70$ eV.68
- Figure 7-1. Potentials of CH_3 (left) and OH rotors in trimethyl-silanol ($Si(CH_3)_3OH$) with maxima at 400 and 175 cm^{-1}77
- Figure 7-2. Mole fraction profiles of the major species along the as a function of height above burner (HAB) in flame A. The points are experimental data and the curved lines are the simulation results. The colored area shows the uncertainty range of the measured data.79
- Figure 7-3. Sensitivity of major species' mole fractions on the measured temperature; simulations are performed with experimental temperature, shifted +100 K up, and shifted -100 K down. The colored areas represent the uncertainties of mole-fraction and temperature measurements. Symbols: experiment; lines: simulations.80
- Figure 7-4. Measured and calculated CH_4 mole-fraction profiles as a function of height above burner (HAB). The colored area represents the uncertainty range of the measurement. Simulations were performed with the C1-C3 mechanism of Ranzi et al. [171] (blue dashed line) and the C1 mechanism from Li et al. [154] (black line)83
- Figure 7-5. Schematics of the reaction pathway for the oxidation of TMS based on the list of reactions in Table 7-3. The red-colored reactions are introduced as global reactions.84

- Figure 7-6. Measured and calculated mole-fraction profiles for TMS in the flame B. The colored area shows the uncertainty range of the measurement. Symbols: experiment; line: simulation..... 85
- Figure 7-7. Measured and simulated mole-fraction profiles of $(\text{CH}_3)_3\text{SiCH}_2\text{O}_2$ and $\text{OSi}(\text{CH}_3)_3$ as a function of HAB for Flame B. The colored area shows the uncertainty range of a factor of two for the measured data. 86
- Figure 7-8. Top: RRKM calculations for reaction $\text{Si}(\text{CH}_3)_2\text{O} \rightarrow (\text{CH}_3)\text{SiO} + \text{CH}_3$, for tautomerization $\text{Si}(\text{CH}_3)_2\text{O} \rightarrow (\text{CH}_3)(\text{OH})\text{SiCH}_2$, and for the reverse process $(\text{CH}_3)(\text{OH})\text{SiCH}_2 \rightarrow \text{Si}(\text{CH}_3)_2\text{O}$. All calculations were carried out for 30 mbar and cover 600–1200 K; Bottom: Relative stationary point energies (values in parentheses are relative to the energy of $\text{Si}(\text{CH}_3)_2\text{O}$) for the unimolecular reactions of $\text{Si}(\text{CH}_3)_2\text{O}$ calculated at the G4 level of theory (present work). 87
- Figure 7-9. Measured and simulated profiles of $\text{Si}(\text{CH}_3)_3\text{OH}$ and $\text{Si}(\text{OH})_3$. The colored area shows the uncertainty range of a factor of two for the measured data. 90
- Figure 7-10. Measured and simulate profiles of SiO_2 and $\text{Si}(\text{OH})_4$. The colored area shows the uncertainty range of a factor of two for the measured data. 91
- Figure 7-11. Reaction pathways of element of Si for gas-phase species at 800 K and 30 mbar. 92
- Figure 7-12. Measured and simulated profiles of $\text{Si}_4\text{O}_{10}\text{H}_4$. The colored area shows the uncertainty range of a factor of two for the measured data. 93
- Figure 7-13. Top: RRKM calculations for CH_4 and H_2O elimination reactions of $\text{Si}(\text{CH}_3)_3\text{OH}$; both calculations were carried out for 30 mbar and 600–1200 K. Bottom: Relative stationary point energies (values in parentheses are relative to the energy of $\text{Si}(\text{CH}_3)_3\text{OH}$) for the unimolecular reactions of $\text{Si}(\text{CH}_3)_3\text{OH}$ calculated at the G4 level of theory (present work). 94
- Figure 7-14. Measured and simulated mole-fraction profiles of major species as a function of HAB for a series of TMS doping concentrations: 400 ppm (flame C), 600 ppm (flame B), and 800 ppm (flame D). Symbols: experiments, lines: simulations. 97
- Figure 7-15. Measured and simulated mole-fraction profiles of Si-containing species along the HAB for a series of TMS doping concentrations: 400 ppm (flame C), 600 ppm (flame B), and 800 ppm (flame D). Symbols: experiments, lines: simulations. 98
- Figure 7-16. Measured and simulated mole-fraction profiles of $\text{Si}_4\text{O}_{10}\text{H}_4$ along the HAB for a series of TMS doping concentrations: 400 ppm (flame C), 600 ppm (flame B), and 800 ppm (flame D). Symbols: experiments, lines: simulations. 99
- Figure 8-1. Measured (symbols) and simulated (lines) mole fraction profiles of main species (e.g. H_2 , H_2O , TMS, O_2 , CO, CO_2) and temperature profiles in neat (open symbols) and doped (closed symbols) $\text{H}_2/\text{O}_2/\text{Ar}/\text{TMS}$ -flames. Error bars show the uncertainties of measured temperature and mole fractions. 105
-

Figure 8-2.	Measured (symbols, scaled) and simulated (lines) mole fraction profiles of O-radicals in neat (open symbols) and TMS-doped (closed symbols) H ₂ /O ₂ /Ar-flames.....	106
Figure 8-3.	Reaction flow analyses of the three most important reactions for the decomposition of TMS.	107
Figure 8-4.	Reaction pathways of silicon-species at $\phi = 1$ at HAB = 10 mm, T = 1013 K (black) and at HAB = 20 mm, T = 1250 K (red). Experimentally detected silicon-species are shaded in grey.	109
Figure 8-5.	Measured (symbols) and simulated (lines) mole fraction profiles of (CH ₃) ₃ Si(CH ₂)OO in TMS-doped H ₂ /O ₂ /Ar - flames.	110
Figure 8-6.	Measured (symbols) and simulated (lines) mole fraction profiles of (a) SiO ₂ , (b) Si(OH) ₄ , (c) Si ₄ O ₁₀ H ₄ in TMS-doped H ₂ /O ₂ /Ar-flames.....	112
Figure 8-7.	Particle size distribution with log-normal fit of data (dashed line) and separate contributions for each size mode (blue and green), the inset shows a part of a TEM micrograph.	113
Figure 9-1.	Measured neutral species (symbols) and simulations (lines). Measurements are shifted towards the burner surface by 1, 2 and 4 mm for lean, stoichiometric and rich flames, respectively.	119
Figure 9-2.	Ion mole fractions from experiments (symbols with dashed lines) and simulations (solid lines in corresponding color) for the lean premixed flame ($\phi = 0.5$). Measured flame temperature (red symbols with red line) also shown. Experimental relative ion profiles have been scaled to match the peak mole fraction of simulated H ₃ O ⁺ . Simulation data include results for C ₂ H ₃ O ⁺ , CH ₅ O ⁺ and H ₃ O ⁺	120
Figure 9-3.	Ion mole fractions from experiments (symbols with dashed lines) and simulations (solid lines in corresponding color) for the stoichiometric premixed flame ($\phi = 1$). Experimental relative ion profiles have been scaled to match the peak mole fraction of simulated H ₃ O ⁺ . Simulation data include results for C ₂ H ₃ O ⁺ , CH ₅ O ⁺ and H ₃ O ⁺	121
Figure 9-4.	Ion mole fractions from experiments (symbols with dashed lines) and simulations (solid lines in corresponding color) for the rich premixed flame ($\phi = 1.5$). Experimental relative ion profiles have been scaled to match the peak mole fraction of simulated H ₃ O ⁺ . Simulation data include results for C ₂ H ₃ O ⁺ , CH ₅ O ⁺ and H ₃ O ⁺	122
Figure 9-5.	Ion mole fractions from experiments (symbols) and simulations (lines) for the stoichiometric flame ($\phi = 1$). Experimental ion profiles have been scaled to match the peak total ion mole fraction from simulation.	123
Figure 9-6.	Sensitivity analysis of H ₃ O ⁺ at the peak and during the decay in lean, stoichiometric and rich flames.....	124
Figure 10-1.	Schematics of the gas/particle inlet systems for a): PI-MBMS (experiment 1), EI-MBMS (experiment 2) and b) ion sampling (experiment 3).	131
Figure 10-2.	Mole fraction profiles of major species for the neat flame A (dashed lines, 0 ppm Fe(CO) ₅) and doped flame B (solid lines, 200 ppm	

- Fe(CO)₅) analyzed with PI-MBMS (experiment 1). Measured temperature profiles of flames A, B. Empty symbols and dashed lines indicates neat flame and filled symbols and filled lines indicates doped flame. The uncertainty of the measurement is indicated by the shaded area between the thin lines for each experimental mole fraction profile. 134
- Figure 10-3. Mole fraction profiles of flame radicals O and OH in the neat flame A (dashed lines, empty symbols) without (w/o) Fe(CO)₅ doping and flame B (filled lines, symbols) with (w) Fe(CO)₅ doping analyzed with PI-MBMS (experiment 1). 135
- Figure 10-4. Measured (symbols) and simulated (lines) mole fraction profiles of the decomposition products of Fe(CO)₅ in flame B (experiment 1). Experimental signal intensity profiles of the decomposition products Fe(CO)_n with $n = 2 - 4$ are scaled to the simulation. 136
- Figure 10-5. Ions in flame D measured with the ion sampling system. Iron hydroxide or oxide structures with $n, m \neq 0$ appear. The dashed line indicates the end of the flame front in the C₂H₄/H₂/O₂/Ar-flames. The filled line indicates the maximum concentration of the iron-containing cations. 137
- Figure 10-6. Species mole fraction profiles of a) CO, H₂O in flame C and H₃O⁺ in flame C and D, b) C₂H₄, H₂, O₂, CO₂ in flame C, c) CH₅O⁺, C₂H₃O⁺ in flame D. Points are experimental data (experiment 2 and 3) and solid lines are simulations. 140
- Figure 10-7. Expanded parts of the mass spectrum at HAB = 7 mm in Fe(CO)₅-doped C₂H₄/H₂/O₂/Ar-flames (flame D, experiment 3) show ions and the hydrate series. Red and blue bars indicate the isotopic pattern of iron with four stable isotopes ⁵⁴Fe, ⁵⁶Fe, ⁵⁷Fe, ⁵⁸Fe. Labels indicate species of the same series with the same core ion. 143
- Figure 10-8. Ion signal profiles in Fe(CO)₅-doped C₂H₄/H₂/O₂/Ar-flames (flame D, experiment 3) of a) $m/z = 90$ (Fe(OH)₂⁺) and $m/z = 91$ (Fe(OH)₂⁺H) and their sampling induced hydrates on $m/z = 126$ (Fe(OH)₂⁺(H₂O)₂) and $m/z = 127$ (Fe(OH)₂H⁺(H₂O)₂), b) on $m/z = 107$ (Fe(OH)₃⁺) and $m/z = 108$ (Fe(OH)₃H⁺) with the hydrates on $m/z = 143$ (Fe(OH)₃⁺(H₂O)₂) and $m/z = 144$ (Fe(OH)₃ H⁺(H₂O)₂), c) spatial variation of the oxidation states of iron species in flame D. Vertical dashed line indicates the end of the flame front. 145
- Figure 10-9. a) Simulated concentration profiles in flame D. b) Ion signal profiles of larger iron-containing ions in the Fe(CO)₅-doped H₂/C₂H₄/O₂/Ar flame (flame D, experiment 3). Symbols with lines indicate experimental data and lines indicate simulations. 148
- Figure 11-1. Schematics of the experimental setup for a) TOF-MBMS with electron ionization (flame A) and b) TOF with electron ionization and expansion sampling (flame B) and ion sampling TOF (flame C). For flame B) and C) the same experimental setup is used and can be switched from expansion sampling with electron ionization to ion sampling. Reprinted from [62] with permission from Elsevier. 156

- Figure 11-2. Computational two-dimensional domain and the boundary conditions for the simulation, exemplarily shown for flame B. White lines schematically show the profiles analyzed in the post processing evaluation of the 2D-Simulation. 159
- Figure 11-3. Measured (dotted lines) and simulated temperature profiles on the centerline (2D simulations, isothermal sampling probe, solid lines) in a) flame A, and b) flame B for various heights above the burner (HAB = 1, 2.25, 3.25, 25 mm). 160
- Figure 11-4. Two-dimensional simulation of the temperature field in flame A (4 a-d) and flame B (4 e-h) and isothermal probes for various heights above the burner (HAB = 1, 2.25, 3.25, 25 mm). 163
- Figure 11-5. Two-dimensional simulation of the radial temperature profiles along the orifice diameter in a) flame A (probe diameter $D = 90 \mu\text{m}$), b) and flame B, C, (probe diameter $D = 550 \mu\text{m}$) at various HAB and c) at various distances parallel to the probe inlet with a distance of 0 mm, 1 mm, 2 mm, 3 mm (solid line for probe diameter $D = 90 \mu\text{m}$ and dashed line for probe diameter $D = 550 \mu\text{m}$)..... 164
- Figure 11-6. Measured (probe diameter $D = 90 \mu\text{m}$, symbols) and simulated (1D- and 2D-simulation, lines) mole fraction profiles of major species on the centerline in flame A. 2D-Simulations are done for an isothermal sampling probe and at various HAB = 1 mm, 2.25 mm, 3.25 mm, 25 mm. 166
- Figure 11-7. Measured (probe diameter $D = 550 \mu\text{m}$, symbols) and simulated (1D- and 2D-simulation, lines) mole fraction profiles of major species on the centerline in flame B. 2D-Simulations are done for an isothermal sampling probe and various HAB = 1 mm, 2.25 mm, 3.25 mm, 25 mm. 167
- Figure 11-8. Measured (Flame A, Probe diameter $D = 90 \mu\text{m}$, symbols) and simulated (1D- and 2D-simulations, lines) mole fraction profiles of CH_3 on the centerline in flame A. 2D-Simulations are done for an isothermal sampling probe and various HAB = 1 mm, 2.25 mm, 3.25 mm, 25 mm..... 168
- Figure 11-9. Two-dimensional simulations of the CH_3 mole fraction field in flame A) are done for an isothermal sampling probe and various HAB = 1 mm, 2.25 mm, 3.25 mm, 25 mm). 169
- Figure 11-10. Two-dimensional simulation of the temperature field with a streamline pattern and a sampling probe position at HAB = 1 mm and HAB = 25 mm a,b) in flame A and e,f) in flame B. Residence time profiles of gas flows sampled at the centerline (dashed line) and on a streamline suctioned from a radial point of the burner by an isothermal sampling probe and various heights above the burner (HAB = 1, 2.25, 3.25, 25 mm) c,d) in flame A and g,h) in flame B. The distance z indicates the traveled length of the fluid element between burner exit and sampling probe inlet. 173
- Figure 11-11. Temperature history of a gas sample from the perturbed flame (T_{TC} , T_{Ma} , T_{FKT}), and during the sampling process (T_{MB} , T_{probe} , T_{W37} , T_{W55} , T_{W73}) obtained from different experimental sources. Thermocouple

- measurement of the perturbed flame (T_{TC}), perturbed flame (T_{Ma} , T_{FKT}), molecular beam temperature in a distance of one mm behind the orifice (T_{MB}). Equilibrium temperatures are calculated by solving Eq. (11-2) for temperature profiles for freezing of the water clusters determined from the equilibrium data for water cluster formation with $m/z = 37$ (T_{W37}), $m/z = 55$ (T_{W55}) and $m/z = 73$ (T_{W73}). 180
- Figure 11-12 a) Measured and simulated mole fraction profile of CH_3OH in flame A, equilibrium mole fraction (Eq. (11-2)) and simulated mole fraction of CH_3OH in flame B, b) Equilibrium mole fraction profile CH_3OH in flame B obtained by equation (Eq. (11-2)) with the measured perturbed temperature profile (T_{FKT} , T_{TC} , T_{MB}) as input. $(CH_3OH)H^+$ signal intensities profile is normalized to the maximum of the 1D-Simulation in flame B. The symbol / indicates the divisor. 182
- Figure 12-1. Scheme for the particle formation in flame synthesis. The violet curve indicates the decomposition of the precursor. The flame temperature is indicated by the yellow line. The first peak corresponds to gaseous Fe which was measured by Kluge et al. [57] and leads to the formation of solid particles [57] close to the burner surface. The second peak corresponds to the iron hydroxides measured by Karakaya et al. [62] which are present behind the flame front. The solid particle formation at the late stage of the flame was measured by Kluge et al. [57]. 189
-

List of table captions

Table 2-1.	Initial reactions of tetramethylsilane, TMS.....	6
Table 2-2.	Routes from monomer to cluster and particles.....	6
Table 2-3.	Reactions and routes of iron in the gas phase	8
Table 6-1.	Calculated ionization energy thresholds (at CCSD(T) and UCCSD(T)/aug-cc-pVTZ level of theory) and molecular geometries of the most abundant silicon containing species. Calibration factor (k) at 17 eV obtained with RICS method. The ionization potentials of most of the abundant silicon containing species are not available in literature.	57
Table 7-1.	Summary of flame conditions in the present work. Flow rates are in standard liter per minute (273.15 K, 1013.25 mbar).	73
Table 7-2.	Standard enthalpies of formation predicted by the G4-method.	78
Table 7-3.	List of reactions for describing TMS oxidation. Units of $k = A T^b \exp(-E_a/RT)$ are cm, s, mol, and K. As described in the text: Simulations were carried out using global reactions 14, 18, and 19. Reactions 14a–e, 18a–f, and 19a–e are suggested to explain the underlying chemistry behind these global processes and are discussed in the text. Also reactions 21 and 25–28 are global reactions. $\text{Si}_2(\text{OH})_8$ is envisioned as a hydrogen-bonded adduct of two $\text{Si}(\text{OH})_4$ molecules.	81
Table 7-4.	Source of reaction rates used in the TMS mechanism.	95
Table 8-1.	Initial flow rates of the flame gases are given in standard liter per minute (slm). Chamber pressure was 30 mbar. Flame A and B are taken from Karakaya et al. [86]. Flames C-H are new data from this work.....	104
Table 9-1.	Flame conditions. The reactant mixture entered the burner at 23 °C for all flames. The cooling water temperature was 25 °C. Chamber pressure was 30 Torr. Flow rates are given in SLPM.	117
Table 10-1.	Flame conditions in standard cubic centimeter per minute (scm).....	129
Table 10-2.	Mass-to-charge ratios (m/z), empirical cation formula and possible structures of ions with $m/z \leq 145$ in flame D. The designation $\cdot(\text{H}_2\text{O})_n$ indicates a hydrate. Bold structures are suggested to be the dominant isomers. $[\text{Si}/\text{SiH}_3\text{O}^+]$ ratios are calculated from integrated ion signal intensities at $\text{HAB} = 7$ mm. An ion signal ratio of zero indicates that the species is expected to be present but was not found in this experiment.	142
Table 11-1.	Flame conditions in standard cubic centimeter per minute. Flame A is analyzed with the aid of electron ionization MBMS, flame B is analyzed with the aid of electron ionization expansion sampling, flame C is analyzed by ion sampling. For flame B) and C) the same experimental setup is switched from expansion sampling with electron ionization to ion sampling.	155

List of publications

Peer-reviewed journal articles

1. Y. Karakaya, J. Sellmann, I. Wlokas, T. Kasper, Influence of the sampling probe on flame temperature, species, residence times and on the interpretation of ion signals of methane/oxygen flames in molecular beam mass spectrometry measurements, *Combust Flame* 209, 111388 (2021)
2. Y. Karakaya, S. Kluge, H. Wiggers, C. Schulz, Mass Spectrometric investigations of combustion of iron pentacarbonyl and the formation of key intermediates in iron oxide synthesis flames, *Chem. Eng. Sci.* 230, 116169 (2020)
3. Y. Karakaya, H. Janbazi, I. Wlokas, A. Levisch, M. Winterer, T. Kasper, Experimental and numerical study on the influence of the equivalence ratio on key intermediates and silica nanoparticles in flame synthesis, *Proc. Combust. Inst.* 38, Issue 1, 1375-1383 (2021)
4. H. Janbazi, Y. Karakaya, T. Kasper, C. Schulz, I. Wlokas, S. Peukert, Development and evaluation of a chemical kinetics reaction mechanism for tertamethylsilane-doped flames, *Chem. Eng. Sci.* 209, 115209 (2019)
5. Y. Karakaya, S. Peukert, T. Kasper, Mass spectrometric study on the combustion of tetramethylsilane and the formation of silicon-oxide clusters in premixed laminar low-pressure synthesis flames, *J. Phys. Chem. A* 122, 36, 7131-7141 (2018)
6. D. Krüger, P. Oßwald, M. Köhler, P. Hemberger, T. Bierkandt, Y. Karakaya, T. Kasper, Hydrogen abstraction ratios: A systematic iPEPICO spectroscopic investigation in laminar flames, *Combust Flame* 191, 343 – 352 (2018)
7. A. Alqaity, B. Chen, J. Han, H. Selim, M. Belhi, Y. Karakaya, T. Kasper, S. Sarathy, F. Bisetti, A. Farooq, New insights into methane-oxygen ion chemistry, *Proc. Combust. Inst.* 36, 1213 (2017)

Submitted journal articles for peer-review

1. T. Bierkandt, P. Oßwald, N. Gaiser, D. Krüger, M. Köhler, M. Höner, S. Shaqiri, D. Kaczmarek, Y. Karakaya, P. Hemberger, T. Kasper. Observation of low-temperature chemistry products in laminar premixed low-pressure flames by molecular-beam mass spectrometry, *Int. J. Chem. Kinet.* (Under review)
-

Conference contributions

This section comprises attendance at scientific conferences with the contribution of an *oral presentation* within year 2015-2021.

1. Y. Karakaya, H. Janbazi, I. Wlokas, A. Levish, M. Winterer, T. Kasper, Experimental and numerical study on the influence of the equivalence ratio on key intermediates and silica nanoparticles in flame synthesis, 38th International Symposium on Combustion, Web-based conference, Adelaide (2020). (Oral presentation)
 2. T. Kasper, Y. Karakaya, M. Gonchikzhapov, Reactions of iron-containing precursors for nanoparticles in synthesis flames, 4th International Symposium of Gas-phase Synthesis of Functional Nanomaterials: Fundamental Understanding, Modeling and Simulation, Scale-up and Application, Web-based conference, University of Duisburg-Essen, Germany (2020). (Oral presentation)
 3. H. Janbazi, Y. Karakaya, T. Kasper, C. Schulz, I. Wlokas, S. Peukert, Development and evaluation of a chemical kinetics reaction mechanism for tetramethylsilane-doped flames, 2020 4th International Symposium of Gas-phase Synthesis of Functional Nanomaterials: Fundamental Understanding, Modeling and Simulation, Scale-up and Application, Web-based conference, University of Duisburg-Essen, Germany (2020). (Oral presentation)
 4. Y. Karakaya, T. Kasper, Mass spectrometric study of the formation of key Intermediates in iron oxide synthesis flames, 2019 MRS Fall Meeting & Exhibition, Boston, Massachusetts, USA, December 1-6, 2019. (Oral presentation)
 5. Y. Karakaya, S. Kluge, I. Wlokas, H. Wiggers, C. Schulz, T. Kasper, Massenspektrometrische Untersuchung von Schlüsselintermediaten in Eisenoxid-Syntheseflammen, 29. Deutscher Flammentag, Ruhr-Universität Bochum, 17.-18. September 2019. (Oral presentation)
 6. Y. Karakaya, T. Kasper, Mass spectrometric investigation of key intermediates in synthesis flames, 3rd International Symposium of Gas-phase Synthesis of Functional Nanomaterials: Fundamental Understanding, Modeling and Simulation, Scale-up and Application, NETZ – NanoEnergyTechnologyCenter, University of Duisburg-Essen, Germany (2018). (Oral presentation)
 7. Y. Karakaya, T. Kasper, The effect of equivalence ratio variation on the flame structures of a laminar low-pressure tetramethylsilane/hydrogen flames, Joint Meeting the German and Italian Sections of the Combustion Institute, Sorrento, Italy (2018). (Oral presentation)
-

8. Y. Karakaya, A. Ditmann, T. Kasper, Massenspektrometrische Untersuchung der Gasphasensynthese siliziumhaltiger Nanopartikel in Flammenreaktoren, Thermodynamik-Kolloquium 2017, Universität Dresden, Germany (2017). (Oral presentation)
9. Y. Karakaya, T. Bierkandt, T. Kasper, Measurement of Protonated Ions as Sensitive Indicator for Neutral Polycyclic Aromatic Hydrocarbon Chemistry in Combustion by Time-of-Flight Mass Spectrometer, 64th American Society of Mass Spectrometry Conference, San Antonio, Texas, USA (2016). (Oral presentation)
10. T. Kasper, T. Bierkandt, Y. Karakaya, M. Köhler, P. Oßwald, D. Krüger, P. Hemberger, A. Bodi, T. Gerber, Multiplexing for isomer resolution in flame chemistry – photoelectron-photoion coincidence (PEPICO) Spectroscopy. 3rd Flame Chemistry Workshop, 30./31.07.2016, Seoul, South-Korea. (Oral presentation)

This section comprises the conferences participations with a *poster presentation* within year 2015-2020.

1. Y. Karakaya, T. Kasper, Mass spectrometric study of iron- and silicon-containing hydroxides and oxides in particle forming flames, Heraeus-Seminar Fuels, Processes, and Combustion Physics in the Energy Transformation, 8.- 12. March 2020, Bad Honneff, Germany. (Poster presentation)
 2. Y. Karakaya, T. Kasper, Massenspektroskopische Studie eisenhaltiger Schlüsselintermediate in Eisenoxid-Syntheseflammen, Thermodynamik-Kolloquium 2019, Universität Duisburg-Essen, Duisburg, 30.09. - 02.10.2019. (Poster presentation)
 3. Bierkandt, Thomas, Dominik Krüger, Patrick Oßwald, Markus Köhler, Dennis Kaczmarek, Yasin Karakaya, Joe Attiah, Patrick Hemberger, and Tina Kasper, Observation of alkyl hydroperoxides in laminar premixed alkane- and alkene-doped hydrogen flames at low-pressure, 29. Deutscher Flammentag, Ruhr-Universität Bochum, September 17-18, 2019. (Poster presentation)
 4. M. Köhler, T. Bierkandt, P. Oßwald, N. Gaiser, T. Kasper, M. Höner, D. Kaczmarek, Y. Karakaya, M. Gonchikzhapov, P. Hemberger, Novel VUV synchrotron-based reactor experiments for high-temperature reaction chemistry. Gordon Research Conference (GRC) Laser Diagnostics in Energy and Combustion Science, 23.-28.06.2019, Les Diablerets, Switzerland. (Poster presentation)
 5. Y. Karakaya, T. Kasper, Comparative mass spectrometric study of gaseous key intermediates from tetramethylsilane and hexamethyldisiloxane in silica synthesis flame, 9th European Combustion Meetin (ECM 2019), PT Meeting Center, Parque das Nações, Lisboa, Portugal, 14-17 April 2019. (Poster presentation)
-

6. T. Kasper, Y. Karakaya, A. Kempf, I. Wlokas, J. Sellmann, S. Kluge, H. Wiggers, R. Chrystie, T. Dreier, C. Schulz, I. Rahinov, Transient particle formation in the gas-phase synthesis of nanoparticles, CENIDE-Jahresfeier, Folkwang Universität der Künste, SANAA-Gebäude, Deutschland (2018). (Poster presentation)
 7. Y. Karakaya, S. Peukert, T. Kasper, Investigation of the decomposition of tetramethylsilane in premixed, laminar low-pressure flames by means of molecular-beam mass spectrometry, 37th International Symposium on Combustion, The Convention Center Dublin (CCD), Ireland (2018). (Poster presentation)
 8. Y. Karakaya, A. Dittmann, T. Kasper, Decomposition of tetramethylsilane in laminar premixed low-pressure flames, International Bunsen Discussion Meeting: Chemistry and Diagnostic for Clean Combustion, Bielefeld, Germany (2017). (Poster presentation)
 9. Y. Karakaya, L. Deng, I. Wlokas, M. Höner, T. Kasper, Molecular-beam mass spectrometric and numerical investigation of the intrusive flame sampling effect on premixed low-pressure flame structure, 65th American Society of Mass Spectrometry Conference, Indianapolis, USA (2017). (Poster presentation)
 10. Y. Karakaya, T. Bierkandt, T. Kasper, Towards quantification of neutral species from naturally occurring ions in laminar low-pressure flames, European Combustion Meeting 2017, Dubrovnik, Croatia (2017). (Poster presentation)
 11. D. Krüger, M. Köhler, P. Oßwald, T. Bierkandt, Y. Karakaya, P. Hemberger, T. Kasper, Systematic iPEPICO spectroscopic investigation on H-abstraction reaction on differently bonded hydrogen atoms in laminar flames, 8th European Combustion Meeting (ECM), 18.-21.04.2017, Dubrovnik, Croatia. (Poster presentation)
 12. D. Krüger, M. Köhler, P. Oßwald, T. Bierkandt, Y. Karakaya, P. Hemberger, T. Kasper, Systematische Untersuchung von H-Abstraktionsreaktionen in laminaren Niederdruckflammen mittels Photoelektronen-Photoionen-Koinzidenz-Spektroskopie (PEPICO). 116. Hauptversammlung der Deutschen Bunsen-Gesellschaft für Physikalische Chemie, 25.-27.05.2017, Kaiserslautern. (Poster presentation)
 13. Y. Karakaya, T. Bierkandt, S. Kluge, T. Kasper, Characterisation of charged decomposition products of iron pentacarbonyl and particle growth of iron oxide nanoparticles in synthesis flames, 2016 MRS (Material Research Society) Fall Meeting & Exhibit, Boston, MA, USA (2016). (Poster presentation)
 14. Y. Karakaya, T. Kasper, Ions as sensitive indicators for neutral polycyclic aromatic hydrocarbon in combustion processes, 36. International Symposium on Combustion, Seoul, South Korea (2016). (Poster presentation)
-

15. D. Krüger, M. Köhler, P. Oßwald, T. Bierkandt, Y. Karakaya, P. Hemberger, T. Kasper, Systematic investigation on fuel radical species in low-pressure hydrogen flames doped with butanes and butenes using iPEPICO spectroscopy, 36. International Symposium on Combustion, 31.07.-05.08.2016, Seoul, Korea. (Poster presentation)

Workshops

Oral presentations in internal workshops within the DFG research unit FOR2284 (year 2015-2021)

DuEPublico

Duisburg-Essen Publications online

UNIVERSITÄT
DUISBURG
ESSEN

Offen im Denken

ub

universitäts
bibliothek

Diese Dissertation wird via DuEPublico, dem Dokumenten- und Publikationsserver der Universität Duisburg-Essen, zur Verfügung gestellt und liegt auch als Print-Version vor.

DOI: 10.17185/duepublico/74528

URN: urn:nbn:de:hbz:464-20210708-102250-6

Alle Rechte vorbehalten.